Department of Condensed Matter Physics

Advanced Force Spectroscopy Applications: Three-Dimensional AFM and Single-Molecule Force Spectroscopy

A thesis submitted to the Universidad Autónoma de Madrid in accordance with the requirements of the degree of Doctor in Philosophy by

Manuel Ralph Uhlig

Director:
Prof. Ricardo García García

Instituto de Ciencia de Materiales de Madrid
Consejo Superior de Investigaciones Científicas

October 2019

Contents

Abstract

When it comes to the nanoscale, the Atomic Force Microscope (AFM) is one of the most widely used tools in science and technology. Its success is based on its atomic-scale resolution and force sensitivity down to the level of individual bonds. The AFM's arguably most particular advantage is, however, its outstanding versatility. It can be applied to virtually any sample, from single molecules at low temperatures in ultra-high vacuum over polymers in ambient conditions to living cells in their liquid growth medium. The reason for this universality lies in its unique working principle based on the sensing of forces. Most intuitively, forces arise primarily from mechanical interactions, which is why the AFM emerged as the reference tool to quantify local mechanical properties at the nanoscale. However, forces are actually footprints of a plethora of physical quantities such as viscosity, charge, surface potential or magnetization. Knowing these quantities in turn opens many avenues to study complex physical, biological and chemical processes.

There is a large number of AFM modes aiming to quantify forces. Some of the most successful ones fall into the category of AFM Force Spectroscopy. Before the invention of the AFM, the field of force spectroscopy was pioneered by the surface force apparatus which paved the way for the understanding of forces between two objects at nanoscale distances. Building on that, AFM force spectroscopy advanced one step further by providing a locally confined probe, which achieves potentially up to atomic-scale spatial resolution in all three dimensions. Some of the most important recent activities and frontiers of the field are related to the speed and sensitivity limits of established force spectroscopy tools. More sophisticated techniques such as high-speed AFM force spectroscopy or 3D-AFM have emerged recently to eventually overcome current limitations. This thesis is dedicated to address some aspects of these techniques in order to improve device performance to gain further insight into complex samples. It is divided into 5 chapters which are briefly outlined in the following.

Chapter 1 introduces the AFM in general, places it in the historical context and summarizes its main functionalities and components. A special focus lies on reviewing AFM approaches to study solid-liquid interfaces, in particular the three-dimensional AFM (3D-AFM).

Chapter 2 is dedicated to the development of a software suite for a 3D-AFM operated in amplitude modulation (AM 3D-AFM). The goal of this chapter is twofold: First, to have a tool at hand for analyzing the data presented throughout this thesis. Second, to provide a foundation for establishing AM 3D-AFM as a technique to study solid-liquid interfaces easily accessible for other scientists.

Chapter 3 presents an application of AM 3D-AFM to a class of materials that has attracted immense interest over the last decade: 2D materials. The solid-liquid interface of a variety of layered materials immersed in ultrapure water is studied, including mono-, few-, and multilayer sheets of graphene and transition metal dichalcogenides. The images reveal a universally occurring structuring of the liquid in the vicinity of the surfaces. It is shown that the observations are related to the hydrophobicity of these surfaces and their interaction with airborne adsorbates.

Chapter 4 follows up on the findings of Chapter 3. 3D-AFM is used to study the solid-liquid interface of pentacene thin-films in electrolyte solution. The obtained results are not only of potentially high relevance for technological applications of this class of materials, but also represent a major step forward in the capabilities of AM 3D-AFM applied on topographically complex surfaces.

Chapter 5 is devoted to an AM 3D-AFM study of the muscovite mica-electrolyte interface. By increasing the sensitivity of the AM 3D-AFM, K+ ions adsorbed to the mica surface are visualized and features of individual ions and their hydration structure are identified. A comparison with reported X-ray reflectivity data verifies the results. The findings strengthen 3D-AFM as a unique tool for studying solid liquid interfaces with very high out-of-plane and unrivaled in-plane resolution.

Chapter 6 addresses three different aspects of force spectroscopy at the single-biomolecule level:

The first section investigates up to which limit the use of the Hooke's law is justified in fast single-molecule force spectroscopy (SMFS). Experiments are performed on the biotin-avidin system that demonstrate deviations from the standard description of forced unbinding. By developing an analytical equation of motion for SMFS the observations are explained in terms of cantilever dynamics occurring at high velocities. With the help of simulations a general criterion is found for the range of accuracy of the Hooke's law. A correction factor is provided and applied on the experimental data to recover the intrinsic unbinding forces at any speed.

The second section is devoted to biorecognition, *i.e.*, SMFS employed to localize and identify species at the nanoscale. The technique is used to verify a functionalization protocol which promotes locally restricted adsorption of avidin onto the active element of a biosensor.

The third section aims to determine the mechanical response of a single antibody by using AFM indentation. A stiffness value for the elastic response of an IgG antibody is obtained and compared to MD simulations performed on the same protein.

Resumen

Cuando se habla de nanoescala, el Microscopio de Fuerza Atómica (AFM, por sus siglas en inglés) es una de las herramientas más usadas en ciencia y tecnología. Su éxito está basado en su resolución a escala atómica y en la sensibilidad de fuerza hasta el nivel de los enlaces individuales. Sin embargo, la mayor ventaja del AFM es probablemente su destacada versatilidad. Puede aplicarse prácticamente a cualquier muestra, desde moléculas individuales a bajas temperaturas en ultra vacío sobre polímeros en condiciones ambientales, hasta células vivas en su medio líquido de crecimiento. La razón de su universalidad reside en su único principio de trabajo basado en la detección de fuerzas. Más intuitivamente, las fuerzas surgen principalmente de interacciones mecánicas, que es por lo que el AFM emergió como la herramienta de referencia para cuantificar propiedades mecánicas locales a nanoescala. Sin embargo, las fuerzas son de hecho rastros de un sinfín de cantidades físicas como la viscosidad, la carga, el potencial superficial o la magnetización. A cambio, conocer estas cantidades ofrece muchas posibilidades para estudiar complejos procesos físicos, biológicos y químicos.

Hay un gran número de modos de AFM dirigidos a cuantificar fuerzas. Algunos de los más exitosos caen en la categoría de AFM espectroscopia de fuerza. Antes de la invención del AFM, el campo de la espectroscopia de fuerza estuvo liderada por el aparato de fuerzas de superficie, que allanó el camino para el entendimiento de fuerzas entre dos objetos a distancias nanométricas. A partir de aquello, la espectroscopia de fuerza AFM avanzó un paso más al proporcionar una sonda confinada localmente, que potencialmente logra resolución espacial a escala atómica en las tres dimensiones. Algunas de las actividades recientes más importantes y fronteras del campo están relacionadas con los límites de velocidad y de sensibilidad de los instrumentos de espectroscopia de fuerza. Técnicas más sofisticadas como la espectroscopia de fuerza AFM de gran velocidad o 3D-AFM han surgido recientemente para superar las limitaciones actuales. La tesis se dedica a abordar algunos aspectos de estas técnicas a fin de mejorar el rendimiento de los dispositivos para comprender mejor muestras complejas. Está dividida en cinco capítulos, que se describen brevemente a continuación.

El **Capítulo 1** introduce el AFM en general, lo localiza en el contexto histórico y resume sus principales funciones y componentes. Se prestará especial atención a revisar los enfoques de AFM que estudian las interfaces sólido-líquido, en particular, en el AFM tridimensional (3D-AFM).

El **Capítulo 2** se dedica al desarrollo de un paquete de software para un 3D-AFM operado en modulación de amplitud (AM 3D-AFM). El propósito de este capítulo es doble: Primero, tener una herramienta disponible para analizar los datos que se presen-

tan en toda la tesis. Segundo, proporcionar una base para establecer AM 3D- AFM como una técnica para estudiar interfaces sólido-líquido fácilmente accesible a otros científicos.

El **Capítulo 3** presenta una aplicación del AM 3D-AFM a una clase de materiales que ha atraído un enorme interés en la última década: los materiales 2D. Se estudia la interfaz sólido-líquido de una variedad de materiales laminados inmersos en agua ultrapura, incluyendo láminas monocapa, de pocas capas y multicapa de grafeno y de los calcogenuros de metales de transición. Las imágenes revelan la estructuración universal del líquido en las proximidades de las superficies. Se muestra que las observaciones están relacionadas con la hidrofobia de estas superficies y su interacción con partículas aéreas disueltas en el agua.

El **Capítulo 4** continúa con los descubrimientos del capítulo 3. La 3D-AFM se usa para estudiar la interfaz sólido-líquido de películas finas de pentaceno sumergidas en una solución electrolítica. Los resultados obtenidos no solo pueden ser de gran relevancia para aplicaciones tecnológicas de esta clase de materiales, sino que también representan un importante avance en las capacidades de la AM 3D-AFM aplicada a superficies topográficamente complejas.

El **Capítulo 5** se dedica a un estudio AM 3D-AFM de la interfaz mica moscovita – electrolito. Al aumentar la sensibilidad del AM 3D-AFM, los iones K+ absorbidos por la superficie de mica se visualizan y se identifican las características de los iones individuales y de su estructura de hidratación. Una comparación con datos de la reflectividad de rayos X publicados, verifica los resultados. Los hallazgos refuerzan al 3D-AFM como una herramienta única para estudiar las interfaces sólido líquido con muy alta resolución fuera del plano y resolución incomparable en el plano.

El **Capítulo 6** aborda tres aspectos diferentes de la espectroscopia de fuerza al nivel de una biomolecula:

La primera sección investiga hasta qué nivel el uso de la ley de Hooke está justificado en espectroscopia de fuerza de moléculas individuales (SMFS, por sus siglas en inglés) de alta velocidad. Los experimentos se llevan a cabo en un sistema de biotina- avidina. Los resultados muestran desviaciones de la descripción estandar de ruptura forzada. Al desarrollar una ecuación analítica del movimiento para SMFS las observaciones se explican en términos de la dinámica de la palanca a grandes velocidades. Con la ayuda de simulaciones se encuentra un parámetro general que permite determinar en qué medida los valores se desvían de la ley de Hooke. Se proporciona un factor de corrección y se aplica en los datos experimentales para recuperar las fuerzas intrínsecas de ruptura a cualquier velocidad.

La segunda sección se dedica al reconocimiento molecular, es decir, SMFS empleado para localizar e identificar especies a nanoescala. La técnica se usa para verificar un protocolo de funcionalización que promueve la absorción restringida local de avidina en el elemento activo de un biosensor.

La tercera sección pretende determinar la respuesta mecánica de un anticuerpo indi-

vidual usando indentación de AFM. El valor de rigidez para la respuesta elástica de un anticuerpo IgG se obtiene y se compara con las simulaciones MD llevadas a cabo en la misma proteína.

1. Introduction

1.1. A Brief History

In 1981, Gerd Binnig and Heinrich Rohrer developed the Scanning Tunneling Microscope (STM) [1]; an invention awarded by the Nobel Prize in physics later in 1986. With the STM researches were capable of detecting displacements as small as 10^{-4} Å, or 10^{-14} m. This was a great step forward in surface science, although the range of samples that could be measured was limited. In order to allow for a tunneling current between the tip and the sample, only samples with a conductive surface, such as semiconductors and metals, can be imaged by the STM. Furthermore, some applications require ultra-high vacuum (UHV). For overcoming these limitations, in 1986, Gerd Binnig, Calvin F. Quate, and Christoph Gerber came up with the idea of sensing mechanical forces with a sharp nanoscale tip as tactile element. By connecting the tip to a tiny leaf spring, the so-called cantilever, the forces acting on the tip were transformed into deflections of the cantilever. By using the STM to read out these deflections, the STM's spacial sensitivity was converted into tactile information. This led to the first experimental implementation of the Atomic Force Microscope (AFM) [2]. Quickly, the AFM proved to be an extremely versatile tool for surface characterization. The AFM is applicable to virtually any kind of sample (irrespective of being conductive or isolating, crystalline or amorphous) and environment (from UHV over ambient air to liquid). Furthermore, it offers subnanometer spatial resolution in three dimensions; not only in terms of sample topography, but also obtaining mechanical information. Simultaneously, magnetic [3], electrical [4] and many other properties can be obtained at the nanoscale. A few noteworthy milestones in the history of AFM are the detecting of the rupture of individual molecular bonds [5], the imaging of chemical bonds by using a CO molecule as tip apex [6] and the video imaging of a walking myosin by high-speed AFM [7]. In 2016, the inventors of the AFM were honored by the *Kavli Prize in Nanoscience*, acknowledging the microscope's "transformative impact on nanoscience and technology" [8].

1.2. AFM Working Principle

Figure 1.1a illustrates schematically the main components and functionalities of an AFM. The basic principle consists in local mechanical sensing of the surface by using a probe. The probe is formed by a nanoscopic tip which is attached to the front end of the cantilever; a microscopic leaf spring. Piezo elements allow for precise movements of the probe relative to the sample in the three spatial dimensions x, y, and z. In addition, it is possible to oscillate the cantilever, typically at one of its resonance frequencies.

The force between the tip and the sample affects the cantilever deflection or, in the case of the oscillating cantilever, its dynamic properties. These changes can be read out with high sensitivity, nowadays typically by using the optical lever principle. To this end, a laser beam (the so-called read-out laser) is focused on the cantilever's back side and its reflex is recorded by a four-quadrant photo diode. Then, the voltage difference between the quadrants allows for determining the cantilever deflection and, if the cantilever is excited, the oscillation amplitude. In the following, the AFM components and operational modes that are relevant for this thesis will be briefly reviewed.

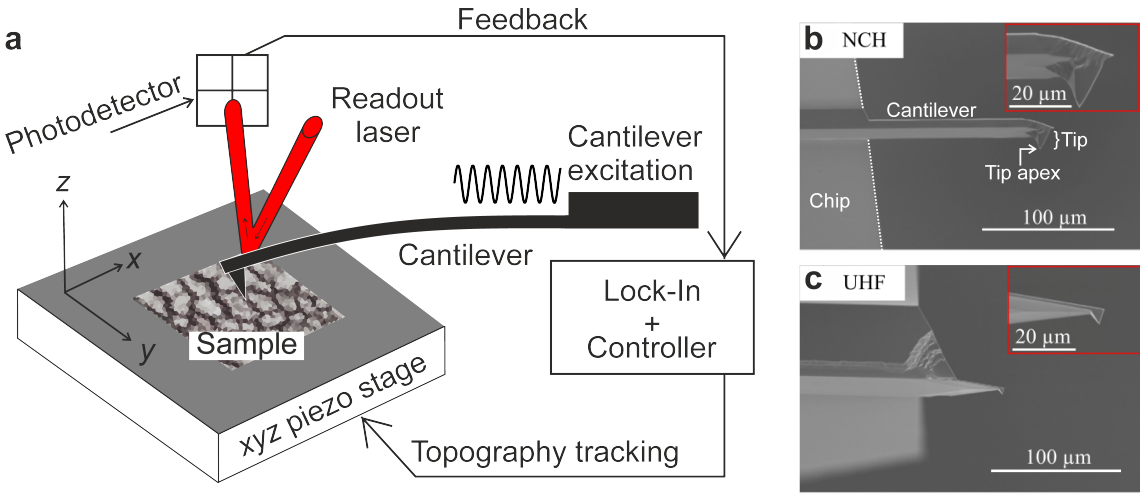

Figure 1.1.: a. Scheme of the main components and working principle of an AFM. **b.** and **c.** SEM images of different cantilevers and tips which were also used in this thesis. Panel b shows a rectangular, standard-sized cantilever (PPP-NCH) while panel c depicts a shorter one with a triangular shape (Arrow UHF). Panel b and c are adapted from Reference [9].

1.2.1. Cantilever and Tip

The AFM probe consists of three elements: the chip, the cantilever and the tip. An example of a widely used AFM probe is shown in Figure 1.1b (PPP-NCH, Nanosensors). The chip is a rather large, macroscopic structure (a few mm) that basically serves for handling and clamping the probe. At the edge of the chip, the cantilever is attached (length of 10-200 µm). The cantilever represents a leaf spring with characteristic static and dynamic properties, that are determined by its dimensions, shape, and material. At the end of the cantilever in turn, the tip is placed (height of 1-15 µm). The very end of the tip, its apex, is of nanoscopic dimension. During a measurement, the tip apex interacts with the sample and experiences the tip-sample forces. Its characteristics are highly important for the imaging process and in particular its shape poses a fundamental limit for the maximum spatial resolution that can be achieved in an AFM experiment. The proper choice of cantilever and tip are key for the performance of the AFM in a given experiment.

In the following, some fundamental considerations regarding the cantilever will be introduced. The cantilever serves different purposes. First, its static properties allow to measure forces by transforming them into a deflection that can be read out by the detector system (see below). Second, with its dynamic properties, the cantilever acts as an oscillator which is key for dynamic AFM modes.

In the static case, the deflection Δz is related to the force F by the Hooks law

$$F = k_0 \Delta z \tag{1.1}$$

where k_0 is the cantilever's static spring constant. For an ideal cantilever with a rectangular cross section, the spring constant k_0 can be determined from the cantilever geometry by [10]

$$k_0 = 3\frac{EI}{L^3} \tag{1.2}$$

where E is the Young's modulus of the cantilever material; and L and I are, respectively, the cantilever's length and area moment of inertia. The latter can be obtained from the cantilever's width, W, and its thickness, T, by $I = WT^3/12$.

However, real cantilevers often have more complex shapes and their fabrication process underlies variations (in particular regarding the thickness) which makes the use of Equation 1.2 impractical for the determination of k_0. Instead it is commonly determined for each cantilever individually by performing a calibration [11]. Since different calibration procedures were used in this thesis, the specific procedure is described in detail in each chapter. The most common ways to calibrate the cantilever stiffness are the Sader method [12] and the thermal method [13]. Both methods actually yield the dynamic cantilever stiffness k_n rather than the static one, k_0. However, both stiffnesses are related as will be shown in the following. In general, the dynamic stiffness k_n is specific for each nth eigenmode of the cantilever. Again, it can be calculated from the cantilever geometry by

$$k_n = \frac{EI}{L^3}\frac{\alpha_n^4}{4} \tag{1.3}$$

where α_n is a mode-specific factor that determines each mode's wavelength, L/α_n [14]. For the first two modes, $\alpha_1 = 1.8751$ and $\alpha_2 = 4.6941$ [14]. Comparing Equation 1.2 and Equation 1.3 yields the ratio $\frac{k_1}{k_0} \approx 1.03$ which is convenient for calculating k_0 after having calibrated k_1. Similar relationships can be found for the stiffness of different modes, k_n, as well as for the respective resonance frequencies f_n, Q factors Q_n (see next section), and inverse optical lever sensitivities (invOLS) σ_n (see below). **Table 1.1** summarizes the respective conversion factors between the modes up to the 2nd one (*i.e.*, $n \leq 2$) [15].

Table 1.1.: Relationships between the stiffnesses k_n, resonance frequencies $f_{r,n}$, Q factors Q_n, and inverse optical lever sensitivities (invOLS) σ_n of the nth modes for a rectangular cantilever up to $n = 2$ [15].

n	f_n	k_n	Q_n	σ_n
0	-	$k_0 = \frac{1}{1.03} k_1$	-	$\sigma_0 = \frac{1}{1.09} \sigma_1$
1	f_1	k_1	Q_1	σ_1
2	$f_2 = 6.27 f_1$	$(f_2/f_1)^2 k_1 = 39.31 k_1$	$(f_2/f_1) Q_1 = 6.27 Q_1$	$\sigma_2 = \frac{1}{3.473} \sigma_1$

For most commercial AFMs, the cantilever deflection or its oscillation are read out using the optical lever principle [16, 17]. It consists of focusing a laser beam (the read-out laser) on the cantilever's back side and recording its reflex with a four-quadrant photo diode (see red laser beam in Figure 1.1). The voltage difference between the quadrants is a measure for the cantilever deflection and, if the cantilever is excited, the oscillation amplitude. By using four quadrants the vertical and horizontal components of the movements can be separated, which allows to measure torsional signals [18], such as lateral friction forces [19] or the oscillation of torsional modes [20].

In order to convert the voltage signal of the photo diode into units of distance, the sensitivity of the optical lever system has to be calibrated [11]. The most common way to perform this calibration is by approaching the tip against a very stiff surface (force-displacement curve). If the tip is in contact with an infinitely stiff surface, it cannot indent. Under this assumption, any downward movement of the z-piezo results in a deflection of the cantilever of the very same magnitude. Then the inverse of the curve's slope in the contact part is equivalent to the inverse optical lever sensitivity (invOLS) for the static deflection, σ_0. Since the invOLS depends on several components within the optical path and furthermore on the individual cantilever, laser spot position, and focus position, it is necessary to perform an individual calibration for each experiment that aims to be quantitative.

1.2.2. Amplitude Modulation AFM

In order to obtain images of the sample surface, different static and dynamic AFM modes are available. One of the most common dynamic AFM modes is amplitude modulation AFM (AM-AFM). It is sometimes also referred to as Tapping Mode™ or intermittent contact mode [10]. The terminology suffers to some extend from ambiguity because different names are used for different regimes of the AM operation. A general classification can be performed by taking into account the tip-sample force. In AM-AFM, the cantilever is excited and oscillates with a certain amplitude. Throughout its oscillation cycle, the tip probes a variety of tip-sample forces. If the net force (the tip-sample force integrated over an entire oscillation cycle) is negative or positive, the oscillation regime of the cantilever can be denoted as *attractive* or *repulsive*. Sometimes, the attractive regime is associated with a *noncontact* operation. This, however, is not true in general. The repulsive regime, in turn, is often connected to the idea that the tip touches the sample surface in the lower turnaround point of the oscillation cycle (hence the name intermit-

tent contact mode or Tapping Mode^{TM}). This characteristic concept is illustrated in **1.2**a. In fact, both regimes are two coexisting solutions of the same differential equation used to describe the cantilever motion [21]. The actual oscillation regime is determined by the given boundary conditions. In an experiment, these conditions are determined by several parameters, such as the behavior of the tip-sample force, the oscillation amplitude, the tip-radius, and others [22]. Irrespective of the particular oscillation regime, the term AM-AFM refers to an AFM operation based on reading out the amplitude and using it as the feedback parameter. This criterion allows a clear disctinction between AM-AFM and the second important dynamic mode, frequency modulation (FM), where the amplitude is not a necessary feedback variable.

AM-AFM combines high-resolution capabilities with low invasiveness, making it attractive for the investigation of fragile surfaces such as soft polymers and biological specimens. This advantage together with its robust operation in different environments promoted AM-AFM to become the most frequently used AFM mode in ambient air as well as liquid. Apart from the topography, qualitative nanomechanical information can be obtained through the phase channel ϕ [23]. The phase channel is obtained from the phase shift between the excitation signal and the cantilever oscillation.

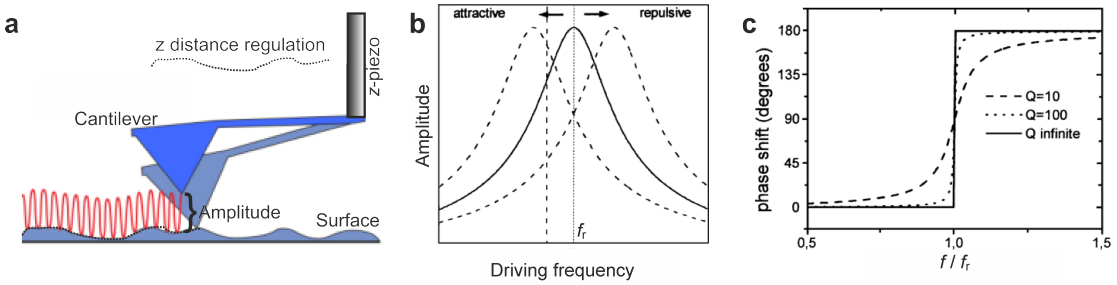

Figure 1.2.: **a.** Simplified illustration of amplitude modulation AFM. The cantilever is oscillating at its resonance frequency and the tip touches the sample surface in the lower turnaround point of the oscillation. **b.** Oscillation amplitude as a function of the drive frequency (solid line). Under the influence of an external force, the cantilever's resonance frequency changes to lower (net attractive force) or higher (net repulsive force) values (dashed lines). **c.** Phase lag between the tip oscillation and the cantilever excitation for different Q factors. Panel b and c adapted from Reference [24].

In the following, some basic theoretical aspects of the AM operation will be briefly reviewed. The cantilever is excited at or close to its first resonance frequency f_1. Sometimes resonance frequencies of higher modes are excited, or even a combination of them [15]. In any case, the resulting tip motion can be described as a simple harmonic oscillator (SHO). To this end, the tip is considered as a point-mass attached to a weightless cantilever spring. In such a system, the tip's effective mass m^* and the spring constant k_1

define the intrinsic angular resonance frequency $\omega_\mathrm{r} = 2\pi f_1$ as

$$\omega_\mathrm{r} = \sqrt{\frac{k_1}{m^*}} \tag{1.4}$$

Taking the excitation into account, the tip motion follows the equation of motion of a driven harmonic oscillator [24]

$$m^*\ddot{z} + kz + \gamma\omega_\mathrm{r}^2\dot{z} = F_\mathrm{ts} + F_\mathrm{d}\cos(\omega_\mathrm{d}t)$$

where γ is the damping coefficient, t the time, z the spatial coordinate, F_ts the overall tip-sample force, and F_d and ω_d are, respectively, the amplitude and the angular frequency of the periodic driving force. It is convenient to express the damping with the Q factor Q given by:

$$Q = \frac{m^*\omega_\mathrm{r}}{\gamma}$$

The oscillation amplitude of a driven harmonic oscillator assumes a maximum at its resonance frequency (see Figure 1.2b, solid line). The free oscillation amplitude, A_0, can range from hundreds of nm to tens of pm, depending on the experiment. An external force F_ts shifts the resonance frequency of the tip-sample system which manifests itself in a change in the amplitude A (Figure 1.2b, dashed lines). When performing an experiment, the oscillation amplitude is permanently monitored by a lock-in amplifier. In AM-AFM, the controller approaches the cantilever in z-direction towards the sample until the tip-sample interaction reduced the amplitude A to the preset set-point amplitude, A_sp. For performing the scanning motion, the piezo actuators raster the tip across the sample in the x and the y direction. At each point (x, y), the oscillation amplitude is measured and fed back to the controller. The controller keeps the actual amplitude as close as possible to the set-point amplitude by regulating the z-position of the cantilever base. The resulting movement of the z-piezo at each position (x, y) can be interpreted as sample topography (this is illustrated in 1.2a). At the same time, the lock-in reads out the phase shift ϕ between the excitation signal and the cantilever oscillation. The phase shift is related to the interplay of conservative and dissipative tip-sample interactions. For an ideal harmonic oscillator that is freely oscillating, the phase lag of the tip is 90 deg relative to the excitation signal (Figure 1.2c) [24]. Note that there are different conventions regarding this value within the AFM community. Throughout this thesis, the phase shift of the freely oscillating cantilever is set to be 90 deg.

1.2.3. Force Spectroscopy

In the AFM mode described in the previous section as well as in many other scanning modes, the tip is rastered horizontally across the sample in order to obtain images (isosurfaces) of the sample. On the other hand, by moving the probe vertically to the sample at a given horizontal position (x,y), spectroscopic measurements can be performed. The simplest way, from the experimental point of view, is performing static force spectroscopy [25]. In static force spectroscopy, or contact-mode force spectroscopy,

the cantilever deflection Δz is monitored while the cantilever base is moved vertically by the z-piezo. If k_0 is known, the corresponding force can be calculated from the measured deflection using Hooke's law, $F = k_0 \Delta z$. Technically, the AFM controls the position of the cantilever's base, z_c. Physically relevant, however, is the tip-sample distance, d. The principle of converting z_c into d can be deduced from a simple geometrical consideration (see **Figure 1.3**a):

$$d = z_c - z_0 + \Delta z \tag{1.5}$$

where z_0 is the z_c-position at which the tip starts to touch the surface. Such a measurement yields a force-displacement $(F - z_c)$ or force-distance $(F - d)$ curve. Usually, a force-distance curve consists of an approach curve and a retraction curve.

As in scanning, also force spectroscopy can be performed while the cantilever is oscillated (dynamic force spectroscopy). This case is illustrated in Figure 1.3b. Then, equation 1.5 has to be modified into

$$d = z_c - z_0 + \Delta z - A \tag{1.6}$$

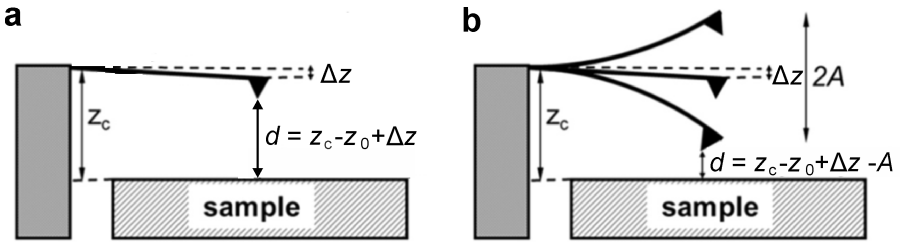

Figure 1.3.: Illustration of the different distances involved when recording AFM spectroscopy curves. **a.** Static AFM force spectroscopy. **b.** Dynamic AFM force spectroscopy. z_c is the position of the cantilever base, Δz the static (average) cantilever deflection, A the cantilever oscillation amplitude, z_0 an offset that accounts for the tip-sample contact point, and d the minimum tip sample distance. Adapted from Reference [26].

In either case, the z-piezo approaches until the observable (typically the deflection in static force spectroscopy and the amplitude in AM force spectroscopy) reaches a user-defined threshold value, the so-called trigger.

1.2.4. Three-Dimensional AFM

In the previous sections, the two types of AFM experiments were introduced: scanning and force spectroscopy. While the former obtains information about an xy plane (2D), the latter measures the tip-sample interaction as a function of the vertical coordinate z (1D). Already quite early attempts were made to measure the interaction between the AFM tip and the specimen in three dimensions (3D). In this way, force data would be obtained that covers a volume including not only the sample surface but also information that belongs to regions above and below the surface [27–30]. Such Force-Volume (FV) modes are realized in two ways: First, by sequential scanning of isosurfaces (xy) that

are individually separated by a vertical offset (z) [31,32]. Second, by acquiring AFM spectroscopy curves (z) over positions in a predefined grid (xy) [33]. In both cases, the obtained data is finally mounted together in a three dimensional matrix to render a volume. **Figure 1.4**a-b illustrates the tip movements for both approaches schematically.

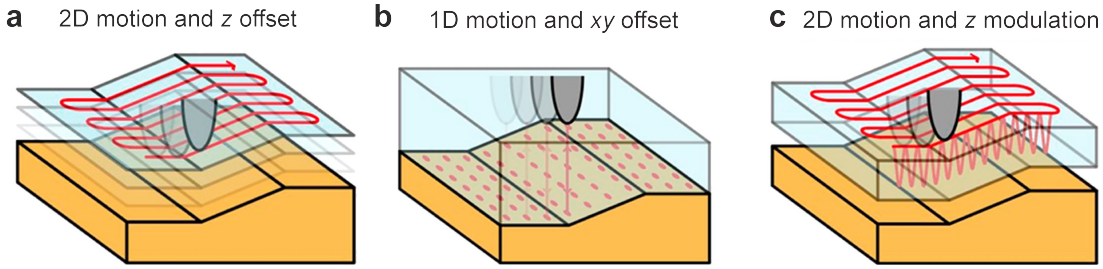

Figure 1.4.: Illustration of the different realizations of three-dimensional AFM data acquisition. **a.** Sequential scanning of isosurfaces (xy) that are individually separated by a vertical offset (z). **b.** Point-by-point trigger-based acquisition of AFM spectroscopy curves (z) over positions in a predefined grid (xy). **c.** Applying a sinusoidal z motion while maintaining the 2D scan motion (xy) controlled by a feedback. Adapted from Reference [34].

The first approach is successfully used in UHV applications at low temperature; conditions that provide the necessary stability for this imaging mode. The acquisition of such an image requires a long time (in the order of hours) and still yields only a pm-sized volume. [31,32,35] In contrast, the latter approach turned out to be very robust and was widely adapted by the AFM community for a variety of applications in ambient air and liquid. The imaged volume can cover up to several µm in all three dimensions. The family of FV techniques found a variety of applications, from polymers [29] over single molecules [36] to cell nanomechanics [30,37]. Several (commercial) developments have optimized the classical FV approach, *e.g.,* PeakForce Quantitative Nanomechanical Mapping (PF QNM) [38], Quantitative Imaging^{TM} (QI) [39], PulsedForce Mode [40], or Jumping Mode [41]. Still, all these modes can be classified as FV approaches since they rely on a trigger-based point-by-point acquisition of force-displacement curves. In spite of the enormous success of FV approaches, they are altogether slow which makes them unsuitable for atomic-scale resolution imaging in liquid. In 2010, Fukuma and coworkers introduced a new technique denoted as three-dimensional scanning force microscopy (3D-SFM, but for simplicity hereafter referred to as 3D-AFM) [42]. 3D-AFM combines a sinusoidal movement in z with scanning along x and y, thereby covering the whole 3D interfacial space (see Figure 1.4c). In contrast to FV-modes, the imaging process in 3D-AFM is based on a feedback instead of a trigger value. By maintaining the standard (feedback-based) in-plane scan motion, the acquisition time for an entire volume can be less than 1 minute while atomic resolution is achieved. The key development was to introduce a sinusoidal z-modulation that is fast enough to be unaffected by the feedback's distance regulation. While Fukuma's version of the 3D-AFM was developed for frequency modulation (feedback on the frequency shift with respect to the actual

resonance frequency, Δf), its working principle is compatible with any dynamic AFM mode. Soon, the groups of García and Kühnle developed 3D-AFMs operating in other modes such as amplitude modulation [43,44] or bimodal AFM [45]. The success of 3D-AFM lies in the fact that it offers a unique tool to investigate solid-liquid interfaces with atomic-scale resolution in all three spatial dimensions.

1.3. Solid-Liquid Interfaces

Solid liquid interfaces (SLIs) are ubiquitous in nature since they form anywhere a solid meets a liquid (**Figure 1.5**). While the solid and liquid are well-characterized by their respective bulk properties, the nanoscopic SLI has a peculiar structure that differs from both the solid and the liquid. This gives rise to unique properties such as a high reactivity which makes SLI very important for a number of processes in nature and technology. Examples of SLI related phenomena of fundamental importance include wetting [46,47], dissolution [48,49], catalysis [50], adhesion [51], biomineralization [52], surface electrochemistry [53], surface fouling [54], nanorheology [55], protein folding [56,57] and molecular recognition [57,58].

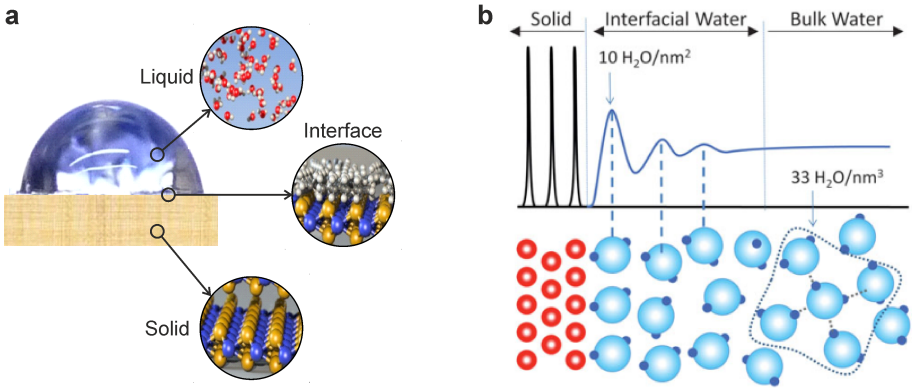

Figure 1.5.: Some fundamental aspects of the interface between a solid and a liquid. **a.** Illustration of the formation of a nanoscopic interface between a bulk solid and a bulk liquid. **b.** Liquid ordering next to a hydrophilic, crystalline solid surface (scheme of an electron density graph as measured by X-ray reflectivity). The solid (oscillating density) and the bulk liquid (constant density) are both characterized by their individual bulk properties. The interfacial water is, however, characterized by a particular structure that is promoted by the proximity of the solid surface. Panel b adapted from Reference [59].

Up to date, only a few methods are available to investigate solid–liquid interfaces *in situ*. Techniques for studying surfaces based on using electrons or ions cannot penetrate through the liquid phase. Only photon- [60] and neutron-based [61,62] techniques can provide information about the solid–liquid interface. In particular X-ray scattering (or X-ray reflectivity, XRR) is widely used to probe the interfacial hydration structure [59,60]. While XRR achieves angstrom-scale spatial resolution in the surface-normal direction, its

Achilles' heel is the restricted lateral resolution. XRR averages the information over the footprint of the beam, thereby losing in-plane information. While lateral information can be achieved to some extend for the case of well-ordered crystalline surfaces by using non-specular rods [60,63,64], information at irregular surfaces or at singular features surface defects such as steps is in principle not accessible. In any case, the technique is limited to flat interfaces. Furthermore, XRR at solid-liquid interfaces requires almost always to be performed at synchroton facilities whose powerful X-ray sources can compensate for the low scattering magnitude at an interface (compared to bulk X-ray crystallography).

A promising candidate to overcome these restrictions are scanning probe techniques. Already before the AFM was invented, the surface force apparatus (SFA) was used to study solid-liquid interfaces. For example, Israelachvili and Pashley provided direct experimental evidence for molecular ordering in confined liquids [65]. When two macroscopic mica sheets were immersed in liquid and brought closely together, an oscillatory force with a periodicity of 0.25 nm was observed a few nm before the mica surfaces touched each other. They ascribed the alternating minima and maxima of the force to the sequential squeezing out of layers of water molecules. The formation of these layers next to the solid surface was ascribed to the confinement of the liquid inbetween the two surfaces. Later, researchers made similar observations using AFM force spectroscopy with sharp, nanoscopic tips. [55,66] AFM force spectroscopy was further widely used to study different properties of SLIs, such as an increased viscosity [55, 67], the effects of ions [68–70], surface hydrophilicity/hydrophobicity [71, 72], or applied voltages [73] on the SLI's structure. Other research groups developed AFM methods based on scanning to directly visualize nanoscale features of the SLI with subnanometer resolution [51, 74–78], often based on phase imaging (AM-AFM) with small free amplitudes and high set-points [51,75,77,79]. To extend the visualization of the SLI into the surface-normal direction, force spectroscopy mapping can be performed along a line to obtain a 2D profile of the solid liquid interface [80–85]. By repeating this procedure for sequential 2D profiles, a 3D image of the SLI can be acquired (force-volume); a technique pioneered in the field of SLI by Yamada's group [81,86–88]. However, a much faster way of recording such a volume was developed by Fukuma and coworkers: the feedback-based 3D-AFM (or 3D-SFM). This technique combines the advantages offered by the individual above-mentioned AFM techniques into a single AFM mode [42, 89]. Pioneering contributions were mostly performed on muscovite mica [42, 80, 86, 88, 89]. Mica is an abundant clay mineral that plays an important role in geology and oil recovery. Furthermore, it is a well-known substrate and testing ground in the AFM community since it is hydrophilic, atomically flat, and easy to cleave [90]. In the early years after the development of 3D-AFM, its measurement principle and imaging process encountered some challenges. It was unclear to which extend the nanoscale features observed in the 3D-AFM images, such as hydration or solvation layers, were a tip-induced phenomenon (due to confinement) or intrinsic properties of the SLI. With the help of theoretical models, such as the 3D reference interaction site model (3D-RISM) [91] and the solvent-tip approximation (STA) [92, 93], the imaging process was closely linked to the tip's hydration structure. Moreover, it was established that the force measured between the tip and the liquid is related to the local liquid density [91–93]. Recenty, the groups of Chacon and Tarazona

used density functional analysis to unravel the influence of the tip and the sample from the 3D-AFM observables [94]. Further insight was gained by extensively comparing 3D-AFM data to molecular dynamics (MD) simulations, mainly by the groups of Foster and Spijker [95–98]. Since mica is a rather complex surface with a pH-dependent surface charge distribution, it was not the first choice for performing MD simulations. Instead, calcite was used as a second model system. Altogether, it was found that the formation of solvation layers next to a solid surface does not necessarily require confinement, but is an intrinsic property of some solid-liquid interfaces. This represented an important step forward for the technique, and further strengthened many findings obtained by 3D-AFM on more complex interfaces such as mica in contact with high-molarity salt solutions [43], point defects in calcite [95], single proteins [45] and DNA molecules [99,100], lipids [101], heterogeneously charged surfaces [102], boundaries between hydrophilic and hydrophobic surfaces [103], or interfacial gas enrichments [87]. Some further contributions aim to extend the capabilities of 3D-AFM to identify species at the solid-liquid interface [104,105]. Other important developments are the implementation of tip-sample interaction models that allow to measure local nanoscale features in the liquid viscosity [87,106], liquid density [97], hydration density [99] or the surface charge density [100]. In this thesis, AM 3D-AFM will be studied, improved, and applied to a variety of solid-liquid interfaces in order to further optimize the capabilities of the technique and the understanding of SLIs.

2. Development of a 3D-AFM Software Suite

2.1. Introduction

3D-AFM is a young technique that was introduced in 2010 by Takeshi Fukuma and coworkers [42]. Since then, the number of research groups using this technique has been growing, but it is still limited to a few [42,43,80,87,88,107]. As a consequence, the data acquisition and analysis is based to a large extend on custom-written software. Primarily, any custom-written software makes data analysis time-efficient for the developer. Unfortunately, the accessibility for newcomers to the field often stays behind. One goal of this thesis is to develop a 3D-AFM software suite that advances one step further towards establishing 3D-AFM as a routine technique. For achieving this goal, it is necessary to have a tool at hand that allows for time-efficient data visualization and transparent analysis. In this chapter, such a 3D-AFM software suite will be developed and its most important functions will be explained. Care was taken that the software will save time on the long run for other researchers that are new to the field. To this end, a graphical user interface was developed that enables for intuitive and rapid access to all software functions. Furthermore, the source code is widely commented and is accompanied by a history document which tracks all software versions and the changes that were made. The software is a result of a step by step process, because it was adapted to the needs that emerged during the experiments and the discussion of the data. Thus, it has a modular architecture and can be easily extended by any user by adding further subroutines. The software is divided in two parts: (1) A first part for the data acquisition and (2) a second part for the data analysis.

The core of the data acquisition part was developed during the PhD thesis of Daniel Martín-Jiménez, a former group member [43, 105, 108]. During the development of this thesis, the core software has been further optimized and implemented into an extensive 3D-AFM software suite. In the following, the basic functionalities of the data acquisition part will be briefly reviewed. More attention will be paid to the modifications made during the development of this thesis. Thereafter, the focus will lie on the data analysis part. Its most important operations will be explained to make transparent the data processing which was crucial for achieving the results presented throughout this thesis. The source code is written in Igor Pro 6.37 (WaveMetrics, Inc., OR, USA) and requires this software to be run.

2.2. 3D-AFM Data Acquisition

In any standard AFM scanning mode, the piezo actuators move the probe in a rastering fashion across the xy plane. The movements in the x and the y direction are typically referred to as the *fast axis* and the *slow axis*. While scanning across the sample along x and y, the z-piezo moves the probe vertically in order to compensate for changes in the feedback observable and for obtaining the topography information. In principle, this way of operation is kept in 3D-AFM. The 3D-AFM movement is realized by an additional vertical movement of the z-piezo, while the raster movement is fully maintained [42]. This procedure is schematically illustrated in **Figure 2.1**. The additional movement will be referred to as the *ultrafast* movement since its modulation frequency, f_z, is much higher than the one of the signals in the x and the y direction (see Table 2.1). The z-piezo performs the ultrafast movement simultaneously with the sample tracking (to obtain the topography). The crosstalk between these two movements is minimized using feedback settings that are optimized for the 3D motion (sometimes referred to as "*loose feedback*" [43], see below). The ultrafast movement is synchronized with the fast and slow movements in such a way that exactly one single approach-retraction cycle is performed in each pixel of the xy plane (see Figure 2.1). As a consequence, each pixel in the xy plane represents an entire observables-displacement curve. This modifies the imaging process in such a way that instead of line-by-line, entire xz panels are acquired, which results at the end of the measurement in a whole xyz cube of data instead of a two-dimensional xy image. In principle, the described 3D-AFM movement is compatible with any dynamic AFM mode, such as frequency modulation [42], amplitude modulation [43, 44], or even bimodal AFM [45]. Here, the focus lies on the amplitude modulation 3D-AFM (AM 3D-AFM). In AM 3D-AFM, the simultaneously recorded channels are by default the two observables (Obs) amplitude, A, and phase shift, ϕ. Additionally, the z-modulation function and the performed feedback movement are recorded as a minimum. A block diagram of the AM 3D-AFM hardware and electronics is provided in **Figure 2.2**.

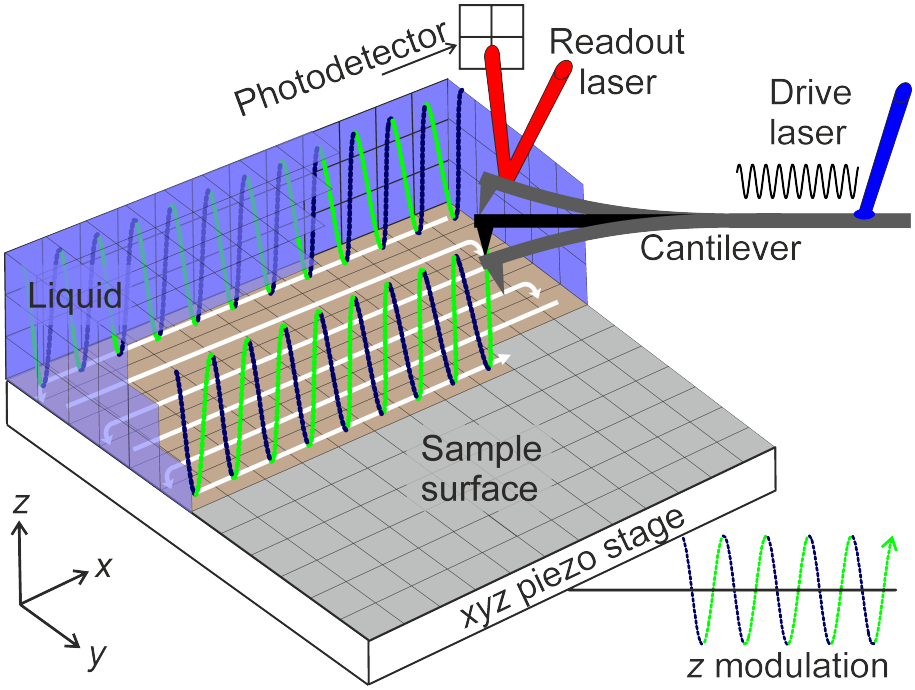

Figure 2.1.: Illustration of the 3D-AFM concept and the involved movements. The cantilever is driven at one of its resonance frequencies by the drive laser (blue) focused at the cantilever's clamped end. A second laser (red) is reflected at the cantilever's free end and its reflex is read out by a photodetector. The sample surface is fully immersed in liquid (light blue). While the cantilever is rastering across the surface, a sinusoidal movement in the z-direction gives rise to the z-depth of a 3D-AFM measurement. The z-modulation is depicted in dark-blue/green. During the first half of the z-movement the cantilever is approaching the sample (dark blue) and during the second half it is retracting (green).

2.2.1. Feedback Optimization for AM 3D-AFM

One of the key differences between FV approaches and 3D-AFM is that the former ones are based on a trigger value, while the latter uses a feedback. By using a feedback instead of a trigger-based approach, a significant reduction of the data acquisition time was achieved [42, 45]. In the following, the concept of the AM 3D-AFM feedback, as it was used throughout this thesis, will be briefly reviewed.

In principle the AM 3D-AFM feedback works as in standard tapping mode: The user sets a free cantilever oscillation amplitude A_0 and a set-point amplitude A_{sp}. During a scan, the AFM electronics reads out the actual amplitude A and compares it to A_{sp}. For $A > A_{\mathrm{sp}}$, the z-piezo is extended to decrease the tip-sample distance and vice versa. As in 2D-AFM, the set-point serves as a way of controlling the average tip-sample distance and thereby the strength of the tip-sample interaction. However, the practical meaning of the set-point amplitude is different in both approaches: In 2D-AFM, A is kept very close to A_{sp} and only deviates due to non-ideal feedback behavior (the feedback response

time). In 3D-AFM, however, A is different from A_{sp} during the major part of the ultrafast movement and a compensation of this difference is not desired. The set-point defined in the user interface can be understood as a technical parameter (an "effective set-point") which serves to control the average tip-sample distance. The actual oscillation amplitude varies around this parameter throughout the ultrafast movement. Within one cycle of the ultrafast movement, the amplitude reaches its lowest value at the closest tip-sample distance. Throughout this thesis, the amplitudes A_{sp} stated for 3D-AFM data are these minimum amplitudes. In this way, a direct comparison between AM 3D-AFM data and tapping mode images is possible.

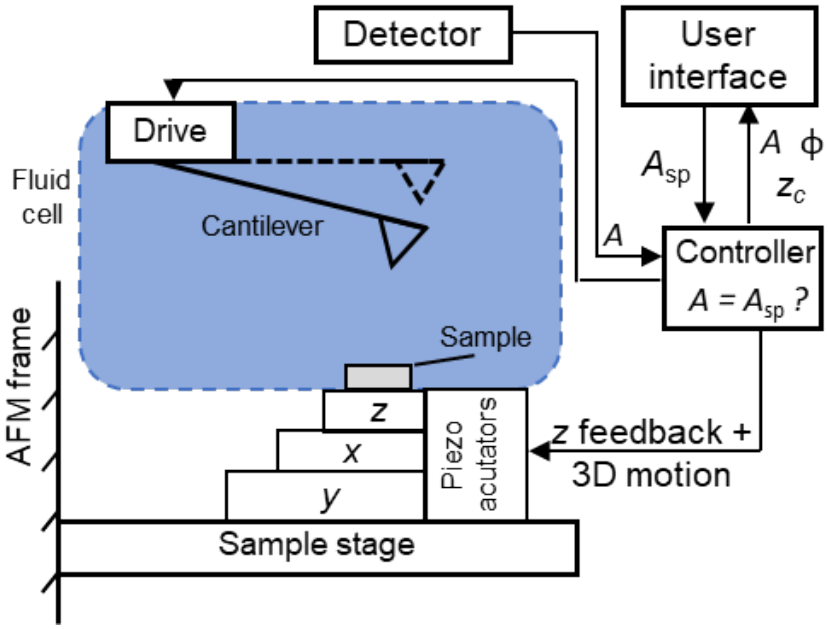

Figure 2.2.: Scheme of the AM 3D-AFM hardware and electronics. The cantilever is driven at one of its resonance frequencies. The controller compares the set-point amplitude A_{sp} with the cantilever's actual oscillation amplitude A read out by the detector. The outcome of the comparison triggers a feedback response at the z-piezo. Simultaneously, the piezo actuators perform the 3D motion. The controller sends all the observables to the user interface for offline processing.

The necessary feedback behavior (*"loose feedback"*) is realized using adapted AM 3D-AFM feedback settings. The feedback parameters are controlled by the main panel of the Cypher electronics, which is depicted in **Figure 2.3**. The strength of the feedback reaction is controlled by a proportional-integral-differential (PID) controller as in AM-AFM. Basically, the controller reads out the error signal $(A - A_{sp})$ to calculate the piezo response with the help of user-defined PID gains. Simplified speaking, the larger the error signal and/or the gains are, the stronger is the piezo response. In turn, if the error signal and/or the gains are close to zero, the piezo responses are very small.

In order to obtain the desired behavior in 3D-AFM, a combination of a very high

effective set-point, $A_{\mathrm{sp}} \gtrsim 0.95A_0$ and very low feedback gains are used (a single integral gain of 2 to 5 in the particular case of the Cypher electronics). Then, during the ultrafast movement, the feedback encounters mainly two situations: Far away from the sample, the controller detects an amplitude larger than the set-point amplitude, $A > A_{\mathrm{sp}}$. This situation provokes a feedback reaction towards the sample. However, due to the high set-point, the error signal is saturated at very small values ($A - A_{\mathrm{sp}} \gtrsim 0$), completely independent of the actual tip-sample distance. In combination with the small gain, the feedback reaction is very small and does hardly interfere with the ultrafast movement. In other words, the cantilever is kept on purpose in a so-called parachuting state [109]. Close to the sample, the opposite situation is found: $A < A_{\mathrm{sp}}$. Now, the asymmetry of the error signal comes into play. In contact, the error signal does not saturate but instead is increasing strongly with increasing tip-sample interaction. Such a situation prompts the feedback to move the tip upwards. However, the small gain prevents an overreaction of the feedback, which avoids instabilities in the surface tracking. Altogether, the adapted feedback settings lead to a stable imaging process, because the feedback compensates for surface topography, sample tilt, z-drift, and z-piezo creep, but does not suppress the ultrafast z-modulation.

During the development of this thesis some modifications were introduced in the data acquisition software. First of all, the code was updated to be compatible with the Asylum Research Software Version 14.48.159. Furthermore, it was adapted in such a way that it is compatible with both the Cypher S and the Cypher ES/VRS (Asylum Research, Oxford Instruments, Santa Barbara, Ca, USA). Both instruments can be controlled by the above-mentioned Asylum Research software. However, their controllers use different amplifiers for the z-piezo voltage, U_z. Hence, U_z has to be calculated for each instrument individually in order to produce the desired z-movement. In either case, the piezo voltage is calculated by

$$U_z = \frac{A^{\mathrm{3D}}_{\mathrm{p\text{-}p}}}{2\chi_z \alpha}$$

where $A^{\mathrm{3D}}_{\mathrm{p\text{-}p}}$ is the desired amplitude (peak to peak) for the ultrafast movement, χ_z the z piezo's sensitivity, and α the amplifier's voltage gain.

The panel for defining the 3D-AFM motion is shown in Figure 2.3b. The basic functionality developed by during the PhD thesis of Daniel Martín-Jiménez was kept [108], so that the panel mainly serves two purposes: First, to set the desired resolution and amplitude (peak-to-peak) in the z direction. Second, to start a 3D-AFM experiment using the previously set parameters ("3D Frame Up" or "3D Frame Down") or stop the 3D motion ("Stop 3D").

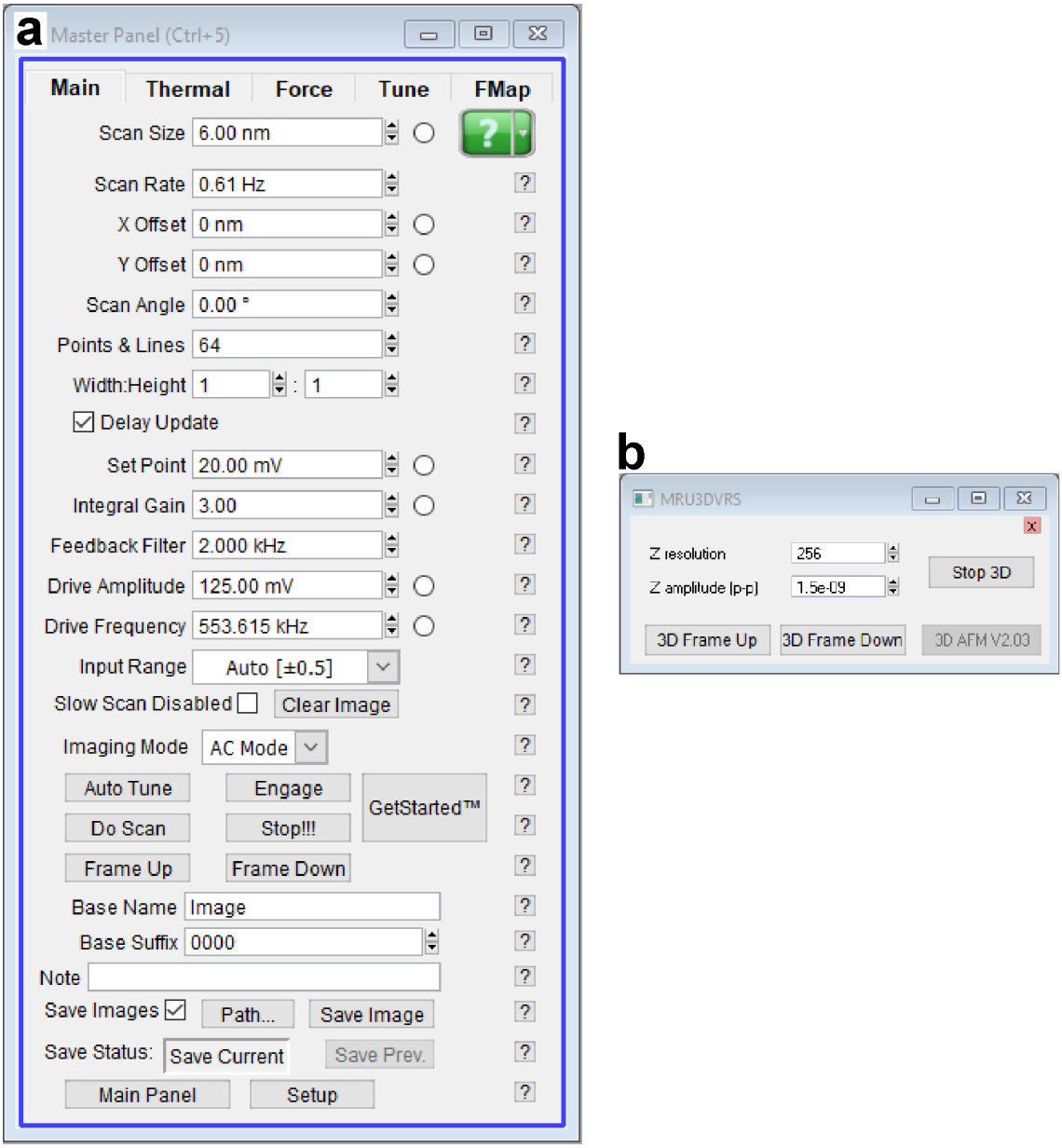

Figure 2.3.: Control panels for the operation of a 3D-AFM experiment. **a.** Main panel for setting up the in-plane scan parameters and controlling the Cypher electronics, in particular the integral gain of the PID controller and the feedback bandwith. **b.** The panel for the z-movement of the AM 3D-AFM data acquisition software. It is used for defining the ultrafast motion and starting or stopping 3D-AFM measurements.

Behind the controls, the code was extended in such a way that the user can now choose freely from a number of different z resolutions. In particular, lower resolutions than 256

pixels can be chosen, which proportionally decreases the acquisition time t_{acq} according to

$$t_{\text{acq}} = \frac{p_x p_y p_z}{s_{\text{data}}}$$

where p_x, p_y and p_z are the number of pixels in the x, y, and z direction, respectively, and s_{data} the readout data rate. In all the experiments performed throughout this thesis, the instrument's maximum data rate of 50000 s^{-1} was used. For some representative z resolutions, the resulting acquisition times are listed in **Table 2.1**.

Resolution $p_x \times p_y \times p_z$	f_x	f_y (s^{-1})	f_z	t^z_{acq} (full curve) (ms)	t^{xy}_{acq} (panel) (ms)	t^{xyz}_{acq} (cube) (s)
80×64×512	0.35	5e-3	50	20.5	1640	104
80×64×256	0.70	1e-2	100	10.2	820	52
80×64×128	1.40	2e-2	200	5.1	410	26
80×64×64	2.80	4e-2	400	2.6	205	13

Table 2.1.: 3D-AFM xyz piezo modulation frequencies f_x,f_y, and f_z, and data acquisition times t_{acq} for some representative z resolutions.

By choosing the resolution in z, the z-frequency f_z is automatically calculated. It is convenient to define the z-frequency rather than the z-speed since the sinusoidal movement is not constant in speed. The software then calculates the z-signal that produces the highest possible piezo speed for the given parameters. As a consequence, by choosing the resolution and the amplitude for the z-movement, the piezo's trajectory and speed are defined. In spite of the low acquisition times and high z-frequencies in 3D-AFM measurements, the absolute cantilever speed is low. **Figure 2.4** shows the average cantilever speed for some combinations of $A^{\text{3D}}_{\text{p-p}}$ and p_z. The area shaded in gray marks the values mostly used for obtaining the data shown throughout this thesis. The speed values are in the range of 150 to 600 nm/s. These small values imply that hydrodynamic effects such as drag forces are small [110,111]. Note that the peak value of the speed during the sinusoidal movement is (in general for sinusoidal signals) by a factor of $\frac{\pi}{2} \approx 1.57$ larger than the stated average values, but still small.

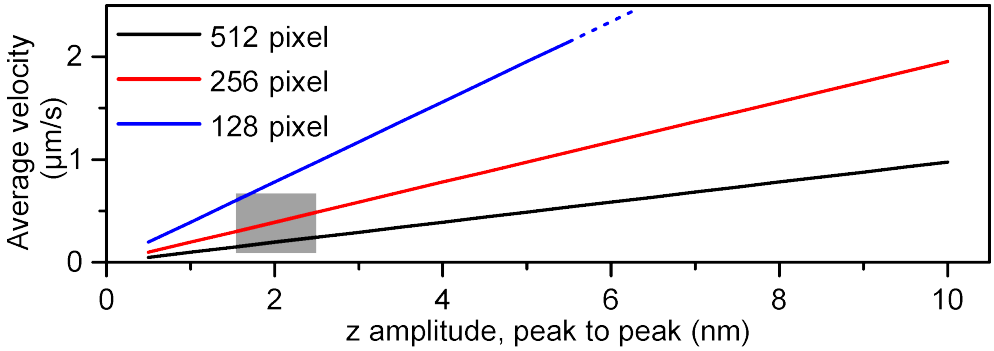

Figure 2.4.: Average cantilever speed in a 3D-AFM measurement for some combinations of z-amplitudes and z-resolutions. The area shaded in gray marks the values mostly used for obtaining 3D-AFM data throughout this thesis.

2.2.2. Static Cantilever Deflection

A new channel was added to be recorded in real-time: the static cantilever deflection Δz. The static deflection measures the net force acting on the cantilever, F_{net}, as described by Hooke's law:

$$F_{\text{net}} = \Delta z k_0 \tag{2.1}$$

where k_0 is the (static) stiffness of the cantilever. As it was suggested earlier [44,107], the static deflection adds useful complementary information to AM 3D-AFM. Although this channel is intrinsically much less sensitive compared to the dynamic observables [10,112], it provides valuable information for several reasons:

(1) It facilitates the data acquisition by providing a quasi-force-distance curve in real-time. To this end, the deflection is averaged over each panel

$$< \Delta z > (z_{\text{c}}) = \frac{\sum_0^{79} \Delta z_i(z_{\text{c}})}{80} \tag{2.2}$$

The resulting $\Delta z(z)$ curve is displayed and updated while running a 3D-AFM measurement. **Figure 2.5** summarizes the data that is output in real-time during a measurement. Figure 2.5a-d shows the default channels for AM 3D-AFM and panel e the $\Delta z(z_c)$ curve. It provides the user with intuitive information about the tip-sample interaction during an experiment. This is useful since it helps to control the tip-sample interaction and keeping repulsive tip-sample forces as low as possible, which is crucial for long-term high-resolution imaging. Furthermore, it provides some valuable insight into the conditions of the tip.

(2) In principle, the cantilever deflection disentangles the actual movement of the tip from the movement of cantilever base. Hence, recording the cantilever deflection is necessary for obtaining actual force-distance curves [25]. Knowing $\delta(z)$ allows to convert the z-position into tip-sample distances, as it is standard in AFM force spectroscopy [25] but not common in 3D-AFM data. Force-distance curves rather than force-displacement curves are required for the obtaining accurate distances from force spectroscopy measurements. Additionally, knowing the tip-sample distance is a requirement for determining

the contact point with the surface. Note that neglecting the static cantilever deflection without further considerations is justified in the vast majority of 3D-AFM data, in particular in experiments regarding hydrophilic samples. This is because the important information obtained from 3D-AFM experiments is within the solid-liquid interface, thus, above the surface (*i.e.*, in the non-contact part of the z-movement). Often, in this part of the z-movement, the net cantilever deflection is reasonably close to zero (for example, when using electrolytes to screen out DLVO forces in the proximity of a charged mica surface [43]). However, recently there are cases (including this thesis) [72, 87, 103, 113], in which the sample choice gave rise to a repulsive background force, that could not be screened out. Such a background force leads to an increase in the static deflection upon approaching the surface. An increase in the static deflection will lead, if ignored, to an overestimation of distances measured in the Obs-z curves compared to the Obs-d curves. The deflection channel can be used to estimate the introduced uncertainty.

(3) The deflection channel is a direct measure for the net force acting on the cantilever throughout the z-cycle. In 3D-AFM, the absolute cantilever speed is rather low since the z-displacements are very small (see Figure 2.4). For example, for a typical measurement with $f_z = 200\,\mathrm{s}^{-1}$ and 2 nm z range, the average (maximum) speed is 390 nm/s (551 nm/s). Considering these slow cantilever movements, the static deflection probes forces in quasi-static equilibrium. This implies that hydrodynamic effects are small [110, 111, 114, 115]. As a consequence, mostly conservative forces are measured by the deflection channel (when approaching the sample). Hence, the deflection channel can serve as a reference for the reconstruction of the conservative tip-sample force as suggested earlier [112]. Note that during cantilever retraction, force hysteresis could always arise from adhesion.

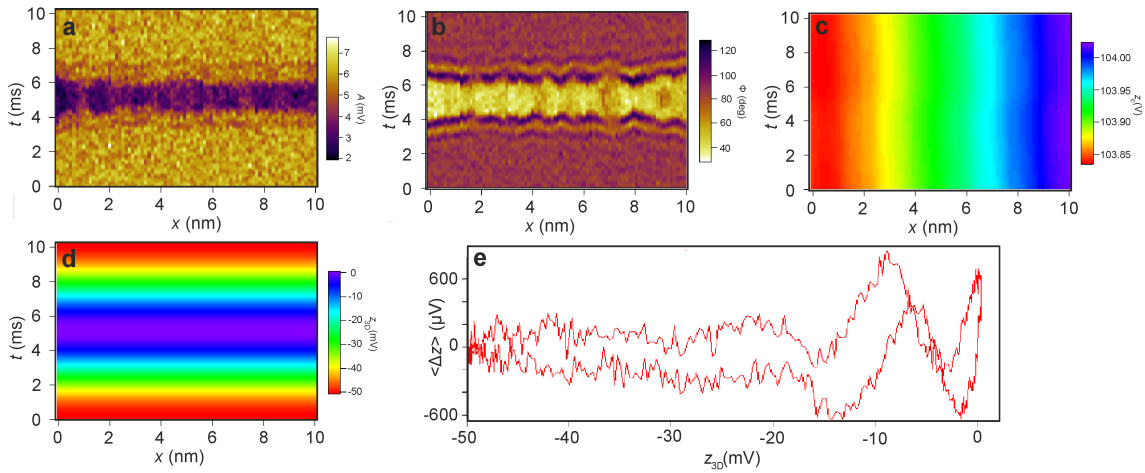

Figure 2.5.: Data displayed in real-time during a 3D-AFM measurement. The data is plotted as a function of the lateral coordinate x and the time t, giving rise to the symmetric appearance of the data. **a.** Cantilever oscillation amplitude $A(x,t)$. **b.** Phase shift $\phi(x,t)$. **c.** Feedback response $z_c(x,t)$. **d.** Displacement added by the ultrafast movement $z_{3\mathrm{D}}(x,t)$. **e.** Quasi-force-displacement curve $< \Delta z > (z_{3\mathrm{D}})$. Note that A, z_c and $z_{3\mathrm{D}}$ are displayed in units of Volts. The data was taken on mica in 200 mM KCl solution (aq.).

2.3. 3D-AFM Data Analysis

In this section the most important features of the 3D-AFM analysis software suite will be explained. The focus will lie on the steps that were critical for the data presented in the next chapters. As a general overview, the main panel of the 3D-AFM analysis software suite is shown in **Figure 2.6**. It is divided into three main sections:

(1) 2D Panels. The left part of the interface mainly controls displaying and transformations of xz panels for a given y. The features contained in this section are pivotal for data analysis and typically the first ones used since they allow to quickly browse through large data sets. A second very important aspect is the transformation of time-domain data into real-space data, *i.e.* $\mathrm{Obs}(x, y, t) \rightarrow \mathrm{Obs}(x, y, z)$, including an optional flattening routine. For deeper analysis, this section contains the transformation of entire $A(x, z)$ and $\phi(x, z)$ panels into force panels.

(2) 1D Spectroscopy. The center part of the software interface serves first of all for displaying and averaging of $A(z)$ and $\phi(z)$ curves for given x and y positions. Advanced key features are the transformation of the Obs-z curves into $F(z)$ curves, the calculation of fits to the force data, subtracting background forces, and providing insight into the cantilever deflection.

(3) 3D Cubes. The right part of the user interface contains buttons for displaying and handling full 3D data sets. Mainly the functionalities of the 2D Panels section are extended to three dimensions. First of all, this allows for easy browsing through the data from three perspectives, including the the front view (xz panels), the side view (yz panels) and the top view (xy planes). Each option can be used in the time-domain as well as in the real-space domain, including an optional flattening routine. Furthermore, the force reconstruction algorithm can be applied for the entire volume. Finally, the data created with the help of this section is compatible with Igor Pro's Gizmo environment. Gizmo is a plug-in for IgorPro for creating 3D plots. Once loaded into Gizmo, different panels and planes can be visualized at the same time and the data can be freely rotated.

Figure 2.6.: User interface for the AM 3D-AFM data analysis software developed during the course of this thesis. It is divided into three main parts (from left to right): 2D panels, 1D spectroscopy, and 3D cubes.

2.3.1. Transformation Time - Real Space

The information obtained by 3D-AFM in the z direction is saved as a function of time rather than piezo extension or tip-sample distance. Every observable $(A, \phi, z_c, U_z, \Delta z)$ is saved in a matrix of the format $x \times y \times t$. This is useful because it allows for rapid data handling and offers a simple route for 2D- and 3D-visualization, since the time channel is always a monotonous and linear function. However, in order to extract distances from the 3D-AFM data, it is pivotal to transform the data into a spatial coordinate system.

First of all, the topography channel of the 3D-AFM operation has to be calculated from the observables. In standard AFM operation, the displacement of the piezo originating from the feedback, z_{fb}, is directly interpreted as topography (or height) channel. In 3D-AFM however, the z-piezo performs two movements at the same time. In order to determine the cantilever's real z-piezo position (z_{c}) both channels have to be summed up. At any given moment t, z_{c} can be calculated from the feedback displacement, z_{fb}, and the displacement added by the ultrafast movement, z_{3D}, with $z_{\mathrm{3D}} = U_z \chi_z \sin(2\pi f_z t)$:

$$z_{\mathrm{c}}(t) = z_{\mathrm{fb}}(t) + z_{\mathrm{3D}}(t) \tag{2.3}$$

Knowing the cantilever position z_{c}, the tip's minimum position z can be calculated through

$$z(t) \quad = \quad z_{\mathrm{c}}(t) - A(t) \tag{2.4}$$

Note that Equation 2.4 denotes the tip-position under the assumption of a negligible net cantilever deflection (see Section 2.3.5). In most of 3D-AFM experiments, this assumption is accurate enough to describe the tip's vertical position. Hence, z is typically used as the spatial coordinate for Obs(z) curves [43, 45, 105]. However, for the visualization of panels, planes or cubes, a simpler algorithm is often used as will be explained in the following (denoted as Algorithm 1). Such a simplification can limit the performance of 3D-AFM as will be pointed out. Hence, an algorithm based on the above equations will be developed in order to increase the accuracy of the transformation (denoted as Algorithm 2). Finally, both approaches will be compared.

Algorithm 1. Up to now, the transformation for 2D and 3D plots was mostly done by simply replacing $t_{\mathrm{acq}}^{\mathrm{1D}}$ with $A_{\mathrm{p\text{-}p}}^{\mathrm{3D}}$. **Figure 2.7** illustrates this transformation for an example data set. The approach and retraction yield largely similar information (as can be seen by comparing Figure 2.7c and d). Hence, in the following figures and throughout this thesis, only approach data will be shown.

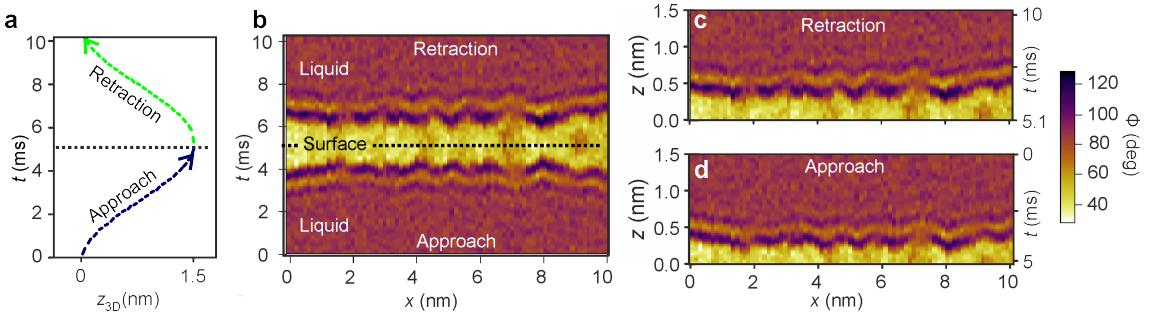

Figure 2.7.: Algorithm 1. Transformation of 3D-AFM raw data into spatial coordinates by replacing the acquisition time by the (zero-to-peak) z-amplitude. **a.** Individual cycle (approach and retraction movement) of the ultrafast movement. The sinusoidal movement consists of an approach and a retraction part, which are marked in dark blue and green, respectively. In this example, both extend over 1.5 nm and are performed within 5.1 ms each. **b.** xt raw data panel (phase channel) as recorded by the 3D-AFM software. The dotted line marks the center of the data. This position coincides closely with the lower turnaround point of the ultrafast movement. **c.** xz phase panel obtained from the upper half of the raw data panel (corresponding to the retraction movement). **d.** xz phase panel obtained by flipping the lower half of the raw data panel (corresponding to the approach movement). The data was taken on mica in 200 mM KCl solution (aq.).

Although this simple transformation preserves the overall dimensions correctly, it implies two approximations: First, the (sinusoidal) piezo movement is assumed to be linear. Second, the movement performed by the feedback loop is ignored. While such a pragmatic approach is a reasonable approximation for flat samples [43, 45, 105], this in not the case in general. The approximations could lead to loss of information or misinterpretations since the actual transformation from the time domain to the spatial domain can be counter-intuitive (see comparison below).

Algorithm 2. During this thesis, an algorithm was developed to fully map the data into a spatial coordinate system, as described in the following. First of all, the topography channel of the data is calculated from the feedback response, $z_c(x,t)$, and the displacement added by the ultrafast movement, $z_{3D}(x,t)$ (see channels in Figure 2.5). The calculation is performed by using Equations 2.3 and 2.4. For storing the new data, an empty xz matrix is created. It's z-range is defined as the one of the corresponding topography channel (see below). For the 3D case, an xyz cube is created whose z-range covers the global topography range. For mapping a given data set into the empty xz matrix, the algorithm passes through the data set that has to be transformed, let's say, a phase image $\phi(x,t)$. At each point, for main steps (I-IV) are performed which are illustrated in **Figure 2.8**.

I. (Panel a) At each position (x_i, t_j), the algorithm reads out the phase value $\phi(x_i, t_j)$. II. (Panel b) For each phase value, the algorithm reads out the corresponding value from the topography channel, $z(x_i, t_j)$. III. (Panel c) Once $z(x_i, t_j)$ is known, the algorithm switches to the column x_i of the newly created xz matrix. Within this column, it calculates the position z_k of the previously determined z-value. IV. (Panel d) The phase value

is assigned at the position (x_i, z_k) to the new matrix. By repeating steps I-IV for all the entries of the initial panel, the data is entirely mapped onto the xz matrix. If multiple $\phi(x,t)$ are to be mapped onto the same (x_i, z_k) position, the last point is displayed. If, on the other hand, no value was assigned to a given position in the new matrix, the respective entry remains empty. In this way, the final map vidualizes at a glance the regions that were accessed by the tip apex (pixels filled with data) and those that were not (marked in gray).

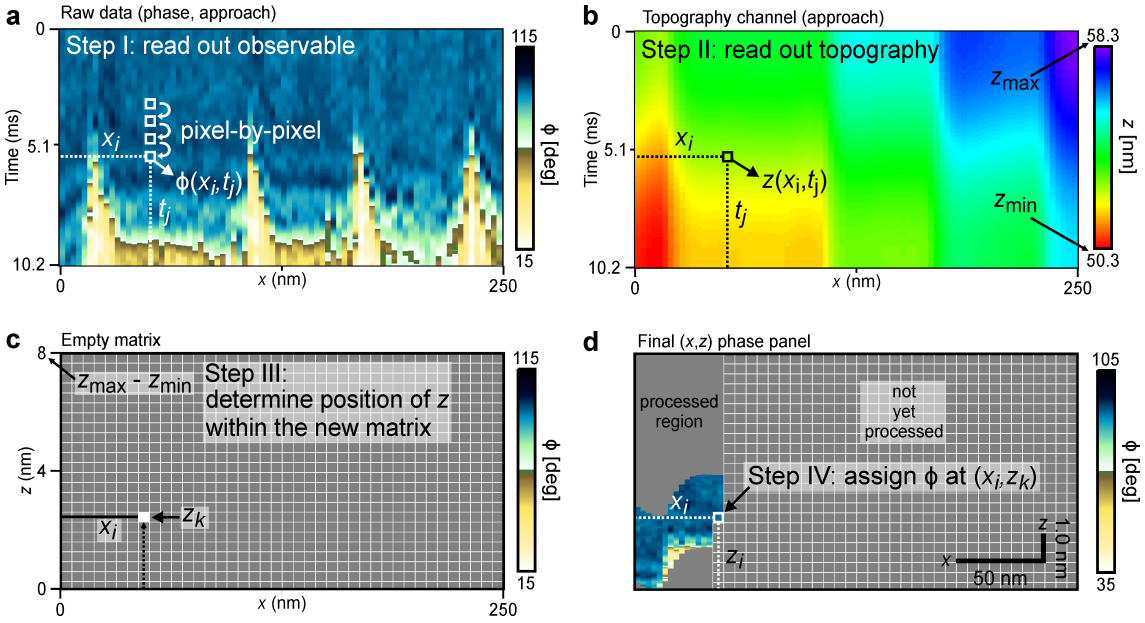

Figure 2.8.: Algorithm 2. Transformation of 3D-AFM raw data into spatial coordinates by mapping the xt data onto an xz-matrix. The nonlinearity of the z_{3D}-movement and the feedback movement are considered. The example data shows phase data measured on a highly corrugated surface (pentacene thin-film). **a.** Approach part of the raw data, $\phi(x,t)$. The algorithm passes pixel-by-pixel through each column (schematically indicated by the arrows) and reads the phase value ϕ at the specific coordinates (x_i, t_j). **b.** Corresponding topography panel $z(x,t)$ calculated from the feedback movement and the 3D z-motion by Equations 2.3 and 2.4. After reading the phase value (panel a), the algorithm reads out the corresponding z value at the same coordinates (x_i, t_j). **c.** Empty xz matrix, spanning over the z-range of panel b. The algorithm determines the coordinates (x_i, z_k) for the previously read z-value. **d.** ϕ is assigned to the respective pixel. By repeating the procedure, the matrix is filled pixel-by-pixel. Some pixels remain empty (gray) because they were not accessed by the tip apex. The data was taken on a pentacene thin-film in 50 mM KCl aqueous solution.

Comparison. Some example raw data of different samples were processed by both algorithm 1 and algorithm 2 and the results are shown in **Figure 2.9**. The left and right column correspond to algorithm 1 and 2, respectively. The first row shows a feature at the surface that at first glance seems to be a dome-like protrusion (panel a). The horizontal

contrast (white dashed line) seems to follow the shape of the protrusion. However, the full transformation (panel b) reveals that the feature actually forms a pit and the stripe contrast is continuous, *i.e.*, unaffected by the feature. The second row shows a step-like feature, which appears be a downward step when transformed with algorithm 1, while algorithm 2 (panel d) reveals that the step is actually directed upwards (imaging direction is from right to left as indicated by the arrows). The third row depicts a strongly corrugated surface (pentacene thin-film). Algorithm 1 suggests the existence of several sharp protrusions (panel e), while the full transformation (panel f) reveals that the imaging contrast actually reproduces five adjacent terraces.

The comparison demonstrates that the approximations of algorithm 1 can distort the aspect of topographic features and lead to misinterpretations. An accurate transformation (algorithm 2) is mandatory to enable correct data interpretation. An important implication is emphasized by the third example: Only with a full transformation into spatial coordinates it is possible to obtain meaningful 3D-AFM data on topographically complex surfaces, such as pentacene terraces (see also Chapter 3, Section 4). The step-height can be directly obtained from the panel and corresponds to indiviual pentacene monolayer steps ($\approx$ 1.4 nm). Throughout this thesis, the time-domain data is always transformed into the spatial coordinate by using algorithm 2. The software suite transforms the data automatically when pressing the corresponding "Real Space" buttons.

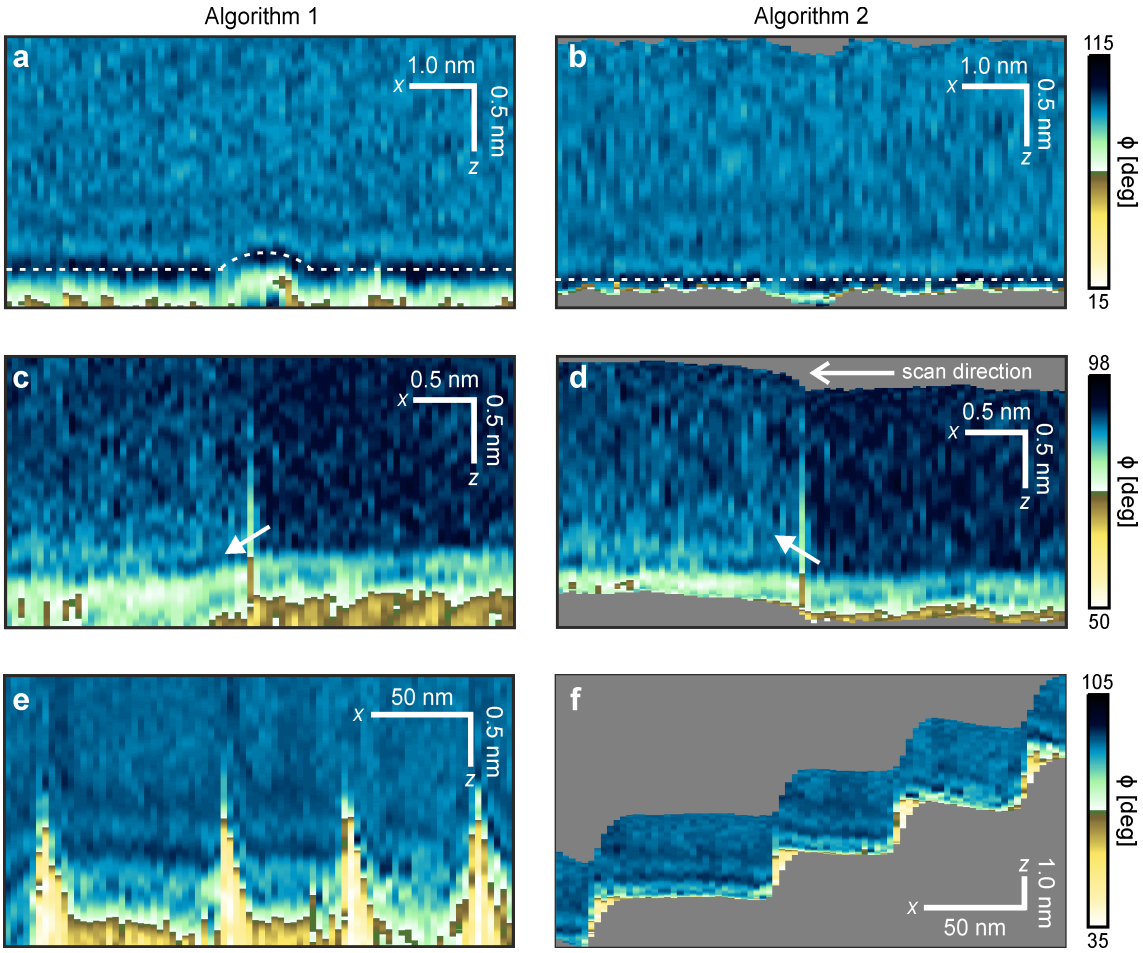

Figure 2.9.: Transformation of 3D-AFM raw data into spatial coordinates. For each row, the figure compares a single set of raw data processed by the two different algorithms (described in the text). **Left column:** Algorithm 1. Transformation by replacing the acquisition time by the (zero-to-peak) z-amplitude. **Right column:** Algorithm 2. Transformation by mapping the xt data into an xz matrix considering the nonlinearity of the z movement and the sample topography. Three examples are shown. The first row shows a feature at the surface that at first glance seems to be a dome-like protrusion (panel **a**). The horizontal contrast (white dashed line) is following the shape of the protrusion. The full transformation (panel **b**) reveals that the feature actually forms a pit and the stripe contrast is unaffected at the feature. The second row shows a step-like feature, which in panel **c** is suggested to be a downward step, while panel **d** reveals that it is actually an upward step (imaging direction is from right to left as indicated by the arrows). The third row depicts a strongly corrugated surface (pentacene thin-film). Panel **e** suggests the existence of four sharp protrusions, while the full transformation (panel **f**) reveals that the imaging contrast actually arised from steps between adjacent terraces. Gray areas have not been accessed by the tip. The data was taken on mica in 200 mM KCl aqueous solution (a-d) and on a pentacene thin-film in 50 mM KCl aqueous solution (e-f).

2.3.1.1. Interpolation

A peculiarity of 3D-AFM data is that the spatial density of data points is not constant throughout the z movement due to the movement's sinusoidal character. The number of data points is higher at the sine's turnaround points and lower in its central part. When mapping the data onto a regular (linear) xz grid, either data is lost at the turnaround points or the central part of the z movement displays gaps in the xz panel. Since the data at the lower turnaround point is of high interest (see for example Chapter 5) it should be preserved which in turn produces gaps in the central part. By default, these gaps are linearly interpolated by the algorithm. The effect of the interpolation is illustrated in **Figure 2.10**. Note that the interpolation serves only an optical purpose and is only necessary for the 2D- and 3D-data real-space visualization. The actual effect on the data is negligible. In any case, the original data is always accessible by clicking the "RAW" button. Data points forming 1D curves are not interpolated.

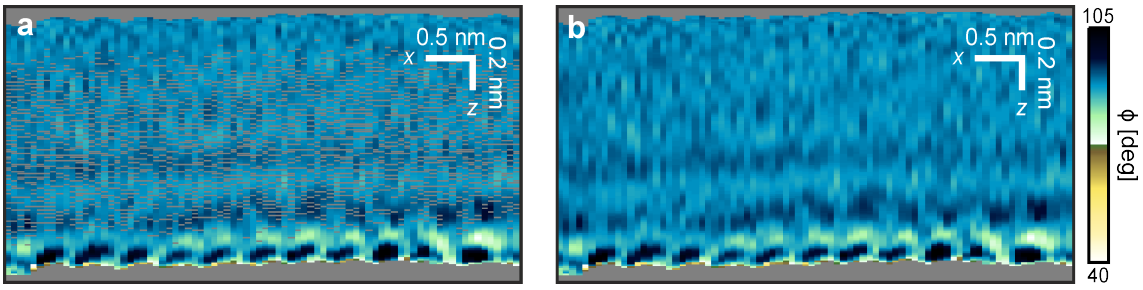

Figure 2.10.: Interpolation of data points for visualization of 3D-AFM data. Due to the sinusoidal z-movement, the spatial density of data points is not constant. The number of data points is higher at the turnaround points and lower in the central part of the z movement. In order to map the data onto a regular xz grid without losing data at the turnaround points, some pixels have to be interpolated in the central part. **a.** xz phase panel extracted from a AM 3D-AFM measurement without interpolation. **b.** The same panel after interpolation. Gray areas have not been accessed by the tip. The data was taken on mica in 200 mM KCl solution (aq.).

2.3.1.2. Flattening

As any other AFM mode, 3D-AFM underlies imaging artifacts. The most frequent one (only visible one after transformation into the spatial coordinate system) is the presence of apparent or real surface inclination. Apparent inclination mainly comes from non-ideal z-piezo movements, while a real inclination is caused by a tilted sample. Both can be distinguished by inspecting the direction of the inclination for sequentially recorded xz panels. If the inclination is real, its direction is independent of the scan direction. An apparent inclination, however, shows an alternating direction for even and odd panels. **Figure 2.11**a depicts a sequence of four xz phase panels (separated by each other by 1 pixel in the y direction). The individual panels are inclined in an alternating manner. The correlation between the direction of the inclination and the direction of the fast movement indicates that the dominant effect is the apparent surface inclination. Such

an observation is caused by the creep of the z-piezo after engaging the sample. Due to the small, but persistent downwards creep (the images were recorded 120 sec after the tip approach), the feedback applies continuously an upwards piezo movement, which is incorrectly interpreted as topography signal.

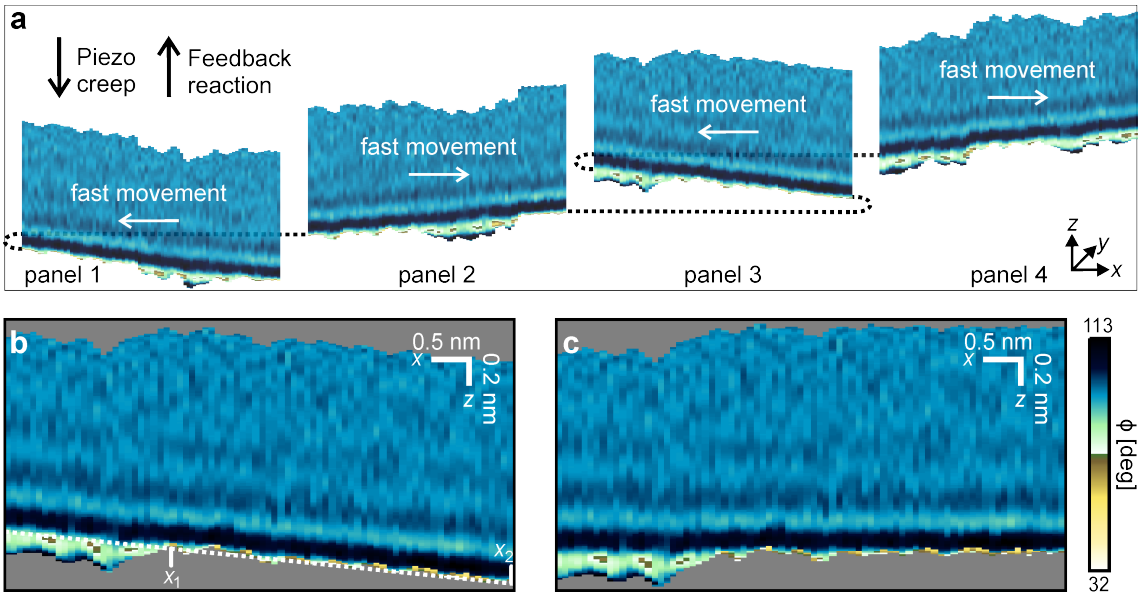

Figure 2.11.: Surface inclination and flattening algorithm. **a.** Sequence of xz phase panels recorded in a row. The panels are individually inclined, and the slope alternates with the scan direction (indicated by white arrows). **b.-c.** Application of the developed flattening algorithm to one of the four panels. Panel b shows the data before the flattening. A clear tilt is visible. A linear function is fitted to the surface relief (formed by the lowest data point of each column; white dashed line). The fit range is specified by the user interface (marked by x_1 and x_2). Then, all the entries in the xz matrix are vertically shifted according to the value of the line fit (result shown in panel c). The data was taken on mica in 200 mM KCl solution (aq.).

These inclinations are in most cases sufficiently linear to be removed by the flattening algorithm which works, in short, as follows. It detects the surface relief (formed by the lowest data point of each column) and fits a linear function to the data points. Then, all the entries in the xz matrix are vertically shifted according to the value of the line fit. While the fit range is user-defined, the shift in the data always affects the entire xz panel (see Figure 2.11b-c). Strong nonlinear creep can be avoided in the first place by letting the system relax after approaching or by disregarding the first panels. Real inclination plays a role for larger-range scans as the ones shown in Chapter 3, Section 4.4.2. Also thermal drift in the z-direction can lead in principle to apparent inclinations and other image distortions. However, the effect of the thermal drift is small in comparison with creep, in particular when using the Cypher ES/VRS equipped with a temperature control unit.

2.3.2. Force Reconstruction

The 3D-AFM used throughout this thesis was operated in the amplitude modulation mode. Such a dynamic approach increases the method's sensitivity while reducing its invasiveness at the same time [10]. In contrast to static modes, dynamic AFM approaches do not yield the force as a direct observable. However, force inversion techniques have been developed in order to provide expressions that link the dynamic observables to forces (or force gradients) [26,67,112,116–119]. Such expressions exist for frequency modulation (FM) AFM [118,119] as well as for AM-AFM [26,67,112,116,117]. In the course of this thesis, Hölscher's [117] and Payam's [26] methods were implemented into the AM 3D-AFM analysis software suite. With the help of the provided expressions, force curves can be obtained from the observables (amplitude and phase shift) as a function of the piezo displacement. For the time being, the functionality is limited to the conservative part of the force. The procedure is illustrated in **Figure 2.12** for the case of an averaged force curve reconstructed by Hölscher's method [117]. First, the raw data of one entire xz panel is averaged (*i.e.*, 80 individual amplitude A and phase shift ϕ curves). Then, the conservative force is calculated according to Ref. [117] from the averaged data. In a first step, a term denoted as $\kappa(z)$ is computed

$$\kappa(z) = \frac{k_0 A^{3/2}}{\sqrt{2}} \left[\frac{a_\mathrm{d} \cos(\phi)}{A} - \frac{f_\mathrm{n}^2 - f_\mathrm{d}^2}{f_\mathrm{n}^2} \right] \tag{2.5}$$

where f_d is the drive frequency and f_n the cantilever's resonance frequency. By choosing $f_\mathrm{d} = f_\mathrm{n}$, the expression can be simplified to

$$\kappa = k_0 a_\mathrm{d} \sqrt{\frac{A}{2}} \cos(\phi) \tag{2.6}$$

where a_d is the drive amplitude that is determined by the transfer function as $a_\mathrm{d} = \frac{A_0}{Q}$ [69]:

$$\kappa = k_0 \frac{A_0}{Q} \sqrt{\frac{A}{2}} \cos(\phi) \tag{2.7}$$

Then, in a second step, the conservative force is calculated from κ by

$$F(z) = -\frac{\partial}{\partial z} \int_z^{z+2A} \frac{\kappa(\zeta)}{\sqrt{\zeta - z}} d\zeta \tag{2.8}$$

where $\zeta(t)$ denotes the temporary position of the tip apex that assumes values between z and $z + 2A$ throughout the oscillation cycle.

In the case of Payam's method, the steps to obtain the conservative force from the observables are the following [26]: Starting again with $f_\mathrm{d} = f_\mathrm{n}$, first a term denoted as $X(z)$ is computed by

$$X(z) = \frac{A_0}{2QA} \cos\phi. \tag{2.9}$$

Then, the conservative force is obtained through

$$F(z) = 2k_0 \int_z^\infty X(\zeta)d\zeta - 2k_c \frac{\partial}{\partial d} \int_z^\infty \left(\frac{A^{3/2}}{\sqrt{2(\zeta - z)}} X\right) d\zeta \tag{2.10}$$

In either case, before computing the respective derivatives, a slight Gaussian smoothing (radius of 2) is applied to avoid introducing high-frequency noise. An example force curve obtained by using Equation 2.8 is shown in Figure 2.12. In the same way, individual force curves at a specific (x, y) position can be calculated without averaging. This is particularly useful to produce xz force panels, such as the ones shown throughout this thesis. To this end, the force conversion is repeated for $x = 0...79$ and the algorithm described in section 2.3.1 is applied. Note that the z-range of the force curve is slightly reduced with respect to the amplitude and phase shift curves. This is mainly because the force reconstruction requires an integration over the oscillation cycle (peak-to-peak oscillation amplitude, *i.e.*, $2A_0$).

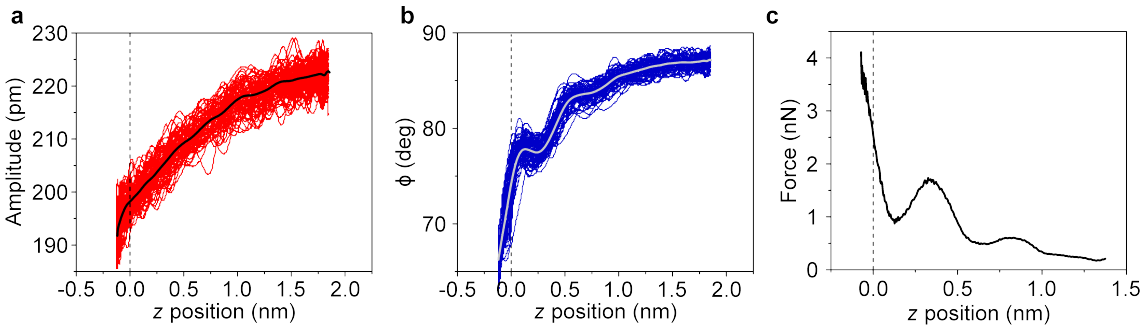

Figure 2.12.: Illustration of the force reconstruction from the AM 3D-AFM raw data using Hölscher's algorithm. **a.** Amplitude (A) and **b.** phase shift (φ) curves forming one entire xz panel. There are 80 individual curves. The average curve is calculated for both observables (highlighted). **c.** Force curve computed from the average amplitude and phase curves as described in Reference [117]. The data was taken on epitaxial graphene in ultrapure water. Adapted from [113].

2.3.3. Background Force

In some cases of solid-liquid interfaces (SLIs), the reconstructed force curve consists of a long-range monotonic background with superimposed oscillations [68, 70, 103, 113]. An example of such a case is shown in Figure 2.12. Sometimes it is useful to separate the background force, F_{bg}, from the oscillatory part of the force curve. First, to determine the background's contribution to the force curve, a monotonic function can be fitted to the reconstructed force curve. A simple exponential function was implemented in the 3D-AFM analysis software suite that by default is fitted to the data

$$F_{bg} = C_1 + C_2 \exp(C_3 z) \tag{2.11}$$

with C_1, C_2, and C_3 as fit parameters. Furthermore, a double exponential fit function was implemented and can be chosen by the user instead of Equation 2.11.

$$F_{\mathrm{bg}} = C_1 + C_2 \exp(C_3 z) + C_3 \exp(C_4 z) \tag{2.12}$$

with C_4 and C_5 as additional fit parameters. The fit range can be freely chosen by using the interface. After successful fitting, the fit curve, the fit range, as well as the fit parameters are displayed. The fitting for the example force curve is shown in red in **Figure 2.13**a. The background component of the force is automatically subtracted from the reconstructed force and both curves are displayed alongside. An example of the force curve after subtraction of the background component is shown in Figure 2.13b (in blue).

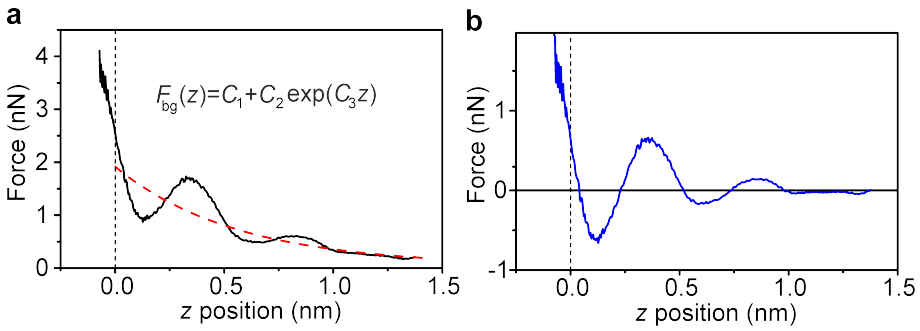

Figure 2.13.: Subtraction of a repulsive background force. **a.** Reconstructed force curve exhibiting a repulsive background (in black). The background is determined empirically by fitting an exponential function to the force curve (in red). **b.** Final force-distance curve after removing the background. The data was taken on epitaxial graphene in ultrapure water. Adapted from [113].

2.3.4. Comparison Force Reconstruction

Two different force reconstruction algorithms are implemented in the AM 3D-AFM software suite to obtain the conservative tip-sample force. Here, both algorithms are performed for AM 3D-AFM data obtained on a hydrophobic sample (MoS_2) in ultra-pure water and compared. **Figure 2.14**a displays the conservative force reconstructed by Payam's method (in red), Hölscher's method (in blue), and the net force obtained from the static deflection (in gray). Both reconstruction algorithms show a repulsive background force upon approaching the sample with some superimposed oscillations. Payam's method determines an overall larger force than Hölscher's. By fitting a simple exponential function to the force curves and subtracting it subsequently from the total force (as explained in the previous section), the oscillatory parts of the force curves can be compared. Figure 2.14b shows the resulting force curves obtained after subtracting the background contributions.

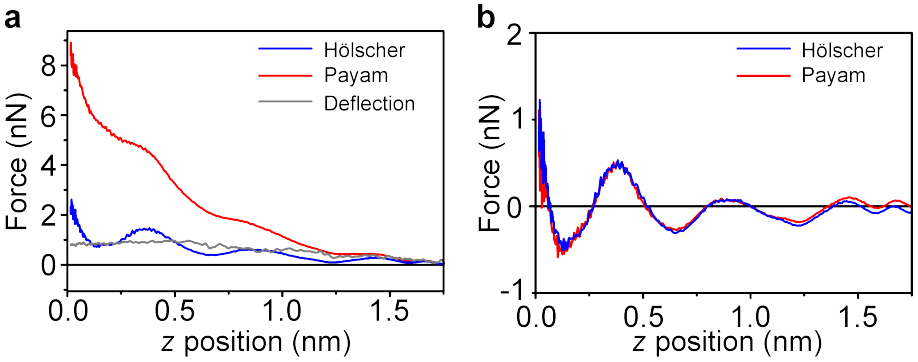

Figure 2.14.: Comparison of force reconstruction methods. **a.** The conservative force reconstructed by Payam's method (in red), Hölscher's method (in blue), and the net force obtained from the static deflection (in gray) are shown. **b.** Both reconstructed force curves from panel a after subtraction of the exponential background force. It becomes evident that both methods determined the same oscillatory part of the force curves. The data was taken on MoS_2 in ultrapure water.

Interestingly, both Payam's method (in red) and Hölscher's method yield very similar results for the oscillatory part. Thus, the difference is caused mainly by the background force component. By calculating the net force acting on the cantilever from the static deflection signal (see section 2.2.2), an additional reference can be obtained as it was done earlier by Katan *et al.*. [112] Under the assumption that the measured deflection curve contains mostly conservative interactions (an assumption that is reasonable due to the small velocities in AM 3D-AFM, see Figure 2.4), at least the order of magnitude can be compared. Figure 2.14a displays the net force (in gray) alongside the reconstructed force curves. The comparison shows that Hölscher's method describes the force measured by the static deflection better. It is desirable to calculate also the dissipative interactions in order to obtain complementary information [120] but this has not been implemented so far.

2.3.5. Deflection Correction

One of the main output of 3D-AFM measurements are amplitude (A) and phase shift (ϕ) spectroscopy curves. Irrespective of the particular method (3D-AFM or Force-Volume approaches), different distances are involved when recording dynamic AFM spectroscopy curves. They are illustrated in **Figure 2.15**. Technically, the AFM controls the position of the cantilever base, z_c, which is directly coupled to the z-piezo's extension. However, physically more relevant is the actual tip-sample distance, d. Both are connected via the simple geometrical relation

$$d = z_c - A + \Delta z \tag{2.13}$$

where δ denotes the cantilever deflection. In 3D-AFM, the cantilever deflection is often small and thereby neglected, apart from a few exceptions [44, 107]. Assuming $\Delta z \approx 0$, an approximate tip-sample distance z can be calculated

$$z = z_c - A \tag{2.14}$$

Such an approach is common in previous works [43,105] and is also by default the spatial coordinate in the 3D-AFM software suite.

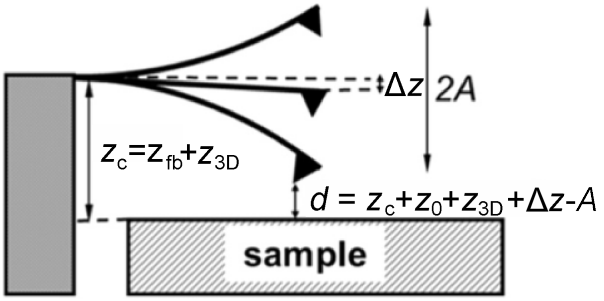

Figure 2.15.: Illustration of the different distances involved in 3D-AFM spectroscopy curves. z_c is the position of the cantilever base, z_fb and z_3D are the movements of the cantilever base due to the feedback and the ultrafast movement, respectively, Δz the static (average) cantilever deflection, A the cantilever oscillation amplitude, z_0 an offset that accounts for the tip-sample contact point, and d the minimum tip sample distance. Adapted from [26].

However, this approximation is only valid before the tip enters into the contact with the sample. Furthermore, recently investigated SLI exhibited monotonic forces that cannot be screened out using electrolyte solutions (see previous Section 2.3.3) [70, 72, 103, 113]. Due to the repulsion, the AFM tip moves less far than the z-piezo when approaching the sample. To disentangle the actual movement of the tip from the movement of cantilever base, the cantilever deflection has to be taken into account. Knowing $\Delta z(z)$ allows in principle to convert the z-position into tip-sample distances. Once converted, the contact point with the surface can be determined. Force-distance curves rather than force-displacement curves are required for the obtaining accurate distances from force spectroscopy measurements. A straightforward way is to record the cantilever deflection during the data acquisition as it is standard in static AFM force spectroscopy [25]. In the 3D-AFM software suite, if selected by the user, a correction according to Equation 2.13 is automatically applied to all distances. However, this approach is often unpractical because it introduces high-frequency noise in the raw data, which renders force reconstruction impossible. An alternative approach is to reconstruct the force neglecting the static cantilever deflection. Then, in a second step the deflection correction can be applied to the obtained force curve according to Equation 2.13. A comparison of two force curves before (black curve) and after the correction (red curve) is displayed in **Figure 2.16**. The distances d_0 and d_1 change, respectively, from 0.36 nm to 0.34 nm and 0.50 nm to 0.47 nm. This means that using z instead of d implies an overestimation of around 5% for the given conditions.

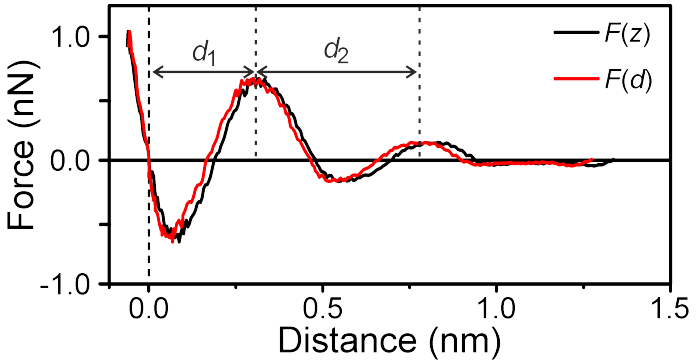

Figure 2.16.: Comparison of two force curves before (black curve) and after the correction (red curve). The distances d_0 and d_1 change, respectively, from 0.36 nm to 0.34 nm and 0.50 nm to 0.47 nm. Neglecting the correction implies an overestimation of around 5 %. The exponential background force has been subtracted. The data was taken on epitaxial graphene in ultrapure water.

2.4. Conclusions

In this chapter, an AM 3D-AFM software suite has been developed and equipped with an intuitive graphical user interface. The software suite is split into two parts, data acquisition and data analysis. With the data acquisition software, the user has an easy-to-use tool at hand for robust and fast 3D-AFM measurements. Once the experiment is done, the data analysis software provides a comprehensive environment for accurate and time-efficient data analysis. It is pointed out that the part of the software which controls the 3D movement is based to a large extend on code originally developed by Dr. Daniel Martín-Jiménez [43,105,108]. Nonetheless, original contributions were added throughout this chapter which are emphasized and explained in detail. More importantly, the data analysis software was developed from the scratch.

Data Acquisition. The data acquisition software was extended by a new channel containing the static cantilever deflection. With the help of the deflection channel, data acquisition is facilitated and complementary information is obtained. It is demonstrated that the additional channel provides useful information in at least two aspects: First, it enables to calculate the true tip-sample distance, as it is standard in force spectroscopy, but not in 3D-AFM. Second, it serves as an independent reference for the force-reconstruction algorithms used in the analysis.

Data Analysis. A comprehensive data analysis software was developed, equipped a plethora of functionalities. The options include basic steps such as time-efficient browsing through the complex 3D data sets or extracting and displaying individual observable-z curves. In addition, it offers advanced features such as the automatic and accurate transformation from the temporal coordinate to the spatial coordinate system in three dimensions, and the application of two different force-reconstruction algorithms in up

to three dimensions. Particular care was taken to perform the data treatment in a transparent way by leaving always the option to display raw data as a comparison. The data analysis improves the way of processing common 3D-AFM data obtained on atomically flat samples. It provides the basis for obtaining meaningful 3D-AFM images on more complex surfaces including terraces and steps. The developed software is used in the following Chapters 3 and 5.

3. Solid-Liquid Interface on Hydrophobic Materials

3.1. Introduction

Solid-liquid interfaces (SLI) are highly relevant for a number of phenomena in nature and technology, including wetting [46, 47], adhesion [51], surface electrochemistry [53], nanorheology [55], patterning [121–123], biomineralization [52], protein folding [56, 57] and molecular recognition [57, 58]. A variety of experimental methods and simulations has led to significant advances in our understanding of how water molecules interact with surfaces [58, 99, 124–126]. However, when it comes to hydrophobic surfaces, the nanoscale water structure and its role in the properties of surfaces immersed in aqueous environments and mediating interactions between them is not well understood. Without reaching a satisfactory conclusion, the findings reported in the literature cover several phenomena caused by the hydrophobic interaction with water molecules. One concept is the formation of a low-density depletion layer of varying thickness (2-4 Å) separating the water molecules from the hydrophobic surface as detected by X-ray reflectivity [127]. However, this idea has been challenged by ellipsometry measurements [128], and neutron reflectivity experiments suggested that such a layer instead consists of hydrogenated airborne organic material [129]. Others have proposed the formation of nanobubbles as suggested by AFM images but their surprising stability remains controversial. [130]. With the recently developed three-dimensional atomic force microscopy (3D-AFM), researchers have a tool at hand to provide atomically resolved three-dimensional images of SLIs. [42,126] On the other hand, a variety of surfaces with different grades of hydrophobicity is provided by two-dimensional (2D) and few-layer materials. 2D materials have moreover attracted considerable interest because of their electronic, optical, thermal, and mechanical properties that arise from their atomic-size thickness [131–134]. Among other applications, those materials have been suggested as active elements in chemical and biological sensors [135–137]. The use of 2D materials as sensing components in chemical, biological, and medical devices can involve their direct interaction with water molecules. Likewise, the interfacial water structure should influence the interactions of 2D materials with other materials, solvents, ions, and biomolecules. In short, the understanding of the interaction of water molecules with 2D materials is relevant for two reasons. First, those materials provide a variety of extended and atomically flat surfaces to investigate hydrophobic interactions with atomic resolution. Second, understanding the interfacial water structure on 2D materials could lead to more efficient 2D materials-based sensors. Macroscopic measurements such as water contact angle measurements show that the hydrophobicity of graphene, few-layer MoS_2, and WSe_2 increases with time due to the

adsorption of airborne hydrocarbon contaminants [138–140]. Those results are supported by theoretical calculations [141]. At the nanometer scale, AFM-based methods have been applied to study the wettability and the condensation of water vapor on graphene and few-layer MoS_2 [135, 142, 143]. Those studies were either focused on the adsorption of water from air under different conditions (temperature and/or relative humidity) [143] and/or the influence of those processes on the electronic or structural properties of the 2D materials [142]. The graphene–water interface has been studied by X-ray reflectivity measurements [59, 144] and molecular dynamics simulations (MD) [145, 146]. Molecular resolution AFM experiments performed on graphitic samples have shown the formation of solvation layers separated by approximately 0.5 nm. [72, 87, 103] This separation is approximately two times larger than the one found on mica ($\approx$ 0.25 nm). In contrast, molecular dynamics (MD) simulations performed on graphene in contact with water have shown the presence of a hydration structure with a periodicity comparable to the size of an individual water molecule [98, 145]. Here, the angstrom resolution capabilities of AM 3D-AFM will be exploited to visualize the SLI on graphene, highly oriented pyrolithic graphite (HOPG), MoS_2, $MoSe_2$, WS_2, and WSe_2. Measurements on mica, an archetypical hydrophilic surface, serve as a reference and allow for a comparison between the materials. The key results are published in: Manuel R. Uhlig, Daniel Martin-Jimenez and Ricardo Garcia. Atomic-scale mapping of hydrophobic layers on graphene and few-layer MoS_2 and WSe_2 in water. *Nature Communications* **10**, 2606 (2019).

3.2. Materials and Methods

Sample Preparation

Graphitic samples. Epitaxial graphene monolayers (98% $\pm$ 5% monolayer coverage) on the silicon face of SiC substrates were purchased from Graphene Nanotech SL, Spain. This type of graphene is grown through selective sublimation of Si surface atoms by high-temperature annealing. Before each experiment, the sample was cleaned by careful rinsing with ultrapure water. Highly oriented pyrolytic graphite (HOPG) samples (grade ZYB) were purchased from Bruker (USA) and cleaved with adhesive tape before each experiment.

Transition Metal Dichalcogenides. Thin flakes of MoS_2 (SPI supplies, USA), WSe_2, $MoSe_2$, and WS_2 (all from HQ Graphene, Netherlands) were mechanically exfoliated with Polydimethylsiloxane (PDMS) stamps and transferred onto clean Si/SiO_2 substrates (see below). For the experiments with transition metal dichalcogenides (TMDC), mostly flakes with a thickness in the range of 5-15 monolayers were chosen as they can be found easily and reliably distinguished from bulk flakes using the optical microscope [147]. A few times, AFM height profiles were obtains in order to identify particularly thin flakes. The thinnest flake investigated yielded a height of 3 nm in an AM-AFM measurement, corresponding to ≤ 5 layers. Also bulk samples were investigated, either by performing experiments on thicker flakes or directly on the crystal.

Muscovite mica. Discs of muscovite mica (Grade V-1, SPI supplies, USA) were freshly cleaved with adhesive tape before the experiments and copiously rinsed with ultrapure

water.

Water

Ultrapure water. Ultrapure water (UPW) was freshly obtained before the experiments (ELGA Maxima, 18.2 MΩ). Some experiments were conducted with water from a different water purifier (of the same type) in order to confirm the results. The water's pH was measured with a calibrated pH meter (Hanna Instruments HI 9024, experimental uncertainty pH±0.2). After a few minutes, the pH reached a value of around 5.6 (see **Figure 3.1**), which is the expected pH value of UPW in equilibrium with air. The solutions of 200 mM KCl were prepared by dissolving KCl (≥99.0%, Sigma-Aldrich) in UPW.

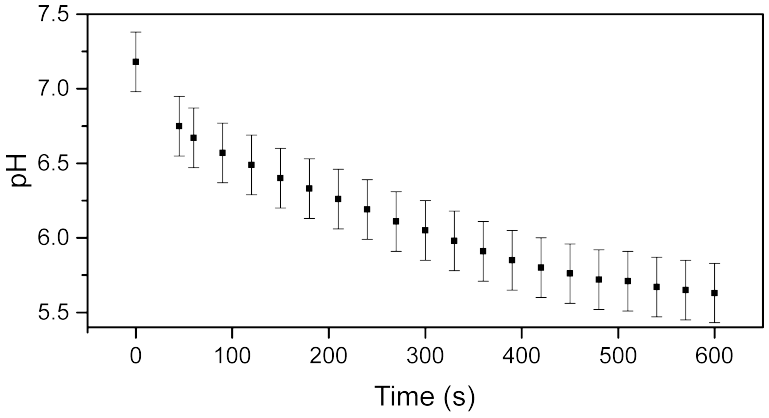

Figure 3.1.: pH value of freshly obtained ultra-pure water. Within 10 minutes after obtaining the water, its pH decreases from initially 7 to 5.6. The observed acidification is due to the dissolution of atmospheric CO_2 into the water. Error bars are upper limits, the manufacturer's specification is smaller.

Highly contaminated water. For reference experiments, UPW mixed with n-octane (≥99%, Sigma-Aldrich) at a concentration of $c_{n-\text{octane}} = 0.7$ mL : 1 L was used. This concentration corresponds to the solubility limit of n-octane in water.

Cleaning protocols

The few-layer TMDCs were deposited on Si/SiO_2 substrates (275 nm SiO_2, thermally oxidized). The substrates were ultrasonicated sequentially in acetone (99.6%, Acros Organics), ethanol (≥99.8%, Sigma-Aldrich), and UPW. After drying the substrates with a nitrogen flow, they were then exposed to oxygen plasma for 15 min (Diener Electronic, Germany). For some experiments the sample was cleaved while being immersed in water to avoid any contact with the ambient air before the experiments. To this end, a small piece of bulk material (HOPG, WSe_2, MoS_2) was glued on a polytetrafluorethen (PTFE) disc and pressed adhesive tape against the dry surface. Then, the sample was

immersed into UPW using a wide glass beaker and the tape was pulled off while being fully immersed.

AFM imaging

After the transfer, the samples were glued on a steel puck and magnetically mounted onto the microscope sample stage. Then, a small droplet of UPW or an electrolyte solution was placed on the surface and the cantilever was immersed into the liquid. Most of the measurements were performed in a Cypher ES/VRS AFM (Asylum Research, Oxford Instruments, Ca, USA) equipped with a closed liquid cell. The temperature was held constant at typically (28.0 ± 0.1)°C by using a temperature control unit.

2D-AFM imaging. Conventional AFM images were performed in the amplitude modulation (AM) mode by exciting the second mode of the cantilever. The cantilever excitation was realized with a photothermal drive. The free amplitudes A_0 were typically in the range of 200-300 pm, with an amplitude set-point ratio of $A_{\mathrm{sp}}/A_0 \approx 0.9$. A few of the scans were performed in a Cypher S (Asylum Research, Oxford Instruments, Ca, USA) equipped with an open liquid cell.

3D-AFM imaging. The three-dimensional AFM was implemented on the Cypher S and ES/VRS platforms as described in Chapter 2. Three-dimensional AFM imaging is performed in the amplitude modulation mode by exciting the cantilever at its 2nd mode, if not stated otherwise. For the sinusoidal signal applied to the z-piezo, amplitudes (peak-to-peak) between 1 and 4 nm and a period (frequency) of 20 ms (50 Hz) were used, if not stated otherwise. The oscillation of the cantilever was driven by photothermal excitation. The free amplitude values A_0 were in the range of 40-360 pm. The effective set-point was chosen to be $A_{\mathrm{sp}} \approx 0.95A_0$. A feedback bandwidth of 1 to 2 kHz and an integral gain of 2 to 5 were used. The z-data was read out every 20 µs and stored in 1024 pixels (512 pixels for approach and 512 pixels for retraction). Each xy plane of the 3D maps contains 80×64 pixels. The total time to acquire such a 3D-AFM image was 105 s.

Cantilevers and Calibration

Silicon cantilevers with silicon tips were used for AFM imaging (PPP-NCHAuD, NanoAndMore, Germany). The cantilevers were first cleaned in a mixture (50:50 in volume) of isopropanol (99.6 %, Acros Organics) and UPW, then rinsed with UPW and finally placed in a UV-Ozone cleaner (PSD-UV3, Novascan Technologies, USA) for ≈ 30 min to remove organic contaminants [148]. Each cantilever was calibrated in liquid once the 3D-AFM data was acquired to prevent tip damage during the calibration. The calibration for most of the cantilevers was performed as follows (the superscript "lq" denotes "in liquid"): First, the inverse optical lever sensitivity (invOLS) for the static deflection, σ_0^{lq}, is obtained from force-displacement curves recorded on a clean, flat and stiff sample (275 nm of thermally grown SiO_2 on Si). The invOLS σ_0^{lq} is determined as the inverse of the curve's slope in the contact part. Second, the cantilever's thermal noise spectrum (power spectral density, PSD) is recorded at about 2 µm above the sample surface [13]. Then, the single harmonic oscillator (SHO) model is fitted to the PSD around the peak of the first

resonance frequency using the calculated invOLS of the first mode, $\sigma_1^{\mathrm{lq}} = 1.09\sigma_0^{\mathrm{lq}}$ [10]. From the fitting we obtain the force constant k_1, quality factor Q_1^{lq}, and resonance frequency f_1^{lq}. Then we measure the resonance frequency of the second mode, f_2^{lq}, from the PSD and calculate the corresponding force constant $k_2 = k_1(f_2^{\mathrm{lq}}/f_1^{\mathrm{lq}})^{2.17}$, as proposed by Labuda *et al.* [149]. Knowing k_2, we then fit the SHO model to the PSD around the peak of the second resonance frequency to obtain the corresponding invOLS σ_2^{lq} and Q_2^{lq}. The parameters used to determine the forces are summarized in Table B.1. Some 3D-AFM experiments have been performed with other cantilevers (PPP-NCSTAuD, NanoAndMore, Germany and AC55TS, Olympus, Japan). No major differences have been observed.

Water Contact Angle Measurements

The contact angle is the angle formed at the phase boundary between a liquid droplet in contact with a solid surface. It carries information about the surface energies of the materials that are in contact. An introduction into the topic can be found for example in the seminal work of Cassie [150]. The equilibrium contact angle Θ is given by

$$\cos\Theta = \frac{\gamma_{\mathrm{sg}}\gamma_{\mathrm{sl}}}{\gamma_{\mathrm{lg}}} \tag{3.1}$$

where γ_{sg}, γ_{sl}, and γ_{lg} are the interfacial energies, respectively, at the solid-gas, solid-liquid, and liquid-gas interfaces (see Figure 3.2) [150]. In the special case of water, a droplet that spreads on a surface indicates a (very) hydrophilic surface, while a sessile droplet with a finite angle implies that the surface is to some extend hydrophobic [151]. Although this description is simplified [152] and the accurate measurement of contact angles is far from being trivial, the overall behavior of a surface in terms of hydrophobicity can be understood intuitively by a water contact angle (WCA) measurement.

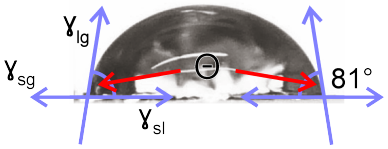

Figure 3.2.: Measurement of the equilibrium water contact angle Θ. γ_{sg}, γ_{sl}, and γ_{lg} are the interfacial energies, respectively, at the solid-gas, solid-liquid, and liquid-gas interfaces. Example data obtained with ultrapure water on an HOPG substrate after exposure to air for 20 min.

A home-built setup consisting of a LED backlight (Asylum Research, Oxford Instruments, Ca, USA) and a high-resolution CCD camera (Panasonic, Japan) was used to measure Θ. For that, 10 µl of ultrapure water were carefully placed on the surface by using a micropipette. After recording a picture aligned with the plane of the sample, the sessile drop's WCA was measured by fitting a straight line to the gas-liquid contact line. Measurements with asymmetric contact angles (due to visible pinning of the three phase contact line) were disregarded. The investigated samples were bulk pieces of mica, HOPG, WSe_2, MoS_2, and the SiC/graphene sample.

3.3. 2D-AFM Results

Figure 3.3a shows the graphene sample immersed in UPW. It exhibits large and flat terraces that are otherwise almost featureless (see also panel b). The topographic steps between the terraces have a height of a few nm each and originate from the underlying SiC substrate [153]. Figure 3.3c-d shows a different spot of the same sample around such a substrate step. Some diffuse structures are visible on both sides of the step. Interestingly, in the phase shift image (Figure 3.3d) some bright patches with periodic structures can be observed. Such structures were observed most of the times when imaging smaller areas of the graphene. Further zooming in reveals the stripe structure clearly (Figure 3.3e and f), mainly in the phase channel but they are also slightly visible in the topography channel. A cross section along the white dashed line drawn in panel f is shown in panel g. The oscillation is characterized by a periodicity of 4.9 nm. The size of these well-ordered structures is independent of scan size, scan rate and scan angle and, hence, they represent a real surface feature. The direction of the stripe pattern does not change at the substrate step. This is expected since the epitaxial graphene covers the whole SiC substrate like a carpet [154]. In contrast, at an actual (monolayer) step within the graphene layer, the direction of the stripe structure does indeed change (see below). Similar structures have been recently imaged in AFM measurements on graphene/SiC in ambient conditions by Giessibl's group [154, 155], and already earlier on HOPG in pure water by the group of Hwang [156–159]. They have been attributed to the adsorption of gasses [155–159]. Recently, similar structures observed on HOPG in pure water were ascribed to *in situ* catalysis of methanol [50].

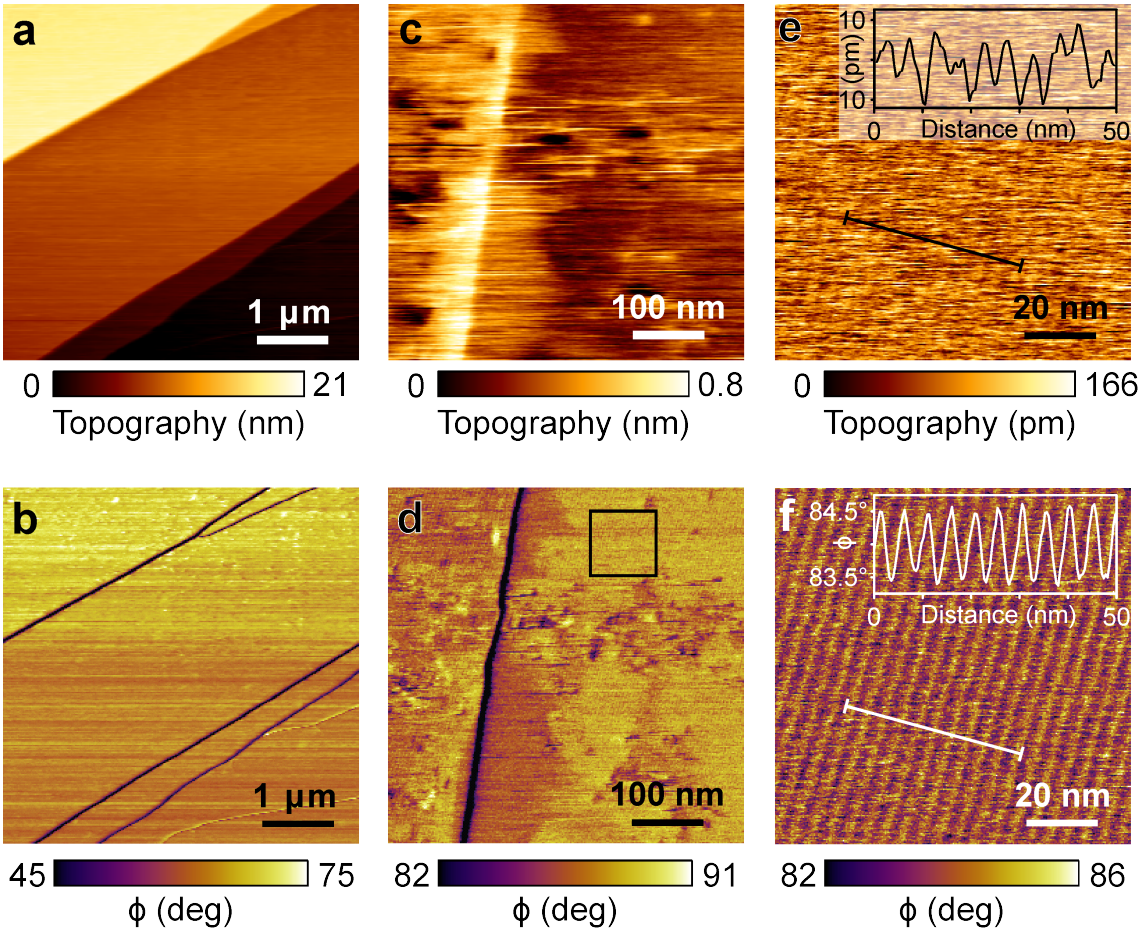

Figure 3.3.: AM-AFM images taken in ultrapure water on SiC/graphene. The top row shows topography images and the bottom row the corresponding phase shift images. The images in the first column (**a-b**) depict the graphene monolayer with large, atomically flat terraces. The surface steps originate from the underlying SiC substrate. The middle column (**c-d**) shows a different spot of the same SiC/graphene sample. Domains with a periodic structure are faintly visible in the phase shift image (panel d), as for example marked by the black rectangle. A zoom-in into this area is shown in the last column (**e-f**). The periodic structures are slightly visible in the topography image and clearly visible in the phase shift image. The insets show cross sections along the lines drawn in the panels. The periodicities are 4.9 nm in both the height and the phase. Scan parameters: free amplitude $A_0 = 240$ pm, amplitude set-point $A_{\mathrm{sp}} = 0.90A_0$, $f_2 = 912.8$ kHz. Adapted from [113].

3.3.1. Lattice Resolution Images in UPW

In order to identify clean and flat areas of the materials, lattice-resolution images of the surfaces immersed in UPW were taken with AM-AFM in regions without adsorbates nor stripe structures. In order to obtain lattice resolution, the scanning was started under the same conditions as described in the previous section (second mode driven

at $A_0 = 240$ pm). Then, the amplitude set-point was reduced to 30-50 % of the free amplitude and the line rate was increased (10-20 Hz) to minimize image distortions. For each of the three mainly investigated materials, a lattice-resolution image is shown in **Figure 3.4**a-c. The hexagonal lattice structure is resolved in the topography and in the phase channel. Two-dimensional fast Fourier transforms (FFT) were applied to the phase images to obtain the crystal structure of the surfaces (panels d-f). The FFT spectra clearly reveal the hexagonal structures of the lattices and allow for reconstructing the corresponding lattice vectors $\vec{a_1}$ and $\vec{a_2}$. Note that in the case of graphene and TMDCs, both lattice vectors are of identical length, *i.e.*, $|\vec{a_1}| = a_1 = |\vec{a_2}| = a_2$ [160]. The lattice vectors obtained from the FFT transforms have average lengths of 0.24 ± 0.01 nm, 0.34 ± 0.02 nm, and 0.31 ± 0.02 nm for graphene, MoS_2 , and WSe_2, respectively. These numbers fit well the expected values of the crystal lattice for the respective materials. [160] Furthermore, they are very similar to values measured with different AFM techniques in ambient conditions on graphene [154], MoS_2 [161], and WSe_2 [162].

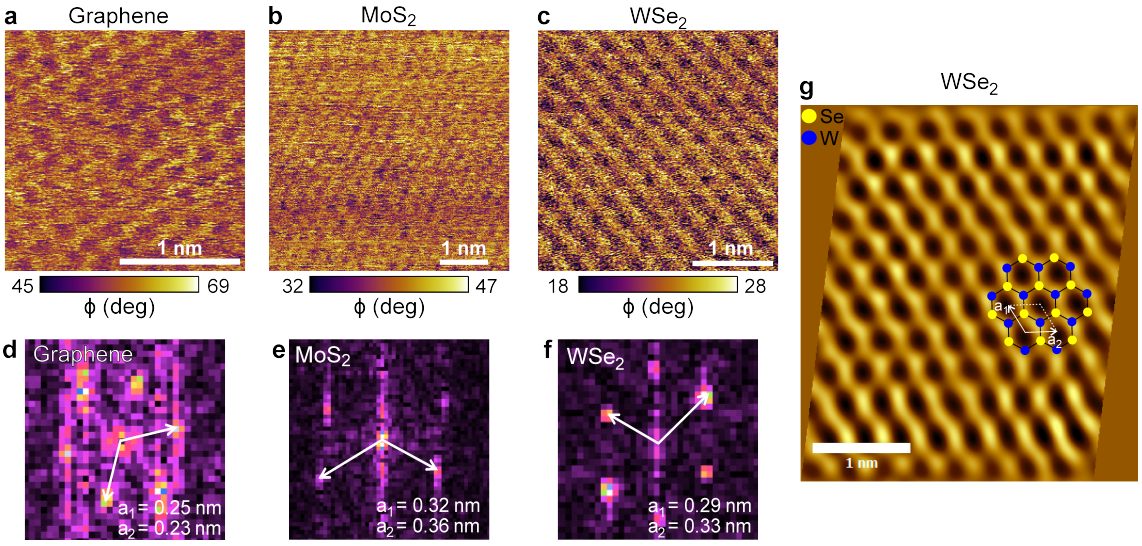

Figure 3.4.: Small-amplitude AM-AFM images with lattice resolution of layered materials in water. **a.-c.** AFM phase images showing the lattice structure of graphene, MoS_2 and WSe_2, respectively. **d.-f.** Fast Fourier transforms (FFT) of (a-c). The reciprocal lattice vectors are depicted as white arrows. The lengths of the corresponding real-space lattice vectors, a_1 and a_2, are stated below. Panel **g** shows the phase image taken on WSe_2 (panel c) after the application of a FFT filter (panel f) and a correction for the image distortion (asymmetric lattice vectors). A possible WSe_2 lattice configuration is illustrated. The AM-AFM was operated with a free amplitude $A_0 = 240$ pm and an amplitude set-point A_{sp} between 0.30 and $0.50A_0$. The imaging was performed at a scan rate of 10 to 20 Hz. Adapted from [113].

3.4. 3D-AFM Results

3.4.1. Hydrophobic Solid-Liquid Interfaces in Ultrapure Water

Having identified a clean and atomically flat area of the materials, 3D-AFM was applied within these areas in order to visualize the solid-liquid interface of the materials immersed in UPW. For each of the three mainly investigated materials (SiC/graphene, WSe_2, MoS_2), a 3D-AFM image is shown in **Figure 3.5**a-c. The images show the phase channel (ϕ) of the AM 3D-AFM (raw data). At the bottom of the cubes the lattice resolution images shown in Figure 3.4 were plotted. The values of the color bar were chosen in such a way that the solid surface appears brownish-yellow, while the volume corresponding to the SLI is represented by a bluish color. For comparison, in Figure 3.5d an xyz phase map measured over mica (in 200 mM KCl, aq.) is shown.

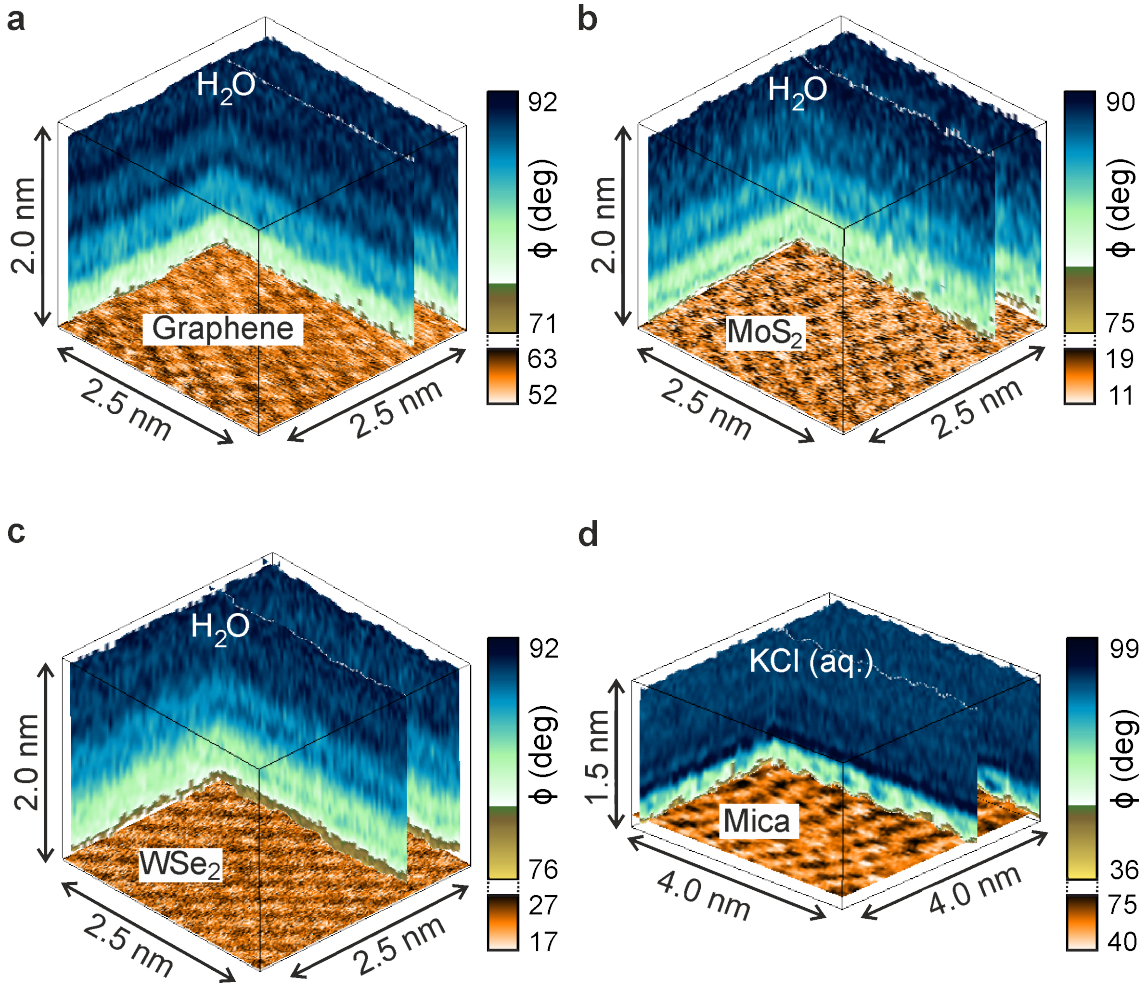

Figure 3.5.: 3D-AFM images of 2D materials-water interfaces in comparison with the mica-water interface. **a.** Epitaxial graphene grown on SiC. **b.** Few-layer MoS_2. **c.** Few-layer WSe_2. **d.** Mica. The images show the phase shift ϕ as function of the xyz position. An alternation of dark and bright horizontal stripes is visible in all the images. At the bottom of the 3D images, lattice resolution images of the different surfaces are plotted. Adapted from [113].

The images show an alternation of dark and bright horizontal stripes in parallel to the surfaces within 2 nm above the solid. For larger distances, no such layers are visible and the phase shift reaches a constant value of around 90 deg (see **Figure 3.10**). Oscillations of the AFM observables were detected earlier above hydrophilic surfaces such as mica [42, 43, 45, 70, 81, 86, 88, 105, 126] or biomolecules [45, 86]. They were related to changes in the solvent number density [96,97], giving rise to a layered structure within the solid-liquid interface. Recently, a few cases of oscillations over hydrophobic substrates, such as HOPG and perfluorodecyltrichlorosilane (FDTS) have been reported [72, 81, 87, 103]. In either case (hydrophilic or hydrophobic), the oscillations within the solid-liquid interface

were ascribed to the presence of solvation layers. Also the materials investigated here belong to the class of hydrophobic surfaces [163].

A qualitative and intuitive way to probe the hydrophilic or hydrophobic character of a surface is measuring the water contact angle (WCA), denoted as Θ. The WCAs of the materials were found to be between 61° and 81°, which implies a (moderately) hydrophobic character (see **Figure 3.6**a-c).

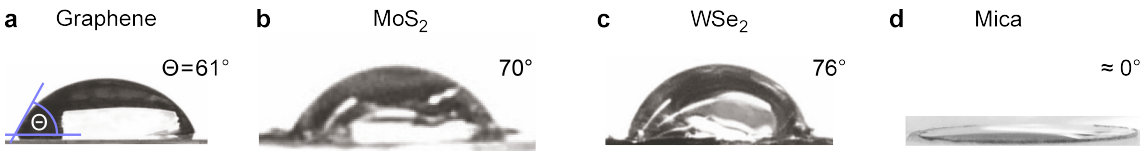

Figure 3.6.: Water contact angle (Θ) measurements. **a.** Epitaxial graphene on SiC. **b.** Bulk MoS_2. **c.** Bulk WSe_2. **d.** Mica. Adapted from [113].

For comparison, in Figure 3.5d an xyz phase map measured over mica (in 200 mM KCl, aq.) is shown. It becomes clear that the extension of the SLI observed on hydrophobic surfaces is larger (2 nm) compared to that over hydrophilic substrates (1 nm). In order to have a detailed view on the data, xz-panels are computed from 3D-AFM measurements. Once the 3D-AFM data is acquired, such xz-maps can be easily extracted as a function of the y position. Here, the observables (A and ϕ) were transformed into forces by using force reconstruction (see Section 2.3.2) [117]. As an example, **Figure 3.7**a shows an xz force panel for MoS_2.

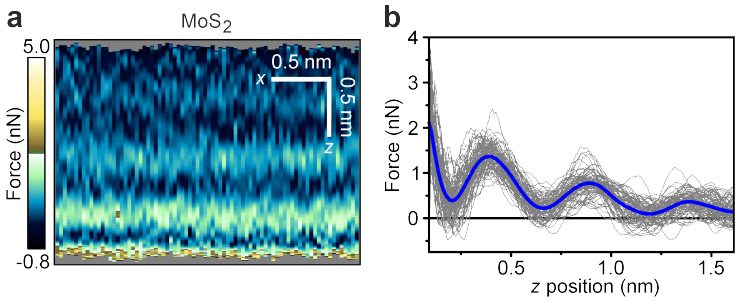

Figure 3.7.: **a.** xz force map extracted from a 3D-AFM measurement performed on a few-layer MoS_2 surface immersed in water. **b.** Unraveling of the xz force map into 80 individual force distance curves (in gray). The oscillations are clearly visible in the individual curves. The average curve (highlighted in blue) preserves the overall behavior of the curves but improves the signal-to-noise ratio.

The contrast in the force channel strongly visualizes the horizontally ordered structures within the SLI. In the same way as in the 3D-AFM images shown above, the solid surface appears in a brownish-yellow color, while the SLI is represented by bluish tones. In an xz force map, each vertical line represents an individual $F(z)$ curve. The set of 80 $F(z)$ curves forming the panel are shown in Figure 3.7b (in gray). The average curve, $<F>(z)$, is highlighted in blue. The individual force curves show clear oscillations

superimposed over a repulsive background force. Both the oscillation's amplitude as well as the background force's magnitude are decaying upon increasing the z-position.

Recently, the solvent-tip-approximation (STA) model was independently introduced by Amano *et al.* and Watkins *et al.* [92,93]. It relates features observed in force maps with changes in the liquid (*i.e.*, the solvent) density [92, 93, 96, 97, 164]. Alternating dark and bright horizontal stripes in the xz-maps correspond to solvent layers with a lower and higher liquid density in comparison with the bulk value. As a consequence, each oscillation in the $F(z)$ curve is related to an individual solvation layer (SL). Hence, the position of the different solvation layers with respect to the position of the solid surface can be deduced from the force-distance curves. It should be noted that the z distances at which maxima of the force are observed are shifted to larger values with respect to the distances of the corresponding maxima in the solvent number density. This observation is intrinsic to the STA model, which establishes that the force at a given site r is proportional to the logarithmic derivative of the solvent number density ρ [92,93,97]:

$$F(r) = \frac{k_{\mathrm{B}}T}{\rho(r)}\frac{\partial\rho(r)}{\partial z} \tag{3.2}$$

where k_{B} is the Boltzmann constant and T the absolute temperature. The position of the solid surface ($z = 0$) is defined here as the z-piezo displacement distance at which the repulsive force equals the maximum of the repulsive force associated with the closest SL. Then, the distances d_0, d_1, and d_2 can be used in order to characterize the oscillations, similar to previous works [43,95]. Here, d_0 is the distance of the first maximum to the solid surface, while d_1 and d_2 are, respectively, the distances between the 1st and 2nd, and the 2nd and 3rd adjacent SL.

For clarity, in the following discussion the focus will lie on the averaged force curves. To further simplify the discussion, the background component of the curve, $F_{\mathrm{bg}}(z)$, will be subtracted by fitting an exponential function to the curve as described in Section 2.3.3. Within the range of the $F(z)$ curves shown here (a few nm), the behavior of the curve can be sufficiently well described by a simple exponential of the form

$$F_{\mathrm{bg}}(z) = C_1 + C_2 \exp(C_3 z)$$

where C_1, C_2, and C_3 are constants. When fitting data taken over a larger z-ranges, it becomes clear that the background force above graphene is indeed well-described by the simple exponential over the entire z-range. In contrast, the background force measured above the TMDCs for larger z-ranges shows a behavior that is better described by a bi-exponential function. Common background forces at SLIs arise for example from electrical double layers (Derjaguin-Landau-Verwey-Overbeek forces, DLVO). However, DLVO forces can be screened out using electrolyte solutions [68, 165], whereas the force observed above TMDC surfaces in UPW does not change upon immersion in electrolyte solution (see below). Similar background forces were observed recently above a graphitic sample [87, 103]. Schlesinger and Sivan found that the background force (as well as the solvation layers) above a HOPG surface can be reduced by using degassed water [87]. The observations suggest that the background force is a property of the hydrophobic

solid-liquid interface, at least when probed by silicon tips. For the time being, the background force is empirically fitted and subsequently subtracted in order to focus on the force oscillations. The fitting parameters can be found in the appendix in Table A.2. Note that the xy force panels shown throughout this thesis always contain the total force including the background.

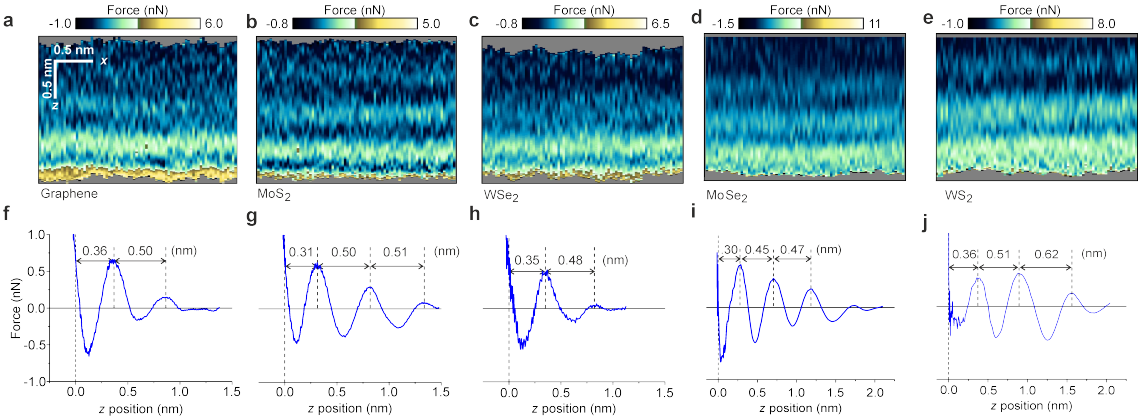

Figure 3.8.: Example xz force maps and force-distance curves of 2D materials-water interfaces. **a.** Graphene. **b.** Few-layer MoS_2. **c.** Few-layer WSe_2. **d.** $MoSe_2$ **e.** WS_2. **f.-j.** Force displacement curves extracted from the panels a-e, respectively. The data shows two to three oscillations in the force. Each peak is associated with a single molecular layer. The exponential background force has been subtracted. Adapted from [113].

Figure **3.8**a-e shows example xz force panels and the corresponding force curves for 5 different hydrophobic materials investigated here. Once the background force has been subtracted, a purely oscillatory force remains for all the materials (Figure 3.8f-j). Upon approaching the surface, the total force changes from positive (repulsive) to negative (attractive) values until the tip enters into mechanical contact with the surface and the cantilever deflects. Note that in the case of graphene, MoS_2, and WSe_2, the force panels and the corresponding $F(z)$ curves in Figure 3.8 are only a few examples out of many measurements showing oscillations.

The number of oscillations is not surface-specific. If oscillations were observed, the number of observed force maxima was always between one and three, with two and three being the most frequent cases. For the materials $MoSe_2$ and WS_2, only one experiment was performed for the time being. The overall extension of the SLI is about 2 nm for all the hydrophobic materials. For larger distances, the force oscillations diminish and the force reaches a constant value. An example for such a long-range measurement is shown in **Figure 3.10**a. For comparison, in **Figure 3.9**a an xz force map measured over mica (in 200 mM KCl, aq.) is shown. It becomes clear that the extension of the SLI observed on hydrophobic surfaces is larger (1.5-2 nm) compared to that over hydrophilic substrates (1 nm). Another interesting observation can be made by comparing the distances d_0, d_1, and d_2 measured on the different materials (see Figure 3.8f-j). The distances for all

the materials extracted from these and other force-distance curves are summarized in Table 3.1. On average, the values on graphene and the TMDC surfaces are $< d_0 >= (0.34 \pm 0.04)$ nm, $< d_1 >= (0.48 \pm 0.03)$ nm, and $< d_2 >= (0.53 \pm 0.07)$ nm. The distances are remarkably similar for all these materials apart from some slight variation. Altogether, the values are notably larger than the corresponding ones measured on mica, namely $< d_0 >= (0.18 \pm 0.01)$ nm, $< d_1 >= (0.34 \pm 0.04)$ nm. These differences become evident when comparing the force curves directly, as depicted in 3.9b. Some recent works detected SL over graphitic samples in water and also found that the distances between them are larger than on mica [72,81,87,103]. A control experiment on HOPG confirmed these earlier results and, furthermore, yielded values slightly larger than the ones of graphene (Figure 3.10d). The difference might be related to the different number of graphite layers, since this number affects the sample's hydrophobicity. [166] In any case, the observation made above the HOPG surface strengthens the findings made on graphene and TMDCs.

In the case of mica, and over hydrophilic substrates in general, the predicted and experimentally measured period of oscillation corresponds to the van der Vaals diameter of a water molecule (0.28 nm). [43,70–72,81,86,87,126] By contrast, the values measured over the hydrophobic samples are significantly larger than that value. Interestingly, MD simulations performed for a wide range of crystalline materials (including hydrophobic ones) such as graphene [145], graphite [98], MoS_2 [167], p-nitroaniline [84], calcite [96] or α-Al_2O_3 [168] covered by water molecules show that the distance between adjacent hydration layers hardly depends on the nature of the surface. The values range from 0.28 to 0.33 nm, as experimentally found in the case of the hydrophilic materials. On the other hand, the distances between adjacent layers measured on graphene, MoS_2 and WSe_2 (0.50 nm on average) are comparable to the values reported for crystalline p-nitroaniline [84] and graphite [169] immersed in hydrocarbon solvents (0.44 nm and 0.45 nm, respectively). Also with this type of solvents, the MD simulations show a correlation between the distances measured between adjacent layers and the molecular size of the solvent [84]. As a consequence, the interfacial structure observed on graphene and TMDCs immersed in UPW cannot be explained solely in terms of the interaction of water molecules with the surfaces.

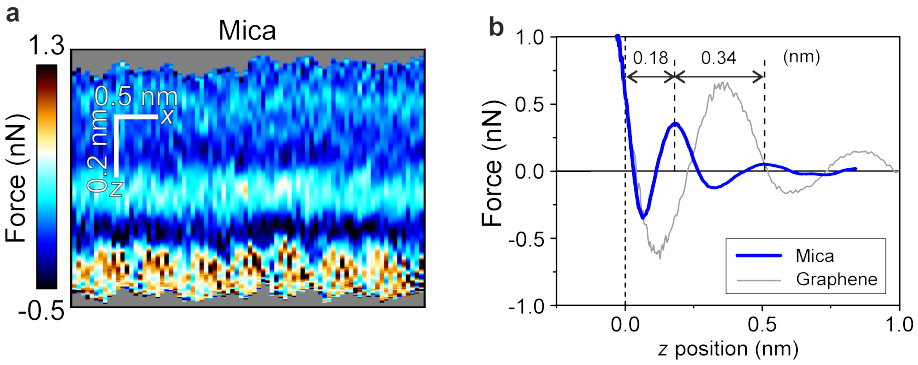

Figure 3.9.: Solid-liquid interface on mica in 200 mM KCl aqueous solution. **a.** xz force map measured over mica. **b**. Force-distance curve extracted from panel a (in blue). In the background, the force displacement curve measured on graphene is show for comparison (in gray). In the case of graphene, an exponential background force has been subtracted. Adapted from [113].

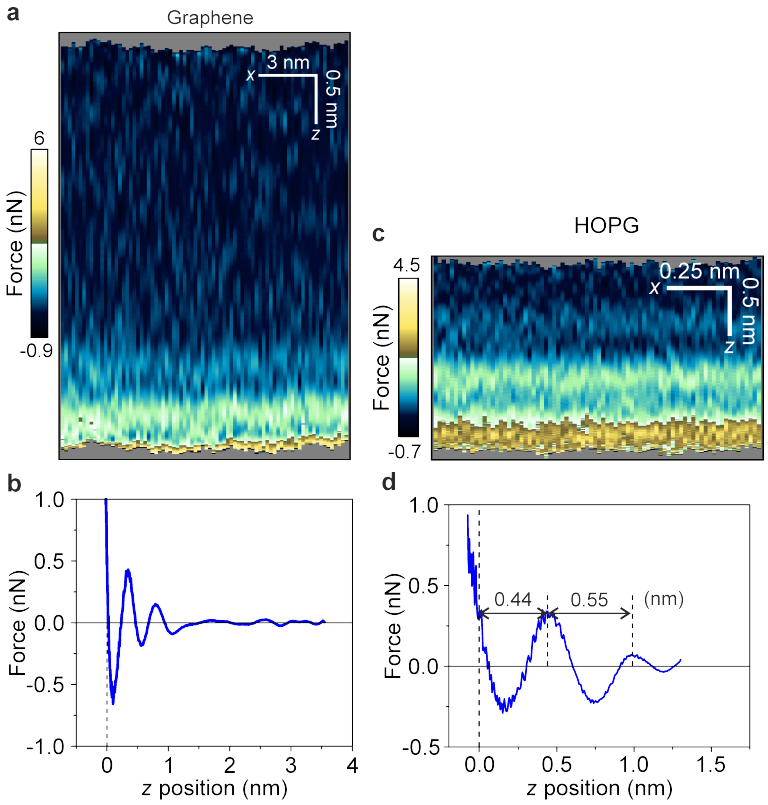

Figure 3.10.: Reference 3D-AFM measurements on different surfaces. **a.** Longer-range xz force map measured over epitaxial graphene in ultra-pure water. **b.** Force-distance curve obtained from panel a. The force shows oscillations up to a distance of 1.5 nm. **c.** xz force map of the HOPG-water interface. The z-scale was adjusted to match the one of panel a. **d.** Force-distance curve extracted from panel c. An exponential background force has been subtracted from the force curves.

Table 3.1.: Distances extracted from xz force maps. d_0 is the distance to the solid surface; d_1 and d_2 are, respectively, the distances between the 1st and 2nd, and 2nd and 3rd adjacent hydrophobic layers. The distances for graphene, HOPG, MoS_2, and WSe_2 are averaged over at least three independent experiments (different tips, samples, solutions). The confidence intervals represent the maximum deviation. In the case of $MoSe_2$ and WS_2, only one experiment was conducted and confidence intervals represent the standard deviation calculated from ten individual curves.

	d_0	d_1	d_2
Graphene	(0.35 ± 0.04)	(0.48 ± 0.04)	(0.52 ± 0.02)
HOPG	(0.41 ± 0.05)	(0.55 ± 0.06)	(0.60 ± 0.04)
MoS_2	(0.35 ± 0.02)	(0.50 ± 0.04)	(0.51 ± 0.03)
WS_2	(0.36 ± 0.04)	(0.51 ± 0.05)	(0.62 ± 0.05)
$MoSe_2$	(0.30 ± 0.02)	(0.45 ± 0.05)	(0.47 ± 0.04)
WSe_2	(0.35 ± 0.02)	(0.48 ± 0.03)	(0.55 ± 0.03)
Mica	(0.18 ± 0.01)	(0.34 ± 0.04)	-

Comparison with literature.
It is well known that different chemical species of airborne character are deposited on hydrophobic surfaces [139, 154–158, 161, 170–173]. In particular, the adsorption of airborne molecules on graphitic surfaces that have been exposed to air and/or water has been the subject of several studies [139, 154–158, 170–172, 174]. A similar phenomenon has been found to affect TMDCs [161, 173]. Airborne species can be roughly classified into two categories worth being considered: First, trace hydrocarbons and, second, gas molecules. Interestingly, both gasses and hydrocarbon molecules have a mainly hydrophobic character [175].

Hydrocarbon contaminants include alkanes, alkenes, alcohol, and aromatic species [139,171]. These contaminants are ubiquitous in ambient air (few parts per billion) [176], even in rather clean environments such as glove boxes [170]. Hydrocarbon contaminants modify some properties of graphitic surfaces [139,170,171]. In particular, it increases the WCA of the surfaces [139, 172]. It was shown that on the pristine surface a layer of hydrocarbons is formed which renders the surface more hydrophobic. A similar mechanism was found to affect MoS_2 [173]. **Figure 3.11** visualizes these findings in a nutshell. A freshly cleaved HOPG surface (panel a) exhibits a WCA of $\Theta \approx 55°$, which is a signature of a mildly hydrophobic character. However, already after 20 min of exposure to ambient air, the WCA has increased to $\Theta \approx 81°$, compatible with the commonly assumed pronounced hydrophobic character of graphitic surfaces. The exposure of the surface to air has lead to the adsorption of a layer comprised of airborne hydrocarbon adsorbates rendering the surface more hydrophobic compared to pristine HOPG [139].

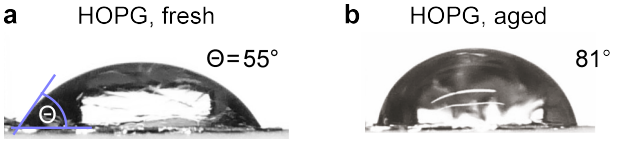

Figure 3.11.: Water contact angle (Θ) measurements. **a.** HOPG (freshly cleaved). **b.** HOPG (aged, exposed to air for 20 min). Adapted from [113].

Also gas molecules (N_2, O_2) could be absorbed from the ambient air [155, 175, 177]. Hwang and co-workers observed the growth of molecular structures on graphite surfaces immersed in water [156–159]. They proposed that the observed structures were composed of condensed nitrogen molecules adsorbed from the air into the water [156–159]. High resolution AFM images of different epitaxial graphene interfaces in air showed the presence of ordered and disordered adsorbates on the graphene surface [154, 155]. Similar structures were found by the same group on TMDCs [161]. Wastl *et al.* pointed out [154] that the ordered (stripe) structure observed in air was similar to the stripe structure observed on graphite samples immersed in water [157]. In the previous section (3.3), different types of adsorbates were observed on the graphene and the TMDC surfaces. The disordered adsorbates on graphene were found to be to a large extend water soluble. On the other hand, it was demonstrated that the stripe structure found in air is not affected by immersing the sample into UPW. More recently, Schlesinger and Sivan have proposed that the solvation structure observed on graphite by 3D-AFM was dominated by the layering of condensed gas molecules [72, 87]. They have also claimed that such a layered gas structure is a general property of hydrophobic surfaces in contact with water.

Finally, it has also been reported that graphite immersed in water spontaneously catalyzes methanol from carbon dioxide present in the liquid water equilibrated with the surrounding air [50, 178]. The adsorption of CO_2 into water is a natural process and becomes evident by measuring the pH of the UPW (see Figure 3.1). However, the proposed chemical reaction has not been described for TMDCs. For this reason, such a chemical reaction is not considered here as a source of the chemical species present in the hydrophobic layers.

3.4.2. Experiments With Controlled Contamination

In the following, some experiments will be discussed that were performed to test the hypothesis that the solvation layers are formed of airborne species. To this end, an experiment was designed to exclude any contact of the hydrophobic surface with air. By cleaving a bulk crystal of some of the samples (MoS_2, WSe_2, and HOPG) while being fully immersed in UPW, a freshly cleaved surface is obtained that has never been in contact with ambient air. An example of such a measurement is shown in **Figure 3.12**a. The solid-liquid interfaces of the so-prepared samples still show oscillations, although much less pronounced. While the distances between the adjacent layers are the same as for the samples that were cleaved in air, the solvation structure is only faintly visible. This implies that the exclusion of the contact between the surface and the air reduces

the amount of adsorbates, but does not fully prevent it. This is expected, since the UPW itself has been in contact with the air.

To further test the compatibility of the interpretations with the adsorption of hydrocarbons the opposite approach was chosen in a next experiment. Instead of preventing contamination, highly contaminated water was prepared by mixing UPW with n-octane ($c_{n\text{-octane}} = 0.7\,\text{mL} : 1\,\text{L}$). This concentration corresponds to the solubility limit of octane in water and, hence, such a liquid fits the definition of highly contaminated water. Then, a MoS_2 surface was immersed in into the mixture. Figure 3.12b shows an xz force map recorded within the MoS_2-octane:water interface. The image shows the characteristic alternation of dark and light stripes observed in purified water. We observe up to 4 hydrophobic layers. The distances between the first two adjacent layers coincide with those obtained with purified water (see Table 1). The map shows four solvation layers over the surface, which was never observed in UPW (number of layers in UPW: ≤ 3). This indicates that the number of hydrophobic layers increases when a MoS_2 surface is immersed in water mixed with a liquid hydrocarbon (n-octane). This result provides additional support for the claim that the hydrophobic layers observed in UPW are formed by dissolved hydrocarbons.

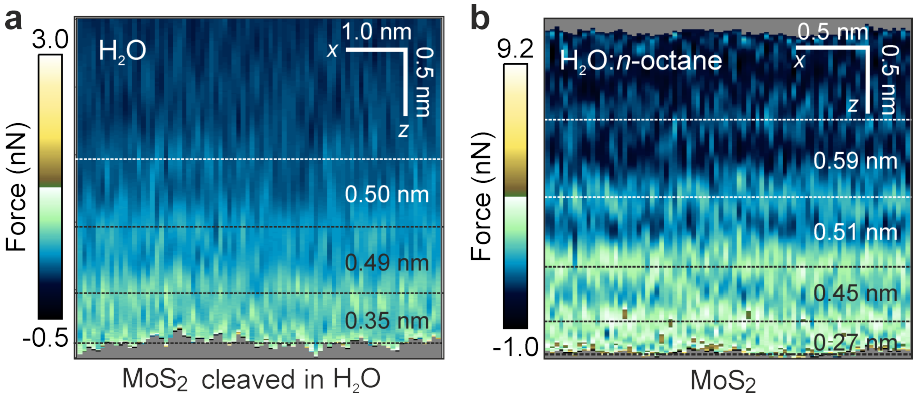

Figure 3.12.: 3D-AFM measurements on pristine surfaces and in contaminated water. **a.** xz force map of the MoS_2-water interface after cleaving the sample in water. The structuring is of liquid within the interface is less pronounced, but still present. **b.** xz force map of the MoS_2-octane:water interface. A strong layering is found within the interface, with an additional fourth solvation layer.

3.4.3. Influence of Solution Conditions

In the following, some experiments are performed in order to investigate how robust the observations are against changes in the environment. Especially the solution conditions and their potential impact on the observed phenomena are of high practical relevance. First of all, the temperature should affect the layering because the energy barrier for the desorption of a (hydrophobic) molecule is weighted by a Boltzmann factor $\exp(-U/k_\text{B}T)$, where U is the activation barrier. By increasing the temperature, the hydrophobic molecules should be eventually removed from the surface [171]. However,

within the small range of temperatures that can be controlled by the instrument used here (Asylum Research Air Temperature Control, between 28 and 33°C), no significant changes on the structure of the hydrophobic layers were observed.

Next, another point of practical relevance is the type of solution which the sample is immersed in. Devices operating in solution, *e.g.*, sensors, most likely operate in physiological buffer rather than in UPW [136]. In order to mimic such an environment, 3D-AFM experiments were performed on a WSe_2 surface immersed in KCl aqueous solution (200 mM). **Figure 3.13** shows an xz force map obtained in this solution. The alternation of regions of high and low force values is very similar to the one obtained in UPW. The separations between the 1st and the 2nd and between the 2nd and the 3rd adjacent layer seem to be larger in the presence of salts (0.58 to 0.68 nm in 200 mM KCl vs. 0.5 to 0.51 nm in UPW). This result is based on a single measurement, however, it clearly demonstrates that the presence of dissolved salts does not prevent the formation of the hydrophobic layers nor change their character substantially.

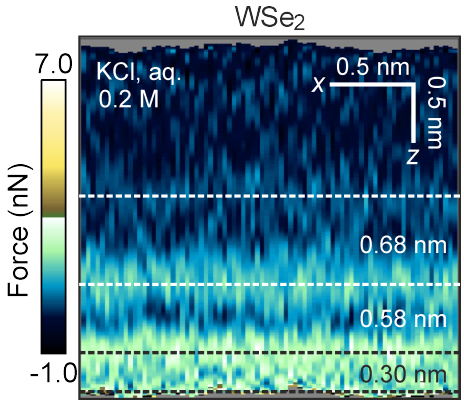

Figure 3.13.: 3D-AFM measurements performed on WSe_2 immersed in a salt solution. **a.** xz force map of WSe_2 immersed in a 200 mM KCl solution. The presence of dissolved salts does not alter the hydrophobic layers substantially.

3.4.4. Influence of Surface Ripples

It has been argued that the observation of stripe structures on the surface is not compatible with the observation of solvation layers. Yang and coworkers compared frequency shift vs. z curves obtained above stripe structures (of ≈ 5.5 nm periodicity and ≈ 0.5 nm of height) grown on graphite layers and above bare graphite layers. They observed oscillations only above the bare graphitic sample [103]. On the other hand, in an earlier work, they made the reverse observation above a stripe structure of 4.2 nm periodicity and 0.45 nm of height [158]. Oscillations were observed in the frequency shift vs. z curves measured above stripe structures but not above bare HOPG. In order to clarify this point for the case of the graphene sample, an additional 3D-AFM experiment was performed within an area covered by the stripe structure.

Figure 3.14a shows an AM-AFM phase image of a stripe pattern on the graphene surface, such as the ones shown in Section A.1. Figure 3.14b shows a 3D-AFM xyt cube

(phase channel) acquired in the region shown in panel a. The cube covers an area of 20×20 nm^2 in order to visualize the stripe pattern at its bottom. An xy phase plane extracted from the cube underneath the solvation layer structure is displayed in panel c. Note that the contrast and color scale was adapted to match the one of panel a. The similarity between panels a and c emphasizes the equivalence of the plane extracted from the 3D-AFM data and the tapping mode AFM phase image shown in panel a. The stripe pattern with a periodicity of ≈ 5 nm can be clearly identified. Finally, panel d shows an xz force panel extracted from the cube shown in panel b. At least two solvation layers are clearly visible (and a third one faintly). The distances between the SL are very similar to the ones measured in areas without the stripe pattern in other experiments (see Table 3.1). The data indicates that the structure of the solid-liquid interface in regions exhibiting ripples is identical to the one in graphene regions without ripples.

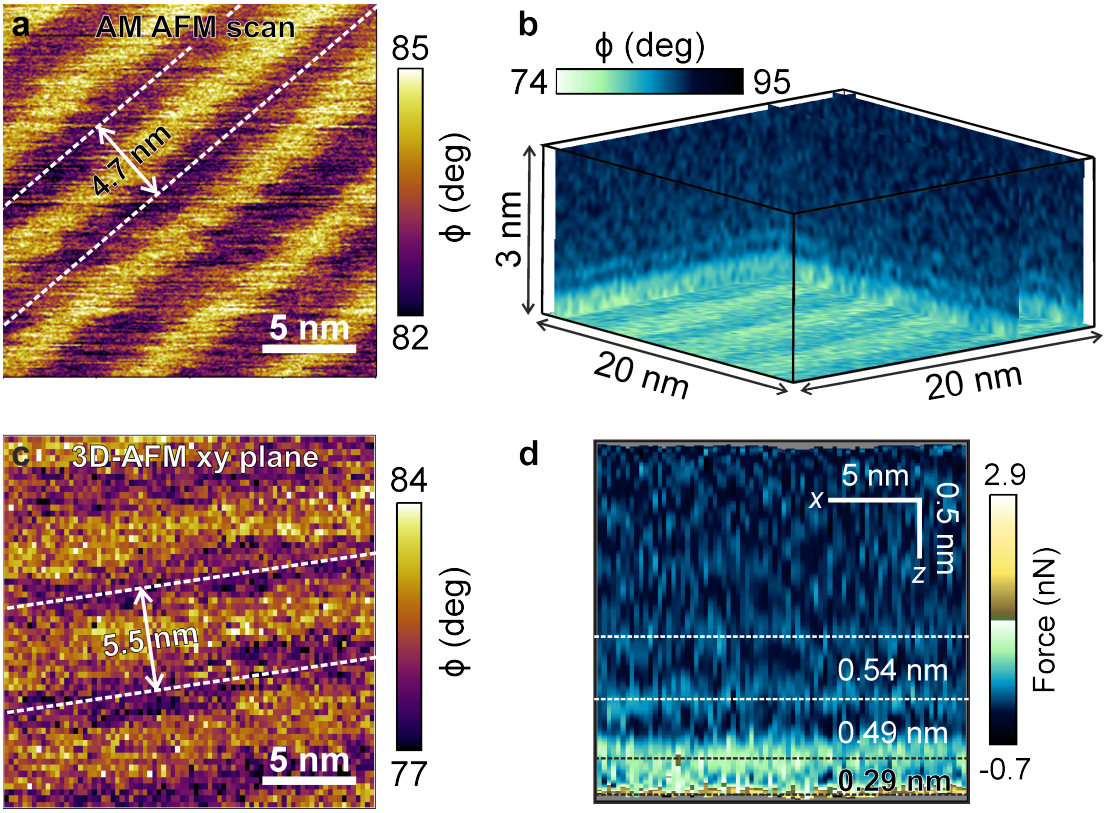

Figure 3.14.: **a.** AM-AFM phase image of ripples on a graphene surface immersed in purified water. **b.** 3D-AFM image obtained on the very same region shown in a. **c.** xy image extracted from the 3D-AFM image shown in b (underneath the hydrophobic layers). The image shows the ripple structure. **d.** xz force map of the graphene ripple-water interface extracted from a 3D-AFM measurement. The structure of the solid-liquid interface in regions exhibiting ripples is identical to the one in graphene regions without ripples.

3.4.5. Discussion

The experimental evidence indicates the formation of molecular-thick hydrophobic layers composed of molecules present in the ambient air and dissolved into the liquid water. The chemical composition of the adsorbates on graphene and graphite-air interfaces has been characterized by different spectroscopy methods [170,171]. These experiments confirmed the presence of airborne hydrocarbon contaminants but they are hard to perform on solid surfaces covered by liquid water [50]. Also gasses have been proposed to be adsorbed at graphitic surfaces and involved in the formation of a solvation structure [72,87,156,175].

The presented data favors airborne hydrocarbon molecules over gasses as the main component of the hydrophobic layers. First, on the macroscale, a correlation between the aging of the surface (time of exposure to air before immersion in water) with the increase of the water contact angle is observed (Figure 3.6), consistent with the literature regarding hydrocarbon adsorption. [139] Second, AM-AFM images in ambient conditions revealed the presence of disordered adsorbates on the graphene surface, compatible with the formation of a hydrocarbon layer measured by spectroscopic ellipsometry on graphitic samples [139, 170]. Third, the easiness to observe the layered structure also correlated with the aging of the surface before immersing it into UPW. The images taken on TMDC surfaces shown in Figure 3.8 were typically taken within 90 min after exfoliating the flakes. Over surfaces that were cleaved while being immersed into UPW and, hence, never were in direct contact with air, force oscillations were more difficult to observe [170]. Fourth, the distances measured between hydrophobic layers (0.45-0.55 nm) are similar to the ones measured on graphite [169] and on organic crystals (p-nitroaniline) [84] immersed in organic solvents (0.44 to 0.46 nm). Fifth, theoretical calculations show that the adsorption energy of layered materials in water is smaller for small adsorbates such as N_2 than the adsorption energy for larger airborne hydrocarbon contaminants [141, 179]. These calculations predict that at room temperature the thicknesses for hydrocarbon and N_2 layers are, respectively, 0.98 and 0.27 nm [141].

Notwithstanding the above arguments, the chemical nature of the hydrophobic layers observed in liquid water, either hydrocarbon contaminants or condensed gas molecules, can only be settled by performing high resolution spectroscopy measurements. Finally, it is possible that a combination of adsorption of hydrocarbons and gas molecules occurs. While the hydrophobic layers are ascribed to adsorbed hydrocarbons due to the above-mentioned reasons, other experimental observations could arise from gas adsorption: in ambient conditions as well as in UPW, a well-organized stripe structure was frequently imaged on the graphene sample. Similar stripe structure have been ascribed to the adsorption of gas molecules based on indirect observation [87, 156–159] and recently to the catalysis of methanol [50]. Since all these observations were made on hydrophobic surfaces, it cannot be ruled out that the two phenomena (hydrocarbon adsorption and gas accumulation) are occurring to some extend simultaneously.

3.4.6. Comparison Hydrophilic Versus Hydrophobic

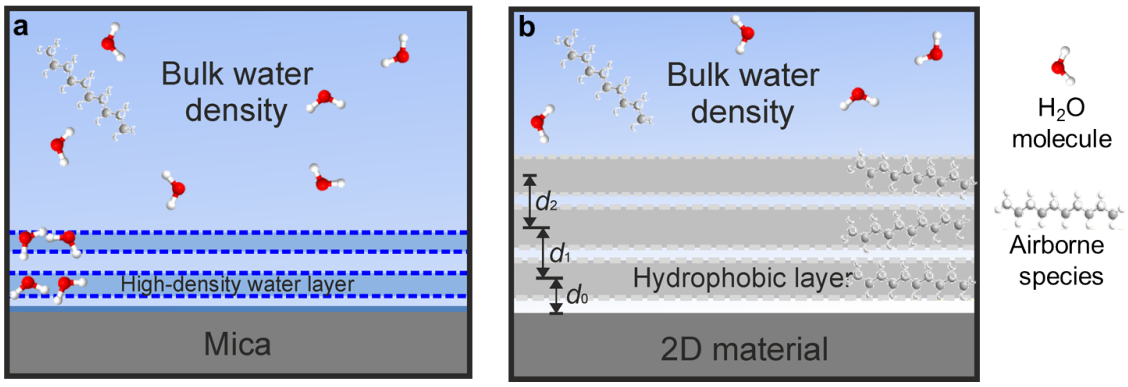

Figure 3.15.: Schemes of the interfacial layering on 2D materials and mica surfaces. **a.** Mica. The water density oscillates around its bulk value. The periodicity is close to the diameter of a water molecule ($\approx$ 0.3 nm). **b.** 2D materials. The water molecules are expelled from the vicinity of the surface. They are replaced by a few hydrophobic layers. These layers are composed of airborne molecular species. The spatial period is about 1.7 as large as the diameter of a water molecule. d_0 is the distance to the solid surface; d_1 and d_2 are, respectively, the distances between the 1st and 2nd, and 2nd and 3rd adjacent hydrophobic layers. Adapted from [113].

Lastly the interfacial structures for mica and hydrophobic materials are compared. In **Figure 3.15** the observations and interpretations are summarized. On mica (Figure 3.9), the layered structure is in good agreement with the distances predicted by MD simulations for hydrophilic surfaces immersed in pure water ($\approx$ 0.30 nm). On 2D materials-water interfaces, a layered structure characterized by separations between adjacent layers in the range of 0.5 nm (Figure 3.8) is observed. Such values cannot be explained solely in terms of water molecules, although the experiments have been performed with purified water. The paradox is resolved by analyzing the hydrophilic-hydrophobic interactions between the solid surface, the water and hydrophobic contaminants. The incorporation of trace airborne contaminants and/or gas molecules into the water is an unavoidable process. Water in equilibrium with the ambient air contains airborne hydrophobic species, either coming directly from the air or being dissolved into the water after they had been adsorbed onto the surface. On moderately hydrophobic surfaces (graphene, MoS_2, $MoSe_2$, WS_2, WSe_2, HOPG), the hydrophobic particles dissolved in the water diffuse to the hydrophobic interface where they displace the water molecules to reduce the free energy. On mica this process does not reduce the free energy because the water molecules are attracted to the negatively charged, very hydrophilic surface. There, in turn, the hydrophobic particles are expelled from the interface. The interaction of the liquid water molecules with a 2D material surface gives rise to a pronounced structuring of the interface characterized by the presence of 2 to 3 hydrophobic layers. The schemes in Figure 3.15 highlight the differences of the interfacial water structure of graphene, HOPG, MoS_2,

$MoSe_2$, WS_2, WSe_2 in comparison with the one of mica.

3.5. Conclusions

In this chapter, 3D-AFM has been applied on a variety of layered, hydrophobic materials including epitaxial graphene monolayer, HOPG, MoS_2, $MoSe_2$, WS_2, and WSe_2 (some of them from few-layer to the bulk). Experimental images with molecular resolution of the solid-liquid interfaces were obtained. These images reveal liquid density oscillations in proximity to the surfaces, giving rise to a layered structure that extends up to 2 nm from the solid surface into the liquid. The structure of the solid-liquid interface is remarkably similar for all the investigated materials, suggesting a common origin causing the formation of solvation layers next to hydrophobic surfaces. The comparison with mica, an archetypical hydrophilic surface, emphasized two differences between the solid-liquid interfaces of hydrophilic and hydrophobic surfaces. First, the overall extension of the solid-liquid interface is larger for the hydrophobic materials (2 nm) in comparison with hydrophilic materials (1 nm). Second, the periodicity of the liquid density oscillation is almost twice as large (0.5 nm versus 0.3 nm). This finding seemingly poses a contradiction to molecular simulation studies. As a consequence, the experimentally observed liquid density oscillations cannot be explained solely by the interaction with water molecules. The conflict is resolved by taking into account the actual phenomena occurring in ambient air. The solvation layers are composed of airborne molecules that were spontaneously absorbed into the liquid, either directly or indirectly by being adsorbed to the surface first. Once dissolved in the water, these contaminants are segregated from the bulk water to form the hydrophobic layers. The hydrophobic molecules minimize the free energy of the interface by displacing the water molecules from the surfaces. Airborne hydrocarbons as well as dissolved gas molecules are worth being considered as the primary layer-forming species. The experimental results presented in this thesis favor hydrocarbons over gas molecules. However, the chemical nature of the hydrophobic layers can only be settled unequivocally by performing high resolution spectroscopy measurements.

The existence of molecular-size hydrophobic layers was demonstrated on epitaxial graphene, HOPG, MoS_2, $MoSe_2$, WS_2, and WSe_2. Those surfaces have different chemical, electronic and optical properties but they share common features such as the existence of atomically flat terraces, their crystallinity, and their hydrophobic character. Altogether, these results provide evidence that the formation of molecular-size hydrophobic layers is a universal property that applies to any atomically flat hydrophobic surface immersed in liquid water equilibrated with ambient air. The existence of hydrophobic layers in the vicinity of 2D materials surfaces should influence the interactions of these materials with molecules, salts or proteins present in the water.

4. Solid-Liquid Interface on Pentacene Thin-Films

4.1. Introduction

In the previous chapter, the formation of solvation layers over graphene and TMDC immersed in UPW was demonstrated and ascribed to hydrophobic molecules coming from the air, dissolved into the UPW, and segregated at the solid-liquid interface. Based on the variety of investigated surfaces, it was proposed that this phenomenon is a universal property that applies to any atomically flat, crystalline, and hydrophobic surface immersed in water equilibrated with ambient air. As a consequence, the presence of hydrophobic layers should influence the interactions of these materials with molecules, salts or proteins present in the solution. Such interactions form part of the working principle of ultrasensitive (bio-)sensors [180]. Several sensor architectures are based on field-effect transistors (FETs), whose sensing elements are formed by different nanostructures, such as 2D-materials [136], nanowires [181], thin films [182] and carbon nanotubes [183]. In this type of sensors, the molecule of interest eventually adsorbs to the channel surface whereupon the charge it is bearing produces a gating effect. The additional gating modifies the electrical properties of the FET such as the channel conductance, which leads in turn to a change in the drain-to-source current. This change represents the sensor signal and can be read out. For biomedical or environmental applications the device is operated in aqueous environment and the gate is formed by the liquid itself and the ions it is containing (electrolyte-gated FET). An attractive choice for the channel material which is in contact with the liquid are organic semiconductors, giving rise to the emergence of electrolyte-gated organic field-effect transistors (EGOFETs) [184]. **Figure 4.1** illustrates the principle of an EGOFET transistor.

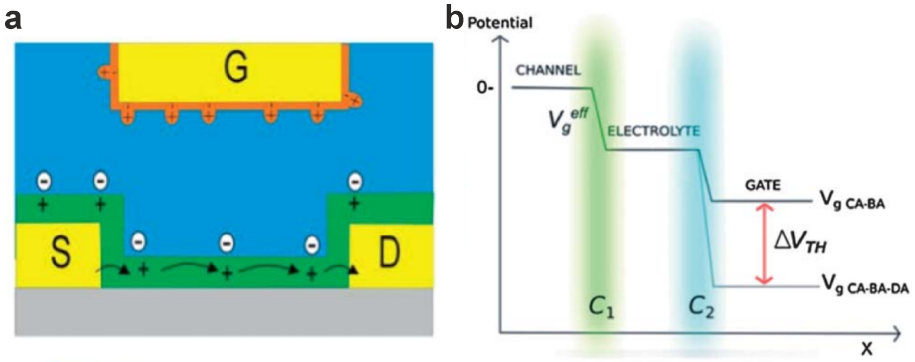

Figure 4.1.: Basic scheme of an Electrolyte-gated organic field-effect transistor (EGOFET). **a.** Principal components of an EGOFET. S, D and G denote the source, drain, and gate electrodes, respectively. **b.** Involved potentials. C_1 and C_2 denote the capacitances of the dielectric layers. Adapted from [184].

One particular promising material for EGOFET channels is pentacene [185]. Here, in order to further test the hypothesis of the previous chapter, 3D-AFM will be applied on pentacene thin-films as an example for a technologically relevant and topographically less ideal surface (compared to van-der-Vaals materials). Pentacene thin-films are fabricated by vacuum deposition on amorphous SiO_2 substrates and exhibit a topographically much more complex surface compared to 2D materials or mica [186]. Up to now, 3D-AFM has been applied mostly to ideal, atomically flat surfaces [126]. However, the 3D-AFM's capability of tracking hydration layers over more complex surfaces such as individual biomolecules was demonstrated [45, 99]. In particular, AM 3D-AFM provides a robust operation in order to access z-ranges of more than just a few nm [43]. Furthermore, with the 3D-AFM software suite developed in this thesis (Chapter 2), it is possible to visualize 3D-AFM data obtained on topographically more complex surfaces including step edges and terraces.

An important question is, how solvation layers behave at corrugated surfaces [45, 99] and singular features such as defects [95] or steps [48]. Miyata and coworkers investigated dissolution processes at step edges of calcite immersed in water with High-Speed FM AFM. With the help of MD simulations and frequency shift vs. z curves, they found an irregular hydration structure within a range of around 0.5 nm at the step edges [48]. However, no experimental 3D-AFM images were provided. Yang and coworkers reported 3D-AFM data measured over the step edge of a thin graphitic layer on mica [103]. Unfortunately, almost no solvation layer structure was resolved in the image. Here, 3D-AFM is applied to pentacene thin-films as they are used for the channel of organic field-effect transistors operating in liquid. Exploiting the robust operation of the AM 3D-AFM together with the developed software suite will allow to investigate the SLI around pentacene step edges and extended terraces.

This Chapter was developed in collaboration with the group of Prof. Fabio Biscarini (UNIMORE). It involves the participation of the graduate students Simone Benaglia (ICMM) who developed the electrical connections and performed some AFM scans, and

Sofia Drakopoulou (UNIMORE) who prepared the pentacene thin-films.

4.2. Materials and Methods

Sample Preparation

Amorphous SiO_2 ($\alpha-SiO_2$) substrates with embedded gold electrodes fabricated by lithography were purchased from the Fondazione Bruno Kessler. Pentacene thin-films were grown on the substrates by thermal deposition in high vacuum [186]. The nominal film thickness was monitored by a quartz microbalance. The crystal structure of a pentacene crystal is shown in **Figure 4.2**.

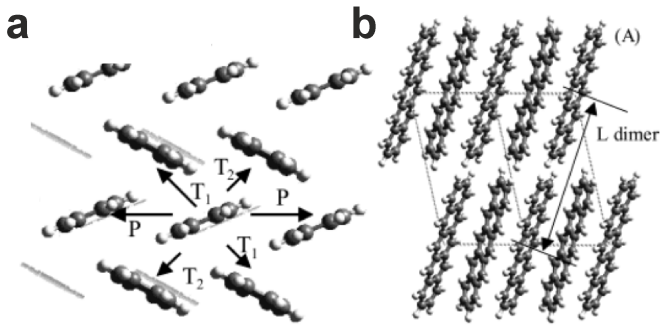

Figure 4.2.: Crystal structure of the pentacene thin-film. **a.** Top view on the vertically stacked pentacene surface. The crystal consists of different types of dimer neighbors; transverse dimers with a spacing of $T_1 = 4.75$ Å and $T_2 = 5.25$ Å, parallel dimers with a spacing of $P = 6.253$ Å. **b.** Side view on the vertically stacked pentacene molecules. The vertical spacing of the arrangement is $L = 14.51$ Å. Adapted from [187].

AFM Imaging

The measurements were performed in a Cypher S AFM (Asylum Research, Oxford Instruments, Ca, USA) equipped with an open liquid cell. The samples were glued on a conductive metal plate, which in turn was glued on a steel puck. The resulting stack was magnetically mounted onto the microscope sample stage. A small droplet of electrolyte solution (50 mM KCl) was placed on the surface with a micropipette. In order to prevent shortcuts, it was necessary to restrict the droplet's extension to inbetween the gold electrodes. This was realized by using only a small amount of electrolyte solution which in turn posed the risk of rapid evaporation. Hence, a home-made one-way perfusion system was developed and mounted on the cantilever holder in order to keep the liquid volume and the salt concentration constant by adding UPW *in situ*. In order to investigate a potential effect of an applied gate voltage (thereby mimicking a characteristic intrinsic to the working principle of an EGOFET device), the sample was wired as shown in **Figure 4.3**. In short, two of the sample's gold electrodes were brought to the same potential by contacting them to the metal plate using indium wires. The aluminum plate was

then connected to a voltage supply (Keithley 2602 SYSTEM SourceMeter, Keithley Instruments, Oh, USA). On the other hand, to provide the gate electrode, the cantilever holder clip was also connected to the voltage supply. All the steps involving electrical connections were conceived and performed by Simone Benaglia.

2D-AFM imaging. Conventional AFM images were performed in the amplitude modulation (AM) mode by exciting the first or the second mode of the cantilever. The cantilever excitation was realized with a photothermal drive. The free amplitudes A_0 were typically in the range of ≤ 1 nm, with an amplitude set-point ratio of $A_{sp}/A_0 \approx 0.8$.

3D-AFM imaging. The three-dimensional AFM was implemented on the Cypher S platform as described in Chapter 2. 3D-AFM imaging was performed in the amplitude modulation mode by exciting the cantilever at its 1st mode. For the sinusoidal signal applied to the z-piezo, amplitudes (peak-to-peak) between 2.5 and 4 nm and a period (frequency) of 10-20 ms (50-100 Hz) were used. The oscillation of the cantilever was driven by photothermal excitation. The free amplitude values A_0 were in the range of 300 pm. The effective set-point was chosen to be $A_{sp} \approx 0.95A_0$. A feedback bandwidth of 1-2 kHz and an integral gain of 2 to15 was used. The z-data was read out every 20 µs and stored in 512 or 1024 pixels (in total for approach and retraction). Each xy plane of the 3D maps contains 80×64 pixels. The total time to acquire the individual 3D-AFM images was 52 to 105 s.

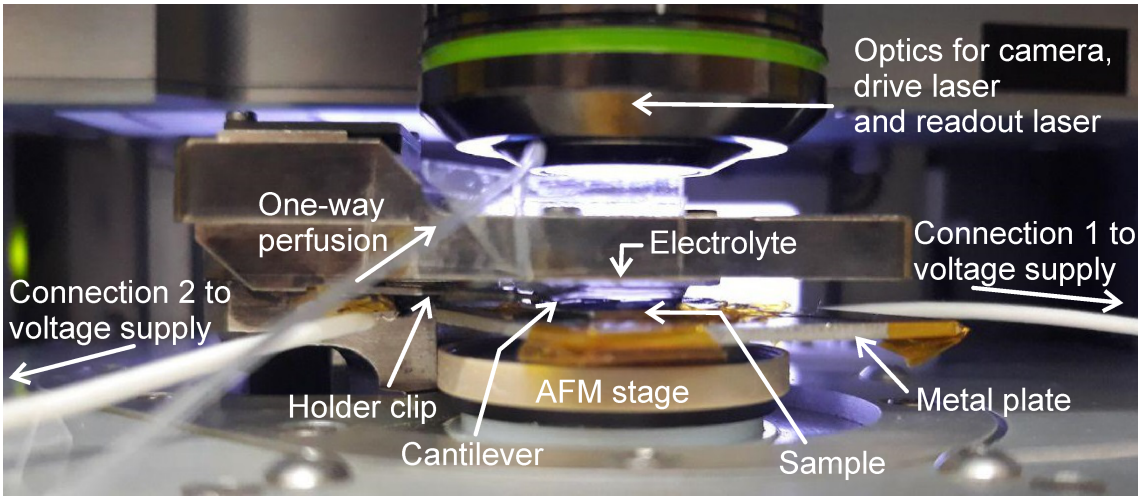

Figure 4.3.: Photograph of the AFM sample stage designed for performing 3D-AFM measurements with applied voltages. The image shows the open liquid cell (droplet holder) with the sample immersed in 50 mM KCL solution. Furthermore, the wires connecting the sample electrodes (1) and the cantilever holder clip (2) to the voltage supply, and the one-way perfusion tube are marked.

Cantilevers and Calibration

Silicon cantilevers with silicon tips were used for AFM imaging (PPP-NCHAuD and ArrowUHFAuD, purchased from NanoAndMore, Germany and AC55TS, Olympus, Japan).

The cantilevers were placed in a UV-Ozone cleaner (PSD-UV3, Novascan Technologies, USA) for ≈ 30 min to remove organic contaminants [148]. Each cantilever was calibrated using the GetReal® feature of the Asylum Research Software [149]. GetReal® provides a contactless calibration method and hence can be performed before the experiment without risking to damage the tip. In short, it works as follows (the superscripts "air" and "lq" denote quantities that correspond specifically to air and liquid, respectively): First, the cantilever's thermal noise spectrum (power spectral density, PSD) is recorded in air. Then, the cantilever's Q factor and first mode's resonance frequency in air, Q_1^{air} and f_1^{air} , are determined from the PSD spectrum. Following the so-called $Qf^{1.3}$ scaling method [149], k_1 can be obtained from Q_1^{air} and f_1^{air} through

$$k_1 = k_{\text{ref}} \left(\frac{Q_1^{\text{air}}}{Q_{\text{ref}}} \right) \left(\frac{f_1^{\text{air}}}{f_{\text{ref}}} \right)^{1.3}$$

with $k_{\text{ref}}, Q_{\text{ref}}$, and f_{ref} being the references values for the first mode's stiffness, Q factor, and resonance frequency, respectively. The reference values were measured *in factory* on a set of cantilevers of the same type using a laser Doppler vibrometer (in air). Once completed this step, the cantilever was immersed in the liquid, and its PSD spectrum was recorded again. Using the calculated k_1, the single harmonic oscillator (SHO) model is fitted to the PSD spectrum around the peak of the first mode's resonance frequency in liquid, f_1^{lq} [13]. From the fit, the corresponding inverse optical lever sensitivity (invOLS) in liquid, σ_1^{lq}, is obtained.

For some measurements also the second mode was calibrated in liquid (only in the case of using PPP-NCHAuD). The procedure for that was the same as described in the previous section, following the idea proposed by Labuda *et al.* [149].

4.3. 2D-AFM Results

First, the pentacene sample was scanned in AM-AFM in order to get an overview of the surface. **Figure 4.4**a shows AM-AFM topography images of the pentacene surface in electrolyte solution (50 mM KCl, aqueous). The images reveal the characteristic island-like morphology of vacuum-deposited pentacene on $\alpha-SiO_2$, similar to previously reported AFM images of pentacene in air [186].

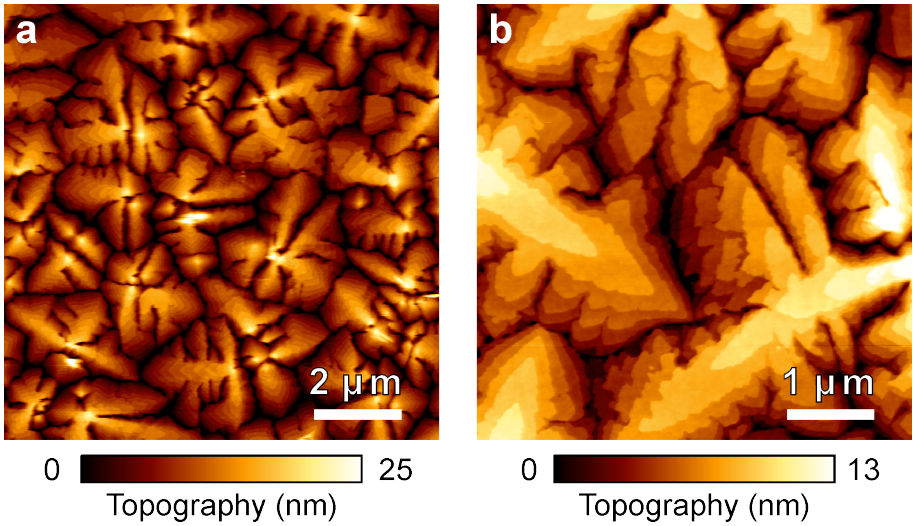

Figure 4.4.: AM-AFM images of pentacene on $\alpha-SiO_2$ in 50 mM KCl aqueous solution. **a.** Overview scan resolving the island like character of pentacene thin films. **b.** Smaller scan area showing that the islands are formed by flat terraces, separated by steps of a few nm.

Within the islands, flat terraces corresponding to different pentacene layers are clearly resolved (Figure 4.4b). Upon decreasing the scan size further, occasionally stripe structures can be observed.

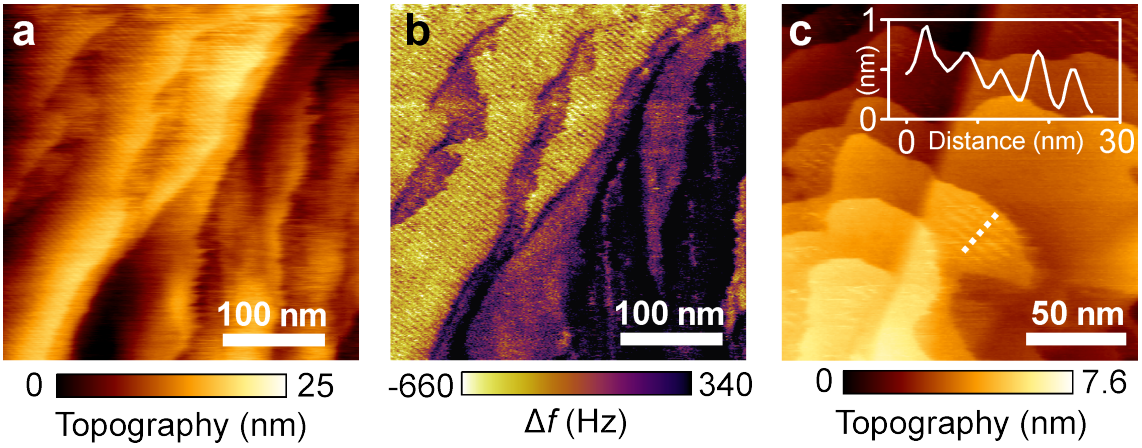

Figure 4.5.: AM-AFM images of ripple structures on pentacene in 50 mM KCl aqueous solution. **a.** Topography image showing some pentacene terraces covered by a well-organized stripe structure. **b.** Frequency-shift image of the same area. The stripe structure is clearly visible in the frequency shift. The terraces are entirely covered by the stripe pattern. **c.** Height image of another pentacene thin film. Patches of stripe structures are visible. A height profile obtained from panel c along the white dashed line is drawn in the same panel. The stripe structure's periodicity is around 5.2 nm.

They are only faintly visible in the topography channel (**Figure 4.5**a) but exhibit a stronger contrast in the frequency shift channel (panel b). While sometimes they cover whole terraces, in other experiments individual patches were found (Figure 4.5c). The stripe structure's periodicity is around 5.2 nm, with a height of roughly 0.4 nm. In appearance and dimensions, the structures are very similar to the ones observed on graphene (Section 3.3), but on pentacene their occurrence is much less frequent than on the graphene sample. It has been argued that the stripe structures observed on graphene and HOPG originate from nitrogen adsorbed at the graphitic surface [155,158]. Pentace is an aromatic hydrocarbon and hence to some extend hydrophobic, similar to graphene or HOPG. In the previous section, it was proposed that on hydrophobic surfaces solvation layers of airborne hydrophobic molecules are formed once the surface is immersed in UPW. Hence, in this section, 3D-AFM is applied in order to investigate and visualize the pentacene-UPW interface.

4.4. 3D-AFM Results

4.4.1. Solid-Liquid Interface of Pentacene in Electrolyte Solution

The first 3D-AFM experiments in order to visualize the pentacene-electrolyte interface were performed in flat areas of the pentacene. In several images, one to to three solvation layers were found close to the pentacene surface. **Figure 4.6**a shows a 3D xz force panel with two clearly visible solvation layers. A third, poorly defined solvation layer can be seen if looking closely. The averaged force curve (panel b) discloses the force oscillations including the small third maximum. Note that an exponential background force was subtracted from the force curve (see Section 2.13. The fit values can be found in the Appendix.). For distances $z \gtrsim 1.8$ nm, no detectable force is measured. The distances d_0, d_1, and d_2 (defined as in Figure 3.15) are, respectively, 0.39 nm, 0.57 nm, and 0.59 nm. The layers' appearance and the measured interlayer distances are similar to the ones measured on graphene and TMDC surfaces. This observation provides further evidence that the SLI's structures of all the investigated materials share a common origin.

By decreasing the effective set-point amplitude, lattice resolution could be obtained in 3D-AFM. Figure 4.6c shows an xy panel extracted from such an experiment. Thanks to the transformation into real-space, a periodic surface corrugation becomes visible, reproducing the pentacene surface relief. The average peak-to-peak spacing is 0.61 nm which is very close to the distance between parallel pentacene dimers (0.625 nm [187]).

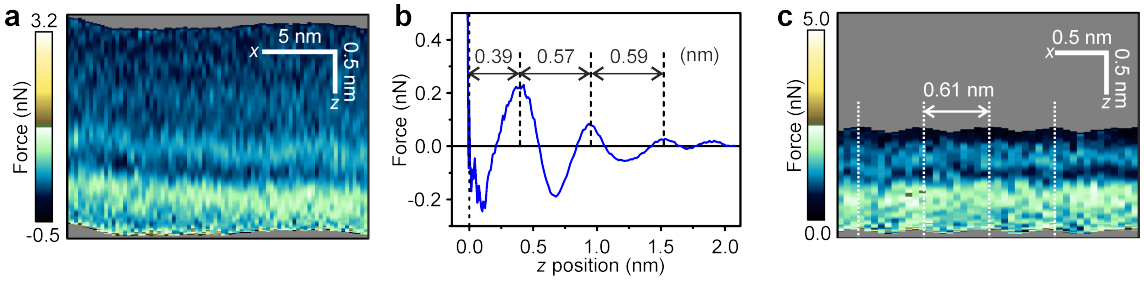

Figure 4.6.: 3D-AFM images of solid-liquid interface of pentacene in 50 mM KCl solution (aqueous). **a.** 3D-AFM xz force panel. The solid-liquid interface is characterized by the presence of up to three solvation layers. **b.** $F(z)$ curve obtained from panel a. Each force oscillation is associated with an individual solvation layer. The exponential background force has been subtracted. **c.** 3D-AFM xz force panel with lattice resolution. A periodic surface corrugation with a peak-to-peak spacing of 0.61 nm is visible. The periodicity matches the distance between parallel pentacene dimers.

4.4.2. Influence of Pentacene Step Edges on the SL Structure

In the next step, 3D-AFM experiments were performed covering larger lateral scan ranges (250 nm), in such a way that the investigated area spans over different pentacene terraces. Due to the small feedback gains and set-points close to 1, 3D-AFM can suffer from tip parachuting [109] at large topography steps. Once the contact is lost, the error signal (A-A_0) is saturated and remains very small, regardless of how far the tip is apart from the sample. In such a situation, the feedback acts only slowly to approach the tip closer to the surface. This is explained in detail in Section 2.2.1. For obtaining high-resolution at the step edges, tip-parachuting has to be avoided and surface tracking improved. A straightforward way to address this issue is performing scanning following the pentacene steps in the upward direction (as indicated in the respective figures). An xz phase panel extracted from such a 3D data set is shown in **Figure 4.7**. Three terraces can be distinguished, with adjacent terraces being vertically separated by approximately 1.5 nm. This is consistent with the monolayer-step height of pentacene thin-films on α−SiO_2 as determined by X-ray diffraction, which yielded either 1.44 nm or 1.54 nm (depending on the exact thin-film phase) [188, 189]. The measured step height implies that the pentacene molecules in the terraces adopt a near-vertical orientation with respect to the α−SiO2 substrate as expected for the sample's growth conditions [190]. The molecular arrangement is schematically shown in Figure 4.7 (drawn to scale in z direction; molecular structure adapted from Ref. [187]). The orientation of the pentacene molecules is further confirmed by lattice-resolution 3D-AFM images.

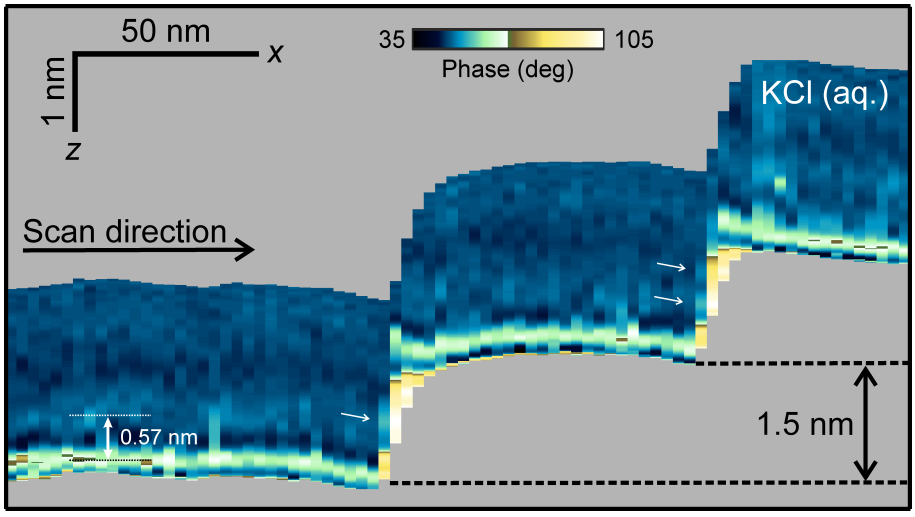

Figure 4.7.: 3D-AFM xy phase panel over pentacene terraces. Three different terraces are imaged. The steps between adjacent terraces are 1.5 nm high, consistent with the monolayer-step height of pentacene thin-films. The molecular arrangement is illustrated schematically in the figure. Two solvation layers are visible, covering the terraces (indicated in the lower terrace with dotted lines). The spacing between individual solvation layers is 0.57 nm. At the steps, some bright spots are visible (indicated by white arrows).

The xz-map reveals the presence of solvation layers spanning over all the terraces. One layer next to the surface can be clearly recognized from the xz-map, with a second one faintly visible farther away from the surface. In accordance, the averaged force curve shows that the AFM tip has to overcome two force maxima upon approaching the surface. The distances d_0 and d_1 are, respectively, 0.27 nm and 0.57 nm. Again, these values are similar to the ones measured on the hydrophobic surfaces of Section 3.4.

The image suggests that at the step edges the solvation layers do not follow the surface topography but instead run horizontally into the steep part of the steps. The steps seem to interrupt the SL structure which otherwise covers the terraces entirely. At the steps, some brighter spots are visible, that seem to be the starting point or the termination of a solvation layer (indicated by white arrows in Figure 4.7). However, it is hard to discern further details reliably. Hence, 3D-AFM experiments were performed with a higher resolution around the step edges in order to resolve more details. **Figure 4.8** shows a xz phase image extracted from such a 3D-AFM experiment. Two terraces can be clearly seen separated by a step in the center of the image. Also in this case, the step height is approximately 1.5 nm, which fits well the expected height of a monolayer formed by vertically oriented pentacene molecules. [188, 189] The 3D-AFM data reveals a detailed view on the solvation layer structure. First, on either side of the step, solvation layers are visible above the pentacene terraces (marked by white dotted lines). Furthermore, and in accordance to Figure 4.7, the SLs do not follow the steep slope but rather are interrupted at the step. However, more details are resolved: At the steep part of the step, three bright spots are visible (indicated by white arrows). These spots seem to be parts

of the solvation layers that appear brighter than over the flat terraces. This indicates that the solvation structure is stronger at the edges than over the terraces.

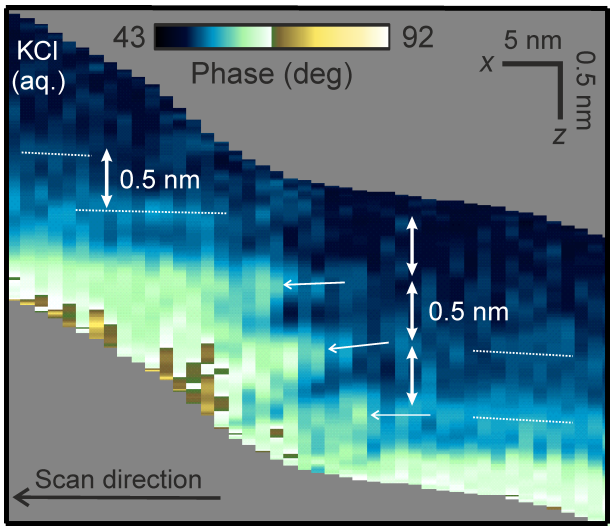

Figure 4.8.: 3D-AFM xy phase panel around a pentacene step edge. The step height is 1.5 nm, representing a monolayer-step of the pentacene thin-film. Solvation layers are visible covering the terraces. At the step, the solvation structure is more pronounced and the solvation layers (indicated by the white dotted lines) appear as bright spots (indicated by white arrows). The spacing between individual solvation layers is 0.5 nm. Each double-headed white arrow represents 0.5 nm.

The upper bright spot seems to be a truncated SL. It could be either the beginning of a SL over the lower terrace, which is otherwise too diffuse to be clearly resolved (because of the large distance to the lower terrace's surface). On the other hand, it could be a solvation layer of the upper terrace, which protrudes horizontally a few nm over the step edge. Lastly, it could be a combination of these two possible cases, *i.e.*, a SL that is shared between the two adjacent terraces. Interestingly, the pentacene step height of approximately 1.5 nm is commensurate with the spacing of the SL (≈ 0.5 nm). Such a commensurability would be conducive to the formation of a shared SL structure. Altogether, a partial overlap of lower and upper terrace's solvation layers could explain why the SL structure is stronger at the edges compared to the one over the terraces. The existence of shared SLs between adjacent terraces was suggested before by MD simulations of the solid-liquid interface around calcite step edges in water [48].

4.4.3. Influence of Gate Voltage on the SL Structure

Pentacene thin films are used as channel material in EGOFETs. Any device based on EGOFETs will operate with an applied gate voltage, U_{G}, and, hence, with a electrical field across the electrolyte solution. In order to deduce practical implications from the findings of this chapter, it is important to investigate a potential influence of an applied

gate voltage on the SL structure. Due to the presence of an aqueous solution, electrochemical reactions within the aqueous environment set limits to the gate voltages that can be applied in EGOFETS [184]. Here, commonly used gate voltages of -700 mV and +200 mV (measured against a AgCl electrode) are applied *in situ* while performing 3D-AFM measurements by using the electric connections shown in Figure 4.3. For simplicity, the measurements are restricted to flat parts of the pentacene sample. **Figure 4.9** shows xz force panels extracted from the 3D-AFM measurements.

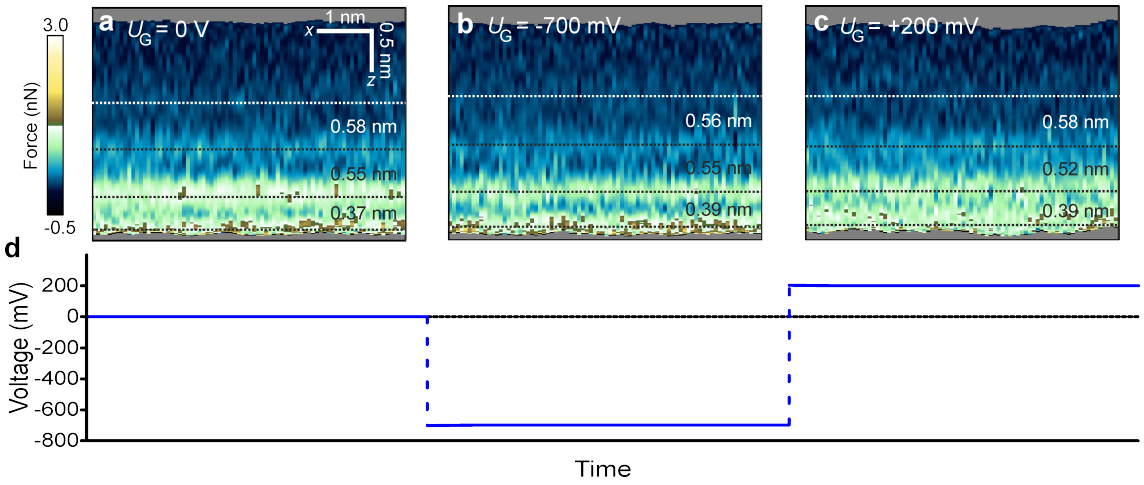

Figure 4.9.: 3D-AFM measurements on pentacene thin-films in 50 mM KCl with an applied gate voltage. The figure shows xy force panels measured at **a.** $U_G = 0$ V. **b.** $U_G = -700$ mV. **c.** $U_G = 200$ mV. Within this range, an applied gate voltage does not interfere with the presence of the solvation layers nor change their structure.

In all the cases, three SL above the pentacene surface are visible. On average, the distances d_0, d_1, and d_2 are 0.38 nm, 0.54 nm, and 0.57 nm, respectively. The individual distances are the same (within the uncertainty of the measurement) for all the three voltages applied. There are no major differences between the SL structures. One could speculate that the individual SLs are slightly thinner at $U_G = -700$ mV. However, it becomes evident that an applied gate voltage between -700 mV and +200 mV does not prevent the formation of SLs over pentacene. These observation are consistent with experiments performed by Hurst and coworkers [174]. They measured a decrease in capacitance over time on an HOPG-electrolyte interface which was ascribed to a segregated layer of airborne hydrocarbons. Upon applying voltages of either -1.222 or 0.778 V (versus AgCl) for 5 min, the capacitance was found to increase again, but only by 1 to 8 %, indicating that the layer of adsorbates remained largely unaffected [174].

4.5. Conclusions

In this chapter, 3D-AFM has been used to image the structure of the pentacene-electrolyte interface in order to test the findings of the previous chapter at a less ideal, technologically

relevant interface. The solid-liquid interface is characterized by a frequent occurrence of a layered structure with a separation of 0.5 nm between adjacent layers. This distance and the overall appearance of the solvation structure is very similar to the one found in the previous chapter on atomically flat, layered, and hydrophobic materials. The fact that pentacene as an aromatic hydrocarbon is hydrophobic together with the similarity of the experimental findings leads to the conclusion that the layers share the same origin: Airborne hydrocarbons are spontaneously incorporated into the electrolyte solution from ambient air, either directly or indirectly by being adsorbed to the pentacene first. Once dissolved in the solution, these contaminants are segregated from the bulk solution to form the hydrophobic layers. The observations made on pentacene strengthen the idea that the formation of molecular-size hydrophobic layers is a universal phenomenon affecting any hydrophobic surface immersed in aqueous solution equilibrated with ambient air. Furthermore, in the particular case of pentacene, the existence of hydrophobic layers in the vicinity of the surfaces could influence the interaction of pentacene thin films with molecules, salts or proteins present in the electrolyte. Pentacene is a promising material for electrolyte-gated organic field-effect transistors (EGOFETs). In an EGOFET configuration, such an interface represents an additional capacity within the electrolyte gate that has not been considered so far. The insight into the interfacial liquid structure on pentacene provided by the 3D-AFM images could lead to more efficient pentacene thin-film based devices such as EGOFETs. In addition, for the first time, 3D-AFM provided detailed images of a solvation structure around step edges. This proves the technique's capability of visualizing topographically more complex surfaces and provides insight into the formation of solvation layers at surface singularities such as step edges.

5. Imaging Ions Adsorbed on Mica with Single-Ion Resolution

5.1. Introduction

The adsorption of ions to surfaces immersed in water plays an important role in nature and technology. Many phenomena at solid-liquid interfaces involve the presence of ions such as electrochemistry [191], crystal growth [75], membrane biology [192, 193], lubrication [194, 195], and energy storage [196]. The ion distribution within the solid-liquid interface of a charged surface was described already more than 150 years ago by Helmholtz [197], who introduced the term *electrical double layer*. Later, Gouy [198] and Chapman [199] refined his theory by incorporating diffusion and Brownian motion, leading to a diffuse layer of ions characterized by an exponential decay in the potential. A further important improvement of these classical approaches was introduced by Stern, who recognized the importance of the ions' finite sizes. By combining the theories of Helmholtz and of Gouy and Chapman, he predicted a layer of ions close to the surface (the Stern layer) and a diffuse layer farther away [200]. Microscopic effects due to the ions' finite sizes and their interactions with each other make the description of the Stern layer far more complex than that of the diffuse layer [82]. Within the Stern layer, ions can adsorb to the surface in different configurations and hydration states. The Stern layer has been shown to be accessible by the AFM [43, 75, 78, 79, 82, 105]. In particular, the adsorption of ions to mica surfaces has been attracting considerable interest. Mica is an abundant clay mineral and its interaction with ions is highly relevant for environmental processes, such as clay swelling [201] and cloud seeding [202], but also for oil and gas extraction [203]. Furthermore, its layered structure provides an atomically flat and easy-to-cleave surface, properties that make mica surfaces a versatile testing ground and substrate for microscopy and scattering techniques [90, 204]. The crystal structure of muscovite mica is shown in **Figure 5.1**.

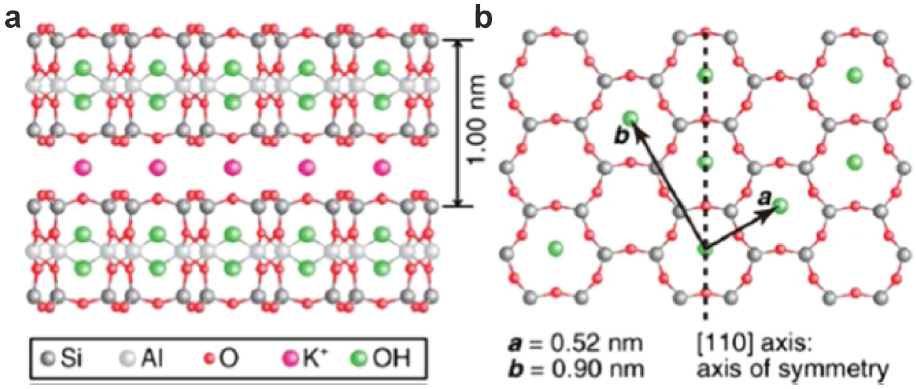

Figure 5.1.: Schemes of the crystal structure of muscovite mica, $KAl_2(AlSi_3O_{10})(OH)_2$. **a.** Side view on a mica crystal. Each 4th Si atom is exchanged randomly for an Al atom, leading to a net charge of the mica tetrahedron sheets. Intercalated K+ ions between the sheets maintain overall charge neutrality. **b.** Top view on the (001) surface of a freshly cleaved muscovite mica surface. Upon cleaving, half of the interlayer K+ ions remain on either surface to preserve charge neutrality. The lattice vectors $\vec{a}$ and $\vec{b}$ have lengths of 0.52 nm and 0.90 nm, respectively. Adapted from Reference [204].

Seminal works of Israelachvili and Pashley using the SFA form the foundations of the understanding how ions affect the DLVO and hydration forces between mica surfaces immersed in different salt solutions [205,206]. With the emergence of the AFM, numerous authors have extended this knowledge by exploiting the AFM's sub-nanometer lateral resolution and high force sensitivity in liquid [42,43,51,68,70,78,79,82,86,105,195,207]. Recent progresses in the field include the developments of new methods, such as of interfacial dissipation microscopy (IDM) [51] and 3D-AFM [42]. IDM is a lowly-invasive atomic-resolution AFM technique based on AM scanning. IDM enabled Ricci *et. al.* to detect individual ions adsorbed at SLIs [75] and to reveal water-induced interactions between Rb+ ions adsorbed to mica [79] (see **Figure 5.2**a). Another promising approach for studying the adsorption of ions at SLIs is 3D-AFM [34, 42, 43]. This dynamic AFM technique enables to visualize SLIs with atomic resolution in all three spatial dimensions. [126] With such an approach, Jimenez and coworkers visualized not only the lateral, but also the vertical organization of ions at mica-electrolyte interfaces (Figure 5.2b) [43].

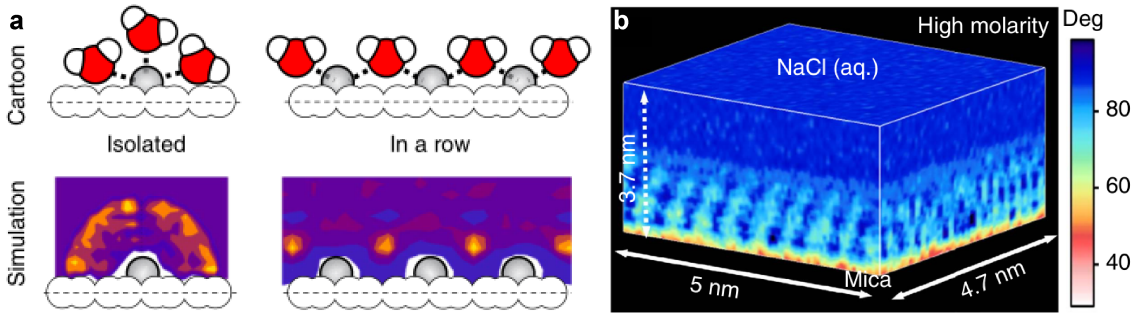

Figure 5.2.: AFM experiments and MD simulations on alkali metal ions at solid-liquid interfaces. **a.** MD simulations underlining that ions preferably adsorb in correlated patterns, induced by a common hydration layer landscape. **b.** 3D-AFM image of a high-molarity solution of NaCl (aq.) in proximity of a mica surface. The interfacial liquid organization extending a few nm into the liquid is directly visualized. Adapted from References [79] and [43].

Up to now, 3D-AFM has been used mostly with standard-sized cantilevers characterized by a nominal stiffness between 40 and 1600 N/m (PPP-NCH 1st and 2nd mode, respectively). In spite of these high stiffnesses, 3D-AFM equipped with such cantilevers is able to visualize the SLI of soft samples such as GroEL [45] or DNA [99]. Stiff levers provide high signal to noise ratios due to their high resonance frequency, and sufficient stability to allow stable operation at minute amplitudes. Nevertheless, it was demonstrated that the sensitivity of 3D-AFM can be further increased by using shorter cantilevers that provide higher resonance frequencies without necessarily increasing the spring constants (or even decreasing it) [9, 95]. The minimum detectable force in dynamic AFM can be calculated from the cantilever's characteristics by [9]

$$F_{\mathrm{min}} = \sqrt{\frac{4k_n k_{\mathrm{B}} T B}{\pi f_{\mathrm{r},n} Q_n}} \tag{5.1}$$

where B is the measurement bandwidth. Table 5.1 summarizes the force F_{min} for different cantilevers and modes for $B = 500$ Hz.

Table 5.1.: Minimum detectable force F_{min} calculated for different cantilevers according to Equation 5.1. The listed cantilever parameters are typical values for the respective cantilever types. n denotes the mode, k_n the stiffness, $f_{\mathrm{r},n}$ the resonance frequency, and Q_n the Q factor.

Cantilever	n	k_n [$\frac{\mathrm{N}}{\mathrm{m}}$]	$f_{\mathrm{r},n}$ [kHz]	Q_n	F_{min} [pN]
PPP-NCHAuD	2	1600	950	20	**14.8**
PPP-NCHAuD	1	40	150	8	**9.35**
AC55TS	1	200	1100	11	**6.59**
Arrow-UHFAuD	1	10	550	5	**3.09**

The use of shorter cantilevers can further increase the force sensitivity and resolution of a 3D-AFM. Furthermore, they will eventually be a key element in the development of a high-speed and high-resolution 3D-AFM. In this chapter, short cantilevers (AC55TS and ArrowUHFAuD) will be used for 3D-AFM measurements on mica-electrolyte interfaces. First, solutions of KCl will be investigated. Potassium cations are the naturally occurring ion species in muscovite mica and they are well-known to adsorb on the mica surface. The obtained images of the solid-liquid interface will be compared with crystal structure data from scattering techniques. A comparison with solutions of divalent ions can be found in the second part.

5.2. Materials and Methods

Sample Preparation

Muscovite Mica. Small discs of muscovite mica (5/16" in diameter) were punched out of larger mica sheets (SPI Supplies, USA). The discs were glued with epoxy resin on a PTFE plate, which in turn was glued on a steel puck. Before each experiment, the mica was cleaved with adhesive tape and rinsed thoroughly (for 10 s) with ultrapure water. Then, the surface was rinsed with the imaging solution contained in a single-use pipette and a small droplet was left on the surface. Finally, the sample was magnetically mounted onto the microscope sample stage. In experiments involving an exchange of salt solutions, special care was taken to avoid any residues from the previous solution. To this end, each time a solution was exchanged, the sample disc and the AFM probe holder including the cantilever was gently but thoroughly rinsed with UPW. Moreover, each time the mica was freshly cleaved and then rinsed again for 10 s with UPW.
Salt Solutions. Ultrapure water (UPW) was freshly obtained before the experiments (ELGA Maxima, 18.2 MΩ). After equilibrating the water with air, its pH reached a value of 5.6 (see Figure 3.1). Then, stock solutions with a concentration of 1 M were prepared by dissolving the respective salt (KCl, $BaCl_2$ ≥99.0%, Sigma-Aldrich) in UPW. From the 1 M stock solution, solutions of the different working concentrations were prepared by step wise diluting with UPW.

AFM Imaging

The measurements were performed in a Cypher VRS AFM (Asylum Research, Oxford Instruments, USA) equipped with a closed liquid cell. A temperature control unit was used in order to maintain the temperature within the AFM enclosure at (28.0 ± 0.1) °C.
Static Force Spectroscopy. For pre-examination, static force spectroscopy measurements were performed using cantilevers with colloidal tips (sQube CP-PNP-SiO, tip material SiO_2, tip radius $R = 6.62$ µm). Force curves were performed slowly (0.5 µm/s) with a maximum force of 3 nN during tip approach. For each solution and concentration, 25 force curves were recorded on different locations of the surface within an area of 2.5 µm × 2.5 µm. The force-displacement curves were transformed into force-distance curves by using Equation 1.5.

3D-AFM imaging. The 3D-AFM was implemented on the Cypher VRS platform as described in Chapter 2. Imaging was performed in the amplitude modulation mode by exciting the cantilever at its 1st or 2nd mode. For the sinusoidal signal applied to the z-piezo, amplitudes (peak-to-peak) of mostly 1.5 nm and a period (frequency) of 5-10 ms (100-200 Hz) were used. The oscillation of the cantilever was driven by photothermal excitation. The free amplitude values A_0 were in the range of 100-140 pm. The effective set-point was chosen to be $A_{\mathrm{sp}}/A_0 \gtrsim 0.95$. A feedback bandwidth of 1-2 kHz and an integral gain of 2 to 5 was used. The z-data was read out every 20 µs and stored in 256 or 512 pixels (in total for approach and retraction). Each xy plane of the 3D maps contains 80×64 pixels. The total time to acquire the individual 3D-AFM images was 26 to 52 s.
Some procedures were followed for stable and high resolution imaging such as maintaining the temperature constant at (28.0 ± 0.1)°C and letting the sample and solution equilibrate for 10 min before starting an experiment. For achieving maximum resolution, however, some extra steps were performed. Piezo creep was identified as the main source of the remaining image instabilities and always monitored during the measurements by reading out the LVDT sensors. In order to avoid closed-loop noise, the 3D-AFM was operated mostly in open loop which made it necessary to minimize piezo creep effects otherwise. In-plane piezo creep was reduced to a minimum by allowing the xy piezos relax for 24-48 h before imaging. Out-of-plane piezo creep is unavoidable after the tip-sample approach, but less critical since the AM feedback compensates for it. However, strong nonlinear z-creep is reduced by maintaining the tip for a few minutes close to the sample before imaging. Furthermore, in order to preserve the sharpness of the tip and to apply small tip-sample forces, the approach is performed as gentle as possible by starting the imaging close to the surface with $A_{\mathrm{sp}}/A_0 \lesssim 1$ and reducing A_{sp} carefully until the tip apex enters into the hydration structure. A further advantage in terms of force sensitivity is achieved by using short, high-resonance frequency cantilevers as summarized in Table 5.1.
Force Reconstruction and Data Analysis. Data analysis was performed using the AM 3D-AFM software suite developed in Chapter 2, in particular the algorithms for transforming the raw data into the spatial domain, reconstruction of forces from the raw data (A,ϕ), and flattening of the xz panels. Force reconstruction was performed using Hölscher's method [117].

Cantilevers and Calibration

Silicon cantilevers with silicon tips were used for AFM imaging (ArrowUHFAuD, PPP-NCHAuD and sQube CP-PNP-SiO purchased from NanoAndMore, Germany and AC55TS from Olympus, Japan). The cantilevers were placed in a UV-Ozone cleaner (PSD-UV3, Novascan Technologies, USA) for ≈ 30 min to remove organic contaminants [148] and rinsed with UPW. ArrowUHFAuD, PPP-NCHAuD and AC55TS cantilevers were individually calibrated using the GetReal® feature of the Asylum Research Software as described in detail in Section 4 [149]. This calibration is contactless and, hence, can be performed before the each experiment without risk of damaging the tip. The ArrowUHF

underlies rather strong variations in its stiffness, which makes an individual calibration particularly important (there is no nominal stiffness provided by the manufacturer).

CP-PNP-SiO cantilevers were calibrated by recording the cantilever's thermal noise spectrum (power spectral density, PSD) in liquid far away from sample surface [13]. Then, the single harmonic oscillator (SHO) model was fitted to the PSD around the peak of the first resonance frequency using the nominal stiffness ($k_1 = 1.03k_0 = 1.03 \cdot 0.08$ N/m= 0.082 N/m). The fit yielded the invOLS of the first mode, σ_1, which then allowed to calculate the static invOLS $\sigma_0 = \sigma_1/1.09 = 80.0\,\mathrm{nm/V}$ [10].

All parameters are summarized in Table B.1 (Appendix).

5.3. Results

5.3.1. Monovalent Ions

When imaging mica immersed in 200 mM KCl (aqueous), different situations were found depending on the applied imaging set-point ratio A/A_0. **Figure 5.3** shows high-resolution 3D-AFM phase images that show apparently very distinct features in spite of being the same cantilever-sample system. In principle both cubes show a few of hydration layers at the bottom. However, the left cube portrays the HL which is closest to the surface in an interrupted manner, with some areas not accessed by the tip. Although the HL itself seems to be continuous, in some parts it is entirely imaged and in others not. By looking closely, a periodic corrugation can often be detected in the respective areas (see white arrows in panel a). Note that the working principle of 3D-AFM reproduces the bottom's corrugation at the top of each panel, which is very convenient for spotting the corrugation. In the right cube, in contrast, the hydration layer is imaged across the entire cube uniformly without interruptions. While the left situation can be achieved at very high set-points, the right situation is found when decreasing the set-point slightly. By increasing the set-point again, the observation is reversible.

The solid-liquid interface of hydrophilic samples is often characterized by the presence of hydration layers. In an AFM experiment, each individual layer poses a barrier for the tip. It was demonstrated earlier that the AFM tip is able to "jump" between different of these energy barriers [74, 208], either induced by set-point changes or randomly due to measurement instabilities and noise. A further source of such an observation could be an unstable hydration structure of the tip, which can lead to the observation of an additional spurious force minimum [97, 126]. Although these phenomena can occur in principle in any AFM measurement within solid-liquid interfaces, they cannot explain the features observed in Figure 5.3a. These features are not caused by a random process because they are observed repeatedly at the same xy position, which suggests that they are related to actual features of the sample surface, comprised of the mica itself, the K+ ions, and the involved hydration landscape.

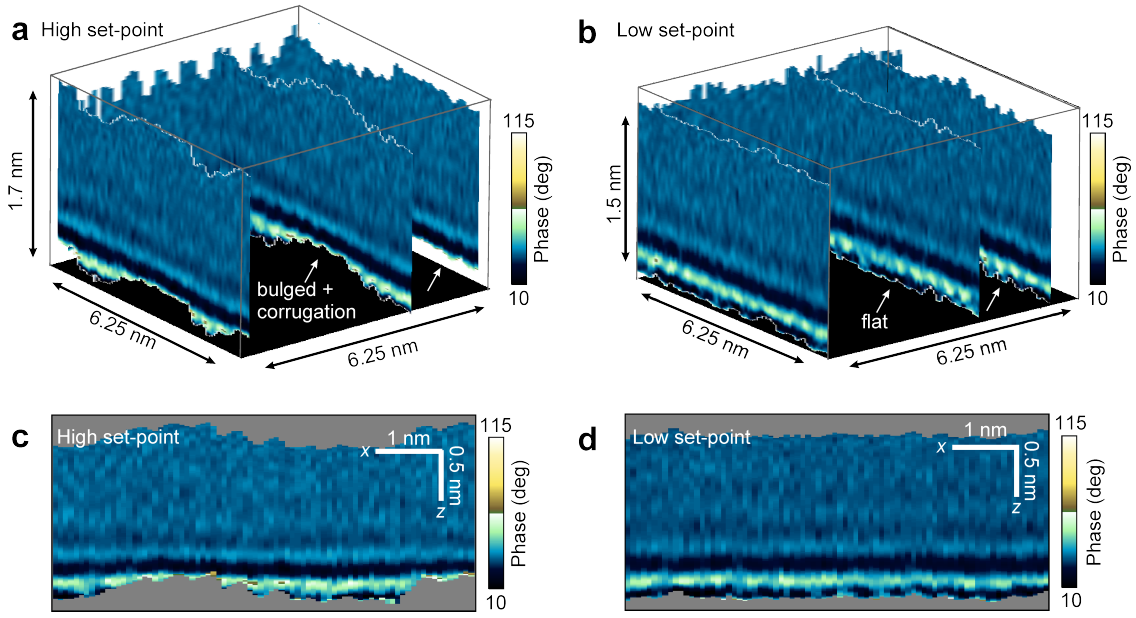

Figure 5.3.: 3D-AFM phase images of mica-KCl (200 mM, aq.) interfaces in soft-tapping conditions (ArrowUHF, $k_1 = 12$ N/m) at different set-point ratios A_{sp}/A_0. **a.** Image with a set-point ratio close to 1. The surface relief at the bottom of each panel shows distinct features (see also the panels' top reliefs). The black plane was included in order to increase the visibility of the features. **b.** The same experiment when the set-point is reduced slightly. **c.** Representative xz phase panel measured at high set-point ratios. The hydration structure shows some corrugation and interruptions. **d.** Representative xz phase panel measured at lower set-point ratios. The hydration structure appears flat. Some lateral structures become visible. The gray areas are not accessed by the tip.

Figure 5.4a shows an xy force map exhibiting distinct features at the bottom that can be grouped into two regions, one where the the tip tracked the mica surface and a second one where the tip tracked the 1st HL. These two regions are denoted as A and B. In x positions that belong to A, the tip indents deeper into the hydration structure than in the x positions corresponding to B, and eventually, the tip reaches the actual mica surface. In B, in contrast, the tip does not break through the 1st HL and, as a consequence, does not enter in contact with the mica. As mentioned above, these two observations are not happening at random positions but rather can be observed consecutively at the same lateral sites. By closely inspecting the 1st HL in the B region, peculiar details can be observed. First, the layer is bulged slightly towards larger z distances. Second, the measured relief shows a repetitive corrugation (≈ 0.5 nm periodicity) that can can also be conveniently spotted at the panel's top relief. Further, by analyzing the magnitude of the involved tip-sample forces, it can be observed that the 1st HL is actually stronger in the B regions than in the A regions, forming a kind of plateau in the force panel. Panel b shows the set of individual force-displacement curves that reconstitute the xz panel, grouped into families corresponding to the A and B region (the force curves in

the transition between A and B were omitted for clarity). Far away from the surface ($z \gtrsim 1$ nm), the tip-sample force is negligible because the tip oscillates in bulk solution. Upon approaching the tip, the force shows two sequential oscillations at ≈ 0.8 nm and ≈ 0.5 nm in both A and B, corresponding to the penetration of the 3rd and 2nd HL, respectively. Approaching the tip further leads to another force oscillation, associated with the 1st HL. Once the tip feels the repulsion arising from penetrating this HL, the tip-sample force is specific for each of the two families. In the case of B, the tip does not indent further at this point but instead the tip-sample force increases monotonously until the amplitude set-point is reached and the tip retracts. In position A, however, the tip passes through a force maximum, and reaches monotonous deflection only after passing through another force minimum, indicating that it penetrated through a further HL (the 1st HL). This observation implies that the HL is stronger in B regions than in A regions.

Where does the increased stability come from? Counting the fractions of the A and B regions yields, respectively, 28 % and 55 % (missing percentages to 100 % correspond to the transition regions). A control experiment conducted in aqueous solution with reduced molarity (2 mM KCl, $k_1 = 9.2$ N/m) yielded larger fractions of A and smaller fractions B (41 % and 43 %, respectively). The correlation of the relative amounts of A and B regions with the ionic strength indicates a connection of the observations with the quantity of ions in the solution. It is well known that mica immersed in electrolyte solution adsorbs cations from the solution in order to neutralize its negative surface charge [209]. Hence, A and B regions are proposed to arise from two situations: (A) The tip is tapping directly on the mica, either because the corresponding xy positions are not occupied by an K+ ion by the time the tip passes by, or because the xy positions are located inbetween ion adsorption sites. (B) The tip is tapping on top of the hydration landscape of adsorbed K+ ions. By inspecting horizontal planes extracted from such 3D-AFM measurements, as proposed earlier [78, 105], the ion coverage can be quantified (see Appendix, Figure B.1). From the relative counts, a K+ ion coverage of 49 % and 39 % is obtained at 200 mM and 2 mM, respectively. The obtained coverage values are in agreement with the expected charge neutrality of the mica surface. Furthermore, the 3D-AFM images suggest the formation of ion patches, as it was observed earlier [78, 79].

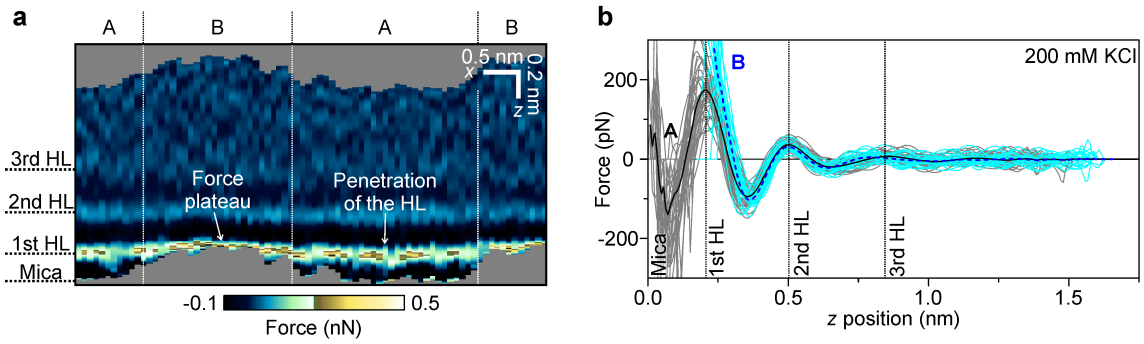

Figure 5.4.: The mica-KCl (200 mM, aq.) interface in soft-tapping conditions (ArrowUHF, $A_{sp}/A_0 \lesssim 1$, $k_1 = 12$ N/m). **a.** 3D-AFM xz force panel. The panel shows the existence of two types of regions in x direction, labeled as A and B. The image shows different features of the hydration structure that are specific for each region. The vertical structuring into three distinct hydration layers (HL) is indicated on the left. The gray areas are not accessed by the tip. **b.** Set of force curves obtained by unraveling the xz force panel. Gray and blue force curves were measured at x positions corresponding to the A and B regions, respectively. The respective average curves are highlighted.

Recently, Ricci and colleagues have demonstrated that the adsorbed ions can spontaneously form ordered structures [79]. The authors observed ions (Rb+) adsorbed in a partially hydrated state, *i.e.,* inner-sphere complexes, which were arranged in rows, hexagons, or larger patches. The mechanism behind the organization was broken down to the hydration landscape forming around the ions. The water molecules induce a correlation between adjacent ions, thereby stabilizing them laterally. The situation observed here could be explained along this line. The K+ ions adsorbed on the mica surface are surrounded (partially) by their hydration shells. The hydration shells of adjacent ions will form a correlated hydration landscape which makes ion adsorption in groups more favorable. If the 3D-AFM technique is sufficiently sensitive, such a stabilized network of ions would be detected without or with little perturbation. Adsorbed ions and their respective hydration shells would then appear as protrusions from the mica plane as observed in the above 3D-AFM images.

In order to test the hypothesis, the experimental data will be compared to the crystal structure of mica including adsorbed K+ ions [210,211]. Thanks to the transformation from time to real-space that was implemented in the AM 3D-AFM software suite, the measured distances, including those close to the turnaround point of the ultrafast 3D motion, can be accurately quantified directly from the xz panels (see Chapter 2, Section 2.3.1). This enables a straightforward comparison between 3D-AFM data and reported data obtained from different X-ray diffraction methods [210,211].

Figure 5.5 summarizes the crystal structure, the involved species and their respective sizes. Panel a depicts a top view on the (001) surface of a schematic muscovite mica surface in order to clarify the involved species. Panel b portrays the corresponding front view to scale with the actual sizes of the species. The van der Waals radii of Al, Si, and

O are, respectively, $r_{Al} = 0.184$ nm, $r_{Si} = 0.210$ nm, and $r_O = 0.152$ nm [212,213]. Since every fourth Si atom is randomly replaced by Al (Si:Al 3:1), Si and Al are depicted in the figure with the same size. The K+ ions adsorb within the ditrigonal cavities and are located at a height of $\Delta z_{K+} = 0.19$ nm above the oxygen basal plane, as determined by XRR [211]. The ionic radius of K+ is $r_{K+} = 0.137$ nm [214]. Ions in aqueous solution are hydrated [215] which increases their effective size. An isolated K+ ion surrounded by its first hydration shell (coordination number N_{K+} =6 [216,217]) has an hydrated ionic radius of $r_{K+}^{Hyd} = 0.33$ nm (illustrated by panel c) [218]. If such a hydrated ion adsorbs onto a surface by forming an inner sphere complex (partially hydrated state), it assumes a configuration as the one shown in panel d.

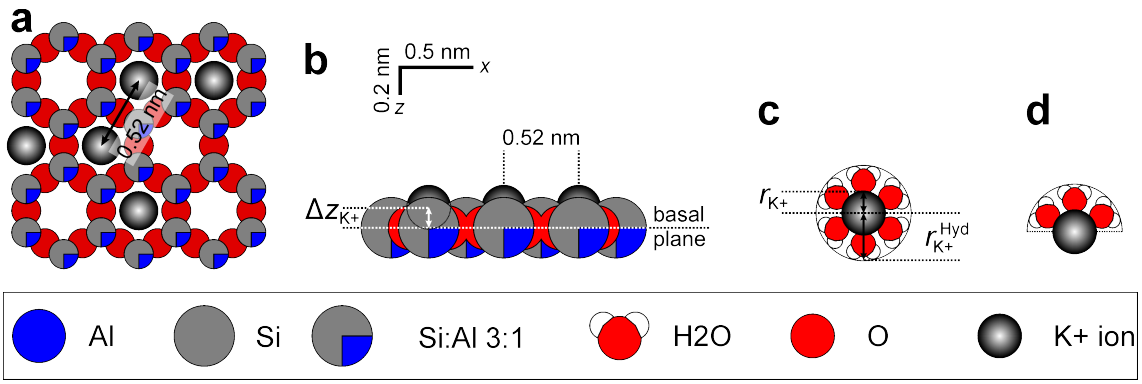

Figure 5.5.: Schemes of the mica crystal structure in aqueous KCl solution. **a.** Top view on a (001) mica surface to identify the involved species. K+ is the ionic species naturally occurring in muscovite mica and fits well into the ditrigonal cavities of the crystal lattice. The distance between adjacent ditrigonal cavities is 0.52 nm. In this schematic example, 50 % of the ditrigonal cavities are occupied by K+ ions. **b.** Front view on the mica surface. Si, O and K+ are represented to scale according to their van-der-Waals and ionic radii: $r_{Al} = 0.184$ nm, $r_{Si} = 0.210$ nm, $r_O = 0.152$ nm, $r_{K+} = 0.137$ nm. The K+ ions are shifted by $\Delta z_{K+} = 0.19$ nm with respect to the oxygen basal plane. **c.** Fully hydrated K+ ion (first hydration shell). Its coordination number is $N_{\mathbf{K+}} = 6$ and its hydrated ionic radius is $r_{\mathbf{K+}}^{\mathbf{Hyd}} = 0.33$ nm. **d.** The same ion in a partially hydrated state assumed upon forming an inner sphere complex.

Next, the crystal lattice with the actual sizes of the involved species and hydrated K+ ions is merged into an experimental xy force panel. To this end, the same xy force panel as the one shown above is plotted with the real aspect ratio in **Figure 5.6**. The mica lattice from Figure 5.5b, whose oxygen basal plane defines $z = 0$, is added at the bottom of the image (colors omitted for clarity). The z-offset of the experimental data with respect to the crystal structure can be determined by assuming that the tip contacted the mica lattice where the lowest overall tip positions were reached. Hence, the xz force data is shifted in the z direction until the lowest points of the experimentally measured surface relief coincide with the van-der-Waals radius of the Si atoms forming the mica lattice (labeled as contact plane in the image).

Once the vertical correlation is established, the horizontal offset can be adjusted following the assumption that the features observed in B regions of the xz panel's surface relief arise from adsorbed K+ ions. The mica lattice is thus filled with K+ ions adsorbed as inner sphere complexes. With the K+ ions being in place, the associated hydration landscape is geometrically defined. For clarity, the water molecules are shown with a smaller size compared to their actual one. However the actual hydration radius is drawn to scale by a fine white line. Then, a horizontal position is found where the measured repetitive corrugation (≈ 0.5 nm periodicity) coincides with the hydration landscape of the K+ ions. Finally the K+ ions in the A regions were removed. The result is shown in Figure 5.6.

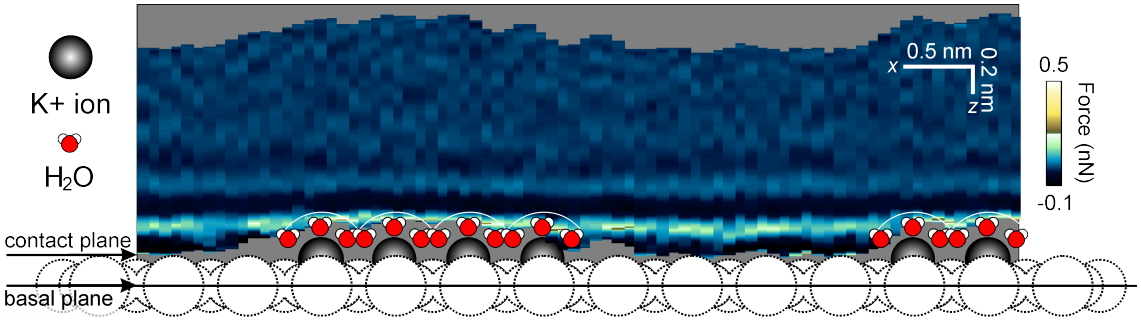

Figure 5.6.: Comparison between 3D-AFM data and reported crystal structure data obtained from different X-ray methods. The upper part of the panel depicts an xz force panel, and the lower part the front view on the (001) mica plane. Both parts have been vertically and horizontally matched as described in the text. Hydrated K+ ions adsorbed in-inner sphere complexes are added in the ditrigonal cavities. Their hydration landscape coincides well with the measured surface relief. Gray and red/white spheres represent the K+ ions and water molecules, respectively. The hydrated ionic radius, $r_{\mathbf{K+}}^{\mathbf{Hyd}} = 0.33$ nm, is indicated for each inner-sphere complex by a fine white line. The gray areas are not accessed by the tip. $k_1 = 12$ N/m.

The same procedure can be repeated for many other xy panels as shown for some examples in the Appendix, Figure B.3 and B.4. In each case, a precise match between the surface corrugation and the hydration landscape is found both horizontally and vertically. To emphasize the remarkable coincidence with the XRR data, a close-up picture taken from Figure 5.6 is provided in **Figure 5.7**. It can be seen that inbetween each two hydration shells, where the hydration radii form a cusp, a dip is visible in the experimental data. The inset of Figure 5.7 shows the density of the water surrounding adsorbed K+ ions on mica calculated by MD simulations [79]. The K+ ions share their hydration shells, leading to regions of higher water density in the cusps, which results in a repulsive force for the tip [93]. Right above the ions dark spots are visible indicating the presence of an attractive force. On average, a minimum force of -129 pN is obtained from the dark spots of the image. The observation of attractive forces was associated earlier with the presence of K+ ions [105].

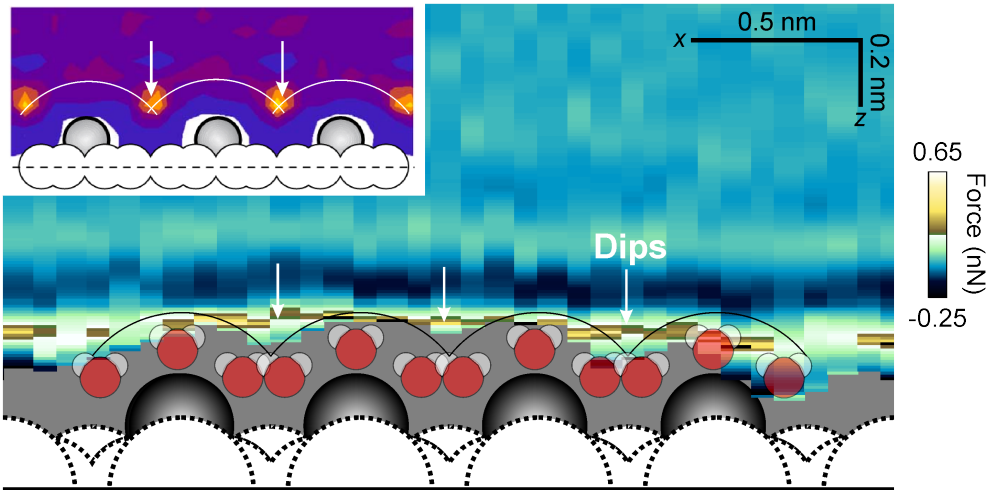

Figure 5.7.: Close-up view of the previous figure. A remarkable match between the experimental data and the hydration landscape of the ions is visible. In each cusp between two adjacent hydration shells, dips in the experimental data are visible (white arrows). The K+ ions and their hydrated ionic radius is shown (black fine lines). $k_1 = 12$ N/m. The inset shows results from MD simulations adapted from Reference [79].

The match between the measured xy force panels and the crystal structure data supports the hypothesis that the observed structures represent the topography of the hydration landscape of K+ ions adsorbed in the inner sphere configuration. Due to the water-induced correlations, the adsorbed complexes are stable enough to withstand the (low) tip-sample interaction forces [79]. Of course, the hydration layers are not a rigid structure, but rather characterized by a permanent exchange of water molecules with the bulk solution. However, due their locally increased water density, they pose a repulsive force that is sensed by the AFM tip [93] and decreases the amplitude upon approaching. When applying a stronger force by decreasing the set-point amplitude during 3D-AFM, the B regions disappear and only A regions are observed in the panels. An example of such data is shown in 5.3b and d. It can be seen that the surface relief appears almost entirely flat. The distance of the 1st HL to the surface is then evenly distributed over the panel and its distance to the surface is the one of the formerly observed region A. This distance is too small to accommodate a hydrated K+ ion. In other words, the observed 1st HL now entirely corresponds to the hydration of the mica itself. This observation is a further confirmation of the hypothesis, since an increasing tip-sample interaction will eventually lead to a local desorption of the K+ ions. Notwithstanding this observation, at any given moments ions will be still adsorbed to the mica outside of the current position of the tip, even though the image appears entirely free of ions. By repeating the experiment with stiffer cantilevers (stiffer ArrowUHF, $k_1 \gtrsim 18$ N/m), this situation is directly obtained irrespective of the set-point, see for example **Figure 5.8**. Figure 5.8 resolves well the lateral features of the mica's hydration landscape that were also seen in Figure 5.3d. When an even higher force is applied by choosing a very stiff cantilever

(PPP-NCHAuD 2nd mode, $k_2 \approx 1875$ N/m), the same pattern is still obtained although with a lower signal-to-noise ratio (see Appendix, Figure B.5). This observation confirms that the hydration structure observed under these conditions is the intrinsic one of the mica because it cannot be easily removed.

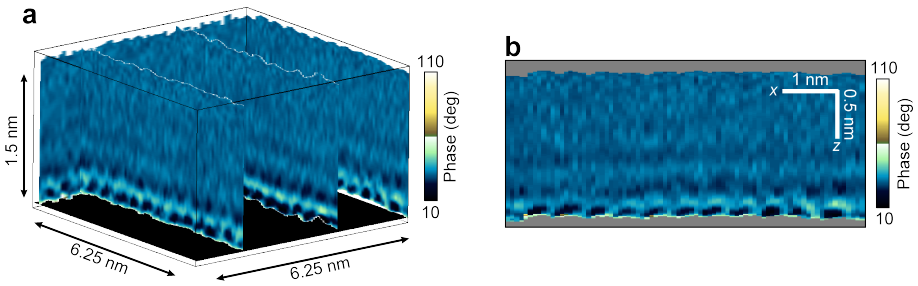

Figure 5.8.: 3D-AFM phase images of mica-KCl (200 mM, aq.) interfaces with a cantilever of higher stiffness (stiffer ArrowUHF, $k_1 = 18$ N/m). **a.** 3D-AFM xyz phase image. The surface relief at the bottom of each panel appears flat. The black plane was included in order to increase the visibility of the features. **b.** Representative xz phase panel obtained from the cube. It shows distinct features corresponding to the mica's hydration landscape. The features are coinciding with the observations made with softer levers at lower imaging set-point ratios. The vertical position of the 1st HL is too small to accommodate hydrated K+ ions. The gray areas are not accessed by the tip.

5.3.2. Divalent Ions

Solutions containing divalent ions represent a far more complex system due to peculiar effects caused by divalent (or multivalent) ions [219]. Phenomena like charge inversion [82,203,206,220,221] or ion-bridging [206,220] between two surfaces can occur. Due to their much larger hydration enthalpy, the adsorption behavior of divalent ions is expected to be very different from that of monovalent ones [206,222]. To investigate ion adsorption with 3D-AFM, it is advantageous to that the ions are bound in inner-sphere complexes to the surface. A divalent type of ion that has been observed to adsorb to mica forming inner sphere complexes is Ba2+ [64, 222]. For pre-examining the different effects of divalent ions on the tip-sample forces, static force curves were measured with a colloidal SiO_2-tip over mica immersed in aqueous solutions of both KCl and $BaCl_2$ at different concentrations (**Figure 5.9**). A measurement performed in ultrapure water serves as a reference. As expected from the DLVO theory, a pronounced long-range repulsion is measured in ultrapure water. In both cases, upon adding ions to the solution, the decay length of the double layer force (Debye length) decreases. However, the effect is much stronger in the case of the divalent ions, as it is well-reported in the literature [68,82,206,223]. The minimum concentration necessary to entirely suppress the repulsion is 200 mM and 20 mM for KCl and $BaCl_2$, respectively. These concentrations will be chosen for the 3D-AFM measurements.

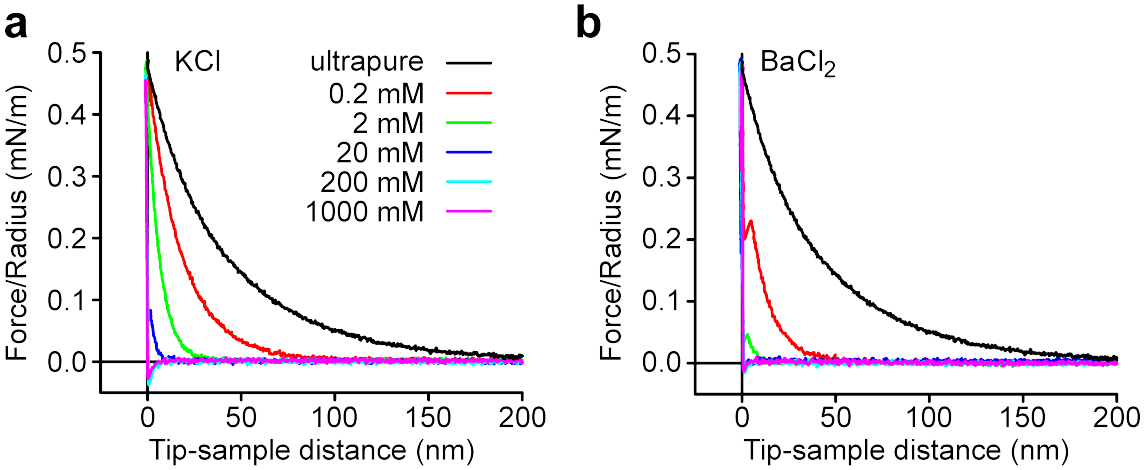

Figure 5.9.: Static force spectroscopy with colloidal tips (SiO_2, 6.62 µm tip radius, k_0 = 0.08 N/m) measured above mica immersed in aqueous solutions at different concentrations. **a.** KCl. **b.** $BaCl_2$. The black line was measured in ultrapure water and serves as a reference. The salt concentrations are indicated in panel a.

Next, 3D-AFM images were recorded in $BaCl_2$ solution (aq.) with the same cantilever that was used in the previous section for KCl ($k_1 \approx 12$ N/m). **Figure 5.10** shows a 3D-AFM phase cube with some representative xz phase panels. At the bottom of the panels, a hydration structure is visible that consists mainly of two HL which show some corrugations, although less than the one found in KCl solution. In the lateral direction some small structures are resolved that follow the corrugation.

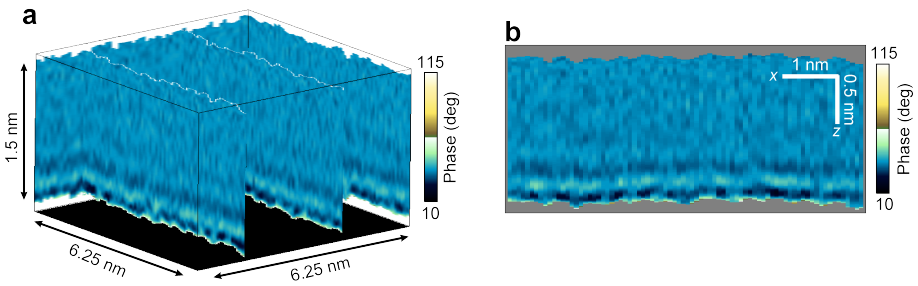

Figure 5.10.: 3D-AFM phase images of mica-$BaCl_2$ (20 mM, aq.) interfaces measured with the same cantilever as in KCl ($k_1 = 12$ N/m). **a.** 3D-AFM xyz phase image. The black plane was included in order to increase the visibility of the features. **b.** Representative xz phase panel obtained from the cube. The hydration structure appears continuous and flat with some corrugations. Some lateral structures are visible. The gray areas are not accessed by the tip.

The flat surface relief suggests two possibilities: Either the mica surface was reached by the tip throughout the whole panel or not at all. In the following, a comparison between

the 3D-AFM data taken in $BaCl_2$ with the previously discussed KCl data will be performed. Since the background force was fully screened out in both cases and furthermore the same tip was used, the measured tip-sample forces can be directly compared between the two experiments. **Figure 5.11** shows force panels extracted from the 3D-AFM data of both solutions. Panel a is the same xz force panel that was discussed above and serves as a reference. Panel b shows an xz force panel measured in $BaCl_2$ in the same color range as panel a. By comparing the force values and matching the positions of the hydration layers, it seems that the surface relief measured in the divalent case actually corresponds to the height of the 1st HL (indicated by the horizontal dotted lines between panels a and b) rather than the mica surface. Accordingly, the involved force curves (see panel c) coincide almost perfectly until the 1st HL. However, once the tip reaches the position of the 1st HL, the curves depart. In the case of $BaCl_2$ the tip deflects at this point and does not indent further.

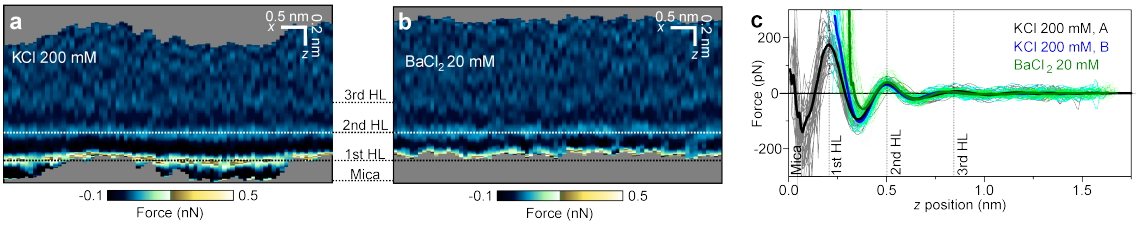

Figure 5.11.: Comparison between mono- and divalent ions in 3D-AFM measurements. **a.** xz force panel of the mica-KCl (200 mM, aq.) interface for reference. The vertical structuring into three distinct hydration layers (HL) is indicated and serves as a height reference. The gray areas are not accessed by the tip. **b.** xz force panel of the mica-$BaCl_2$ (20 mM, aq.) interface. **c.** Set of force curves obtained by unraveling the xz force panels. Green curves correspond to $BaCl_2$. Gray and blue force curves were measured in KCl at x positions corresponding to the A and B regions, respectively. The corresponding average curves are highlighted. $k_1 = 12$ N/m.

Following the interpretations of the previous section on monovalent solutions, this observation suggests that the $BaCl_2$ ions are adsorbed at the surface and their strong hydration landscape is not indented by the tip. The Ba2+ ion has a very similar ionic radius and adsorption position within the ditrigonal cavities as the K+ ion. The values are $r_{Ba2+} = 0.149$ nm and $\Delta z_{Ba2+} = 0.198$ nm, respectively [64,222]. The hydrated ionic radius, $r^{Hyd}_{Ba2+} = 0.281$ nm, is slightly smaller than in the case of KCl [224], reflecting its 4.3 times larger hydration enthalpy [222]. Its coordination number is $N_{\mathbf{Ba2+}} = 8.1$ [224].

By comparing the crystal structure data with the measurement, it can be verified if the above idea is compatible with the dimensions of the involved species. The contact plane can be estimated from the comparison in Figure 5.11. The KCl panel serves as a reference with known contact point. The distance between the mica surface and the respective first HL depends on the hydrated ionic radius of the involved species. Hence, the difference in the hydration radii of the two species (49 pm) has to be subtracted. The

result is shown in **Figure 5.12**. Also in this case, a good match between the measured features and the schematic hydration landscape is found. Although the corrugation at the surface is small, also in this case a periodicity can be found matching the pattern of the hydration shells.

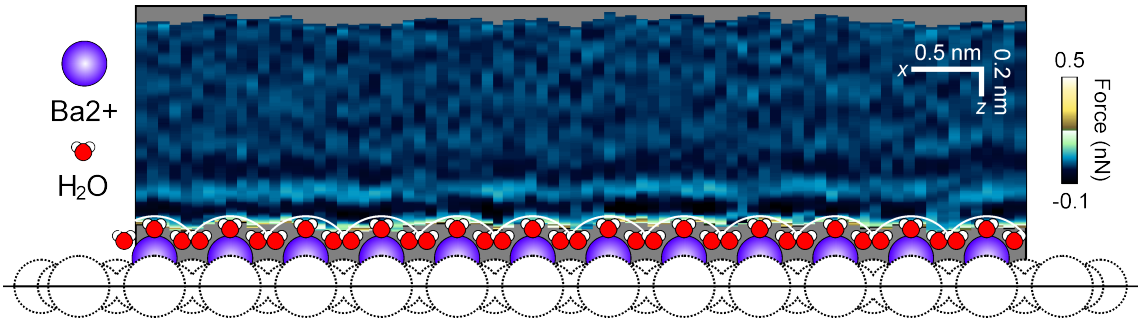

Figure 5.12.: Comparison between 3D-AFM data measured on mica in $BaCl_2$ (20 mM, aq.) and reported crystal structure data obtained from different X-ray methods. The upper part of the panel depicts an xz force panel, and the lower part the front view on the (001) mica plane. Both parts have been vertically and horizontally matched as described in the text. Hydrated Ba2+ ions adsorbed in inner sphere complexes are added in the ditrigonal cavities. Their hydration landscape coincides with the measured surface relief. Purple and red/white spheres represent the Ba2+ ions and water molecules, respectively. The hydrated ionic radius, $r^{\mathbf{Hyd}}_{\mathbf{Ba+}} = 0.281$ nm, is indicated for each inner sphere complex by fine a white line. The gray areas are not accessed by the tip. $k_1 = 12$ N/m.

A close-up image extracted from Figure 5.12 is shown in **Figure 5.13**. White arrows indicate periodic dips in the xz force panel that match the corrugation of the schematically shown hydration shells. Furthermore a dark spot is visible above each ion, indicating an attractive force of around -90 pN measured above each ion. Such attractive forces have been observed earlier by Jimenez and Garcia and ascribed to the presence of adsorbed ions [105]. The images shown in Figure 5.12 and 5.13, however, would be at odds with the expected coverage of 25 % to reach ideal charge compensation of the mica surface [64, 222]. It could be argued that the ions adsorb in nanoscale patches with 100 % coverage while other regions are empty. Such patches could be formed due to correlation effects as observed in the case of monovalent ions or induced by the presence of the negatively charged tip [79]. Earlier, Vakarelski and coworkers observed dense layers of monovalent ions adsorbed on mica surfaces that could not be penetrated by a colloidal SiO2 tip when the tip-sample contact time was below 50 ms [218,225]. In 3D-AFM, the tip apex is in contact with the hydration structure for < 5 ms per z-cycle (for the given conditions, see *e.g.* Figure 2.7b). The above conditions might favor the observation of such an apparently stable layer of adsorbed ions.

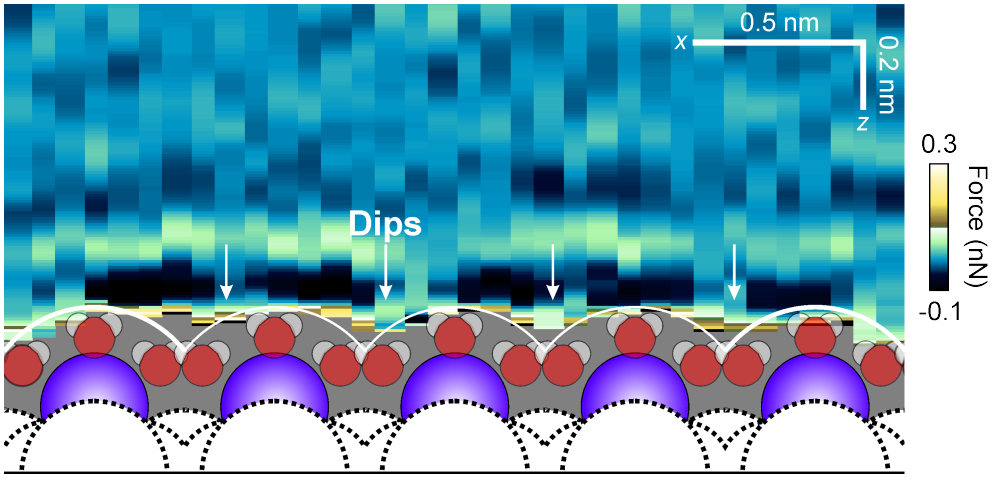

Figure 5.13.: Close-up view of the previous figure. A remarkable match between the experimental data and the hydration landscape of the ions is visible. In each cusp between two adjacent hydration shells, dips in the experimental data are visible (white arrows). The Ba2+ ions are shown with their hydrated ionic radius (white lines). $k_1 = 12$ N/m.

Some experiments were also conducted using stiff cantilevers (AC55TS, $k_1 = 191$ N/m). In these cases sometimes dome-like structures were observed, as the ones shown in **Figure 5.14**. The structure resembles a hydration layer (bright layer enclosed in two darker layers) that is not extended in parallel the surface but rather forms a dome-like shape. A few of them can be identified in the same panel, but they as individual objects with varying distances from each other, as can be seen in panel a. Interestingly, they can be scanned repeatedly apparently without being modified. This enables to obtain a 3D-AFM images of such structures (panel b and c) resolving the dome like hydration structure in x, y and z. The imaging period spans over at least 20 s.

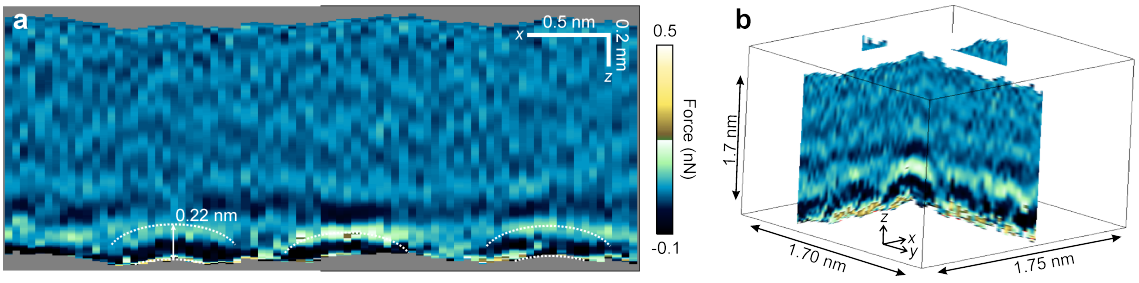

Figure 5.14.: 3D-AFM measurements on a Mica-$BaCl_2$ (20 mM, aq.) interface obtained with a stiff cantilever (AC55TS, $k_1 = 191$ N/m). **a.** xz force panel showing dome-like structures next to the apparent surface (indicated by white dotted lines). The height of the structures is around 0.22 nm. The gray areas are not accessed by the tip. **b.** 3D-AFM cube around the center feature. It is well-resolved in x and y direction, which implies repeated scanning over the feature during 20 sec. **c.** Close-up image (extracted from b).

The comparison with the measurements performed with other cantilevers (see Appendix, Figure B.6) suggests that the object is sitting at the mica surface, although the comparison is less clear due to the higher force noise of the AC55TS cantilever. The height of the structure is around 0.22 nm in the highest point. It is likely that the object appears wider than it actually is due to the tip convolution that affects isolated objects in 3D-AFM as in standard scanning. In the 3D-view, the aspect of the structures somehow resembles that of an ion's hydration shell (compare isolated hydrated ion in Figure 5.2a). However, the measured height is quite small for the Ba2+ ion whose hydration shell has a radius of 0.28 nm [217]. Similar stable objects were imaged also sometimes in KCl solutions. However, further experiments are necessary to clarify the origin of these observations.

5.4. Conclusions

In this chapter, AM 3D-AFM was applied to investigate the adsorption of K+ ions to a muscovite mica surface. By using softer cantilevers compared to standard 3D-AFM measurements, the tip-sample interaction force was reduced and singular atomic-scale features of the solid-liquid interface were resolved that cannot be seen with stiffer cantilevers. Within the SLI, regions where observed where the tip was tapping directly on the mica, and others, where the tip was tapping on top of the hydration shells formed by adsorbed adjacent K+ ions. The results suggest that the adsorbed ions, together their hydration landscape, are stable enough to be topographically imaged by the AFM tip.

The developments of Chapter 2 enabled a direct comparison between the obtained 3D-data and results from XRR experiments reported in the literature. The geometrical match between both types of results is remarkably and supports the idea that the tip can interact with the shared hydration shells between adjacent adsorbed ions without inducing a desorption of the ions from the surface. From a more general point of view, the precise match in both the vertical and the horizontal direction further strengthens 3D-AFM as a technique. The results emphasize that 3D-AFM can not only match XRR in vertical resolution, but furthermore provides complementary lateral information with atomic-scale resolution. The increased force sensitivity of shorter cantilevers will also help to develop a high-resolution and non-invasive high-speed 3D-AFM.

6. Force Spectroscopy on Single Biomolecules

6.1. Introduction

Force spectroscopy (FS) is a powerful and highly versatile toolbox for obtaining information at the nanoscale [226], most importantly regarding mechanics [23, 25, 227, 228], but also other sample characteristics attract increasing attention, such as (electro-)chemical [32, 53], magnetic [3, 229] and electrical [4, 69, 230, 231] properties. The success of AFM force spectroscopy has been accompanied and also promoted by the development of a number of (commercial) techniques based on static [25, 41], dynamic [31, 228, 232, 233], and even multimodal operation [234,235]. Among the most common ones, there are force-volume imaging, PeakForce Tapping® [38], PulsedForce Mode [40], Jumping Mode [41], Quantitative Imaging™ (QI) [39], multi-set point intermittent contact (MUSIC) mode, [232, 236], topography and recognition imaging (TREC) [237, 238], and photothermal off-resonance tapping (PORT) [239]. The capabilities of these methods in terms of force sensitivity and spatial resolution have been exploited to study tip-sample interactions down to the scale of individual molecules. FS approaches to study single molecules could be classified in two groups: Approaches that are based on pulling at single molecules on one hand, and those that are pushing on single molecules on the other hand [240]. In this chapter, methods from both groups will be used to address different aspects of the technique itself, as well as its applications. It is divided into four sections:

The first section introduces some theoretical aspects of AFM Single-Molecule Force Spectroscopy (SMFS). SMFS measures the forces that arise from the unbinding of a individual receptor-ligand pair. Knowing these forces offers a unique way to study biomolecular interactions, processes and properties in biophysics and mechanobiology [5,37,241–244]. The field of SMFS has been dominated for a long time by optical tweezers [245], molecular flow chambers [246], and biomolecular force probes [247]. In 1994, Gaub's group demonstrated that also the AFM is capable of detecting such forces. [5,248] Since then, AFM single-molecule force spectroscopy (AFM SMFS) has been applied widely throughout the community [249], sometimes under pseudonyms such as Multi-parametric Imaging [250], Dynamic Force Spectroscopy [249], or Molecular Recognition Imaging [251]. Recent applications include the visualization of the first binding steps of a virus to cell receptors [252] and revealing the existence of intermediate steps in the unfolding of membrane proteins [253].

The basic concept of each unbinding experiment using the AFM consists of three steps: First, the receptor and ligand are far away from each other, but each is firmly attached to

either the AFM tip or the sample. Second, receptor and ligand are brought in contact by approaching the tip to the sample. Once mechanical contact between the receptor and the ligand is established, a bond can form. Then, in the third step, the tip is withdrawn from the sample. If a bond was formed, the involved molecules are stretched in a spring-like manner upon tip withdrawal which loads the bond until it eventually breaks. Such an unbinding process is equivalent to thermal escape stimulated by an external force.

Already in the 1940s, Kramers described unbinding as a thermodynamically activated process [254]. As a consequence, the force necessary to break a bond depends on the rate with that the bond is loaded. As later established by the theories of Bell [255] and Evans [242], the force that the bond can withstand is the higher, the faster the pulling is performed. The Bell-Evans model has been applied successfully to SMFS data obtained from a variety of receptor-ligand systems and techniques [247, 249, 256–262].

The second section builds on the first one and is dedicated to a fundamental aspect of AFM SMFS experiments: How does the cantilever's dynamic behavior affect the obtained results in SMFS? Recent pivotal developments in AFM instrumentation [263] led to the development of High-Speed SMFS (HS SMFS), which allowed researches to pull faster than ever before on bonds [244]. With this technique, Rico and coworkers achieved to measure the bond rupture at speeds comparable to the ones used in molecular dynamics (MD) simulations [244,264,265]. In HS SMFS, the cantilever reaches speeds up to the order of 10 mm/s [244, 264, 265]. However, the description of the cantilever in AFM SMFS is commonly based on that of a static spring (Hooke's law), while other AFM modes are backed up by detailed theories [24]. Recently, it was predicted that the static approach fundamentally limits the reliability of force spectroscopies at high speeds [111].

In this section, experiments are performed on the well-known biotin-avidin system, whose bond represents one of the strongest noncovalent bonds in biology [266]. Biotin is a vitamin that plays an important role in the human metabolism. Avidin is a tetrameric protein that is found in egg-white. Each of its four subunits can bind one biotin molecule with a very high affinity constant ($2.5 \cdot 10^{13}\,\mathrm{M}^{-1}$) [266]. The experiments reveal a decrease in the measured force at high rates. This result is at first glance at odds with the established Bell-Evans theory. Using the Euler-Bernoulli beam equation, a theory is developed that explains the observations by unraveling the different components of the force. It is revealed that significant contributions arise from inertial and hydrodynamic forces generated during the breaking of the bond at high loading rates. An analytically derived correction factor is provided to incorporate those effects into the Bell-Evans theory and to accurately recover the force that is necessary to unbind the molecular complex. This section was developed in collaboration with Dr. Carlos Álvarez Amo, who deduced the theory, performed the simulations, and wrote the code for the software used to detect the unbinding events. The key results of this chapter are published in: Manuel R. Uhlig, Carlos A. Amo and Ricardo Garcia. Dynamics of breaking intermolecular bonds in high-speed force spectroscopy. *Nanoscale* **10**, 17112 (2018).

The third section presents an application for AFM SMFS as a powerful tool for local

biorecognition [137,237,238,259,267]. With this technique, a specific molecule of interest that is adsorbed to a surface can be chemically localized with single-molecular resolution. In this section, SMFS will be applied on a silicon nanowire (SiNW) that forms part of an FET-based ultrasensitive biosensor designed to detect ultralow concentrations of avidin molecules. In order to achieve localized adsorption, the sensitive area of the device is functionalized to promote avidin adsorption. AFM SMFS is used to map the sample topography and simultaneously localize specific unbinding events. Locally selective adsorption of avidin onto the SiNW will enhance the device's performance when it comes to detecting ultra-low concentrations of the target molecule. This section was developed in collaboration with Dr. Francisco Miguel Espinosa Barea, who prepared the SiNW sample and performed the tip functionalization.

The fourth section presents an approach to study single biomolecules under a compressive force instead of a pulling force. Protein conformational changes under compressive force have been recently explored quantitatively using the Bell-Evans framework commonly used for pulling experiments [261, 268]. In a broader context, a variety of indentation approaches is used to probe the flexibility of a protein, since it determines a protein's ability for conformational changes and hence has a strong influence on the protein's function and biological activity such as binding to antigens or ligands [269,270]. Different AFM techniques are available for mapping the Young's modulus or the flexibility of proteins down to the level of single molecules [233, 271–275]. In this section, the nanomechanical properties of individual proteins are addressed by force spectroscopy with single-molecular resolution. A fast force spectroscopy approach in combination with molecular dynamics simulations will be applied on a single immunoglobulin antibody in order to gain insights into submolecular features of its mechanical response. This section was developed in collaboration with Dr. J. Guilherme Vilhena and Prof. Dr. Rubén Pérez (Universidad Autónoma de Madrid), who performed the MD simulations. Dr. Alma Eva Perez Perrino provided help with the sample preparation.

6.2. Theory of Unbinding Kinetics

In this section, the basic theoretical concepts of unbinding will be briefly introduced. A more comprehensive overview is given, for example, by the book of Bizzarri and Cannistraro [249].

A biomolecular complex consists of a receptor-ligand pair which recognize each other by system-specific molecular interactions. Bonds between receptors and ligands are non-covalent, *i.e.*, governed by interactions such as van der Waals forces, hydrogen or ionic bonds, hydrophobic forces, and others. In terms of energy, any bond represents a minimum position within an energy landscape. **Figure 6.1**a shows a simple, one-dimensional energy landscape $U(x)$. In this example, the energy landscape consists of a single energy barrier ‡, that is characterized by its position x_β along the reaction coordinate, its unbinding rate (or off-rate) K_{off}, and the difference in energy between the bound and un-

bound state, ΔG_{bu}. When the complex is bound, its free energy is minimal. In order to unbind, receptor and ligand have to separate from each other along the reaction coordinate. When moving away from the minimum position, the system's free energy increases, until it reaches its maximum. Upon further separation, the free energy decreases and reaches a constant value. There, the complex is unbound and the interactions between receptor and ligand have vanished.

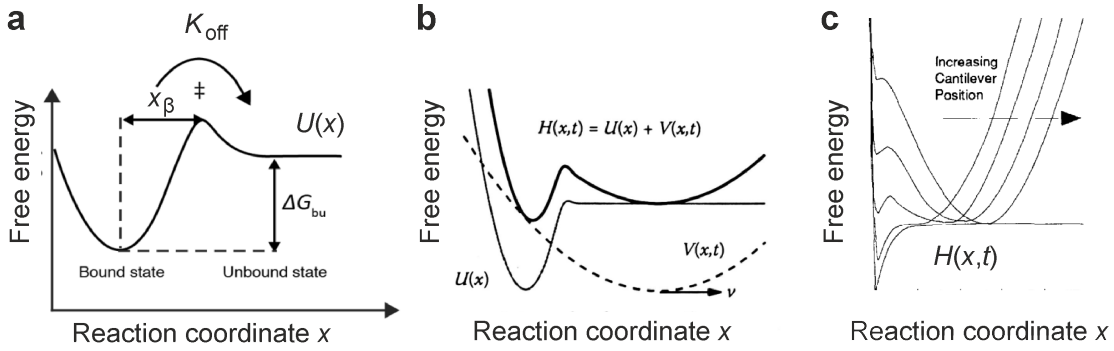

Figure 6.1.: Illustrations of the unbinding process. **a.** Simple energy landscape $U(x)$ with a single energy barrier ‡ at the position x_β. The escape rate over the barrier is K_{off} and the difference in energy between the bound and unbound state is ΔG_{bu}. **b.** The superposition of the bond's energy landscape, $U(x)$, with the spring-like potential of an AFM cantilever, $V(x,t)$, defines the total potential, $H(x,t)$. **c.** Evolution of the total energy landscape $H(x,t)$ when the cantilever's potential is moving outwards. Panels a, b, and c adapted from Reference [276], [249], and [277], respectively.

The transition over the energy barrier can be described by the kinetic constants: The on-rate, K_{on}, and the off-rate, K_{off}. The idea of these two parameters can be understood through the simple qualitative relationship:

$$\mathrm{A} + \mathrm{B} \underset{K_{\mathrm{off}}}{\overset{K_{\mathrm{on}}}{\rightleftarrows}} \mathrm{AB} \tag{6.1}$$

where A and B represent a receptor and its ligand, respectively, and AB the corresponding complex. In the following, we will only focus on the off-rate, K_{off}, which is also called the dissociation rate. The dissociation rate of a given complex is related to a bond's lifetime and one goal of SMFS is to obtain this parameter. In the case of AFM SMFS, K_{off} can be determined indirectly from the measured unbinding forces using theoretical models (see below).

6.2.1. The Transition Rate Under Force: The Bell-Evans Model

The theoretical description of the unbinding process in AFM SMFS is based on the concept of thermal escape, stimulated by an external force. The molecular complex is connected to an AFM cantilever that behaves in a spring-like manner. For the one-dimensional case there is only one degree of freedom, let's say, x. The cantilever dis-

placement, the force applied to the complex, and the molecular separation is assumed to take place along x. Figure 6.1b depicts this situation in terms of the energy landscape.

The gray line shows an energy landscape of a simple complex, $U(x)$, that is characterized by a single well and a single energy barrier. The dashed line shows the cantilever potential $V(x)$, which is the parabolic potential of a spring:

$$V(x) = \frac{1}{2}k_0(x - v_\mathrm{p}t)^2$$

where k_0 is the cantilever spring constant, v_p the speed of displacement of the cantilever base, and t the time. Linking the molecular complex to the AFM cantilever leads to a perturbation of the intermolecular potential by the cantilever potential which is expressed by adding up both. The resulting total energy of the system, $H(x,t)$ is depicted for a given intermolecular separation x in Figure 6.1b (black line). In general, one can write

$$H(x,t) = U(x) + V(x,t) \tag{6.2}$$

When the cantilever is moving away from the surface, $V(x,t)$ is swept along x, where $x(t) = vt$. As a consequence, the total potential $H(x,t)$ is warped in a time- and cantilever-dependent manner (commonly referred to as "tilted") [277, 278]. Figure 6.1c illustrates this concept for a number of cantilever positions. This implies that the force acting on the bond increases continuously and the cantilever bends downwards. For a sufficiently soft cantilever, the system passes through a bistable state and the transition between the two minima can happen abruptly. In this moment, the bond ruptures and the cantilever moves to its rest position. The rupture forces can be linked to intrinsic properties of the bond. In the following, some theoretical considerations will be introduced to establish such a link.

In the bound state, one can think of the molecular complex as a particle sitting in the potential's well. Such a particle is subject to the thermal energy and, hence, Brownian motion and diffusion. Consequently, the particle fluctuates around the minimum position within the well. Assuming a parabolic shape for the energy well and the energy barrier, Kramers calculated the escape rate K_off for a population of such particles to be [254]

$$K_\mathrm{off} = \frac{\sqrt{\kappa_\mathrm{o}\kappa_\beta}}{2\pi\eta}\mathrm{e}^{-\Delta U/k_\mathrm{B}T} \tag{6.3}$$

where $\kappa_\mathrm{o}, \kappa_\beta, \eta, k_\mathrm{B}$ and T are the curvatures of the energy landscape at the minimum position and at the barrier position, the system's damping coefficient, the Boltzmann constant, and the absolute temperature, respectively. Equation 6.3 shows that the escape rate depends on the shape of the energy landscape, expressed by κ_o and κ_β. For a stable compound, the energy barrier is much larger than the thermal energy, making spontaneous unbinding unlikely (although > 0). However, in SMFS the situation is different since an external force is applied. As explained above, an external force modifies the energy landscape's shape (Figure 6.1). Bell derived an expression for the escape rate as a function of the applied force F,

$$K_\mathrm{off}(F) = K^0_\mathrm{off} e^{Fx_\beta/k_\mathrm{B}T} \tag{6.4}$$

with $K^0_{\text{off}} \equiv K_{\text{off}}(0)$, the unperturbed escape rate, and x_β, the position of the energy barrier [255]. Later, Evans developed an expression for the force at which a given bond will most likely break [242]. Using the transition rate derived by Bell, the most probable rupture force F^*_{rup} is

$$F^*_{\text{rup}} = \frac{k_{\text{B}}T}{x_\beta} \ln \left[\frac{r x_\beta}{K^0_{\text{off}} k_{\text{B}} T} \right] \tag{6.5}$$

with r being the loading rate. Equation 6.5 is often referred to as the Bell-Evans model. It has been applied very successfully to SMFS data obtained from a variety of receptor-ligand systems and techniques [247, 249, 256–262]. Also, a number of models has been developed to account for deviations from the Bell-Evans model [279–281].

6.3. Newton Dynamics in High-Speed Single-Molecule Force Spectroscopy

In AFM SMFS, the rupture force has been postulated to coincide with the measured force, *i.e.*, the cantilever deflection at the rupture distance as predicted by the Hooke's law. In contrast to other AFM modes, there is no equation of motion (EOM) for the AFM cantilever in SMFS. Instead, although being a static description, the above postulate is considered valid with independence of the measurements speed. In a broader context, it is a long standing question if forces measured in SMFS are related solely to the bond rupture, or, if they are to some extend affected by artifacts that come from the apparatus and its components, such as the linker and the cantilever [282]. It is known that the cantilever's properties, such as its stiffness and resonance frequency, affect the results in AFM SMFS [253, 283–287]. The cantilever contributions can be classified into two categories, (1) Contributions that arise from the fact that the presence of the cantilever changes the unbinding process itself and, hence, the force that is measured upon unbinding [282, 285–287]. (2) Contributions that arise from the cantilever as a force sensor, which in principle affect any measurement of a given force probed by a force spectroscopy approach [110, 111, 115, 283]. With regard to the second class, Amo and Garcia pointed out recently that the characteristics of the cantilever pose a fundamental upper speed limit for quasi-static force spectroscopy approaches [111]. With MD simulations, the authors observed an underestimation of adhesion forces at high measurement speeds (see **Figure 6.2**a-b). A recently developed HS force spectroscopy method (photothermal off-resonance tapping) found a similar effect when experimentally measuring (unspecific) adhesion forces (see Figure 6.2c) [239].

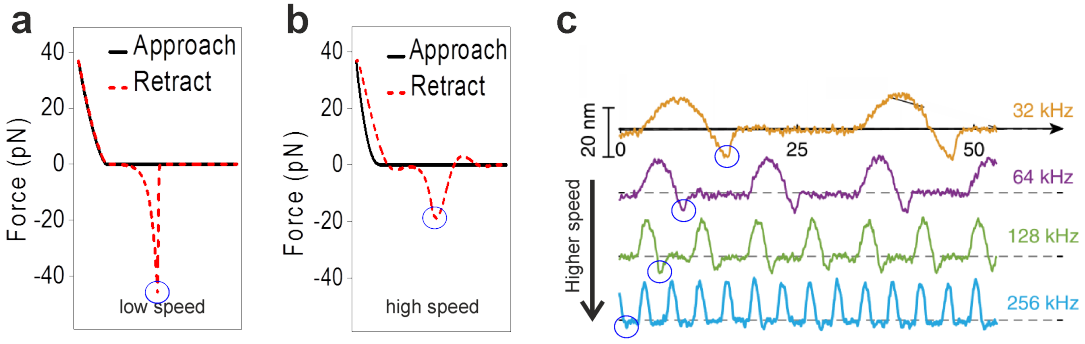

Figure 6.2.: Effects of Newton dynamics in high-speed force spectroscopy. **a.** Simulation of a single-molecule force spectroscopy measurement performed at low speed. **b.** Simulation of the same measurement performed at higher speed. The measured attractive force is much lower than in panel a (marked by blue circle). **c.** Dependence of the unbinding force on the measurement velocity (Simulations). **d.** Experimentally obtained data using a high-speed force spectroscopy method. With increasing measurement frequency, the adhesion force diminishes (marked by blue circles). Panels a-b and c are adapted from Reference [111] and [239], respectively.

During an experiment, the cantilever represents an extended object moving through a fluid and, hence, underlies hydrodynamic effects. In particular with increasing speed, such effects become more pronounced. In HS SMFS, the cantilever reaches speeds up to the order of 10 mm/s. Nevertheless, the general description of the cantilever's behavior is still based on that of a static spring (Hooke's law) and empiric corrections are applied subsequently for the occurring hydrodynamics. In this section it will be discussed how the cantilever's dynamic behavior affects the results in AFM SMFS. Experiments are performed on the well-known biotin-avidin system which reveal that the measured force decreases with the loading rate at high rates. This result is at odds with the established Bell-Evans theory that predicts a monotonic increase of the rupture force with the loading rate. Using the Euler-Bernoulli beam equation, a theory is developed that explains the observations. Unraveling the different components of the force reveals that significant contributions arise from inertial and the hydrodynamic forces generated during the breaking of the bond at high loading rates. A correction factor is analytically derived that incorporates those effects into the Bell-Evans theory recovers the force that is necessary to unbind the molecular complex [114].

6.3.1. Materials and Methods

Tip and Sample Preparation

AFM SMFS experiments require a number of preparation steps regarding the tip and the sample. Here, the tip functionalization consists of two main steps following a protocol provided by Dr. Andra Christina Dumitru. First, the silanization of the tips with APTES and, second, the subsequential functionalization with NHS-PEG27-biotin. The

sample is an avidin monolayer physisorbed onto a mica substrate.
Phosphate buffered saline (PBS) powder, ethanol, 30 % hydrogen peroxide, 1 N (0.5 mol/L) sulfuric acid, 3-aminopropyltriethoxysilane (APTES) 99 %, trimethylamine $\geq$ 99 %, and avidin from egg-white $\geq$ 98 % were purchased from Sigma-Aldrich (Madrid, Spain). The N-Hydroxysuccinimid (NHS)-polyethylenglycol (PEG27) - biotin linkers were purchased from the JKU Linz [288].

Silanization with APTES. Silicon nitride cantilevers (MSCT, Bruker, CA, USA) were cleaned thoroughly by immersing them for 30 min in piranha solution, a mixture of 0.5 N sulphuric acid and 30 % hydrogen peroxide (4:1 ratio in volume). Then, the cantilevers were rinsed with ultrapure water and dried carefully using a flow of N_2. Afterwards, the cantilevers were immediately transferred into a mixture of APTES : ultrapure water : ethanol (5:5:90 ratio in volume) to initiate the silanization of the tips. After another 30 min, the cantilevers were rinsed with ethanol and ultrapure water and finally dried with N_2.
Functionalization with PEG-biotin. 1 mg of the NHS-PEG27-Biotin linkers [288] was dissolved in trichloromethane (0.5 ml). The obtained solution was transferred into a PTFE chamber and 30 µl of tryethylamine were added as catalyst. Then, the silanized tips were immersed into the chamber. After an incubation time of 2 hours, the cantilevers were removed from the chamber, rinsed three times with trichloromethane, and dried with N_2.
Avidin monolayer sample. The freeze-dried avidin was dissolved in 15 mM NaCl to obtain a solution with an avidin concentration of 0.1 mg/ml. Immediately afterwards, 33 µl of the solution were deposited on a freshly cleaved mica sheet. After 15 min of adsorption time, the mica was rinsed carefully 10 times with 1 mM NaCl and subsequently 3 times with 10 mM PBS.

Cantilevers and Calibration

A rectangular silicon nitride cantilever (MSCT-B, Bruker, CA, USA) was used throughout the experiments. The cantilever's force constant k, its resonance frequency f_r, and its quality factor Q were calibrated in liquid. The calibration was performed after the experiment to prevent tip damage during the calibration. The procedure was realized as follows: First, the inverse optical lever sensitivity (invOLS) for the static deflection, σ, was obtained from force-displacement curves recorded on the bare glass Petri dish next to the mica substrate. The invOLS σ is determined as the inverse of each curve's slope in the contact part and then averaged over 100 curves. Second, the cantilever's thermal noise spectrum (power spectral density, PSD) is recorded at about 15 µm above the sample surface [13]. Then, the single harmonic oscillator (SHO) model is fitted to the PSD around the peak of the first resonance frequency using the calculated invOLS of the first mode, $\sigma_1 = 21.8\,\mathrm{nm/V}$ [10]. The fitting yields the force constant $k_1 = 30.2$ pN/nm, quality factor $Q_1 = 1.6$, and resonance frequency $f_1 = 3.05$ kHz. The static force constant and invOLS can then be calculated by $k_0 = k_1/1.03 = 29.32$ pN/nm and $\sigma_0 = \sigma_1/1.09 = 20.0$ nm/V, respectively. All parameters are summarized in Table

C.1 (Appendix).

Linear Drag

In liquid environments the cantilever movement is highly damped and hydrodynamic effects are of great importance [110, 289]. The associated force depends on the direction of the motion: When the cantilever approaches it is repulsive and when the cantilever retracts it is attractive. Until now, several research groups have investigated how a moving cantilever is affected by drag forces [110, 115, 289]. The general behavior of a moving object through a fluid can be characterized by the Reynolds number, Re. It is calculated from the liquid's density ρ and viscosity η, and the object's characteristic length l and its speed v relative to the liquid by [110]:

$$Re = \frac{\rho v l}{\eta} \tag{6.6}$$

Considering $\rho = 1$ g/cm^3, $\eta = 10^{-3}$ Pa·s, $l = 100$ µm and the maximum velocity reached in the FS experiments performed here ($v_\mathrm{p} = 100$ µm/s), Equation 6.6 yields $Re = 10^{-2}$. Hence, even at the maximum cantilever velocity, Re is low enough to consider low Reynolds number conditions ($Re < 1$). Even though recent SMFS experiments were performed at higher speeds (in the order of 10^{-3} m/s) the above condition holds because ultrashort cantilevers with smaller characteristic lengths were used [244, 264, 265]. In such conditions, the drag force F_drag is linear in velocity

$$F_\mathrm{drag} = -b \cdot v_\mathrm{c} \tag{6.7}$$

where b and v_c are a cantilever-specific drag factor and the velocity of the cantilever base, respectively [110]. It is important to point out that Equation 6.7 is sufficient to fully describe the drag force only when the tip is off-contact. Once the tip experiences a force, its velocity is different from that of the cantilever base. This implies that the viscous force is nonuniformely distributed along the cantilever, *i.e.,* a different drag force is acting on the front part of the cantilever than on it's base. Janovjak *et al.* proposed to modify equation 6.7 by replacing the cantilever base speed with the tip speed [115]. Liu *et al.* modelled the cantilever as a rotating rigid beam to approximate the velocity profile and the resulting viscous force during an experiment [290]. Amo and Garcia proposed to use a dynamic description for force spectroscopy measurements, which intrinsically considers hydrodynamics [111].

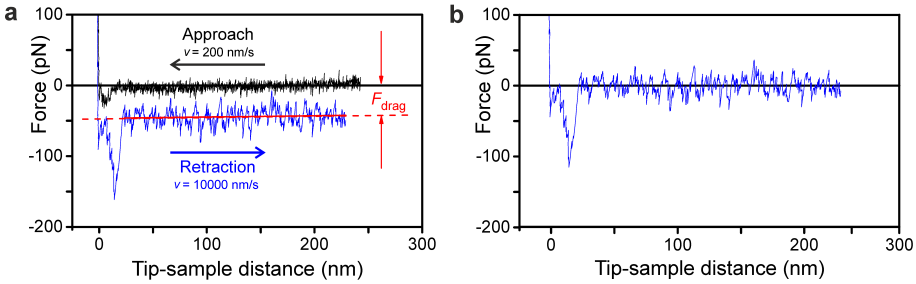

Figure 6.3.: Example of an SMFS curve obtained at a pulling speed of 10 µm/s. Black shows approaching tip movements, while blue corresponds to tip retraction. **a.** Raw data before applying the drag correction. The red line shows the drag force. **b.** The same curve after the subtraction of the linear drag (approach curve omitted for clarity). Adapted from [114].

Here, during the cantilever approach, the drag force is negligible due to the low approach speed. However, in the retraction part of the SMFS curve, the drag force can be significant. **Figure 6.3** shows an example SMFS retraction curve obtained at a pulling speed of 10 µm/s. The drag force causes an effective attractive force that persists in the noncontact part of the curve (baseline). As a first step to account for this effect, we fit a linear function to the baseline of the retraction part (red line in Figure 6.3a), subtract it from the raw data, and obtain the drag-free force curve (Figure 6.3b). This correction is applied to every individual SMFS curve before measuring the unbinding force. From the fit, one can also calculate the drag factor b by applying Equation 6.7. For the MSCT-B cantilever, a value of $b = 4.4$ pNs/µm was obtained, close to the expected value for this type of cantilever (≈ 5 pNs/µm). Note that strictly speaking, the drag factor b is a function of the tip-sample separation [110]. When the cantilever approaches the sample, b increases monotonically due to squeeze-film damping. However, in the case of the SMFS experiments shown in this thesis, this effect is neglected since the used cantilevers are equipped with sharp, long tips (8 µm for the rectangular MSCT-B cantilever versus 1 µm for the rectangular cantilever in Reference [110]). Furthermore, the range of the tip-sample distance in our experiments is much smaller than the effect's decay length [110]. Commonly, the effect is neglected in SMFS or shown to be very small [115].

AFM SMFS Protocol

Single molecule force spectroscopy experiments were performed on a NanoWizard III AFM (JPK Instruments AG, Berlin, Germany) equipped with an open liquid cell. The experiments were carried out in 10 mM PBS at pH 7.4 at a temperature of $T = 302$ K. The SMFS curves were acquired by applying a periodic, approximately triangular modulation to the cantilever base with an amplitude of $A_\mathrm{p} = 250$ nm. **Figure 6.4**a-b illustrates the data acquisition protocol. First, the cantilever base is approached to the sample with a constant speed of 200 nm/s until a force of 150 pN is reached (black curve). At this extension, the piezo is held for 20 ms. Then, the cantilever base is retracted with a constant pulling speed v_p (blue curves). Pulling speeds in the range of 100 nm/s to

100 µm/s were used in the experiments. The piezo motion is shown in Figure 6.4a for different pulling speeds. The piezo displacement was controlled using a calibrated closed-loop system. For each pulling speed value between 100 and 600 individual SMFS curves were acquired, with a spatial separation of 0.1 µm×0.1 µm inbetween individual curves. The data sampling rate was adjusted for each speed value to keep the number of data points per piezo displacement distance constant [257].

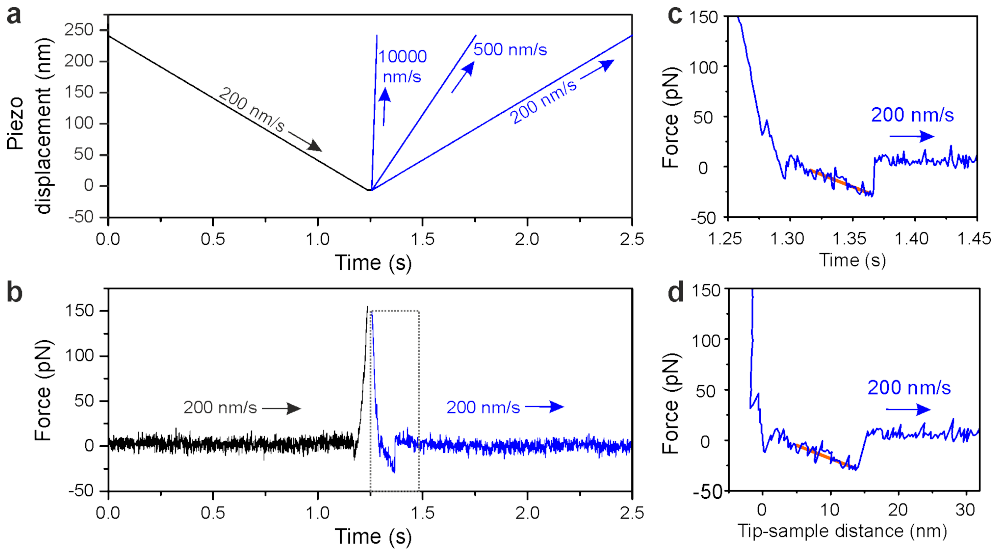

Figure 6.4.: AFM SMFS data acquisition protocol. Black shows approaching tip movements, while blue corresponds to tip retraction. **a.** The triangular modulation applied to the cantilever base for different pulling speeds. **b.** Example of an SMFS curve obtained at a pulling speed of 200 nm/s. **c.** Zoom-in into the force vs time curve around the unbinding event marked by the gray dashed box in panel b. The red line shows a linear fit to the data just before the unbinding event, whose slope corresponds to the effective loading rate. **d.** The same force data as in panel c, but plotted versus the tip-sample distance. The red line shows a linear fit to the data just before the unbinding event, whose slope corresponds to the cantilever-linker system's stiffness. Adapted from [114].

AFM SMFS Data Analysis

For analyzing the 3100 force-distance curves, a semi-automatic algorithm was written in MATLAB (MathWorks, MA). The software was developed mainly by Dr. Carlos Álvarez Amo. It fits the retraction part of the SMFS curves with a polynomial function of grade 7. Then, the minima of the polynomial are determined and the algorithm searches in their vicinity for minima in the raw data. Minima with a force value smaller than the 1.5-fold of the baseline noise are disregarded to avoid spurious peaks. The unbinding events were selected by applying general criteria of specific unbinding events [258,291]). Only events were considered that showed rupture distances d_{rup} in the 5 to 20 nm range to match the length of the PEG27 linker (10 nm ± 5 nm for a slightly shorter PEG24 [258] plus an

uncertainty of 2 nm due to the indentation of the avidin layer [288]). Furthermore, in each curve only the last specific unbinding event is analyzed to exclude the influence of multiple and spurious unbinding events. All the selected SMFS curves and the corresponding specific unbinding events can be individually displayed and visually inspected to rule out false positives. A total of 846 curves showed features ascribed to specific unbinding events, *i.e.*, a fraction of 27.3 %. This is in agreement with former avidin-biotin studies [288,292].

Loading rate

The loading rate r has been determined in two ways. First, it can be calculated by multiplying the effective force constant of the system, k_{eff},with the pulling speed, v_{p},

$$r = k_{\mathrm{eff}} v_{\mathrm{p}} \tag{6.8}$$

For a triangular waveform, the pulling speed is constant and defined by $v_{\mathrm{p}} = A_{\mathrm{p}} f_{\mathrm{p}}$, where A_{p} and f_{p} are the waveform's amplitude and modulation frequency, respectively. In this case, Equation 6.8 reads $r = 2k_{\mathrm{eff}} A_{\mathrm{p}} f_{\mathrm{p}}$. The effective spring constant of the cantilever-PEG system can be obtained from the force versus distance data. It is equivalent to the slope of the retraction curves before the jump-off-contact (see Figure 6.4d). In this way, an average value of $k_{\mathrm{eff}} = 7.32$ pN/nm was obtained. From this value, the linker stiffness can be calculated, because the AFM cantilever and the PEG linker represent a system of two springs in series [249]:

$$k_{\mathrm{PEG27}} = \frac{k_0 k_{\mathrm{eff}}}{k_0 - k_{\mathrm{eff}}} \tag{6.9}$$

A value of $k_{\mathrm{PEG27}} = 9.8$ pN/nm is obtained.

Alternatively, the effective loading rate can be obtained from the force versus time data. The curve's slope just before the unbinding event is equivalent to r (see Figure 6.4c). Both approaches gave similar values. The obtained loading rates are summarized in **Figure 6.5**.

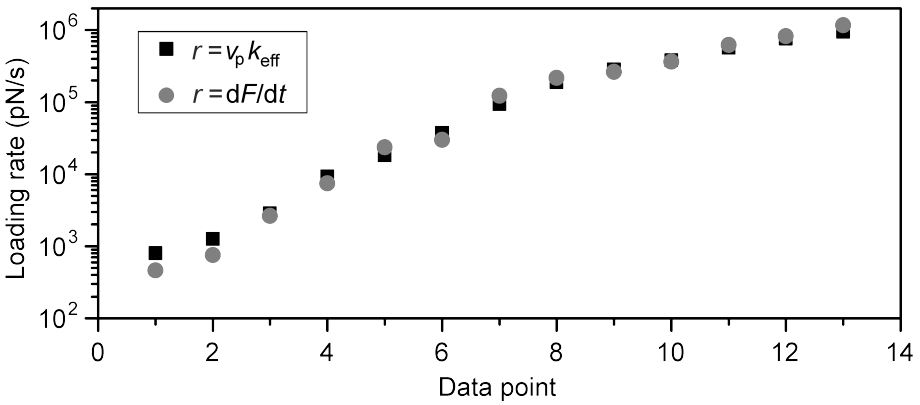

Figure 6.5.: Two ways of determining the loading rate. First, by multiplying the pulling speed with the effective force constant of the system (black squares). Second, by fitting the force versus time data just before the unbinding event (gray circles). Adapted from [114].

6.3.2. Results

For investigating the Newton dynamics effects, it is necessary to choose a well-known reference system in order to identify deviations from the expected behavior. The prototype ligand-receptor system in SMFS is the biotin-avidin complex that has been well-characterized experimentally [5,247–249,262,288,292,293] and by MD simulations [247, 294].

Here, AFM SMFS experiments were performed with a biotin-functionalized tip using an avidin monolayer as the sample [288]. As an example of the obtained data, **Figure 6.6**a shows the retraction part of a force-distance curve for a pulling speed of $v_\mathrm{p} = 4000\,\mathrm{nm/s}$. Upon tip withdrawal, an increasing attractive force is observed. Then, at a certain tip-sample distance d_rup, the force jumps abruptly back to the baseline (zero force). Such a feature is the signature of a single unbinding event: First, the polyethylene glycol (PEG27) linker is stretched leading to the typical nonlinear force [288, 295]. The increasing force is sustained by the biotin-avidin bond, until it eventually breaks at a distance of $d_\mathrm{rup} = 14.0$ nm and a measured force of $F_\mathrm{m} = 135$ pN. The force F necessary to stretch the PEG27 linker over a distance d can be described by polymer extension models, such as the freely jointed chain (FJC) model

$$d(F) = L_\mathrm{C}\left[\coth\left(\frac{Fl_\mathrm{K}}{2k_\mathrm{B}T}\right) - \frac{2k_\mathrm{B}T}{Fl_\mathrm{K}}\right] \tag{6.10}$$

where L_C is the contour length and $l_\mathrm{K} = 0.70$ nm the Kuhn length of the PEG27 linker [36,258,295]. Fitting Equation 6.10 to the data (shown in blue) yields $L_\mathrm{C} = 14.82$ nm. This length is within the expected range for a PEG27 linker ($10\,\mathrm{nm} \pm 5$ nm for a slightly shorter PEG24 [258]), which confirms that the event is caused by a specific biotin-avidin unbinding process.

The acquisition of such force-distance curves was then repeated at a variety of different pulling speeds, v_p, and each time F_m was extracted from the data. The number of individual force-distance curves varied between 100 and 600 for each pulling speed, of which on average 27 % showed specific biotin-avidin events. Figure 6.6b illustrates some representative force curves taken at different pulling speeds. For each value of v_p, a distribution of force values is measured as it is expected for a thermodynamically activated process (see below). To emphasize the trend, in Figure 6.6b one force distance curve is displayed for each speed whose F_m value corresponds roughly to the distribution's average. For low to moderate pulling speeds, the force increases with the speed. At $v_\mathrm{p} = 3 \cdot 10^4$ nm/s the measured force reaches a maximum and then decreases upon further increase of v_p. The actual distributions can be seen in Figure 6.6c. The trend can be also clearly seen in the histograms. Additionally it becomes clear that the histogram's width increases with increasing pulling speed, as observed previously [247].

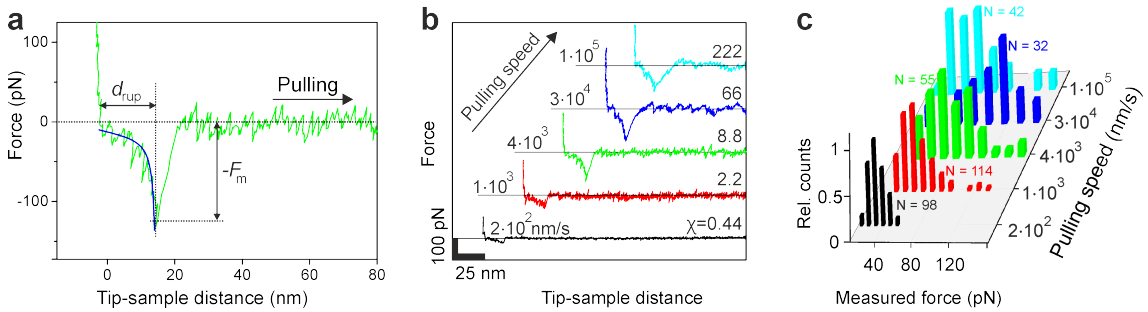

Figure 6.6.: AFM-based SMFS experiments on biotin-avidin. **a.** A force-distance curve showing a specific avidin-biotin unbinding event. The stretching of the PEG27 linker molecule is fitted by the freely jointed chain model (FJC) (shown in blue). **b.** Force-distance curves acquired at different pulling speeds. F_m increases with the pulling speed until a certain threshold is reached. From then on the value of the measured force decreases with increasing pulling speed. **c.** Force histograms of biotin-avidin bonds reveal a maximum in the mean value of F_m as a function of the pulling speed. The panel depicts the number of specific unbinding events N used to build the histograms. Adapted from [114].

For quantitative analysis, it is necessary to transform the pulling speeds into loading rates as explained above (see Figure 6.5). **Figure 6.7** shows the averaged measured force $F_m^*(r) =< F_m(r) >$ for all the loading rates r that were applied during the experiment. The data is displayed in a semi-log plot, *i.e.*, data that follows the Bell-Evans law appears as a straight line. The slope of the force as a function of the loading rate shows three different regions. From $\approx 10^3$ to $\approx 10^4$ pN/s, the measured force grows linearly with the logarithm of the loading rate. Between $\approx 10^4$ and $\approx 10^5$ pN/s, the increase is still linear but the slope is larger, leading to a kink in the data at $r \approx 10^4$. For loading rates $\gtrsim 10^5$ pN/s, the measured force shows a decrease with the rate.

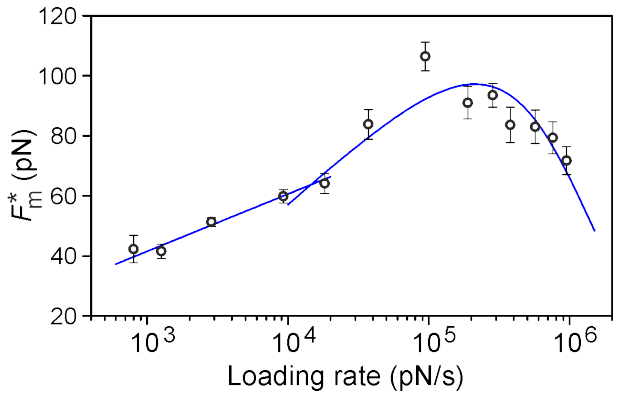

Figure 6.7.: The mean value of the measured force F_m^* is shown as a function of the loading rate r. The data shows three different slopes. The first two (from low to high loading rates) are related to different energy barriers within the bond's energy landscape. The last slope is negative, indicating that other force components dominate the measured net force. Error bars represent the standard error of the mean. Adapted from [114].

The existence of multiple linear regions was observed before in SMFS experiments on biotin-avidin [247, 249, 292, 296] and is associated with the existence of different energy barriers within the energy landscape. [247, 249, 256, 292] Simplified speaking, different loading rate regimes tilt the energy landscape to different extends which makes, for a given loading rate, one energy barrier more relevant than the others. The biotin-avidin bond is known to have (at least) three such activation barriers [247]. The observed negative slope, however, cannot be explained by the Bell-Evans model nor by more sophisticated models [279, 280, 297]. Instead, as suggested by Reference [111], the decrease in force is attributed to the generation of dynamic forces by the cantilever during the rupture of the molecular bond. In the following, an equation of motion (EOM) for the cantilever will be developed to verify this idea. The derivation of the equations can be found in detail in Reference [114].

To describe the dynamics of the pulling device, the tip-linker-bond system can be approximated by a 1D model [298]. It was shown that the Euler-Bernoulli equation under the application of force at its free end becomes the Newton equation for a point-mass model [299]. The general EOM for this system is

$$F_{\mathrm{ts}}(d(t), \dot{d}(t)) = k_0 z + \frac{m^* \omega_{\mathrm{r}}}{Q} \dot{z} + m^* \ddot{z} \tag{6.11}$$

with

$$d(t) = z_{\mathrm{c}} + \Delta z(t) + A_{\mathrm{p}} g(\omega_{\mathrm{p}} t) \tag{6.12}$$

where F_{ts} is the instantaneous tip-sample force, $f_{\mathrm{r}} = \omega_{\mathrm{r}}/2\pi$ is the cantilever's resonance frequency, Q its quality factor, z_{c} the average probe height and Δz the cantilever deflection. The function $g(t)$ is the distance modulation (in this case triangular) characterized by its amplitude, A_{p}, and frequency, $f_{\mathrm{p}} = \omega_{\mathrm{p}}/2\pi$. Equation 6.11 shows that the tip-sample force contains the cantilever deflection and two additional terms that express the

hydrodynamic and inertial and forces acting on the moving cantilever. When the bond is breaking, the tip-sample force is given by the rupture force, $F_{\mathrm{ts}} = F_{\mathrm{rup}}$. However, what is actually measured in SMFS is $F_{\mathrm{m}} = k_0 \Delta z_{\mathrm{rup}}$, neglecting the two remaining terms. As shown by Equation 6.11, in general $F_{\mathrm{rup}} \neq F_{\mathrm{m}} = k \Delta z_{\mathrm{rup}}$. In the following, some results from computer simulations are discussed in order to understand which role the additional force components play. **Figure 6.8** summarizes the main outcomes of the simulations.

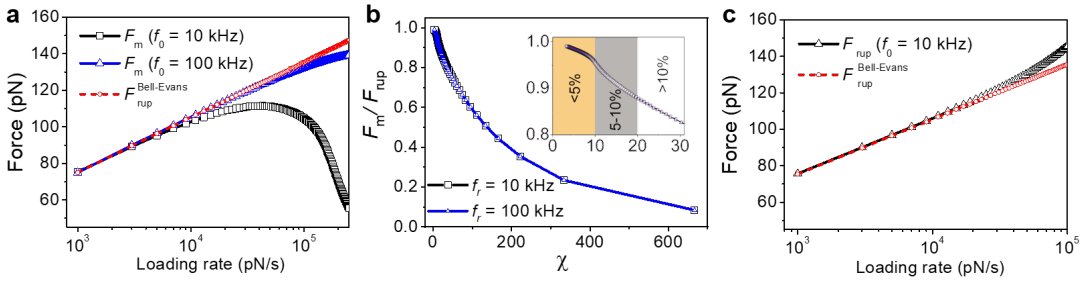

Figure 6.8.: Figure 3. Simulations of the ligand-receptor bond strength spectrum. **a.** Force dependence on the loading rate obtained by solving Equation 6.11 for cantilevers with $f_{\mathrm{r}} = 10$ kHz (black squares) and with $f_{\mathrm{r}} = 100$ kHz (blue triangles). By increasing the resonance frequency of the cantilever, the deviation between F_{m} and F_{rup}at high rates is reduced. **b.** Ratio between the measured and the rupture force as a function of the frequency ratio χ for both cantilevers. The inset shows the relative error for selected ranges of frequency ratios. **c.** Comparison between the rupture force and the corrected rupture force for the cantilever characterized by $f_{\mathrm{r}} = 10$ kHz after using the correction factor $N(r)$. Simulation parameters: $f_{\mathrm{r}} = 10$ kHz (black squares), $f_{\mathrm{r}} = 100$ kHz (blue triangles), $k_0 = 20$ pN/nm, $x_\beta = 0.138$ nm, $K_{\mathrm{off}}^0 = 12.2\mathrm{s}^{-1}$, $A_{\mathrm{p}} = 250$ nm, $Q = 1$. The simulations were performed by Dr. Carlos Álvarez Amo. Adapted from [114].

Figure 6.8a compares the force obtained by taking into account the deflection, $F_{\mathrm{m}} = k \Delta z_{\mathrm{rup}}$, to the actual rupture force provided by Equation 6.5. The measured force is simulated by solving the EOM (Equation 6.11). The left side of the EOM is approximated by using an exponential expression [114]:

$$F_{\mathrm{ts}}(d,r) = \begin{cases} -F_{\mathrm{rup}}(r) \frac{e^{\alpha d}-1}{e^{\alpha d_{\mathrm{rup}}}-1}, & d \leq d_{\mathrm{rup}} \\ 0, & d > d_{\mathrm{rup}} \end{cases} \tag{6.13}$$

where α is parameter related to the stretching of the linker. This approximation will later allow to solve the EOM analytically (see below). A comparison between the approximation and the FJC model is shown in the Appendix (Figure C.1). The rupture force F_{rup} is calculated from the Bell-Evans law (Equation 6.5) using $x_\beta = 0.138$ nm and $K_{\mathrm{off}}^0 = 12.2\,\mathrm{s}^{-1}$. The simulations are performed for two different cantilevers with $f_{\mathrm{r}} = 10$ and 100 kHz (shown in black and blue squares, respectively). The Bell-Evans model serves as a reference, providing a linear increase of the rupture force with the logarithm of the loading rate (red squares). The forces obtained by solving the EOM are indistinguishable from the Bell-Evans model, as long as the loading rates are small

enough. For larger loading rates, the curves start to deviate from the Bell-Evans model. This happens at different loading rates for the two cantilevers. For the one with $f_\mathrm{r} = 10\,\mathrm{kHz}$, the curves depart above $r \approx 10^4$ pN/s. For $f_\mathrm{r} = 100\,\mathrm{kHz}$, the curves depart above $r \approx 10^5$ pN/s. Below the stated rates, the Hook's law is a reasonable approximation. Above them, however, the inertial and hydrodynamic contributions start to dominate the cantilever deflection. By comparing the two contributions to each other, it becomes clear that the hydrodynamic contribution quantitatively largely dominates. Nevertheless, the inertial component is taken into account because it provides the physical behavior of the cantilever such as overshooting or ringing effects, thereby confirming the validity of the simulations [111].

Cantilevers with higher resonance frequencies extend the loading rate range where the curves overlap towards higher loading rates. It is desirable to find a general criterion for the position of this transition. Earlier it was suggested to use the ratio between the resonance frequency of the cantilever and the modulation frequency, $\varpi = \frac{f_\mathrm{r}}{f_\mathrm{p}}$ as a criterion [111]. Indeed, it is not an uncommon practice to refer to the modulation frequency instead of the pulling speed, in particular when a sinusoidal modulation is used [36,276]. However, using the modulation frequency is impractical here, because it alone does not define the pulling speed unequivocally. A suitable parameter can be found by rewriting the EOM (Equation 6.11). For a monotonic probe displacement ζ it can be written

$$F_\mathrm{ts}(\zeta) = k_0 z(\zeta) + \frac{k_0 x_\mathrm{c\text{-}c}}{Q}\chi\frac{\mathrm{d}z}{\mathrm{d}\zeta} + k_0 x_\mathrm{c\text{-}c}^2\chi^2\frac{\mathrm{d}^2 z}{\mathrm{d}\zeta^2} \tag{6.14}$$

where χ is the ratio between the pulling speed and the resonance frequency of the cantilever

$$\chi = \frac{v_\mathrm{p}}{f_\mathrm{r} x_\mathrm{c\text{-}c}} \tag{6.15}$$

In order to provide a dimensionless definition of χ, a normalization by the mean carbon-carbon distance in an amino acid chain, $x_\mathrm{c\text{-}c}$, was introduced. The hydrodynamic and inertial components in Equation 6.14 exhibit, respectively, a linear and quadratic dependence on the frequency ratio χ. Figure 6.8b shows the dependence of the ratio $F_\mathrm{m}/F_\mathrm{rup}$ as a function of χ. For small frequency ratios ($\chi \approx 1$) the measured force coincides with the value of the rupture force. For higher χ values, the measured force underestimates the value of the rupture force. For example, $\chi = 10$ corresponds to a relative error $(F_\mathrm{rup} - F_\mathrm{m})/F_\mathrm{rup}$ of 4.5 % while for $\chi = 15$ and 60, the relative errors are ≈ 9 % and ≈ 30 %, respectively. Figure (6.8b) emphasizes that χ is a suitable criterion because the data for the two cantilevers overlap, although the resonance frequencies are different by a factor of 10.

Since the additional terms arising from the Newton dynamics cannot be neglected in general, a model was developed that incorporates these contributions into the Bell-Evans framework. With the exponential approximation in Equation 6.13 for the stretching of the linker, the EOM can be analytically solved and yields [114]:

$$F_\mathrm{rup}^* = k_0 z_\mathrm{rup}\left[1 + (\frac{r\alpha}{k_\mathrm{eff} f_\mathrm{r}})^2 + \frac{r\alpha}{k_\mathrm{eff} f_\mathrm{r} Q}\right] \tag{6.16}$$

The above equation enables to split up the rupture force F^*_{rup} in two factors $F^*_{\mathrm{rup}} = F^*_{\mathrm{m}}(r)N(r)$, where the first factor corresponds to the measured force and the second one summarizes the contributions that arise from the Newton dynamics. By rearranging the equation and replacing F^*_{rup} by the Bell-Evans equation (Equation 6.5), one obtains

$$F^*_{\mathrm{m}}(r) = \frac{F^*_{\mathrm{rup}}}{N(r)} = \frac{\frac{k_{\mathrm{B}}T}{x_\beta} \ln\left[\frac{r x_\beta}{K^0_{\mathrm{off}} k_{\mathrm{B}} T}\right]}{1 + (\frac{r\alpha}{k_{\mathrm{eff}} f_{\mathrm{r}}})^2 + \frac{r\alpha}{k_{\mathrm{eff}} f_{\mathrm{r}} Q}} \tag{6.17}$$

The resulting equation can be fitted to the data shown in Figure 6.7. The fit clearly describes the trend of the data (shown by the blue line) and already serves for extracting the fit parameters K^0_{eff} and x_β. However, instead of modifying the Bell-Evans equation, $N(r)$ can also be understood as a correction factor for the data. First, this will be demonstrated using the results from the simulations. By multiplying the simulated F^*_{m} from Figure 6.8a ($f_0 = 10$ kHz) with $N(r)$, the expected values of the rupture force are closely recovered for higher loading ratios (Figure 6.8c). In other words, the multiplication transforms the F_{m} values into F^*_{rup} values that can be introduced directly into the original Bell-Evans law. Consequently, the correction factor was applied to the experimental data shown in Figure 6.7. The obtained values are shown in **Figure 6.9** (red data points). For low loading rates, the corrected values almost coincide with the measured ones (gray data points). However, with increasing r, the corrected values are increasingly larger than the raw data. In particular, the corrected values do not show a decrease for high loading rates. Instead, two regimes with a linear behavior are revealed.

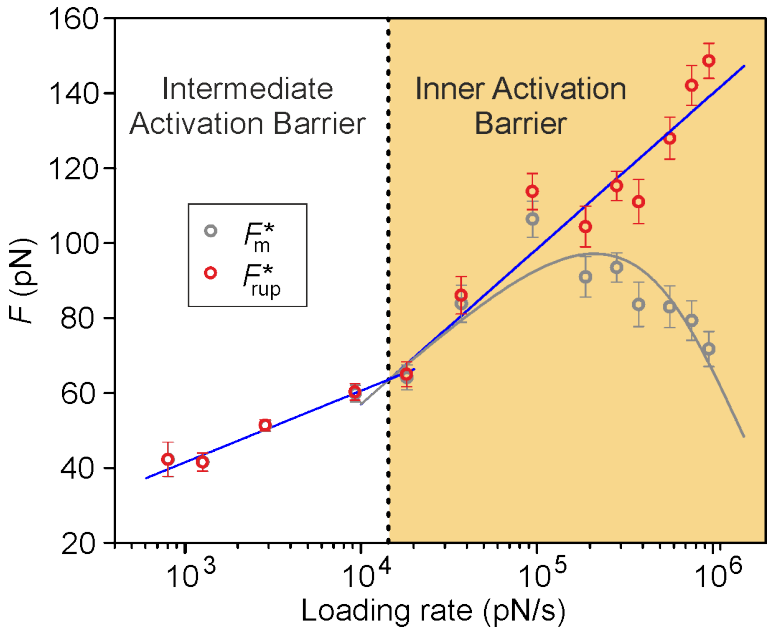

Figure 6.9.: Correction of the measured force values by the application of the factor $N(r)$. The raw data points (F^*_{m}) are shown in gray. The resulting forces after the correction, F^*_{rup}, exhibit two regimes with a linear behavior (red data points). The two regimes can be associated with the intermediate (for low loading rates) and the inner activation barrier (for higher loading rates) of the biotin-avidin bond's energy landscape. The Bell-Evans model is fitted to both regimes individually (blue lines). The fit parameters corresponding to the intermediate and inner activation barrier are, respectively, $x_\beta = 0.5 \pm 0.06$ nm and $K_{\mathrm{off}} = 0.8 \pm 0.54\,\mathrm{s}^{-1}$, and $x_\beta = 0.226 \pm 0.053$ nm and $k_{\mathrm{off}} = 23.6 \pm 19.9\,\mathrm{s}^{-1}$. Error bars represent the standard error of the mean. Adapted from [114].

The biotin-avidin bond is known to have (at least) three activation barriers: The outer, the intermediate, and the inner one [247]. The transition between the two slopes in Figure 6.9 is observed at $r \approx 2 \cdot 10^4$ pN/s. Comparing this value to biomembrane force probe (BFP) [247] and AFM SMFS [292] measurements on the same system, the two observed regimes can be associated with the intermediate (for lower loading rates) and the inner activation barrier (for higher loading rates). The previously observed outer activation barrier is not probed by the experiments performed here. In order to access that energy barrier, loading rates one to two orders of magnitude lower than the ones used here are necessary [247, 292]. By fitting the unmodified Bell-Evans model to the corrected forces, both regimes are described well (Figure 6.9). For the low-r regime, the fitting provides the bond parameters $x_\beta = 0.5 \pm 0.06$ nm and $K^0_{\mathrm{off}} = 0.8 \pm 0.5\,\mathrm{s}^{-1}$, corresponding to the intermediate energy barrier [247]. For the high-r regime, the fit yields $x_\beta = 0.23 \pm 0.05$ nm and $K^0_{\mathrm{off}} = 24 \pm 20\,\mathrm{s}^{-1}$, in agreement with the characteristics of the inner activation barrier [247]. The kinetics parameters are within the range of values obtained in other SMFS experiments on the same system [247, 249, 292].

Discussion

The experimental determination of the rupture of a bond in the presence of an external mechanical force is controlled by the thermal activation on one hand and by the cantilever dynamics on the other hand. For frequency ratios $\chi < 1$, which for standard-sized and sufficiently soft cantilevers ($f_r = 1 - 10$ kHz in liquid) means loading rates below 10^4 pN/s, the inertial and the hydrodynamic contributions to the force are negligible and the measured force coincides with the rupture force predicted by the Bell-Evans theory. For frequency ratios above 10, which for the same type of cantilever is equivalent to loading rates of 10^5 pN/s, the experimental data shows that the measured force decreases with the loading rate. This dependence is confirmed by the theory that states that inertial and hydrodynamic contributions are significant for frequency ratios above 10. For frequency ratios above 60, the additional contributions dominate the measured force. The competition between a thermally activated process, mechanical loading and Newton dynamics leads to the observed maximum in the measured force. The above results demonstrate that the forces measured in HS SMFS can be affected significantly by the dynamic behavior of the cantilever. In particular, the hydrodynamic interaction between the cantilever and the fluid plays an important role. There are many force spectroscopy techniques that involve fast cantilever movements, but still these approaches are commonly described with the Hooke's law since they are off-resonance. The validity of such a static approach is limited and it is not clear *a priori* to which extend the postulate is justified. It is, however, well known that the hydrodynamics cause drag forces on the cantilever, which has been addressed by a number of publications for different AFM modes [110, 115, 289, 290, 300, 301]. Mostly, empirical corrections are applied in order to correct for the drag forces and recover the tip-sample interaction. However, the validity of these approaches has not been rigorously demonstrated. One way to navigate around the issue is to use (ultra-)short cantilevers which reduce the hydrodynamic forces strongly. Although this approach shifts the limitations of the static description up to higher velocities, the principle phenomenon remains unchanged (see Figure 6.8b). Furthermore, using ultrashort cantilevers requires special equipment, such as a modified read-out optics [302]. It is thus necessary to correct for the occurring dynamic effects. Empirical hydrodynamic forces associated with the dissipative interactions of the fluid with either the tip and/or the cantilever body have been proposed [115, 290]. In the following, the similarities and differences of the approach developed here in comparison to existing methods will be discussed briefly.

In SMFS, the viscous interaction between the cantilever and the fluid gives rise to two types of hydrodynamic forces. They could be classified into local and extended hydrodynamic forces. A local hydrodynamic force acts on the cantilever due to the dynamics of the tip [301,303] while the latter arises from the net movement of the cantilever body [110,115,289,290,300]. Equation 6.11 contains the local hydrodynamic force acting on the projection of the cantilever at the tip position which is expressed by Q. This local hydrodynamic force is the main reason for the observed deviations between the measured force and the Bell-Evans model at high loading rates, as emphasized by the theory and simulations. The extended hydrodynamic force is commonly called the hydrodynamic

drag force [110,115,289,290,300]. This force is associated with the net movement of the cantilever body and introduces an additional deflection which complicates the determination of the rupture forces (see Figure 6.3) but does not participate in the phenomenon observed here, as explained in the methods section. In 2005, Janovjak *et al.* reported an AFM SMFS experiment on a multi-domain protein at a high pulling speed using a low-resonance frequency cantilever (a situation similar to the one in this chapter) [115]. The authors concluded that the difference in the tip speed with respect to the speed of the cantilever base leads to an apparent reduction of the forces measured during unfolding of the protein. Following the terminology suggested in this section, their experiments were performed with a frequency ratio of $\chi \approx \frac{30\,\mu\mathrm{m/s}}{2000\,\mathrm{s}^{-1}0.15\,\mathrm{nm}} = 100$. Under such conditions, the above model predicts a relative error in the rupture force of 41 % which is close to their findings ($\approx 50\,\%$) [115], indicating that such an empirical approach yields comparable results as the one developed here.

6.4. Molecular Recognition on a Silicon-Nanowire Based Biosensor

As shown in the previous section, one of the main goals of SMFS is to gain insight into the kinetics of a molecular complex. Besides, SMFS is also a powerful tool for local biorecognition [237,238,259,267,304]. As mentioned in the introduction, there is a number of AFM-based techniques available that can obtain topography images simultaneously when performing SMFS [38,39,237,267]. With such techniques, a specific type of molecules that is adsorbed to a surface can be chemically identified and at the same time localized within the surface with single molecular resolution. In this section, SMFS will be applied on a silicon nanowire (SiNW). SiNWs can be used as sensing elements in FET-based ultrasensitive biosensors [305]. As described in Section 4, this kind of sensor is immersed in the testing liquid which is supposed to contain the species of interest [180]. The target molecules then adsorb to the channel surface, where the charge they are bearing produces a gating effect. This modifies the electrical properties of the FET such as the channel conductance leading to a change in the drain-to-source current which can be read out. In order to further increase the sensitivity of such a sensor, it is desirable that the (potentially very few) target molecules adsorb as selectively as possible in the sensitive area of the device. Selective adsorption can be achieved by local functionalizations of the device's sensitive and non-sensitive areas. Here, a SiNW-based FET sensor is investigated that is designed to detect ultralow concentrations of avidin molecules. In order to achieve localized adsorption, the sensitive area of the device (the SiNW's surface) will be functionalized with APTES to promote avidin adsorption. The non-sensitive surroundings of the SiNW, however, will be covered by an octadecyltrichlorosilane (OTS) layer, which prevents adsorption of avidin. FV-based SMFS will be used to verify local adsorption of avidin molecules. At the same time, the approach provides a test if the species has remained bioactive upon adsorption [137]. The experiments were performed in collaboration with Dr. Francisco Miguel Espinosa Barea, who fabricated all the samples and prepared the functionalized cantilevers.

6.4.1. Materials and Methods

Tip and Sample Preparation

The tip functionalization consists of two main steps. First, the silanization of the tips with APTES and, second, the subsequential functionalization with NHS-PEG27-biotin. Phosphate buffered saline (PBS) powder, ethanol, 30% hydrogen peroxide, 3-aminopropyl triethoxysilane (APTES) 99 %, trimethyl amine $\geq$ 99 %, and avidin from egg-white $\geq$ 98 % were purchased from Sigma-Aldrich (Madrid, Spain). The N-Hydroxysuccinimid (NHS)-polyethylene glycol (PEG27) - biotin linkers were purchased from the JKU Linz [288].

Silanization with APTES. Silicon nitride cantilevers (MSCT, Bruker, CA, USA) were cleaned thoroughly by an RCA clean. This procedure consists of three subsequent baths in a mixture of ammonia solution : hydrogen peroxide (30 %) : ultrapure water (1 : 1 : 5 ratio in volume). Then, the cantilevers were rinsed with ultrapure water and dried carefully using a flow of N_2. Afterwards, the cantilevers were exposed to oxygen plasma (Diener Electronic, Germany) for 1 min at a power of 100 W under a pressure of 0.4 bar. Next, the cantilevers were transferred into a mixture of APTES : ethanol (1 : 5000 ratio in volume) initiate the silanization of the tips. After 45 min, the cantilevers were rinsed with ethanol and ultrapure water and dried with N_2. Finally, the cantilevers were placed in a desiccator for 1 h.
Functionalization with PEG-biotin. The functionalization of the cantilevers with NHS-PEG27-Biotin linkers [288] followed the same protocol as described in the previous section.
SiNW. The SiNW were fabricated by oxidation scanning probe lithography (o-SPL) as described elsewhere [306]. Then, three main surface treatments are performed: Covering the sample with an OTS monolayer, functionalizing the SiNW with APTES, and, finally, immobilizing avidin molecules on the APTES layer.

Before the first step (OTS), the sample is exposed to oxygen plasma for 30 s at a power of 50 W under a pressure of 0.4 bar. Then, the sample is immediately immersed in toluene and passed into a glove box with N_2 atmosphere. There, the samples are moved into a solution of toluene with 3 µL of OTS. After 105 s, the sample is returned to the pure toluene bath and ultrasonicated for 10 min. The ultrasonication is repeated subsequently in chloroform, ethanol, and water, and then the sample is dried with a flow of N_2. Finally, the sample is cured for 1 min on a hot plate at 80°C. Now the entire sample is covered in an OTS monolayer. For removing the OTS locally, contact-mode scanning is performed repeatedly within the area of the SiNW. Then, the uncovered area of the sample is functionalized with APTES by transferring the sample into a mixture of APTES : ethanol (1 : 5000 ratio in volume) for 45 min. After rinsing with ethanol and ultrapure water and drying with N_2, the sample is cured for another 30 min on the hot plate. Finally, freeze-dried avidin was dissolved in 1 mM NaCl to obtain a solution with an avidin concentration of 500 pM. 100 µl of the solution were deposited on SiNW sample for 1 min. Afterwards, the sample was rinsed carefully with 1 mM NaCl and subsequently with 20 mM PBS.

Cantilevers and Calibration

Cantilevers of the types MSCT-C and MSCT-D were used for the scanning and the SMFS experiments, respectively. The MSCT-C cantilevers used for scanning were not calibrated. For the cantilevers used for SMFS, the calibration was performed in the same way as described in the previous chapter, *i.e.* by performing a force-distance curve on mica and using the thermal method [13]. The obtained calibration values for the cantilevers used here are $k_0 = 32$ pN/nm (Experiment 1) and $k_0 = 39$ pN/nm (Experiment 2). All parameters are summarized in Table C.1 (Appendix).

AFM Experiments

All the experiments were performed on a NanoWizard III AFM (JPK Instruments AG, Berlin, Germany) equipped with an open liquid cell. The experiments were carried out in 10 mM PBS at pH 7.4 at a temperature of $T = 302$ K. First, the SiNW was localized by contact mode scanning using an MSCT-C cantilever. Then, the position was marked in the optical image from the camera, and the laser spot was moved to the next cantilever on the chip (MSCT-D. The MSCT chip provides 5 different cantilevers in parallel). The new cantilever was then moved to the previously marked position and an SMFS measurement was started without further imaging. This procedure was developed to prevent damage of the tip functionalization due to contact mode scanning of large areas. SMFS experiments were performed in the force volume mode. This enables to later correlate the obtained curves with the topography of the SiNW. The individual curves were acquired by applying a periodic trapezoidal modulation to the cantilever base with an amplitude of $A_\mathrm{p} = 150$ nm. First, the cantilever base is approached to the sample with a constant speed of 200 nm/s until a force of 140 pN is reached. This force value was chosen to avoid damage of the biotin. At this extension, the piezo is held for 200 ms. Then, the cantilever base is retracted with a constant pulling speed of $v_\mathrm{p} = 1000$ nm/s. FV images were performed on different SiNW and covered different areas. For experiment 1 (experiment 2), it consisted of 20×40 (40×60) force curves in an area of 0.5×1.0 µm^2 (1.0×1.5 µm^2), resulting in a total of 800 (2400) force curves.

AFM SMFS Data Analysis

For detecting the specific unbinding events, the same software was used as described in the previous section. In total, < 2 % of the retraction curves exhibited features of specific unbinding events. Due to this low number of curves, the further data processing was performed manually for the selected curves using the JPK Data Processing software. The software fits a FJC model to each curve to detect the unbinding event and reads out the unbinding force F_m. Furthermore, it determines the loading rate r directly from the individual curves by fitting the force versus time data just before the unbinding event.

6.4.2. Results

Figure 6.10a shows the topography maps obtained from the SMFS force volume image. The image shows the SiNW in the center, surrounded by the OTS-covered substrate. Each pixel corresponds to an individual force-distance curve. While most of the retraction curves are featureless (Figure 6.10b), some curves exhibited a specific unbinding event. The positions of these curves are marked in blue and light blue, depending on if the position corresponds to the SiNW, or to the OTS-covered substrate, respectively. Some example curves for both categories are shown in Figure 6.10c-d. In total, 14 out of 800 force-distance curves showed specific events, from which 12 where located on the SiNW or right next to it. The SiNW has a width of approximately 6 pixels in the image, and consequently covers an area equivalent to 240 pixels. Thus, 800 force distance curves correspond to the SiNW. As a consequence, on the SiNW, the chance to obtain a specific unbinding event is 5.0 %, while on the OTS substrate it is < 0.4 %. This clearly proves that the functionalization of the SiNW significantly increases the chance that the target molecule (avidin) adsorbs on the SiNW's surface. The overall rate of recognition (5.0 %) is low in comparison with the previous chapter and the literature (around 27-29 %) [288]. Such a difference can be explained by the degrees of immobilization of the avidin. In the previous chapter, the avidin was physisorbed to mica while here it is bound to the APTES layer which covers the SiNW. The stronger binding to the APTES results in a lower flexibility of the avidin and hence reduces the probability that the biotin can connect to one of the avidin's four binding sites during the moment of contact. In other words, the avidin has lost its bioactivity partially reducing the probability of binding. In any case, the key result here is that the binding probability found on the SiNW is one order of magnitude larger than the one found on the OTS substrate. A second experiment performed on a similar SiNW (Appendix, Figure C.2) confirmed this finding, albeit the selectivity was slightly lower (5.7 % on the SiNW versus 1.0 % on the OTS-covered substrate).

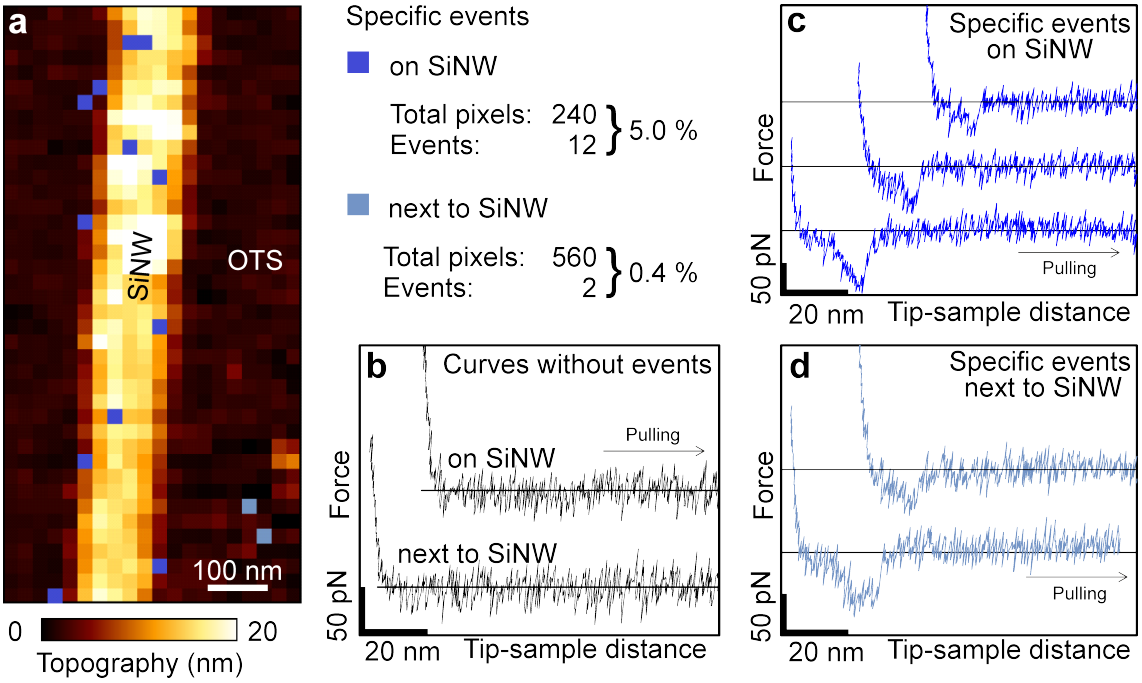

Figure 6.10.: Detection of specific unbinding events on a functionalized silicon nanowire (SiNW) surrounded by an octadecyltrichlorosilane (OTS) layer. **a.** Topography image obtained over the SiNW by force-volume imaging. Each pixel corresponds to an entire force-distance curve. Pixels where specific avidin-biotin events were detected are marked in blue tones (blue: on the SiNW, light blue: next to the SiNW). **b.** Example force-distance curves without events. **c.** Example force-distance curves with specific unbinding events taken on the SiNW. **d.** Force-distance curves with specific unbinding events taken on the OTS layer. The sample was fabricated by Dr. Francisco Miguel Espinosa Barea.

In order to verify the specificity of the observed unbinding events, the two data sets are analyzed quantitatively in the following. **Figure 6.11**a shows the overall distribution of force values. The average measured force, $F_{\mathrm{m}}^{*} = 60.8$ pN, agrees well with reported data obtained with a cantilever of similar stiffness [292] and also with the results presented in the previous chapter. Next, the data will be analyzed by using the Bell-Evans equation. Although both experiments were performed using the same pulling speed, the used cantilevers differed in their stiffness. This leads to different loading rates, since $r = v_{\mathrm{p}} k_{\mathrm{eff}}$. Figure 6.11b shows the two resulting average force values (red stars). For the used measurement conditions, the frequency ratio is given by $\chi = \frac{v_{\mathrm{p}}}{f_{\mathrm{r}} x_{\mathrm{c\text{-}c}}} = \frac{1000\,\mathrm{nm/s}}{3000\,\mathrm{s^{-1}} 0.15\,\mathrm{nm}} \approx 2.2$. This means that the dynamic terms are very small and neglecting them leads to an error of less than 1 % (see Figure 6.8b). Hence, the data can be described correctly by the standard Bell-Evans law. In order to increase the number of data points, it can be useful to plot the individual data points instead of the averaged ones [252,276,307]. Fitting the data points using Equation 6.5 describes the data well (both the average force values and the individual ones). The fit yields $x_{\beta} = (0.21 \pm 0.06)$ nm and $K_{\mathrm{off}} = (21.4 \pm 14.1)$ s^{-1}

which is close to the values obtained previously for the inner activation barrier. Altogether, it can be concluded that the observed features are signatures of specific biotin-avidin unbinding events.

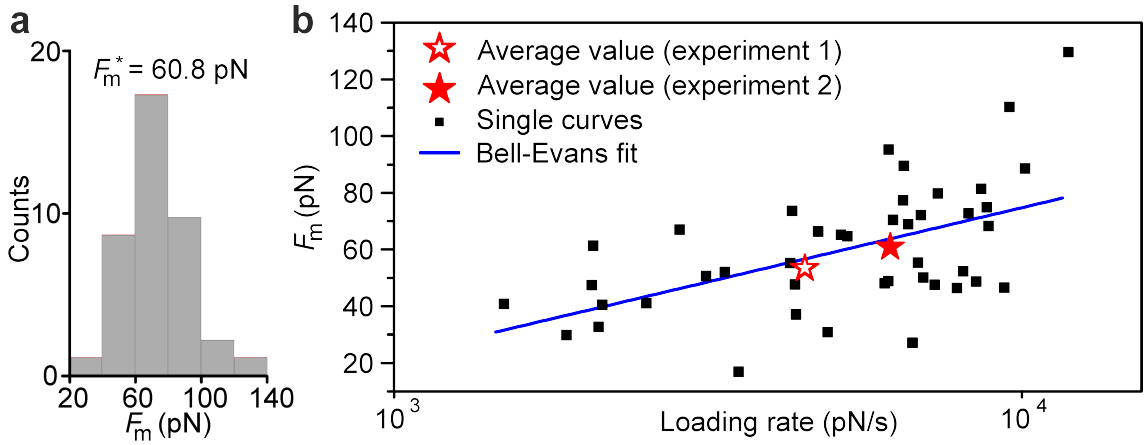

Figure 6.11.: Quantitative analysis of the observed unbinding events. **a.** Histogram of the measured forces F_m with an average value of $F_m^* = 60.8$ pN (data from experiment 2). **b.** Measured forces versus the loading rate. The data from all individual curves is shown (black squares) as well as the averaged values (red stars). The Bell-Evans fit including all black squares is shown in blue. The fit parameters are $x_\beta = (0.21 \pm 0.06)$ nm and $K_{off} = (21.4 \pm 14.1)$ s^{-1}.

The above results confirm that the employed functionalization of the SiNW provides a selective adsorption site for avidin molecules. By having the avidin molecules preferably adsorbed onto the SiNW rather than the substrate, the sensor device's sensitivity for avidin at an ultra-low concentration is enhanced.

6.5. Force Spectroscopy on an Individual IgG Antibody

In the previous sections, force spectroscopy was used in a pulling manner in order to gain insight into the characteristics of a receptor-ligand bond. On the other hand, by pushing instead of pulling, the AFM can serve as a nanoscale indenter to directly probe local mechanical properties down to the level of single molecules [23, 240, 261, 271, 272, 308]. The flexibility of a protein allows for conformational changes and hence is closely related to its biological functions such as binding to antigens or ligands [269, 270]. Measuring the flexibility of proteins has been addressed by a number of researchers due to its potential influence on protein stability, function and activity [309]. Among the AFM based methods, static [261, 272, 274, 275, 310] and dynamic [233, 271, 273, 311, 312] approaches were used to quantify nanomechanical properties of proteins at the single-molecule level. One class of proteins that has been investigated by AFM is formed by the immunoglobulin (Ig*) antibodies [137, 271–273, 313, 314]. In particular, some of their nanomechanical properties have been addressed [271–273]. Recently, the stress-strain curve of a single IgM

antibody was reconstructed from AFM measurements (shown in **Figure 6.12**a). [273] The class of immunoglobulin antibodies plays a major role in the immune system of mammals, among them the aforementioned pentameric IgM, but in particular the variety IgG [315]. IgG is a glycoprotein complex formed by four peptide chains arranged in a characteristic Y-shape. Figure 6.12b shows the secondary structure of an IgG molecule. The Y-shape gives rise to three protein arms, namely the left and right antigen-binding fragments (Fab), and the crystallizable fragment Fc. When deposited on a substrate, IgG antibodies adsorb in different configurations, depending on the environment and the antibody-substrate interactions [137, 259]. If the antibody adsorbs with all three fragment onto a substrate (Figure 6.12b), the configuration is referred to as flat-on. Here, the nanomechanical properties of IgG proteins adsorbed in the flat-on configuration are addressed on the single-molecule level using AFM force spectroscopy and MD simulations. This section was developed in collaboration with Prof. Rubén Pérez and Dr. J. Guilherme Vilhena (Universidad Autónoma de Madrid) who developed and performed the MD simulations.

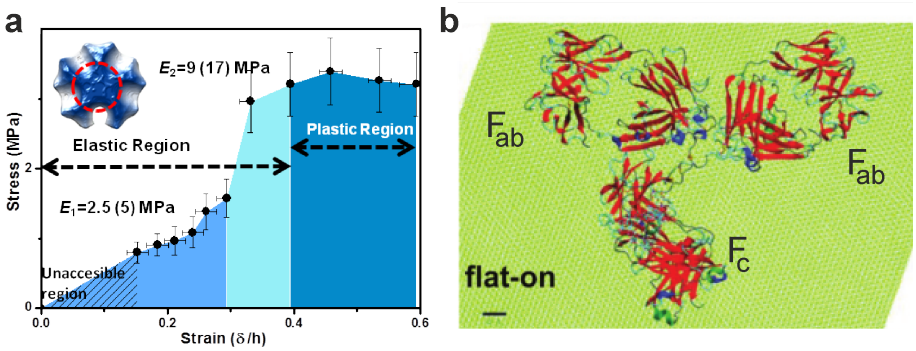

Figure 6.12.: a. Stress-strain curve of an individual IgM antibody determined from dynamic AFM measurements. **b.** Secondary structure of an IgG molecule adsorbed in the flat-on configuration onto graphene. Panels a and b adapted from Reference [273] and [137], respectively.

6.5.1. Materials and Methods

Sample Preparation

A concentrated solution of IgG antibodies was purchased at Sigma Aldrich. The stock solution was diluted in 0.02 M PBS to a concentration of 1 µg/1 ml. First, a droplet containing 10 µL $NiCl_2$ solution was deposited on a freshly cleaved mica sheet for 10 s, followed by injection of 15 µL of the dilute antibody solution. Adding a low molarity solution of divalent metal ions enhances the adsorption of antibodies to the negatively charged mica surface [314,316]. After 30-60 s (depending on the desired surface coverage), the sample was rinsed with the imaging buffer (ultra-pure water or 0.02 M PBS) in order to remove non adsorbed proteins and subsequently it was mounted in the microscope. Some samples were prepared by Dr. Alma Eva Perez Perrino.

Cantilevers and Calibration

The cantilevers used for AM-AFM imaging and QI mode^{TM} imaging, respectively, were FastScan D (Bruker, Ca, USA) and BioLever Mini AC40TS (Olympus, Japan). Cantilevers were calibrated as described in the previous chapter, *i.e.* by performing a force-distance curve on mica and using the thermal method [13]. The obtained calibration values for the cantilevers used here are summarized in Table C.1.

AFM Experiments

2D-AFM imaging. AFM images were obtained in the amplitude modulation (AM) mode scanning by exciting the first mode of the FastScan D cantilever. The excitation was realized by the photothermal drive laser. The free amplitudes A_0 were typically in the range of 2-4 nm, with an amplitude set-point ratio of $A_{sp}/A_0 = 60 - 90\,\%$. The measurements were performed in a MultiMode AFM equipped with a NanoScope V controller (Bruker, Ca, USA). The AFM was modified with a home-built AFM head equipped with photothermal drive, a laser focusing optics for small cantilevers, and an open liquid cell [302]. The samples were mounted magnetically to the scanner by using a mica sheet glued on a steel plate. Care was taken that the droplet always covered the sample by injecting imaging buffer through perfusion openings.

Force spectroscopy. The experiments were performed in a NanoWizard III AFM (JPK Instruments AG, Berlin, Germany) equipped with an open liquid cell. The mica discs were glued on a glass Petri dish which was mounted in the AFM. Then, the Petri dish was filled with imaging buffer. A fast force volume technique, denominated as Quantitative Imaging (QI) mode^{TM}, was used for obtaining static force spectroscopy curves and height maps of individual antibodies. QI mode^{TM} is similar to force spectroscopy but with a piezo movement that is optimized for fast and high-resolution nanomechanical mapping. The optimization includes a smoothing of the upper turnaround point of the z-motion in order to prevent cantilever ringing. Furthermore, the data is taken only when the lateral movement is performed from right to left in order to reduce the effects of piezo creep. The individual curves were acquired by applying an approximately triangular modulation to the cantilever base with an amplitude of $A_p = 25$ nm and a frequency of $f_p = 200$ Hz, corresponding to a piezo velocity of 10 µm/s. The maximum force was limited to 100 pN. QI mode^{TM} images covered areas between 100×100 nm^2 and 250×250 nm^2, containing between (64×64) and (256×256) individual force curves, resulting in a total of 4096 - 65536 force curves per image.

AFM SMFS Data Analysis

An algorithm was written in MATLAB (MathWorks, MA) to process the QI data. The algorithm transforms force-displacement data into force-distance data by applying Equation 1.5. Next, the contact point ($d \equiv 0$) was determined as the closest tip-sample distance where the force crosses the zero. Afterwards, different quantities are computed from the individual force curves and maps are reconstructed from the values and their respective xy positions. Indentation maps are calculated by reading out the tip-sample distance

at $F = 100$ pN and multiplying the resulting values by -1 (negative tip-sample distances are defined as positive indentations). Maps of the relative deformation are calculated by dividing the indentation map by the topography map. Interaction stiffness maps are calculated by fitting a linear function to the contact part of the force-displacement data. Alternatively, the fit could be performed using the force-distance data, in order to obtain k_{sample} instead of k_{ts}.

MD Simulations

Atomistic MD simulations were performed to simulate indentation into an individual IgG antibody. The molecule is adsorbed in the flat-on orientation onto a slab of three-layer graphene [137]. A diamond half-sphere with a radius of 2 nm was used as the AFM tip. The liquid environment was simulated using an explicit solvent (water molecules) which preserves the proteins structure upon adsorption. Altogether, the MD system contains the protein (25000 atoms), the AFM tip (3000 atoms), the substrate surface (50000 atoms), and 570000 water molecules. Atom-atom interactions were described according to the AMBER force field and the MD trajectories were calculated using the AMBER simulation [145, 317]. The indentation was simulated for a temperature $T = 300$ K, a total time of $t = 150$ ns and a tip speed of $v = 0.1$ m/s. The MD simulations were developed and performed by Dr. J. Guilherme Vilhena and Prof. Dr. Rubén Pérez (Universidad Autónoma de Madrid).

6.5.2. Results

When IgG antibodies are deposited on a substrate, the individual molecules adsorb in at least 4 different adsorption orientations [137]. The particular adsorption orientation influences the protein's bioactivity and plays an important role in sensing applications [258]. Here, the orientation of interest is the flat-on configuration, which is advantageous for studying the nanomechanical properties of the three IgG fragments by indentation. In AM-AFM images in 0.02 M PBS, individual adsorbed of IgG antibodies are observed that assume a variety of conformations (**Figure 6.13**a) as observed previously [258,314]. While some of the molecules appear as globular structures, some others (marked by white arrows) exhibit the Y-shape indicative for the flat-on adsorption. Figure 6.13b-c shows some detail images taken by scanning individual IgG antibodies adsorbed in the flat-on configuration in different environment (water and PBS). Cross sections taken along the lines marked in the panels b and c reveal that the apparent antibody dimensions depend on the imaging buffer. In water, the width a maximum height of the molecule is 20 nm and 2.4 nm, respectively, while in PBS the numbers are 24 nm and 4.0 nm. A comparison with the literature confirms that the values measured in PBS are close to the ones measured by Yamada's group (4 nm of height in 0.01 M sodium acetate buffer) [314]. This observation can be readily explained by electrostatic forces [165,223]. In pure water, the different surface charges of the mica and the antibody give rise to different electrostatic forces, preventing direct contact of the tip with the respective surfaces. In PBS, the electrostatic forces are screened-out due to the presence of ions,

and the tip measures the molecule's height correctly and with high-resolution [223,318]. Tip-induced deformation [273] can be ruled out as the source of the height difference since the applied force was higher in the case of water in comparison with the case of PBS (measurement in water: $k_1^{\text{nom}} = 0.09$ N/m, in PBS: $k_1^{\text{nom}} = 0.25$ N/m, both: $A_0 \approx 2$ nm, $A_{\text{sp}} \approx 0.80$ A_0). The Fc-fragments appear lower in the height profile than the Fab fragments (black profile in panel e) which has been observed previously in the literature [314] and could be related with a higher flexibility of the Fc fragment.

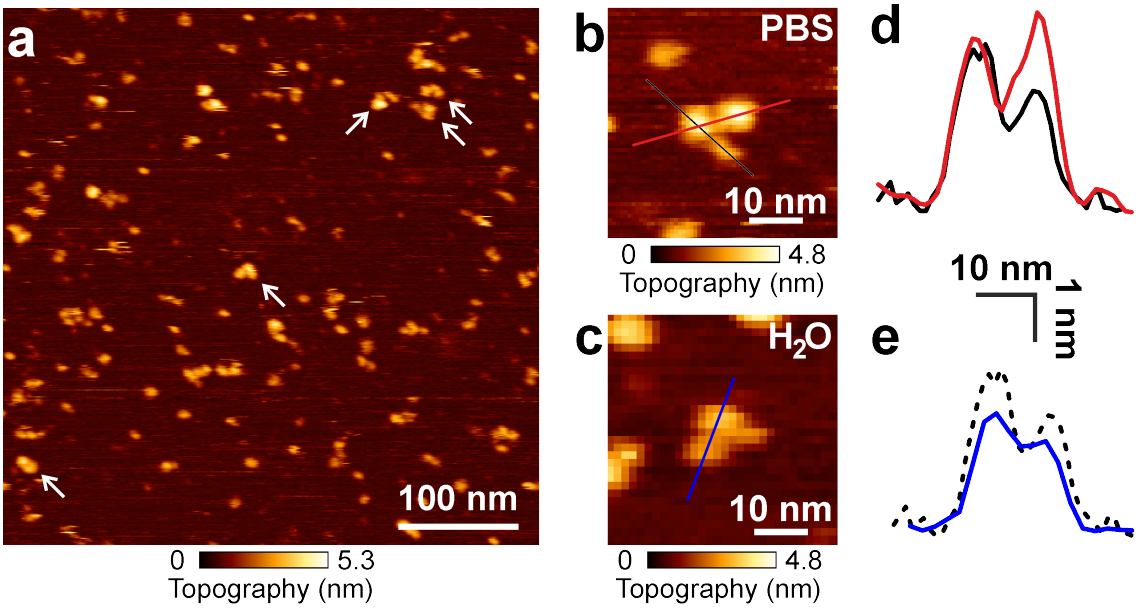

Figure 6.13.: AM-AFM height images of IgG molecules in buffer solution adsorbed on mica. **a.** Overview scan showing IgG molecules in a variety of adsorption orientations. Molecules adsorbed in the flat-on configuration are indicated by white arrows. **b.** AM-AFM height image of a single IgG molecule (flat-on) in water. **c.** AM-AFM height image of a single IgG molecule (flat-on) in 0.02 M PBS. **d.** Height profile obtained from panel b (blue). The black dashed line depicts a cross section obtained in PBS and serves as comparison. **e.** Height profiles obtained from panel c.

In order to obtain nanomechanical information about individual IgG molecules, JPK QI mode$^{\text{TM}}$ images were recorded in areas like the one shown in Figure 6.13a. In contrast to images obtained by scanning, the QI mode$^{\text{TM}}$ records force spectroscopy curves at sequential xy positions across the surface, very similar to force-volume images. **Figure 6.14**a shows a detail of such a height map (containing 1225 individual force curves) depicting a single IgG antibody adsorbed in the flat-on configuration. Panel b shows two cross sections determined from the image. The maximum height of 3.7 nm is close to the value measured in the AM-AFM scan shown above. Two of the force curves are provided in panels c and d (corresponding to the mica substrate and the IgG, respectively). The curve recorded above the mica substrate exhibits a steeper slope in the contact part

compared with the one obtained on the IgG. In the following, the differences between the curves will be quantified.

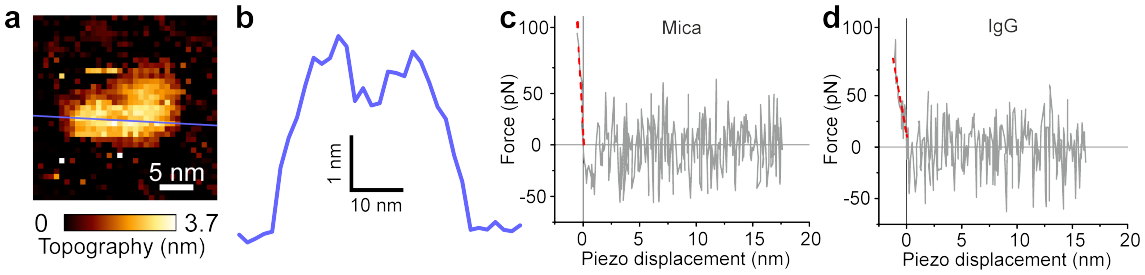

Figure 6.14.: Force spectroscopy (QI) measurements on an IgG molecule in 20 mM PBS adsorbed on mica. **a.** Detail of a height image, comprised of 1225 force curves. **b.** Height profile obtained along the blue line marked in panel a. **c.** Example force-displacement curve measured above the mica substrate. **d.** Example force-displacement curve measured above the IgG. Red dashed lines are linear fits to the data for determining the interaction stiffness.

A custom software was written in order to extract and analyze the individual force curves and create maps of the determined quantities. **Figure 6.15**a shows a map of the maximum indentation (at $F = 100$ pN) extracted from $F - d$ curves. The antibody appears darker than the surrounding mica substrate because the tip indents farther on the antibody than on the mica, indicating the antibodies lower Young's modulus. On average, the indentation on the antibody reaches around 0.4 -0.6 nm when a force of 100 pN is applied. To further quantify the molecules stiffness without further assumptions, the interaction stiffness, k_{ts}, can be measured [25,233,319]. The interaction stiffness offers a simple way to characterize local flexibility without the necessity of continuum models [320,321]. Once a tip-sample contact is formed, the cantilever and the sample behave like two springs in series (strictly speaking, the substrate is a third spring [322,323]). The interaction stiffness of such a system is given by [25]:

$$k_{\mathrm{ts}} = \frac{k_0 k_{\mathrm{sample}}}{k_0 + k_{\mathrm{sample}}} \tag{6.18}$$

where k_{sample} is the sample's effective force constant and $k_0 = 129$ pN/nm the cantilever constant for the probe used here. k_{ts} can be obtained as illustrated in Figure 6.14c-d. A linear function is fitted to the force-displacement curves in the contact part (red lines), and the obtained slope is equal to the interaction stiffness. The two example curves yield $k_{\mathrm{ts}}^{\mathrm{Mica}} = 190$ pN/nm and $k_{\mathrm{ts}}^{\mathrm{IgG}} = 60$ pN/nm. When performing the process for each of the 1225 force displacement curves, a k_{ts}-map is obtained (Figure 6.15c). The area corresponding to the IgG appears darker in the k_{ts} map compared to the mica substrate. Qualitatively, the smaller k_{ts} values obtained on the IgG indicate a softer behavior, consistent with the higher indentation. Panel c shows a histogram of the k_{ts}-map, exhibiting two clearly separated peaks. Fitting the distribution with a double Gaussian yields two distributions centered around 73 pN/nm and 149 pN/nm,

respectively. The right peak (corresponding to the area of the mica) can be understood as a limiting case of Equation 6.18. For $k_{\mathrm{sample}} = k_{\mathrm{mica}} >> k_0$ one obtains $k_{\mathrm{ts}} \approx k_0$. In other words, if the sample spring behaves infinitely stiff, then the right peak corresponds to the cantilever spring constant only. Indeed, the peak's mean value is close to the cantilever's spring constant ($k_{\mathrm{ts}} = 149$ pN/nm to $k_0 = 129$ pN/nm) with a relative error of $(149\,\mathrm{pN/nm} - 129\,\mathrm{pN/nm})/(129\,\mathrm{pN/nm}) = 15.5$ %. The deviation can be attributed to the general uncertainty of the cantilever calibration [11] and the low signal-to-noise ratio in the experiment due to working with subnanometer deflections and indentations. Nonetheless, the right peak confirms the validity of the approach to obtain the stiffness and serves a reference for the uncertainty. The left peak contains both contributions from the cantilever and the IgG antibody, and can be used to calculate the antibody's effective force constant k_{IgG}. By rewriting Equation 6.18 one obtains $k_{\mathrm{IgG}} = k_{\mathrm{sample}} = k_0 k_{\mathrm{ts}}/(k_0 - k_{\mathrm{ts}}) = (129\,\mathrm{pN/nm} \cdot 73\,\mathrm{pN/nm})/(129\,\mathrm{pN/nm} - 73\,\mathrm{pN/nm}) = 168.16$ pN/nm. By assuming the relative error determined from the right peak (15.5 %), the average antibody force constant is $k_{\mathrm{IgG}} = (168 \pm 26)$ pN/nm. For the three regions marked in Figure 6.15c, one obtains average values of 170, 185, and 185 pN/nm, respectively, for the regions labeled as 1, 2, and 3. Given the uncertainty of the measurement, the experimental result is more reliably described by an overall averaged value, as obtained from the histogram.

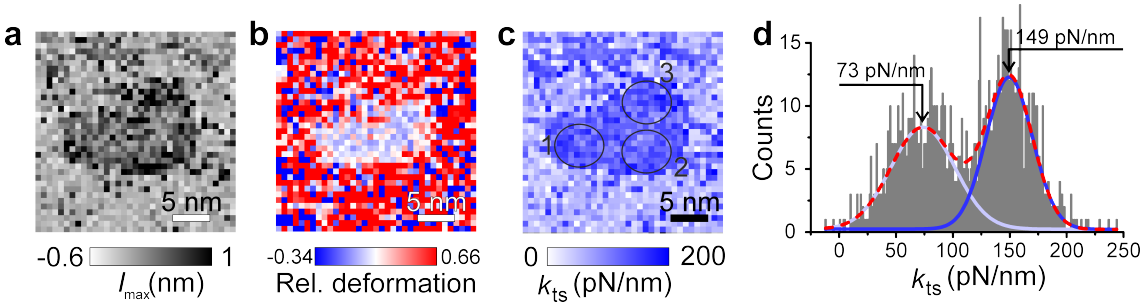

Figure 6.15.: Force spectroscopy (QI) measurements on an IgG molecule in 0.02 M PBS adsorbed on mica. **a.** Map of the maximum tip indentation reached during the experiment (at $F = 100$ pN) **b.** Map of the relative deformation (=indentation/height). **c.** Map of the interaction stiffness k_{ts} extracted from the slope of the force curves. **d.** Histogram of the data shown in panel c. The left and right peak correspond to data taken on the IgG and the mica substrate, respectively. The lines are a double-Gaussian fit to the data (light blue: first Gaussian, blue: second Gaussian, red dashed line: sum of both). The respective mean values are indicated.

In order to gain deeper insight into the nanomechanical properties of the IgG antibody, protein indentation was simulated using MD. The simulations were performed involving an individual IgG antibody adsorbed in the flat-on orientation on a three-layer graphene substrate [137]. A diamond half-sphere with a radius of 2 nm was used as the AFM tip and the remaining volume of the simulation cell was filled with water molecules (omitted in the figure for clarity). **Figure 6.16**a illustrates the set-up. Panel b portrays a top-

view of the same antibody. Indentation was simulated by vertically approaching the tip to 9 different sites of the molecule (indicated by circles).

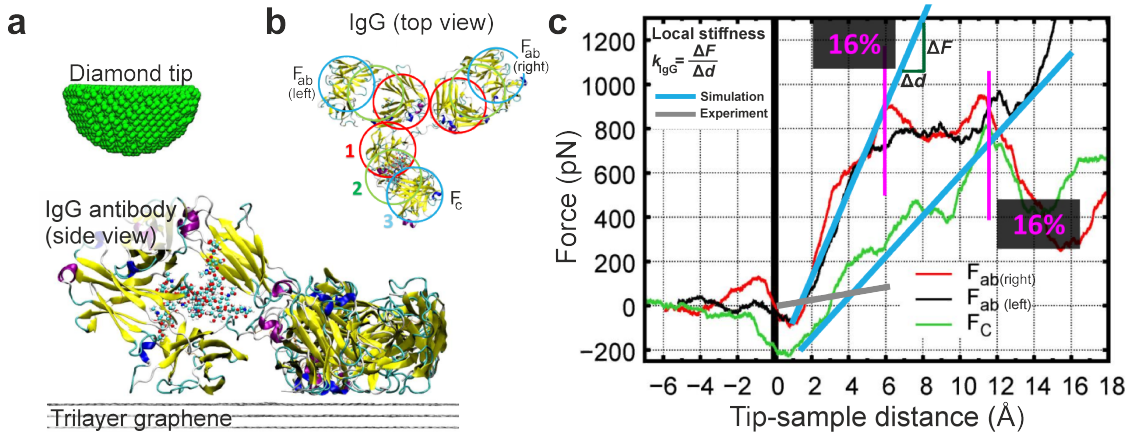

Figure 6.16.: Molecular dynamics (MD) simulations of an AFM tip indenting an IgG antibody. a. The simulations include a diamond tip, a single IgG molecule adsorbed onto trilayer graphene, and water molecules (omitted for clarity). b. Top view of the adsorbed IgG molecule. The circles mark the sites where indentation has been simulated. c. Simulated force-distance curves, one for each of the three antibody fragments (left and right Fab, and Fc). The vertical magenta-coloured lines mark 16 % relative deformation. The light blue lines indicate the slope of the simulated force distance curves. For comparison, the experimentally obtained slope is indicated by the gray line. Figure adapted from Dr. J. Guilherme Vilhena.

The obtained force distance curves show small differences between all the 9 different indentation sites. For simplicity, here only one force curve for each of the three IgG fragments (left and right Fab, and Fc) is shown (Figure 6.16c). Each of the individual force distance curves is characterized by three regimes: First, an attractive force can be observed at the contact point ($d \approx 0$), followed by an approximately linearly increasing repulsive force. Finally, for larger indentations (and forces), the curves show a kink and the slope of the curve flattens out. Snapshots of the MD simulations reveal that the first regime (attraction) is governed by attractive hydrophobic interactions between the tip and the sample, causing a vertical elongation of the protein (snap-on). The second regime (linear repulsion) arises from the spring-like behavior of the antibody (see below). The third regime (leveling out of the slope) is caused by horizontal sliding of the respective antibody fragment in order to release tip-induced tension, leading to an apparently softer response. The transition from the second to the third regime is controlled by the relative deformation (approximately 16 % as indicated by the vertical magenta lines). In the case of the Fc fragment, the transition happens at a higher absolute indentation because the fragment's height is larger and, hence, a larger indentation is required to reach the same relative deformation.

The overall behavior of the curves obtained on the two Fab fragments is very similar to each other. In comparison, the curve corresponding to the Fac fragment is characterized

by a stronger attraction in the moment of first contact, and in the following repulsive part by overall lower forces. One way to quantify the differences between the force curves is measuring the curve's slope, $\Delta F/\Delta d$, which is equal to the (local) antibody stiffness or effective force constant, k_{IgG}. From the force curves one obtains $k_{\mathrm{IgG}}^{\mathrm{Fab}} \approx 1950$ pN/nm and $k_{\mathrm{IgG}}^{\mathrm{Fc}} \approx 910$ pN/nm for the Fab and the Fc fragment, respectively (indicated by the light blue lines in Figure 6.16c).

Discussion

The experimental approach allows to quantify the antibody's nanomechanical response in terms of deformation and (local) stiffness. By limiting the applied force to 100 pN, the tip-induced deformation are restricted to the elastic regime of the antibody [273]. The obtained average value of the effective force constant,$k_{\mathrm{IgG}} = (168 \pm 26)$ pN/nm, will first be compared to previously reported experimental stiffness (or flexibility) values of single proteins of different types. Preiner *et al.* mapped the effective force constant of periplasmic loops of single aquaporine molecules using HS AFM and obtained values between 32 and 44 pN/nm [311]. Dong *et al.* mapped the effective force constant of bacteriorhodopsin patches with single-protein resolution and reported values ranging from 80-170 pN/nm (cytoplasmic side) to 320-430 pN/nm (extracellular side) [233]. Similar values were found by Rico *et al.* (60-100 pN/nm for the cytoplasmic side) [275]. Perrino *et al.* and Voss *et al.* provide Young's moduli of single IgM antibodies in the 2.5 - 34 MPa range but do not explicitly state force constants [272,273]. However, the reported force-distance data allows to estimate the values for k_{IgM} to be between 38 and 884 pN/nm. In the same way, the force constant of a single proteasome can be determined from Young's modulus maps and deformation data reported by Benaglia *et al.,* yielding approximately 307 pN/nm [312].

The IgG's force constant obtained in the experiments shown here (168 pN/nm) falls well into the range of reported protein stiffnesses, confirming the validity of the experimental approach. In a second step, the experimental data will be compared to the MD simulations. The experimentally determined average antibody force constant is 5-12 times smaller than the one obtained in the simulation (168 pN/nm versus $910 - 1950$ pN/nm). For comparison, the experimental value is illustrated by the gray line in Figure 6.16c. The line's slope is quite similar to the one of the simulated data in the third regime, *i.e.*, above 16 % relative deformation, where the indentation process is characterized by a sidewise slipping of the IgG molecule. It is not clear if a slipping motion like the one observed in the simulations occurs in the experiment, since the IgG-substrate interactions are different in both cases (experiment: mica+divalent ions, MD: graphene). In the MD simulations, slipping was provoked for relative protein deformations above 15 %. The experimentally induced maximum relative deformation is on average 15.1 % (Figure 6.15b), indicating that most of measured response would not be affected by the slipping motion. An important difference between the experiments and the simulations is the indentation speed, which is four orders of magnitude larger in the case of the simulations (< 10 µm/s and 0.1 m/s for the experiments and the simulations, respectively). It could be argued that the significantly higher deformation speed causes an additional

force component arising from viscous interaction within the protein [324] or between the protein and the liquid environment [254].

The MD simulation considered indentations into different regions of the IgG molecule, each of them showing a different mechanical response. Within the Fab fragments, the overall response was quite similar apart from subtle differences. However, the Fc fragment turned out to be more compliant than the Fab ones (approximately 50 %). Such differences in the flexibility could be linked to the biological functions of the individual fragments. However, from the obtained experimental data it is difficult to reach a reliable conclusion in this regard. The experimentally observed local differences in k_{ts} are smaller than the uncertainty. In principle, the experimental approach (point by point force curves) is well suited for probing such a site-dependency. By optimizing the experimental set-up, this question could be addressed with more detail, *e.g.*, by using softer cantilevers in order to increase the signal-to-noise ratio or sharper tips to improve the spatial resolution.

6.6. Conclusions

In this chapter, AFM based force spectroscopy was applied to three different topics on the single-molecule scale. First, the role of cantilever dynamics in the unbinding of individual receptor-ligand pairs is investigated. Second, biorecognition experiments were performed on a silicon-nanowire based biosensor in order to localize individual adsorbed avidin molecules. Third, the nanomechanical properties of a single IgG protein were probed by using AFM-based nanoindentation. In the following, the conclusions of each section are summarized.

Cantilever dynamics in SMFS: AFM SMFS and other off-resonance measurements performed at high speeds are mostly described by the Hooke's law, *i.e.*, a static approach. In this section, unbinding experiments were performed on the biotin-avidin complex, a well-known test system for single-molecule force spectroscopy. The experiments demonstrate the existence of an upper speed limit set by the dynamic behavior of the cantilever. By choosing a standard cantilever for measuring at elevated unbinding speeds, the universally occurring dynamic effects of a moving cantilever could be singled out. An analytical expression was developed to describe the force contributions during the unbinding process beyond the (still common) static approach. The comparison with simulations provided understanding of how the observed effects depend on the experimental set-up. A simple criterion is provided (χ) in order to evaluate the significance of the dynamic contributions in a given experiment. Altogether, to transform observables into rupture forces requires the use of two speed-dependent parameters. First, there is the loading rate that enables to deduce the kinetic parameters of the bond. The other parameter is χ, the ratio between the pulling rate and the resonance frequency. Small ratios ($\chi < 10$) are needed to justify the use of Hooke's law, *i.e.*, to measure the rupture force directly from the cantilever deflection. Otherwise, the measured force underestimates the value of the force needed to break the bond. The findings offer two possible ways to overcome the limits

posed by the cantilever. The straightforward solution is to employ (ultra-)short cantilevers which combine sufficiently low spring constants with high resonance frequencies. However, also with these cantilevers one will eventually encounter a fundamental limit up to which they can be described sufficiently well by the Hooke's law. At this point, it is inevitable to add Newton dynamics to the description of the force measurement. To this end, an analytically deduced correction factor is provided that incorporates cantilever dynamics into the well-established Bell-Evans framework (or any other model describing the rupture force). Finally, it is demonstrated that the correction recovers the accurate unbinding forces throughout the entire range of loading rates. Taking into account the cantilever dynamics, AFM SMFS can provide accurate data at any speed.

Biorecognition experiments on a SiNW:

In this section, the capabilities of AFM for biorecognition at the single-molecule level were exploited in order to verify the specific adsorption of the target molecule within the active area of a biosensor. Avidin was deposited on a silicon-nanowire based device designed to detect ultra-low concentrations of this protein. Force-volume based SMFS was used in order to image the SiNW at the same time that biorecognition was performed. By using biotin as a probe, adsorbed avidin was localized mainly on the SiNW and much less in the non-active surrounding area. The obtained unbinding forces were compared with the values predicted by the Bell-Evans law proving the specificity of the detected unbinding events. The results confirmed that the fabrication process of the SiNW is suitable to create an active biosensor element that selectively adsorbs avidin molecules and hence to enhance the sensitivity of the device.

The stiffness of a single IgG protein:

The last section of the chapter shed light on the nanomechanical properties of an individual protein. Using a fast force-volume technique, the flexibility of a single IgG molecule is probed. The induced deformations are maintained in the elastic regime, thereby preserving the antibody's integrity. A flexibility value of $k_{\mathrm{IgG}} = (168 \pm 26)$ pN/nm is determined, a number that falls in the range of stiffness values reported for IgM antibodies and other single proteins. With the help of molecular dynamics simulations, the tip-IgG interaction can be explored in great detail, underlining submolecular features of the flexibility. It was found that the mechanical response of the Fc fragment differs from the one of the Fab fragments, exhibiting a lower overall stiffness. Such differences can be related to the biological function of the different protein fragments. The comparison between experiments and MD simulations points out a possible speed-dependency of the antibody's flexibility due to intramolecular dissipation or interaction with the liquid environment.

General Conclusions

1. A versatile and user-friendly environment for AM 3D-AFM data analysis was developed. The software allows for time-efficient, accurate, and transparent data analysis in three dimensions. It formed the foundation for obtaining the results presented in this thesis and is key for establishing AM 3D-AFM as a routine AFM technique. The existing data acquisition software was implemented in a new AFM set-up and improved by recording the deflection channel..

2. The interfacial water organization next to layered, hydrophobic materials immersed in ultrapure water was visualized with atomic-scale resolution. 3D-AFM images of HOPG, epitaxial graphene monolayers and four different TMDCs in ultrapure water were obtained. Samples were investigated covering a range from 2D materials to bulk, including mono-, few-, and multilayer structures. The 3D images demonstrate the universal existence of liquid density oscillations extending up to 2 nm into the liquid. The periodicity of the oscillations was measured to be 0.5 ± 0.05 nm for all the materials. Experiments with a hydrophilic mica surface revealed a different solid-liquid interface, extending only 1 nm into the liquid with a periodicity of 0.28 nm. The differences between hydrophilic and hydrophobic surfaces are explained in terms of water molecules and airborne (hydrocarbon) adsorbates.

3. 3D-AFM was applied to investigate the solid liquid interface of pentacene thin-films in electrolyte solution. 3D images were obtained over distances ranging from 5 to 250 nm. The images reveal the existence of liquid density oscillations similar to the one observed on layered materials. Visualization of the interfacial liquid organization was not only in atomically flat areas achieved, but also images spanning over entire adjacent pentacene terraces are provided. Furthermore, detailed images of solvation layers around step edges were obtained. A sample stage was designed that allowed to perform 3D-AFM measurements in liquid with simultaneously applied voltages. Voltages between +200 and -700 mV were applied *in situ* demonstrating that the liquid layering is compatible with the working conditions of an EGOFET.

4. The adsorption of alkali metal ions to muscovite mica immersed in electrolyte solutions was studied with 3D-AFM. Short, high-frequency cantilevers with a minimum detectable force of ≈ 3 pN were used to improve the sensitivity of the instrument. 3D images of hydrated K+ ions adsorbed in the ditrigonal cavities of the mica surface were achieved. K+ ions were observed to form in patches and correlated patterns. A comparison between 3D-AFM images and reported crystal structure data was performed. The agreement confirmed the accuracy of the 3D-AFM measurements in all three dimensions.

5. The effects of cantilever dynamics in AFM SMFS were investigated. Experiments on the biotin-avidin bond demonstrate that at high unbinding speeds the measured rupture force underestimates the force predicted by the Bell-Evans law by about 50 %. A theory was developed that explains this observation with cantilever dynamics contributions. In particular the hydrodynamic effect acting on the moving cantilever leads to an apparent decrease in the rupture force. Simulations were performed to investigate the dependency of the contributions on the cantilever choice. The resonance frequency of the cantilever sets an upper speed limit for accurate unbinding force measurements in AFM SMFS. A criterion χ is proposed to estimate the deviations and to facilitate the right choice of the cantilever for a given experiment. A correction factor is provided and is used to recover the actual rupture forces from the experimental data. Fitting the corrected data with the Bell-Evans law yielded $x_\beta = 0.5 \pm 0.06$ nm and $K_{\text{off}} = 0.8 \pm 0.54\,\text{s}^{-1}$ for the intermediate and $x_\beta = 0.226 \pm 0.053$ nm and $k_{\text{off}} = 23.6 \pm 19.9\,\text{s}^{-1}$ for the inner biotin-avidin activation barrier.

6. AFM SMFS was applied to verify the adsorption of the target molecule in selected areas of a SiNW-based ultrasensitive biosensor. Using a biotin-functionalized tip, the presence of avidin was locally detected by performing FV measurements in areas of $0.5\,\mu\text{m} \times 1.0\,\mu\text{m}$ including the SiNW. The probability to find specific unbinding events within the SiNW, *i.e.*, the active sensor area, was 5 % and thereby 12.5 times higher than in non-active areas. Fitting the unbinding forces with the Bell-Evans law yielded $x_\beta = (0.21 \pm 0.06)$ nm and $K_{\text{off}} = (21.4 \pm 14.1)\ \text{s}^{-1}$, confirming the specificity thereof.

7. Individual IgG antibodies adsorbed in the flat-on configuration are imaged by AM-AFM and the QI-mode$^{\text{TM}}$. The fast AFM force spectroscopy approach (QI) was used to investigate the mechanical properties of a single antibody. The induced deformations are maintained in the elastic regime. An average stiffness of $k_{\text{IgG}} = (168 \pm 26)$ pN/nm is obtained from the experiments. MD simulations of the indentation into IgG antibodies further revealed submolecular differences in the mechanical response of the antibody's individual fragments.

Conclusiones Generales

1. Se ha desarrollado un entorno versátil e intuitivo para el análisis de datos de AM 3D-AFM. El software permite un análisis temporalmente eficiente, preciso y transparente de los datos en tres dimensiones. Esto formó la base para obtener los resultados presentados en esta tesis y es clave para establecer el AM 3D-AFM como técnica rutinaria de AFM. El software de adquisición de datos ha sido implementado en una nueva configuración del AFM y ha sido mejorado al registrar el canal de defleción.

2. La organización interfacial del agua cerca de materiales laminados hidrofóbicos inmersos en agua ultrapura se visualizó con resolución a nivel molecular. Se obtuvieron imágenes 3D-AFM de HOPG, monocapas epitaxiales de grafeno, y cuatro TMDCs diferentes en agua ultrapura. Las muestras se investigaron cubriendo un rango de materiales 2D hasta el volumen, incluyendo estructuras monocapa, de pocas capas y multicapa. Las imágenes 3D muestran la existencia universal de oscilaciones en la densidad del líquido que se extienden hasta 2 nm hacia el interior del líquido. Se ha medido que la periodicidad de las oscilaciones es de 0.5 ± 0.05 nm para todos los materiales. Experimentos con una superficie hidrófila de mica revelaron una interfaz sólido-líquido diferente, que se extiende solo 1 nm en el interior del líquido con una periodicidad de 0.28 nm. Las diferencias entre superficies hidrófobas e hidrófilas se explican en términos de moléculas de agua y partículas aéreas (hidrocarburo) disueltas en el agua.

3. Se usó 3D-AFM para investigar la interfaz sólido-líquido de películas finas de pentaceno en una solución electrolítica. Las imágenes 3D se obtuvieron para distancias que varían entre 5 y 250 nm. Las imágenes revelan la existencia de oscilaciones de densidad en el líquido similares a las que se observaron para los materiales laminados. La visualización de la organización interfacial del líquido no se consiguió solo en áreas atómicamente planas, sino que también se proporcionan imágenes que se extienden sobre terrazas adyacentes del pentaceno. Además, se obtuvieron imágenes detalladas de capas de solvatación alrededor de los extremos de los escalones. La preparación de la muestra se diseñó de manera que permitiera desarrollar medidas 3D-AFM en líquido con voltajes aplicados simultáneamente. Voltajes entre +200 y -700 mV se aplicaron in situ, probando que la laminación del líquido es compatible con las condiciones de trabajo de un EGOFET.

4. La absorción de iones de metales alcalinos a la mica muscovita inmersa en soluciones electrolíticas se estudió con 3D-AFM. Las micropalancas cortas y de alta frecuencia con una mínima fuerza detectable de ≈ 3 pN se usaron para mejorar la

sensibilidad del instrumento. Se consiguieron imágenes 3D de los iones K+ hidratados absorbidos en las cavidades ditrigonales de la superficie de la mica. Se observó que los iones K+ formaron parches y patrones correlacionados. Se llevó a cabo una comparación entre las imágenes 3D-AFM y datos publicados de la estructura del cristal. La concordancia confirmó la fiabilidad de las medidas 3D-AFM en las tres dimensiones.

5. Los efectos de la dinámica de la micropalanca en AFM SMFS se investigaron. Los experimentos con el enlace biotina-avidina demuestran que a altas velocidades de ruptura, la fuerza de rotura medida desprecia la fuerza predicha por la ley de Bell-Evans en un 50 %. Se desarrolló una teoría que explica esta observación con contribuciones de la dinámica de la micropalanca. En particular, el efecto hidrodinámico que actúa sobre la micropalanca en movimiento lleva a una aparente reducción de la fuerza de rotura. Se desarrollaron simulaciones para investigar la dependencia de las contribuciones con la elección de micropalanca. La frecuencia de resonancia de la micropalanca fija un límite superior de velocidad para poder realizar mediciones precisas de fuerza de ruptura. Se propone el parámetro χ para estimar las desviaciones y para facilitar la elección correcta de micropalanca para un experimento dado. Se proporciona un factor de corrección y se usa para recuperar las fuerzas de ruptura reales de los datos experimentales. Ajustar los datos corregidos con la ley de Bell- Evans produjo $x_\beta = 0.5 \pm 0.06$ nm y $K_{\text{off}} = 0.8 \pm 0.54\,\text{s}^{-1}$ para la barrera intermedia y $x_\beta = 0.226 \pm 0.053$ nm y $k_{\text{off}} = 23.6 \pm 19.9\,\text{s}^{-1}$ para la barrera de activación interior de la biotina-avidina.

6. Se aplicó AFM SMFS para verificar la absorción de la molécula objetivo en áreas seleccionadas de un sensor ultrasensitivo basado en SiNW. Usando una punta funcionalizada de biotina, la presencia de avidina se detectó localmente al llevar a cabo medidas FV en áreas de 0.5 µm × 1.0 µm incluyendo el SiNW. La probabilidad de encontrar eventos de ruptura específicos en el SiNW, es decir, en el área activa del sensor, era del 5 % y, por consiguiente, 12.5 veces mayor que en las áreas no activas. Ajustar los valores de la fuerza de ruptura con la ley de Bell- Evans dio como resultado $x_\beta = (0.21 \pm 0.06)$ nm y $K_{\text{off}} = (21.4 \pm 14.1)$ s^{-1}, confirmando la especificidad de los eventos.

7. Anticuerpos IgG individuales absorbidos en la configuración horizontal se imaginan con AM-AFM y el QI-mode. La técnica de espectroscopia de fuerza AFM rápida (QI) se usó para investigar las propiedades mecánicas de un anticuerpo individual. Las deformaciones inducidas se mantienen en el régimen elástico. Se obtiene de los experimentos una rigidez media del $k_{\text{IgG}} = (168 \pm 26)$ pN/nm. Las simulaciones MD de la indentación sobre anticuerpos IgG revelaron, además, diferencias submoleculares en la respuesta mecánica de los fragmentos individuales del anticuerpo.

References

Bibliography

[1] Binnig, G., Rohrer, H., Gerber, C. & Weibel, E. Surface studies by scanning tunneling microscopy. *Physical review letters* **49**, 57 (1982).

[2] Binnig, G., Quate, C. F. & Gerber, C. Atomic force microscope. *Physical review letters* **56**, 930 (1986).

[3] Martin, Y. & Wickramasinghe, H. K. Magnetic imaging by force microscopy with 1000 angstrom resolution. *Applied Physics Letters* **50**, 1455–1457 (1987).

[4] Terris, B., Stern, J., Rugar, D. & Mamin, H. Contact electrification using force microscopy. *Physical Review Letters* **63**, 2669 (1989).

[5] Florin, E.-L., Moy, V. T. & Gaub, H. E. Adhesion forces between individual ligand-receptor pairs. *Science* **264**, 415–417 (1994).

[6] Gross, L., Mohn, F., Moll, N., Liljeroth, P. & Meyer, G. The chemical structure of a molecule resolved by atomic force microscopy. *Science* **325**, 1110–1114 (2009).

[7] Kodera, N., Yamamoto, D., Ishikawa, R. & Ando, T. Video imaging of walking myosin v by high-speed atomic force microscopy. *Nature* **468**, 72 (2010).

[8] The kavli prize in nanoscience (2016). URL `http://kavliprize.org/prizes-and-laureates/prizes/2016-kavli-prize-nanoscience`.

[9] Fukuma, T., Onishi, K., Kobayashi, N., Matsuki, A. & Asakawa, H. Atomic-resolution imaging in liquid by frequency modulation atomic force microscopy using small cantilevers with megahertz-order resonance frequencies. *Nanotechnology* **23**, 135706 (2012).

[10] García, R. *Amplitude modulation atomic force microscopy* (John Wiley & Sons, 2011).

[11] Schillers, H. *et al.* Standardized nanomechanical atomic force microscopy procedure (snap) for measuring soft and biological samples. *Scientific reports* **7**, 5117 (2017).

[12] Sader, J. E., Chon, J. W. & Mulvaney, P. Calibration of rectangular atomic force microscope cantilevers. *Review of scientific instruments* **70**, 3967–3969 (1999).

[13] Hutter, J. L. & Bechhoefer, J. Calibration of atomic-force microscope tips. *Review of Scientific Instruments* **64**, 1868–1873 (1993).

[14] Butt, H.-J. & Jaschke, M. Calculation of thermal noise in atomic force microscopy. *Nanotechnology* **6**, 1 (1995).

[15] Garcia, R. & Herruzo, E. T. The emergence of multifrequency force microscopy. *Nature nanotechnology* **7**, 217 (2012).

[16] Meyer, G. & Amer, N. M. Novel optical approach to atomic force microscopy. *Applied physics letters* **53**, 1045–1047 (1988).

[17] Alexander, S. *et al.* An atomic-resolution atomic-force microscope implemented using an optical lever. *Journal of Applied Physics* **65**, 164–167 (1989).

[18] Sahin, O., Magonov, S., Su, C., Quate, C. F. & Solgaard, O. An atomic force microscope tip designed to measure time-varying nanomechanical forces. *Nature nanotechnology* **2**, 507 (2007).

[19] Bennewitz, R. Friction force microscopy. In *Fundamentals of Friction and Wear on the Nanoscale*, 3–16 (Springer, 2015).

[20] Kawai, S., Kitamura, S.-i., Kobayashi, D. & Kawakatsu, H. Dynamic lateral force microscopy with true atomic resolution. *Applied Physics Letters* **87**, 173105 (2005).

[21] Garcia, R. & San Paulo, A. Dynamics of a vibrating tip near or in intermittent contact with a surface. *Physical Review B* **61**, R13381 (2000).

[22] Garcia, R. & San Paulo, A. Attractive and repulsive tip-sample interaction regimes in tapping-mode atomic force microscopy. *Physical Review B* **60**, 4961–4967 (1999).

[23] García, R., Magerle, R. & Perez, R. Nanoscale compositional mapping with gentle forces. *Nature materials* **6**, 405 (2007).

[24] Garcıa, R. & Perez, R. Dynamic atomic force microscopy methods. *Surface science reports* **47**, 197–301 (2002).

[25] Butt, H.-J., Cappella, B. & Kappl, M. Force measurements with the atomic force microscope: Technique, interpretation and applications. *Surface science reports* **59**, 1–152 (2005).

[26] Payam, A. F., Martin-Jimenez, D. & Garcia, R. Force reconstruction from tapping mode force microscopy experiments. *Nanotechnology* **26**, 185706 (2015).

[27] Knoll, A., Magerle, R. & Krausch, G. Tapping mode atomic force microscopy on polymers: where is the true sample surface? *Macromolecules* **34**, 4159–4165 (2001).

[28] Roduit, C. *et al.* Stiffness tomography by atomic force microscopy. *Biophysical journal* **97**, 674–677 (2009).

[29] Spitzner, E.-C., Riesch, C. & Magerle, R. Subsurface imaging of soft polymeric materials with nanoscale resolution. *Acs Nano* **5**, 315–320 (2010).

[30] Guerrero, C. R., Garcia, P. D. & Garcia, R. Subsurface imaging of cell organelles by force microscopy. *ACS nano* (2019).

[31] Hölscher, H., Langkat, S., Schwarz, A. & Wiesendanger, R. Measurement of three-dimensional force fields with atomic resolution using dynamic force spectroscopy. *Applied physics letters* **81**, 4428–4430 (2002).

[32] Albers, B. J. *et al.* Three-dimensional imaging of short-range chemical forces with picometre resolution. *Nature nanotechnology* **4**, 307 (2009).

[33] Radmacher, M., Cleveland, J. P., Fritz, M., Hansma, H. G. & Hansma, P. K. Mapping interaction forces with the atomic force microscope. *Biophysical journal* **66**, 2159–2165 (1994).

[34] Fukuma, T. & Garcia, R. Atomic-and molecular-resolution mapping of solid–liquid interfaces by 3d atomic force microscopy. *ACS nano* **12**, 11785–11797 (2018).

[35] Martin-Jimenez, D. *et al.* Bond-level imaging of the 3d conformation of adsorbed organic molecules using atomic force microscopy with simultaneous tunneling feedback. *Physical review letters* **122**, 196101 (2019).

[36] Pfreundschuh, M. *et al.* Identifying and quantifying two ligand-binding sites while imaging native human membrane receptors by AFM. *Nature communications* **6**, 8857 (2015).

[37] Dufrêne, Y. F. *et al.* Imaging modes of atomic force microscopy for application in molecular and cell biology. *Nature nanotechnology* **12**, 295 (2017).

[38] Smolyakov, G., Formosa-Dague, C., Séverac, C., Duval, R. & Dague, E. High speed indentation measures by fv, qi and qnm introduce a new understanding of bionanomechanical experiments. *Micron* **85**, 8–14 (2016).

[39] Chopinet, L., Formosa, C., Rols, M., Duval, R. & Dague, E. Imaging living cells surface and quantifying its properties at high resolution using afm in qi mode. *Micron* **48**, 26–33 (2013).

[40] Krotil, H.-U. *et al.* Pulsed force mode: a new method for the investigation of surface properties. *Surface and Interface Analysis* **27**, 336–340 (1999).

[41] De Pablo, P., Colchero, J., Gomez-Herrero, J. & Baro, A. Jumping mode scanning force microscopy. *Applied Physics Letters* **73**, 3300–3302 (1998).

[42] Fukuma, T., Ueda, Y., Yoshioka, S. & Asakawa, H. Atomic-scale distribution of water molecules at the mica-water interface visualized by three-dimensional scanning force microscopy. *Physical review letters* **104**, 016101 (2010).

[43] Martin-Jimenez, D., Chacon, E., Tarazona, P. & Garcia, R. Atomically resolved three-dimensional structures of electrolyte aqueous solutions near a solid surface. *Nature communications* **7**, 12164 (2016).

[44] Marutschke, C. *et al.* Three-dimensional hydration layer mapping on the (10.4) surface of calcite using amplitude modulation atomic force microscopy. *Nanotechnology* **25**, 335703 (2014).

[45] Herruzo, E. T., Asakawa, H., Fukuma, T. & Garcia, R. Three-dimensional quantitative force maps in liquid with 10 piconewton, angstrom and sub-minute resolutions. *Nanoscale* **5**, 2678–2685 (2013).

[46] Verdaguer, A., Sacha, G., Bluhm, H. & Salmeron, M. Molecular structure of water at interfaces: Wetting at the nanometer scale. *Chemical reviews* **106**, 1478–1510 (2006).

[47] Mugele, F. & Baret, J.-C. Electrowetting: from basics to applications. *Journal of physics: condensed matter* **17**, R705 (2005).

[48] Miyata, K. *et al.* Dissolution processes at step edges of calcite in water investigated by high-speed frequency modulation atomic force microscopy and simulation. *Nano letters* **17**, 4083–4089 (2017).

[49] Miyata, K. *et al.* Variations in atomic-scale step edge structures and dynamics of dissolving calcite in water revealed by high-speed frequency modulation atomic force microscopy. *The Journal of Physical Chemistry C* (2019).

[50] Foster, W., Aguilar, J. A., Kusumaatmaja, H. & Voïtchovsky, K. In situ molecular-level observation of methanol catalysis at the water–graphite interface. *ACS applied materials & interfaces* **10**, 34265–34271 (2018).

[51] Voïtchovsky, K., Kuna, J. J., Contera, S. A., Tosatti, E. & Stellacci, F. Direct mapping of the solid–liquid adhesion energy with subnanometre resolution. *Nature Nanotechnology* **5**, 401 (2010).

[52] Spitzner, E.-C., Röper, S., Zerson, M., Bernstein, A. & Magerle, R. Nanoscale swelling heterogeneities in type i collagen fibrils. *ACS nano* **9**, 5683–5694 (2015).

[53] Collins, L. *et al.* Probing charge screening dynamics and electrochemical processes at the solid–liquid interface with electrochemical force microscopy. *Nature communications* **5**, 3871 (2014).

[54] Molino, P. J. *et al.* Hydration layer structure of biofouling-resistant nanoparticles. *ACS nano* **12**, 11610–11624 (2018).

[55] Li, T.-D. *et al.* Structured and viscous water in subnanometer gaps. *Physical Review B* **75**, 115415 (2007).

[56] Bizzarri, A. R. & Cannistraro, S. Molecular dynamics of water at the protein-solvent interface (2002).

[57] Levy, Y. & Onuchic, J. N. Water mediation in protein folding and molecular recognition. *Annu. Rev. Biophys. Biomol. Struct.* **35**, 389–415 (2006).

[58] Laage, D., Elsaesser, T. & Hynes, J. T. Water dynamics in the hydration shells of biomolecules. *Chemical Reviews* **117**, 10694–10725 (2017).

[59] Fenter, P. & Lee, S. S. Hydration layer structure at solid–water interfaces. *MRS Bulletin* **39**, 1056–1061 (2014).

[60] Fenter, P. A. X-ray reflectivity as a probe of mineral-fluid interfaces: A user guide. *Reviews in mineralogy and geochemistry* **49**, 149–221 (2002).

[61] Doshi, D. A., Watkins, E. B., Israelachvili, J. N. & Majewski, J. Reduced water density at hydrophobic surfaces: Effect of dissolved gases. *Proceedings of the National Academy of Sciences* **102**, 9458–9462 (2005).

[62] Schwendel, D. *et al.* Interaction of water with self-assembled monolayers: neutron reflectivity measurements of the water density in the interface region. *Langmuir* **19**, 2284–2293 (2003).

[63] Pintea, S. *et al.* Solid–liquid interface structure of muscovite mica in cscl and rbbr solutions. *Langmuir* **32**, 12955–12965 (2016).

[64] Pintea, S., de Poel, W., de Jong, A. E., Felici, R. & Vlieg, E. Solid–liquid interface structure of muscovite mica in srcl2 and bacl2 solutions. *Langmuir* **34**, 4241–4248 (2018).

[65] Israelachvili, J. N. & Pashley, R. M. Molecular layering of water at surfaces and origin of repulsive hydration forces. *Nature* **306**, 249 (1983).

[66] O'shea, S. & Welland, M. Atomic force microscopy at solid- liquid interfaces. *Langmuir* **14**, 4186–4197 (1998).

[67] De Beer, S., Van den Ende, D. & Mugele, F. Dissipation and oscillatory solvation forces in confined liquids studied by small-amplitude atomic force spectroscopy. *Nanotechnology* **21**, 325703 (2010).

[68] Kilpatrick, J. I., Loh, S.-H. & Jarvis, S. P. Directly probing the effects of ions on hydration forces at interfaces. *Journal of the American Chemical Society* **135**, 2628–2634 (2013).

[69] Ebeling, D., Van den Ende, D. & Mugele, F. Electrostatic interaction forces in aqueous salt solutions of variable concentration and valency. *Nanotechnology* **22**, 305706 (2011).

[70] van Lin, S., Grotz, K., Siretanu, I., Schwierz, N. & Mugele, F. Ion specific and ph-dependent hydration of mica-electrolyte interfaces. *Langmuir* (2019).

[71] Kaggwa, G. B., Nalam, P. C., Kilpatrick, J. I., Spencer, N. D. & Jarvis, S. P. Impact of hydrophilic/hydrophobic surface chemistry on hydration forces in the absence of confinement. *Langmuir* **28**, 6589–6594 (2012).

[72] Schlesinger, I. & Sivan, U. New information on the hydrophobic interaction revealed by frequency modulation AFM. *Langmuir* **33**, 2485–2496 (2017).

[73] Utsunomiya, T., Yokota, Y., Enoki, T. & Fukui, K.-i. Potential-dependent hydration structures at aqueous solution/graphite interfaces by electrochemical frequency modulation atomic force microscopy. *Chemical Communications* **50**, 15537–15540 (2014).

[74] Fukuma, T., Higgins, M. J. & Jarvis, S. P. Direct imaging of individual intrinsic hydration layers on lipid bilayers at ångstrom resolution. *Biophysical Journal* **92**, 3603–3609 (2007).

[75] Ricci, M., Spijker, P., Stellacci, F., Molinari, J.-F. & Voïtchovsky, K. Direct visualization of single ions in the stern layer of calcite. *Langmuir* **29**, 2207–2216 (2013).

[76] Voïtchovsky, K. Anharmonicity, solvation forces, and resolution in atomic force microscopy at the solid-liquid interface. *Physical Review E* **88**, 022407 (2013).

[77] Ebeling, D. & Solares, S. D. Amplitude modulation dynamic force microscopy imaging in liquids with atomic resolution: comparison of phase contrasts in single and dual mode operation. *Nanotechnology* **24**, 135702 (2013).

[78] Ricci, M., Trewby, W., Cafolla, C. & Voïtchovsky, K. Direct observation of the dynamics of single metal ions at the interface with solids in aqueous solutions. *Scientific reports* **7**, 43234 (2017).

[79] Ricci, M., Spijker, P. & Voïtchovsky, K. Water-induced correlation between single ions imaged at the solid–liquid interface. *Nature communications* **5**, 4400 (2014).

[80] Kimura, K. *et al.* Visualizing water molecule distribution by atomic force microscopy. *The Journal of chemical physics* **132**, 194705 (2010).

[81] Suzuki, K., Oyabu, N., Kobayashi, K., Matsushige, K. & Yamada, H. Atomic-resolution imaging of graphite–water interface by frequency modulation atomic force microscopy. *Applied Physics Express* **4**, 125102 (2011).

[82] Siretanu, I. *et al.* Direct observation of ionic structure at solid-liquid interfaces: a deep look into the stern layer. *Scientific reports* **4**, 4956 (2014).

[83] Imada, H., Kimura, K. & Onishi, H. Water and 2-propanol structured on calcite (104) probed by frequency-modulation atomic force microscopy. *Langmuir* **29**, 10744–10751 (2013).

[84] Spijker, P. *et al.* Understanding the interface of liquids with an organic crystal surface from atomistic simulations and AFM experiments. *The Journal of Physical Chemistry C* **118**, 2058–2066 (2014).

[85] Minato, T. *et al.* Interface structure between tetraglyme and graphite. *The Journal of chemical physics* **147**, 124701 (2017).

[86] Kobayashi, K. *et al.* Visualization of hydration layers on muscovite mica in aqueous solution by frequency-modulation atomic force microscopy. *The Journal of chemical physics* **138**, 184704 (2013).

[87] Schlesinger, I. & Sivan, U. Three-dimensional characterization of layers of condensed gas molecules forming universally on hydrophobic surfaces. *Journal of the American Chemical Society* **140**, 10473–10481 (2018).

[88] Labuda, A. *et al.* Comparison of photothermal and piezoacoustic excitation methods for frequency and phase modulation atomic force microscopy in liquid environments. *Aip Advances* **1**, 022136 (2011).

[89] Fukuma, T. Water distribution at solid/liquid interfaces visualized by frequency modulation atomic force microscopy. *Science and technology of advanced materials* **11**, 033003 (2010).

[90] de Poel, W. *et al.* Muscovite mica: Flatter than a pancake. *Surface Science* **619**, 19–24 (2014).

[91] Harada, M. & Tsukada, M. Tip-sample interaction force mediated by water molecules for AFM in water: Three-dimensional reference interaction site model theory. *Physical Review B* **82**, 035414 (2010).

[92] Watkins, M. & Reischl, B. A simple approximation for forces exerted on an AFM tip in liquid. *The Journal of chemical physics* **138**, 154703 (2013).

[93] Amano, K.-i., Suzuki, K., Fukuma, T., Takahashi, O. & Onishi, H. The relationship between local liquid density and force applied on a tip of atomic force microscope: A theoretical analysis for simple liquids. *The Journal of chemical physics* **139**, 224710 (2013).

[94] Hernández-Muñoz, J., Chacón, E. & Tarazona, P. Density functional analysis of atomic force microscopy in a dense fluid. *The Journal of chemical physics* **151**, 034701 (2019).

[95] Söngen, H. *et al.* Resolving point defects in the hydration structure of calcite (10.4) with three-dimensional atomic force microscopy. *Physical review letters* **120**, 116101 (2018).

[96] Fukuma, T. *et al.* Mechanism of atomic force microscopy imaging of three-dimensional hydration structures at a solid-liquid interface. *Physical Review B* **92**, 155412 (2015).

[97] Miyazawa, K. *et al.* A relationship between three-dimensional surface hydration structures and force distribution measured by atomic force microscopy. *Nanoscale* **8**, 7334–7342 (2016).

[98] Zhang, Z., Ryu, S., Ahn, Y. & Jang, J. Molecular features of hydration layers probed by atomic force microscopy. *Physical Chemistry Chemical Physics* **20**, 30492–30501 (2018).

[99] Kuchuk, K. & Sivan, U. Hydration structure of a single dna molecule revealed by frequency-modulation atomic force microscopy. *Nano letters* **18**, 2733–2737 (2018).

[100] Kominami, H., Kobayashi, K. & Yamada, H. Molecular-scale visualization and surface charge density measurement of z-dna in aqueous solution. *Scientific reports* **9**, 6851 (2019).

[101] Asakawa, H., Yoshioka, S., Nishimura, K.-i. & Fukuma, T. Spatial distribution of lipid headgroups and water molecules at membrane/water interfaces visualized by three-dimensional scanning force microscopy. *ACS nano* **6**, 9013–9020 (2012).

[102] Umeda, K. *et al.* Atomic-resolution three-dimensional hydration structures on a heterogeneously charged surface. *Nature communications* **8**, 2111 (2017).

[103] Yang, C.-W., Miyazawa, K., Fukuma, T., Miyata, K. & Hwang, S. Direct comparison between subnanometer hydration structures on hydrophilic and hydrophobic surfaces via three-dimensional scanning force microscopy. *Physical Chemistry Chemical Physics* **20**, 23522–23527 (2018).

[104] Söngen, H. *et al.* Chemical identification at the solid–liquid interface. *Langmuir* **33**, 125–129 (2016).

[105] Martin-Jimenez, D. & Garcia, R. Identification of single adsorbed cations on mica–liquid interfaces by 3d force microscopy. *The journal of physical chemistry letters* **8**, 5707–5711 (2017).

[106] Umeda, K., Kobayashi, K., Minato, T. & Yamada, H. Atomic-level viscosity distribution in the hydration layer. *Physical Review Letters* **122**, 116001 (2019).

[107] Söngen, H., Nalbach, M., Adam, H. & Kühnle, A. Three-dimensional atomic force microscopy mapping at the solid-liquid interface with fast and flexible data acquisition. *Review of Scientific Instruments* **87**, 063704 (2016).

[108] Martín-Jiménez, D. *Development of a three-dimensional atomic force microscope for imaging solid-liquid interfaces.* Ph.D. thesis, Universidad Autónoma de Madrid (2017).

[109] Ando, T., Uchihashi, T. & Scheuring, S. Filming biomolecular processes by high-speed atomic force microscopy. *Chemical reviews* **114**, 3120–3188 (2014).

[110] Alcaraz, J. *et al.* Correction of microrheological measurements of soft samples with atomic force microscopy for the hydrodynamic drag on the cantilever. *Langmuir* **18**, 716–721 (2002).

[111] Amo, C. A. & Garcia, R. Fundamental high-speed limits in single-molecule, single-cell, and nanoscale force spectroscopies. *ACS nano* **10**, 7117–7124 (2016).

[112] Katan, A. J., Van Es, M. H. & Oosterkamp, T. H. Quantitative force versus distance measurements in amplitude modulation AFM: a novel force inversion technique. *Nanotechnology* **20**, 165703 (2009).

[113] Uhlig, M. R., Martin-Jimenez, D. & Garcia, R. Atomic-scale mapping of hydrophobic layers on graphene and few-layer mos 2 and wse 2 in water. *Nature communications* **10**, 2606 (2019).

[114] Uhlig, M. R., Amo, C. A. & Garcia, R. Dynamics of breaking intermolecular bonds in high-speed force spectroscopy. *Nanoscale* **10**, 17112–17116 (2018).

[115] Janovjak, H., Struckmeier, J. & Müller, D. J. Hydrodynamic effects in fast AFM single-molecule force measurements. *European Biophysics Journal* **34**, 91–96 (2005).

[116] Hu, S. & Raman, A. Inverting amplitude and phase to reconstruct tip–sample interaction forces in tapping mode atomic force microscopy. *Nanotechnology* **19**, 375704 (2008).

[117] Hölscher, H. Quantitative measurement of tip-sample interactions in amplitude modulation atomic force microscopy. *Applied Physics Letters* **89**, 123109 (2006).

[118] Sader, J. E. & Jarvis, S. P. Accurate formulas for interaction force and energy in frequency modulation force spectroscopy. *Applied Physics Letters* **84**, 1801–1803 (2004).

[119] Sader, J. E. *et al.* Quantitative force measurements using frequency modulation atomic force microscopy - theoretical foundations. *Nanotechnology* **16**, S94 (2005).

[120] Umeda, K., Kobayashi, K., Minato, T. & Yamada, H. Atomic-level viscosity distribution in the hydration layer. *Physical Review Letters* **122**, 116001 (2019).

[121] Garcia, R., Martinez, R. V. & Martinez, J. Nano-chemistry and scanning probe nanolithographies. *Chemical Society Reviews* **35**, 29–38 (2006).

[122] Dago, A. I., Ryu, Y. K. & Garcia, R. Sub-20 nm patterning of thin layer wse2 by scanning probe lithography. *Applied Physics Letters* **109**, 163103 (2016).

[123] Garcia, R., Knoll, A. W. & Riedo, E. Advanced scanning probe lithography. *Nature nanotechnology* **9**, 577 (2014).

[124] Meyer, E. E., Rosenberg, K. J. & Israelachvili, J. Recent progress in understanding hydrophobic interactions. *Proceedings of the National Academy of Sciences* **103**, 15739–15746 (2006).

[125] Björneholm, O. *et al.* Water at interfaces. *Chemical reviews* **116**, 7698–7726 (2016).

[126] Fukuma, T. & Garcia, R. Atomic-and molecular-resolution mapping of solid–liquid interfaces by 3d atomic force microscopy. *ACS nano* **12**, 11785–11797 (2018).

[127] Poynor, A. *et al.* How water meets a hydrophobic surface. *Physical review letters* **97**, 266101 (2006).

[128] Mao, M., Zhang, J., Yoon, R.-H. & Ducker, W. A. Is there a thin film of air at the interface between water and smooth hydrophobic solids? *Langmuir* **20**, 1843–1849 (2004).

[129] Seo, Y.-S. & Satija, S. No intrinsic depletion layer on a polystyrene thin film at a water interface. *Langmuir* **22**, 7113–7116 (2006).

[130] Tyrrell, J. W. & Attard, P. Images of nanobubbles on hydrophobic surfaces and their interactions. *Physical Review Letters* **87**, 176104 (2001).

[131] Guiney, L. M., Wang, X., Xia, T., Nel, A. E. & Hersam, M. C. Assessing and mitigating the hazard potential of two-dimensional materials. *ACS nano* **12**, 6360–6377 (2018).

[132] Samorì, P., Palermo, V. & Feng, X. Chemical approaches to 2d materials. *Advanced Materials* **28**, 6027–6029 (2016).

[133] Castellanos-Gomez, A. Why all the fuss about 2d semiconductors? *Nature Photonics* **10**, 202 (2016).

[134] Liu, X. & Hersam, M. C. Interface characterization and control of 2d materials and heterostructures. *Advanced Materials* **30**, 1801586 (2018).

[135] Li, Q., Song, J., Besenbacher, F. & Dong, M. Two-dimensional material confined water. *Accounts of chemical research* **48**, 119–127 (2014).

[136] Sarkar, D. *et al.* Mos2 field-effect transistor for next-generation label-free biosensors. *ACS nano* **8**, 3992–4003 (2014).

[137] Vilhena, J. *et al.* Adsorption orientations and immunological recognition of antibodies on graphene. *Nanoscale* **8**, 13463–13475 (2016).

[138] Chow, P. K. *et al.* Wetting of mono and few-layered ws2 and mos2 films supported on si/sio2 substrates. *ACS nano* **9**, 3023–3031 (2015).

[139] Li, Z. *et al.* Effect of airborne contaminants on the wettability of supported graphene and graphite. *Nature materials* **12**, 925–931 (2013).

[140] Gao, J. *et al.* Aging of transition metal dichalcogenide monolayers. *ACS nano* **10**, 2628–2635 (2016).

[141] Zhou, Y. & Reed, E. J. Microscopic origins of the variability of water contact angle with adsorbed contaminants on layered materials. *The Journal of Physical Chemistry C* **122**, 18520–18527 (2018).

[142] Melios, C., Giusca, C. E., Panchal, V. & Kazakova, O. Water on graphene: review of recent progress. *2D Mater.* **5**, 022001 (2018).

[143] Song, J. *et al.* Evidence of stranski–krastanov growth at the initial stage of atmospheric water condensation. *Nature communications* **5**, 4837 (2014).

[144] Zhou, H. *et al.* Understanding controls on interfacial wetting at epitaxial graphene: Experiment and theory. *Physical Review B* **85**, 035406 (2012).

[145] Vilhena, J. *et al.* Atomic-scale sliding friction on graphene in water. *ACS nano* **10**, 4288–4293 (2016).

[146] Willard, A. P. & Chandler, D. The molecular structure of the interface between water and a hydrophobic substrate is liquid-vapor like. *The Journal of chemical physics* **141**, 18C519 (2014).

[147] Li, H. *et al.* Rapid and reliable thickness identification of two-dimensional nanosheets using optical microscopy. *ACS nano* **7**, 10344–10353 (2013).

[148] Voïtchovsky, K. High-resolution AFM in liquid: what about the tip? *Nanotechnology* **26**, 100501 (2015).

[149] Labuda, A. *et al.* Calibration of higher eigenmodes of cantilevers. *Review of Scientific Instruments* **87**, 073705 (2016).

[150] Cassie, A. Contact angles. *Discussions of the Faraday society* **3**, 11–16 (1948).

[151] Vogler, E. A. On the origins of water wetting terminology. *Water in biomaterials surface science* 149–182 (2001).

[152] Van Oss, C. & Giese, R. The hydrophilicity and hydrophobicity of clay minerals. *Clays and Clay minerals* **43**, 474–477 (1995).

[153] Emtsev, K. V. *et al.* Towards wafer-size graphene layers by atmospheric pressure graphitization of silicon carbide. *Nature materials* **8**, 203 (2009).

[154] Wastl, D. S., Weymouth, A. J. & Giessibl, F. J. Atomically resolved graphitic surfaces in air by atomic force microscopy. *ACS nano* **8**, 5233–5239 (2014).

[155] Wastl, D. S. *et al.* Observation of 4 nm pitch stripe domains formed by exposing graphene to ambient air. *ACS nano* **7**, 10032–10037 (2013).

[156] Lu, Y.-H., Yang, C.-W., Fang, C.-K., Ko, H.-C. & Hwang, S. Interface-induced ordering of gas molecules confined in a small space. *Scientific reports* **4**, 7189 (2014).

[157] Lu, Y.-H., Yang, C.-W. & Hwang, S. Atomic force microscopy study of nitrogen molecule self-assembly at the hopg–water interface. *Applied Surface Science* **304**, 56–64 (2014).

[158] Lu, Y.-H., Yang, C.-W. & Hwang, I.-S. Molecular layer of gaslike domains at a hydrophobic–water interface observed by frequency-modulation atomic force microscopy. *Langmuir* **28**, 12691–12695 (2012).

[159] Ko, H.-C. *et al.* High-resolution characterization of preferential gas adsorption at the graphene–water interface. *Langmuir* **32**, 11164–11171 (2016).

[160] Ding, Y. *et al.* First principles study of structural, vibrational and electronic properties of graphene-like mx2 (m= mo, nb, w, ta; x= s, se, te) monolayers. *Physica B: Condensed Matter* **406**, 2254–2260 (2011).

[161] Pürckhauer, K., Kirpal, D., Weymouth, A. J. & Giessibl, F. J. Analysis of airborne contamination on transition metal dichalcogenides with atomic force microscopy revealing that sulfur is the preferred chalcogen atom for devices made in ambient conditions. *ACS Applied Nano Materials* (2019).

[162] Schimmel, T., Küppers, J. & Lux-Steiner, M. Lattice-resolution AFM on the layered dichalcogenide wse2 in the sliding regime. *Thin solid films* **264**, 212–216 (1995).

[163] Annamalai, M. *et al.* Surface energy and wettability of van der waals structures. *Nanoscale* **8**, 5764–5770 (2016).

[164] Amano, K.-i. *et al.* Number density distribution of solvent molecules on a substrate: a transform theory for atomic force microscopy. *Physical Chemistry Chemical Physics* **18**, 15534–15544 (2016).

[165] Müller, D. J., Fotiadis, D., Scheuring, S., Müller, S. A. & Engel, A. Electrostatically balanced subnanometer imaging of biological specimens by atomic force microscope. *Biophysical journal* **76**, 1101–1111 (1999).

[166] Rafiee, J. *et al.* Wetting transparency of graphene. *Nature materials* **11**, 217 (2012).

[167] Luan, B. & Zhou, R. Wettability and friction of water on a mos2 nanosheet. *Applied Physics Letters* **108**, 131601 (2016).

[168] Argyris, D., Phan, A., Striolo, A. & Ashby, P. D. Hydration structure at the α-al2o3 (0001) surface: Insights from experimental atomic force spectroscopic data and atomistic molecular dynamics simulations. *The Journal of Physical Chemistry C* **117**, 10433–10444 (2013).

[169] Krass, M.-D., Krämer, G., Dellwo, U. & Bennewitz, R. Molecular layering in nanometer-confined lubricants. *Tribology Letters* **66**, 87 (2018).

[170] Li, Z. *et al.* Water protects graphitic surface from airborne hydrocarbon contamination. *ACS nano* **10**, 349–359 (2015).

[171] Martinez-Martin, D. *et al.* Atmospheric contaminants on graphitic surfaces. *Carbon* **61**, 33–39 (2013).

[172] Kozbial, A. *et al.* Understanding the intrinsic water wettability of graphite. *Carbon* **74**, 218–225 (2014).

[173] Kozbial, A., Gong, X., Liu, H. & Li, L. Understanding the intrinsic water wettability of molybdenum disulfide (mos2). *Langmuir* **31**, 8429–8435 (2015).

[174] Hurst, J. M., Li, L. & Liu, H. Adventitious hydrocarbons and the graphite-water interface. *Carbon* **134**, 464–469 (2018).

[175] Sivan, U. The inevitable accumulation of large ions and neutral molecules near hydrophobic surfaces and small ions near hydrophilic ones. *Current opinion in colloid & interface science* **22**, 1–7 (2016).

[176] Millet, D. B. *et al.* Atmospheric volatile organic compound measurements during the pittsburgh air quality study: Results, interpretation, and quantification of primary and secondary contributions. *Journal of Geophysical Research: Atmospheres* **110** (2005).

[177] Sendner, C., Horinek, D., Bocquet, L. & Netz, R. R. Interfacial water at hydrophobic and hydrophilic surfaces: Slip, viscosity, and diffusion. *Langmuir* **25**, 10768–10781 (2009).

[178] Voïtchovsky, K., Giofre, D., Segura, J. J., Stellacci, F. & Ceriotti, M. Thermally-nucleated self-assembly of water and alcohol into stable structures at hydrophobic interfaces. *Nature communications* **7**, 13064 (2016).

[179] Azhagiya Singam, E. *et al.* Thermodynamics of adsorption on graphenic surfaces from aqueous solution. *Journal of chemical theory and computation* **15**, 1302–1316 (2018).

[180] Lowe, B. M., Sun, K., Zeimpekis, I., Skylaris, C.-K. & Green, N. G. Field-effect sensors–from ph sensing to biosensing: sensitivity enhancement using streptavidin–biotin as a model system. *Analyst* **142**, 4173–4200 (2017).

[181] Zheng, G., Patolsky, F., Cui, Y., Wang, W. U. & Lieber, C. M. Multiplexed electrical detection of cancer markers with nanowire sensor arrays. *Nature biotechnology* **23**, 1294 (2005).

[182] Dinelli, F. *et al.* Spatially correlated charge transport in organic thin film transistors. *Physical review letters* **92**, 116802 (2004).

[183] Star, A., Gabriel, J.-C. P., Bradley, K. & Grüner, G. Electronic detection of specific protein binding using nanotube fet devices. *Nano letters* **3**, 459–463 (2003).

[184] Cramer, T. *et al.* Water-gated organic field effect transistors–opportunities for biochemical sensing and extracellular signal transduction. *Journal of Materials Chemistry B* **1**, 3728–3741 (2013).

[185] Khan, H. U., Jang, J., Kim, J.-J. & Knoll, W. In situ antibody detection and charge discrimination using aqueous stable pentacene transistor biosensors. *Journal of the American Chemical Society* **133**, 2170–2176 (2011).

[186] Brillante, A. *et al.* Structure and dynamics of pentacene on sio 2: From monolayer to bulk structure. *Physical Review B* **85**, 195308 (2012).

[187] Deng, W.-Q. & Goddard, W. A. Predictions of hole mobilities in oligoacene organic semiconductors from quantum mechanical calculations. *The Journal of Physical Chemistry B* **108**, 8614–8621 (2004).

[188] Minakata, T., Imai, H., Ozaki, M. & Saco, K. Structural studies on highly ordered and highly conductive thin films of pentacene. *Journal of applied physics* **72**, 5220–5225 (1992).

[189] Mattheus, C. C. *et al.* Identification of polymorphs of pentacene. *Synthetic metals* **138**, 475–481 (2003).

[190] Fritz, S. E., Martin, S. M., Frisbie, C. D., Ward, M. D. & Toney, M. F. Structural characterization of a pentacene monolayer on an amorphous sio2 substrate with grazing incidence x-ray diffraction. *Journal of the American Chemical Society* **126**, 4084–4085 (2004).

[191] Hugelmann, M., Hugelmann, P., Lorenz, W. & Schindler, W. Nanoelectrochemistry and nanophysics at electrochemical interfaces. *Surface science* **597**, 156–172 (2005).

[192] Boström, M., Williams, D., Stewart, P. & Ninham, B. Hofmeister effects in membrane biology: the role of ionic dispersion potentials. *Physical Review E* **68**, 041902 (2003).

[193] Trewby, W., Faraudo, J. & Voïtchovsky, K. Long-lived ionic nano-domains can modulate the stiffness of soft interfaces. *Nanoscale* **11**, 4376–4384 (2019).

[194] Donose, B. C., Vakarelski, I. U. & Higashitani, K. Silica surfaces lubrication by hydrated cations adsorption from electrolyte solutions. *Langmuir* **21**, 1834–1839 (2005).

[195] Cafolla, C. & Voïtchovsky, K. Lubricating properties of single metal ions at interfaces. *Nanoscale* **10**, 11831–11840 (2018).

[196] Mizushima, K., Jones, P., Wiseman, P. & Goodenough, J. B. Lixcoo2 (0< x<-1): A new cathode material for batteries of high energy density. *Materials Research Bulletin* **15**, 783–789 (1980).

[197] Helmholtz, H. V. Studien über electrische Grenzschichten. *Annalen der Physik* **243**, 337–382 (1879).

[198] Gouy, M. Sur la constitution de la charge électrique à la surface d'un électrolyte. *J. Phys. Theor. Appl.* **9**, 457–468 (1910).

[199] Chapman, D. L. Li. a contribution to the theory of electrocapillarity. *The London, Edinburgh, and Dublin philosophical magazine and journal of science* **25**, 475–481 (1913).

[200] Stern, O. Zur Theorie der Elektrolytischen Doppelschicht. *Zeitschrift für Elektrochemie und angewandte physikalische Chemie* **30**, 508–516 (1924).

[201] Karaborni, S., Smit, B., Heidug, W., Urai, J. & van Oort, E. The swelling of clays: molecular simulations of the hydration of montmorillonite. *Science* **271**, 1102–1104 (1996).

[202] Edwards, G., Evans, L. & Zippear, A. Two-dimensional phase changes in water adsorbed on ice-nucleating substrates. *Transactions of the Faraday Society* **66**, 220–234 (1970).

[203] Mugele, F. *et al.* Ion adsorption-induced wetting transition in oil-water-mineral systems. *Scientific reports* **5**, 10519 (2015).

[204] Christenson, H. K. & Thomson, N. H. The nature of the air-cleaved mica surface. *Surface Science Reports* **71**, 367–390 (2016).

[205] Pashley, R. Dlvo and hydration forces between mica surfaces in li+, na+, k+, and cs+ electrolyte solutions: A correlation of double-layer and hydration forces with surface cation exchange properties. *Journal of colloid and interface science* **83**, 531–546 (1981).

[206] Pashley, R. & Israelachvili, J. Dlvo and hydration forces between mica surfaces in mg2+, ca2+, sr2+, and ba2+ chloride solutions. *Journal of Colloid and Interface Science* **97**, 446–455 (1984).

[207] Siretanu, I., van den Ende, D. & Mugele, F. Atomic structure and surface defects at mineral-water interfaces probed by in situ atomic force microscopy. *Nanoscale* **8**, 8220–8227 (2016).

[208] Loh, S.-H. & Jarvis, S. P. Visualization of ion distribution at the mica- electrolyte interface. *Langmuir* **26**, 9176–9178 (2010).

[209] Gaines Jr, G. L. The ion-exchange properties of muscovite mica. *The Journal of Physical Chemistry* **61**, 1408–1413 (1957).

[210] Richardson, S. M. & Richardson, J. W. Crystal structure of a pink muscovite from archer's post, kenya: implications for reverse pleochroism in dioctahedral micas. *American Mineralogist* **67**, 69–75 (1982).

[211] Lee, S. S., Fenter, P., Nagy, K. L. & Sturchio, N. C. Monovalent ion adsorption at the muscovite (001)–solution interface: Relationships among ion coverage and speciation, interfacial water structure, and substrate relaxation. *Langmuir* **28**, 8637–8650 (2012).

[212] Bondi, A. van der waals volumes and radii. *The Journal of physical chemistry* **68**, 441–451 (1964).

[213] Mantina, M., Chamberlin, A. C., Valero, R., Cramer, C. J. & Truhlar, D. G. Consistent van der waals radii for the whole main group. *The Journal of Physical Chemistry A* **113**, 5806–5812 (2009).

[214] Shannon, R. D. Revised effective ionic radii and systematic studies of interatomic distances in halides and chalcogenides. *Acta crystallographica section A: crystal physics, diffraction, theoretical and general crystallography* **32**, 751–767 (1976).

[215] Sakuma, H. & Kawamura, K. Structure and dynamics of water on li+-, na+-, k+-, cs+-, h3o+-exchanged muscovite surfaces: A molecular dynamics study. *Geochimica et Cosmochimica Acta* **75**, 63–81 (2011).

[216] Soper, A. K. & Weckström, K. Ion solvation and water structure in potassium halide aqueous solutions. *Biophysical chemistry* **124**, 180–191 (2006).

[217] Marcus, Y. Effect of ions on the structure of water: structure making and breaking. *Chemical reviews* **109**, 1346–1370 (2009).

[218] Vakarelski, I. U., Ishimura, K. & Higashitani, K. Adhesion between silica particle and mica surfaces in water and electrolyte solutions. *Journal of colloid and interface science* **227**, 111–118 (2000).

[219] Misra, R. P., de Souza, J. P., Blankschtein, D. & Bazant, M. Z. Theory of surface forces in multivalent electrolytes. *Langmuir* **35**, 11550–11565 (2019).

[220] Tan, Q. *et al.* Experimental observation of the ion–ion correlation effects on charge inversion and strong adhesion between mica surfaces in aqueous electrolyte solutions. *Langmuir* **30**, 10845–10854 (2014).

[221] Lyklema, J. Overcharging, charge reversal: chemistry or physics? *Colloids and Surfaces A: Physicochemical and Engineering Aspects* **291**, 3–12 (2006).

[222] Lee, S. S., Nagy, K. L. & Fenter, P. Distribution of barium and fulvic acid at the mica–solution interface using in-situ x-ray reflectivity. *Geochimica et Cosmochimica Acta* **71**, 5763–5781 (2007).

[223] Müller, D. & Engel, A. The height of biomolecules measured with the atomic force microscope depends on electrostatic interactions. *Biophysical journal* **73**, 1633–1644 (1997).

[224] Persson, I., Sandström, M. & Yokoyama, H. Structure of the solvated strontium and barium ions in aqueous, dimethyl sulfoxide and pyridine solution, and crystal structure of strontium and barium hydroxide octahydrate. *Zeitschrift für Naturforschung A* **50**, 21–37 (1995).

[225] Vakarelski, I. U. & Higashitani, K. Dynamic features of short-range interaction force and adhesion in solutions. *Journal of colloid and interface science* **242**, 110–120 (2001).

[226] Müller, D. J. & Dufrene, Y. F. Atomic force microscopy as a multifunctional molecular toolbox in nanobiotechnology. In *Nanoscience And Technology: A Collection of Reviews from Nature Journals*, 269–277 (World Scientific, 2010).

[227] Helenius, J., Heisenberg, C.-P., Gaub, H. E. & Muller, D. J. Single-cell force spectroscopy. *Journal of cell science* **121**, 1785–1791 (2008).

[228] Cellini, F., Gao, Y. & Riedo, E. Å-indentation for non-destructive elastic moduli measurements of supported ultra-hard ultra-thin films and nanostructures. *Scientific reports* **9**, 4075 (2019).

[229] Saenz, J. *et al.* Observation of magnetic forces by the atomic force microscope. *Journal of applied physics* **62**, 4293–4295 (1987).

[230] Fumagalli, L., Esteban-Ferrer, D., Cuervo, A., Carrascosa, J. L. & Gomila, G. Label-free identification of single dielectric nanoparticles and viruses with ultraweak polarization forces. *Nature materials* **11**, 808 (2012).

[231] Gramse, G., Edwards, M., Fumagalli, L. & Gomila, G. Dynamic electrostatic force microscopy in liquid media. *Applied Physics Letters* **101**, 213108 (2012).

[232] Spitzner, E.-C. *et al.* Multi-set point intermittent contact (music) mode atomic force microscopy of oligothiophene fibrils. *ACS Macro Letters* **1**, 380–383 (2012).

[233] Dong, M., Husale, S. & Sahin, O. Determination of protein structural flexibility by microsecond force spectroscopy. *Nature nanotechnology* **4**, 514 (2009).

[234] Dietz, C. Sensing in-plane nanomechanical surface and sub-surface properties of polymers: local shear stress as function of the indentation depth. *Nanoscale* **10**, 460–468 (2018).

[235] Labuda, A., Kocuń, M., Meinhold, W., Walters, D. & Proksch, R. Generalized hertz model for bimodal nanomechanical mapping. *Beilstein journal of nanotechnology* **7**, 970–982 (2016).

[236] Dehnert, M. & Magerle, R. 3d depth profiling of the interaction between an AFM tip and fluid polymer solutions. *Nanoscale* **10**, 5695–5707 (2018).

[237] Stroh, C. M. *et al.* Simultaneous topography and recognition imaging using force microscopy. *Biophysical journal* **87**, 1981–1990 (2004).

[238] Stroh, C. *et al.* Single-molecule recognition imaging microscopy. *Proceedings of the National Academy of Sciences* **101**, 12503–12507 (2004).

[239] Nievergelt, A. P., Banterle, N., Andany, S. H., Gönczy, P. & Fantner, G. E. High-speed photothermal off-resonance atomic force microscopy reveals assembly routes of centriolar scaffold protein sas-6. *Nature nanotechnology* **13**, 696 (2018).

[240] Ikai, A., Afrin, R. & Sekiguchi, H. Pulling and pushing protein molecules by AFM. *Current Nanoscience* **3**, 17–29 (2007).

[241] Hinterdorfer, P., Baumgartner, W., Gruber, H. J., Schilcher, K. & Schindler, H. Detection and localization of individual antibody-antigen recognition events by atomic force microscopy. *Proceedings of the National Academy of Sciences* **93**, 3477–3481 (1996).

[242] Evans, E. & Ritchie, K. Dynamic strength of molecular adhesion bonds. *Biophysical journal* **72**, 1541–1555 (1997).

[243] Popa, I., Kosuri, P., Alegre-Cebollada, J., Garcia-Manyes, S. & Fernandez, J. M. Force dependency of biochemical reactions measured by single-molecule force-clamp spectroscopy. *Nature protocols* **8**, 1261 (2013).

[244] Rico, F., Gonzalez, L., Casuso, I., Puig-Vidal, M. & Scheuring, S. High-speed force spectroscopy unfolds titin at the velocity of molecular dynamics simulations. *Science* **342**, 741–743 (2013).

[245] Kellermayer, M. S., Smith, S. B., Granzier, H. L. & Bustamante, C. Folding-unfolding transitions in single titin molecules characterized with laser tweezers. *Science* **276**, 1112–1116 (1997).

[246] Alon, R., Hammer, D. A. & Springer, T. A. Lifetime of the p-selectin-carbohydrate bond and its response to tensile force in hydrodynamic flow. *Nature* **374**, 539 (1995).

[247] Merkel, R., Nassoy, P., Leung, A., Ritchie, K. & Evans, E. Energy landscapes of receptor–ligand bonds explored with dynamic force spectroscopy. *Nature* **397**, 50 (1999).

[248] Moy, V. T., Florin, E.-L. & Gaub, H. E. Intermolecular forces and energies between ligands and receptors. *Science* **266**, 257–259 (1994).

[249] Bizzarri, A. R. & Cannistraro, S. *Dynamic Force Spectroscopy and Biomolecular Recognition* (CRC Press, 2012).

[250] Dufrêne, Y. F., Martinez-Martin, D., Medalsy, I., Alsteens, D. & Müller, D. J. Multiparametric imaging of biological systems by force-distance curve–based AFM. *Nature methods* **10**, 847 (2013).

[251] Hinterdorfer, P. & Van Oijen, A. *Handbook of single-molecule biophysics* (Springer Science & Business Media, 2009).

[252] Alsteens, D. *et al.* Nanomechanical mapping of first binding steps of a virus to animal cells. *Nature nanotechnology* **12**, 177 (2017).

[253] Yu, H., Siewny, M. G., Edwards, D. T., Sanders, A. W. & Perkins, T. T. Hidden dynamics in the unfolding of individual bacteriorhodopsin proteins. *Science* **355**, 945–950 (2017).

[254] Kramers, H. A. Brownian motion in a field of force and the diffusion model of chemical reactions. *Physica* **7**, 284–304 (1940).

[255] Bell, G. I. Models for the specific adhesion of cells to cells. *Science* **200**, 618–627 (1978).

[256] Rico, F. & Moy, V. T. Energy landscape roughness of the streptavidin–biotin interaction. *Journal of Molecular Recognition: An Interdisciplinary Journal* **20**, 495–501 (2007).

[257] Guo, S., Ray, C., Kirkpatrick, A., Lad, N. & Akhremitchev, B. B. Effects of multiple-bond ruptures on kinetic parameters extracted from force spectroscopy measurements: revisiting biotin-streptavidin interactions. *Biophysical journal* **95**, 3964–3976 (2008).

[258] Dumitru, A. C., Herruzo, E. T., Rausell, E., Ceña, V. & Garcia, R. Unbinding forces and energies between a sirna molecule and a dendrimer measured by force spectroscopy. *Nanoscale* **7**, 20267–20276 (2015).

[259] Casalini, S. *et al.* Multiscale sensing of antibody–antigen interactions by organic transistors and single-molecule force spectroscopy. *ACS nano* **9**, 5051–5062 (2015).

[260] Oh, Y. J., Plochberger, B., Rechberger, M. & Hinterdorfer, P. Characterizing the effect of polymyxin b antibiotics to lipopolysaccharide on escherichia coli surface using atomic force microscopy. *Journal of Molecular Recognition* **30**, 2605 (2017).

[261] Chowdhury, S. R., Cao, J., He, Y. & Lu, H. P. Revealing abrupt and spontaneous ruptures of protein native structure under piconewton compressive force manipulation. *ACS nano* **12**, 2448–2454 (2018).

[262] Lo, Y.-S., Simons, J. & Beebe, T. P. Temperature dependence of the biotin- avidin bond-rupture force studied by atomic force microscopy. *The Journal of Physical Chemistry B* **106**, 9847–9852 (2002).

[263] Ando, T., Uchihashi, T. & Fukuma, T. High-speed atomic force microscopy for nano-visualization of dynamic biomolecular processes. *Progress in Surface Science* **83**, 337–437 (2008).

[264] Takahashi, H., Rico, F., Chipot, C. & Scheuring, S. α-helix unwinding as force buffer in spectrins. *ACS nano* **12**, 2719–2727 (2018).

[265] Rico, F., Russek, A., González, L., Grubmüller, H. & Scheuring, S. Heterogeneous and rate-dependent streptavidin–biotin unbinding revealed by high-speed force spectroscopy and atomistic simulations. *Proceedings of the National Academy of Sciences* 201816909 (2019).

[266] Chilkoti, A. & Stayton, P. S. Molecular origins of the slow streptavidin-biotin dissociation kinetics. *Journal of the American Chemical Society* **117**, 10622–10628 (1995).

[267] Kim, D. & Sahin, O. Imaging and three-dimensional reconstruction of chemical groups inside a protein complex using atomic force microscopy. *Nature nanotechnology* **10**, 264 (2015).

[268] Chowdhury, S. R. & Lu, H. P. Spontaneous rupture and entanglement of human neuronal tau protein induced by piconewton compressive force. *ACS Chemical Neuroscience* (2019).

[269] Falke, J. J. & Koshland, D. E. Global flexibility in a sensory receptor: a site-directed cross-linking approach. *Science* **237**, 1596–1600 (1987).

[270] Feinstein, A., Richardson, N. & Taussig, M. I. Immunoglobulin flexibility in complement activation. *Immunology today* **7**, 169–174 (1986).

[271] Martinez-Martin, D., Herruzo, E. T., Dietz, C., Gomez-Herrero, J. & Garcia, R. Noninvasive protein structural flexibility mapping by bimodal dynamic force microscopy. *Physical review letters* **106**, 198101 (2011).

[272] Voss, A., Dietz, C., Stocker, A. & Stark, R. W. Quantitative measurement of the mechanical properties of human antibodies with sub-10-nm resolution in a liquid environment. *Nano research* **8**, 1987–1996 (2015).

[273] Perrino, A. P. & Garcia, R. How soft is a single protein? the stress–strain curve of antibody pentamers with 5 pn and 50 pm resolutions. *Nanoscale* **8**, 9151–9158 (2016).

[274] Rico, F., Picas, L., Colom, A., Buzhynskyy, N. & Scheuring, S. The mechanics of membrane proteins is a signature of biological function. *Soft Matter* **9**, 7866–7873 (2013).

[275] Rico, F., Su, C. & Scheuring, S. Mechanical mapping of single membrane proteins at submolecular resolution. *Nano letters* **11**, 3983–3986 (2011).

[276] Pfreundschuh, M., Harder, D., Ucurum, Z., Fotiadis, D. & Müller, D. J. Detecting ligand-binding events and free energy landscape while imaging membrane receptors at subnanometer resolution. *Nano letters* **17**, 3261–3269 (2017).

[277] Shapiro, B. E. & Qian, H. A quantitative analysis of single protein-ligand complex separation with the atomic force microscope. *Biophysical chemistry* **67**, 211–219 (1997).

[278] Shapiro, B. E. & Qian, H. Hysteresis in force probe measurements: a dynamical systems perspective. *Journal of theoretical biology* **194**, 551–559 (1998).

[279] Bullerjahn, J. T., Sturm, S. & Kroy, K. Theory of rapid force spectroscopy. *Nature communications* **5**, 5463 (2014).

[280] Friddle, R. W., Noy, A. & De Yoreo, J. J. Interpreting the widespread nonlinear force spectra of intermolecular bonds. *Proceedings of the National Academy of Sciences* **109**, 13573–13578 (2012).

[281] Dudko, O. K., Hummer, G. & Szabo, A. Theory, analysis, and interpretation of single-molecule force spectroscopy experiments. *Proceedings of the National Academy of Sciences* **105**, 15755–15760 (2008).

[282] Cossio, P., Hummer, G. & Szabo, A. On artifacts in single-molecule force spectroscopy. *Proceedings of the National Academy of Sciences* **112**, 14248–14253 (2015).

[283] Bull, M. S., Sullan, R. M. A., Li, H. & Perkins, T. T. Improved single molecule force spectroscopy using micromachined cantilevers. *ACS nano* **8**, 4984–4995 (2014).

[284] Viani, M. B. *et al.* Small cantilevers for force spectroscopy of single molecules. *Journal of Applied Physics* **86**, 2258–2262 (1999).

[285] Blass, J., Albrecht, M., Wenz, G., Zang, Y. N. & Bennewitz, R. Single-molecule force spectroscopy of fast reversible bonds. *Physical Chemistry Chemical Physics* **19**, 5239–5245 (2017).

[286] Heymann, B. & Grubmüller, H. Dynamic force spectroscopy of molecular adhesion bonds. *Physical Review Letters* **84**, 6126 (2000).

[287] Walton, E. B., Lee, S. & Van Vliet, K. J. Extending bell's model: how force transducer stiffness alters measured unbinding forces and kinetics of molecular complexes. *Biophysical journal* **94**, 2621–2630 (2008).

[288] Riener, C. K. *et al.* Simple test system for single molecule recognition force microscopy. *Analytica Chimica Acta* **479**, 59–75 (2003).

[289] Vinogradova, O. I., Butt, H.-J., Yakubov, G. E. & Feuillebois, F. Dynamic effects on force measurements. i. viscous drag on the atomic force microscope cantilever. *Review of scientific instruments* **72**, 2330–2339 (2001).

[290] Liu, R., Roman, M. & Yang, G. Correction of the viscous drag induced errors in macromolecular manipulation experiments using atomic force microscope. *Review of Scientific Instruments* **81**, 063703 (2010).

[291] Duanis-Assaf, T., Razvag, Y. & Reches, M. Forsdat: an automated platform for analyzing force spectroscopy measurements. *Analytical Methods* (2019).

[292] De Paris, R., Strunz, T., Oroszlan, K., Güntherodt, H.-J. & Hegner, M. Force spectroscopy and dynamics of the biotinavidin bond studied by scanning force microscopy. *Single Molecules* **1**, 285–290 (2000).

[293] Lee, G. U., Kidwell, D. A. & Colton, R. J. Sensing discrete streptavidin-biotin interactions with atomic force microscopy. *Langmuir* **10**, 354–357 (1994).

[294] Izrailev, S., Stepaniants, S., Balsera, M., Oono, Y. & Schulten, K. Molecular dynamics study of unbinding of the avidin-biotin complex. *Biophysical journal* **72**, 1568–1581 (1997).

[295] Oesterhelt, F., Rief, M. & Gaub, H. Single molecule force spectroscopy by AFM indicates helical structure of poly (ethylene-glycol) in water. *New Journal of Physics* **1**, 6 (1999).

[296] Yuan, C., Chen, A., Kolb, P. & Moy, V. T. Energy landscape of streptavidin- biotin complexes measured by atomic force microscopy. *Biochemistry* **39**, 10219–10223 (2000).

[297] Hummer, G. & Szabo, A. Kinetics from nonequilibrium single-molecule pulling experiments. *Biophysical journal* **85**, 5–15 (2003).

[298] Preiner, J., Ebner, A., Chtcheglova, L., Zhu, R. & Hinterdorfer, P. Simultaneous topography and recognition imaging: physical aspects and optimal imaging conditions. *Nanotechnology* **20**, 215103 (2009).

[299] Guzman, H. V., Garcia, P. D. & Garcia, R. Dynamic force microscopy simulator (dforce): A tool for planning and understanding tapping and bimodal AFM experiments. *Beilstein journal of nanotechnology* **6**, 369–379 (2015).

[300] Kühner, F. & Gaub, H. E. Modelling cantilever-based force spectroscopy with polymers. *Polymer* **47**, 2555–2563 (2006).

[301] Basak, S., Raman, A. & Garimella, S. V. Hydrodynamic loading of microcantilevers vibrating in viscous fluids. *Journal of applied physics* **99**, 114906 (2006).

[302] Adams, J. D. *et al.* High-speed imaging upgrade for a standard sample scanning atomic force microscope using small cantilevers. *Review of Scientific Instruments* **85**, 093702 (2014).

[303] Herruzo, E. T. & Garcia, R. Frequency response of an atomic force microscope in liquids and air: Magnetic versus acoustic excitation. *Applied Physics Letters* **91**, 143113 (2007).

[304] Sotres, J. *et al.* Unbinding molecular recognition force maps of localized single receptor molecules by atomic force microscopy. *Chemphyschem* **9**, 590–599 (2008).

[305] Li, J. *et al.* Direct real-time detection of single proteins using silicon nanowire-based electrical circuits. *Nanoscale* **8**, 16172–16176 (2016).

[306] Kyoung Ryu, Y., Aitor Postigo, P., Garcia, F. & Garcia, R. Fabrication of sub-12 nm thick silicon nanowires by processing scanning probe lithography masks. *Applied Physics Letters* **104**, 223112 (2014).

[307] Fuhrmann, A. & Ros, R. Single-molecule force spectroscopy: a method for quantitative analysis of ligand–receptor interactions. *Nanomedicine* **5**, 657–666 (2010).

[308] Ikai, A. *The world of nano-biomechanics* (Elsevier, 2016).

[309] Zaccai, G. How soft is a protein? a protein dynamics force constant measured by neutron scattering. *Science* **288**, 1604–1607 (2000).

[310] Martín-González, N. *et al.* Atomic force microscopy of protein shells: Virus capsids and beyond. In *Single Molecule Analysis*, 281–296 (Springer, 2018).

[311] Preiner, J. *et al.* High-speed AFM images of thermal motion provide stiffness map of interfacial membrane protein moieties. *Nano letters* **15**, 759–763 (2014).

[312] Benaglia, S., Gisbert, V. G., Perrino, A. P., Amo, C. A. & Garcia, R. Fast and high-resolution mapping of elastic properties of biomolecules and polymers with bimodal AFM. *Nature protocols* **13**, 2890 (2018).

[313] Kienberger, F., Mueller, H., Pastushenko, V. & Hinterdorfer, P. Following single antibody binding to purple membranes in real time. *EMBO reports* **5**, 579–583 (2004).

[314] Ido, S. *et al.* Immunoactive two-dimensional self-assembly of monoclonal antibodies in aqueous solution revealed by atomic force microscopy. *Nature materials* **13**, 264 (2014).

[315] Pier, G. B., Lyczak, J. B. & Wetzler, L. M. *Immunology, infection, and immunity* (ASM press, 2004).

[316] Rodriguez-Ramos, J., Perrino, A. P. & Garcia, R. Dependence of the volume of an antibody on the force applied in a force microscopy experiment in liquid. *Ultramicroscopy* **171**, 153–157 (2016).

[317] Wang, J., Wolf, R. M., Caldwell, J. W., Kollman, P. A. & Case, D. A. Development and testing of a general amber force field. *Journal of computational chemistry* **25**, 1157–1174 (2004).

[318] Kumar, S. *et al.* Direct imaging of protein organization in an intact bacterial organelle using high-resolution atomic force microscopy. *ACS nano* **11**, 126–133 (2016).

[319] Kocun, M., Labuda, A., Meinhold, W., Revenko, I. & Proksch, R. Fast, high resolution, and wide modulus range nanomechanical mapping with bimodal tapping mode. *ACS nano* **11**, 10097–10105 (2017).

[320] Heinrich, H. Über die berührung fester elastischer körper. *Journal für die reine und angewandte Mathematik* **92**, 156–171 (1881).

[321] Derjaguin, B. V., Muller, V. M. & Toporov, Y. P. Effect of contact deformations on the adhesion of particles. *Journal of Colloid and interface science* **53**, 314–326 (1975).

[322] Dimitriadis, E. K., Horkay, F., Maresca, J., Kachar, B. & Chadwick, R. S. Determination of elastic moduli of thin layers of soft material using the atomic force microscope. *Biophysical journal* **82**, 2798–2810 (2002).

[323] Garcia, P. D. & Garcia, R. Determination of the elastic moduli of a single cell cultured on a rigid support by force microscopy. *Biophysical journal* **114**, 2923–2932 (2018).

[324] Ariyaratne, A., Wu, C., Tseng, C.-Y. & Zocchi, G. Dissipative dynamics of enzymes. *Physical review letters* **113**, 198101 (2014).

[325] Zitzler, L., Herminghaus, S. & Mugele, F. Capillary forces in tapping mode atomic force microscopy. *Physical Review B* **66**, 155436 (2002).

[326] Dago, A. I., Sangiao, S., Fernández-Pacheco, R., De Teresa, J. M. & Garcia, R. Chemical and structural analysis of sub-20 nm graphene patterns generated by scanning probe lithography. *Carbon* **129**, 281–285 (2018).

Appendix

A. Supporting Information Chapter 3

In order to better understand the formation of the stripe structure, additional experiments were performed in ambient conditions using similar scanning conditions as in water (in particular driving the cantilever at its second mode with an angstrom-scale free amplitude of $A_0 \lesssim 300$ pm). Tapping-mode imaging in air commonly has to be performed with large amplitudes in order to prevent bistabilities due to nonlinear tip-sample interactions [22] and capillary interactions caused by adsorbed water layers [325]. However, driving the cantilever at its second mode increases its dynamic stiffness significantly ($k_2 \approx 39k_1$), which allows stable operation in ambient air even with very small amplitudes. In this way, long-term high-resolution imaging is possible without damaging the tip nor the sample. Such scanning conditions are moreover comparable to the ones reported by Wastl *et al.* using a tuning fork sensor (qPlus®) [155]. By varying the free amplitude, it turns out that small amplitudes $A_0 \leq 1$ nm are necessary for resolving the stripe pattern in the AFM images (see Appendix, Figure A.8).

A.1. Ordered and Disordered Adsorbates on Graphene

A large-scale overview scan of the graphene surface in air shows terraces (**Figure A.1**a), similar to the case of the graphene immersed in UPW. However, the graphene surface is not as smooth as in UPW and instead shows a random pattern of particles, as it was reported earlier by Wastl *et al.* [155]. The authors suggested that these features are airborne adsorbates [155]. Within the terraces, some ridges are visible (marked by white arrowheads). Figure A.1b shows a scan taken on an individual terrace that exhibits such ridges (marked by arrowheads). Around the ridges, within a certain domain , the adsorbates form a different pattern (some of these domains are marked by dotted lines in panel b). A higher-resolution scan around the boundary of such a domain is provided in panel c. It reveals the flat graphene surface inbetween the adsorbates. The differences in the adsorbate structures can be summarized as follows: In the domains around defects (denoted as II), the fraction of the surface covered by the adsorbates is lower, but the adsorbed particles have a larger height (around 2 nm). Outside of these domains (denoted as I), the adsorbates cover a larger surface area, but are less high (around 1 nm).

Wastl *et al.* have observed a similar situation and have shown that the two domain types correlate to the existence of mono- and bilayer graphene in the respective areas [155]. They found that most of the SiC surface was covered by a monolayer of graphene, while bilayer graphene nucleated on both sides of defects such as surface ridges. It was concluded that bilayer graphene has a lower affinity to the adsorbates than monolayer graphene. Moreover, on the bilayer graphene a highly ordered stripe pattern was observed, but not on the monolayer graphene. Accordingly, the domains in

Figure A.1 and the following ones are denoted as I and II, corresponding to mono- and bilayer graphene, respectively. Indeed, both domains are separated by a monolayer step (see below).

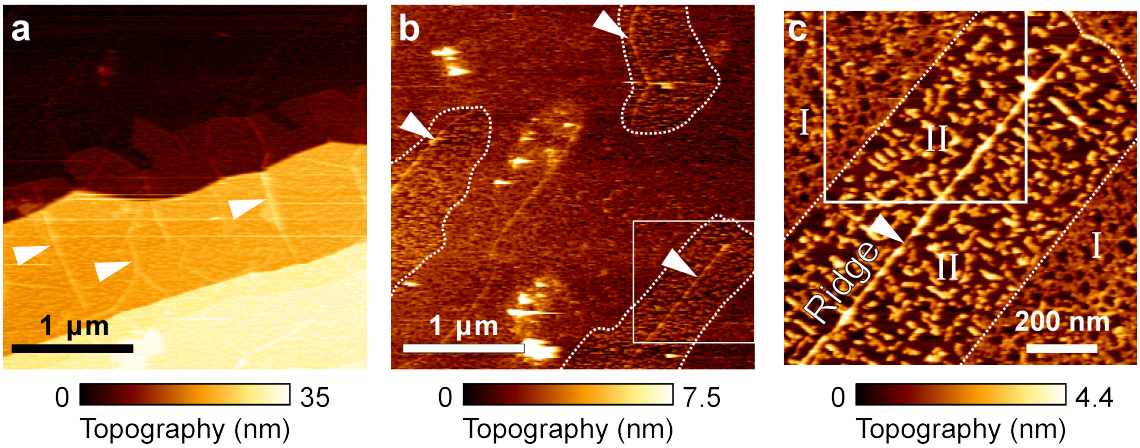

Figure A.1.: AM-AFM topography images taken in ambient air on SiC/graphene. Panel **a** depicts the graphene surface with large, flat terraces. Some defects (ridges) are visible in the terraces, as indicated by white arrowheads. The surface steps and ridges originate from the underlying SiC substrate. **b.** Zoom-in into the uppermost terrace. The surface is covered by adsorbates. Around ridges (marked by white arrowheads), domains with a different adsorbate structure are visible (outlined by dotted lines). **c.** Magnification of the area marked by the white rectangle in b. The domain around the SiC ridge has a lower adsorbate coverage, but the features are higher. Domains marked by I and II are ascribed to mono- and bilayer graphene according to Reference [155]. Scan parameters: free amplitude $A_0 = 185$ pm, amplitude set-point $A_{\mathrm{sp}} = 0.90A_0$, $f_2 = 1.81$ MHz.

Figure A.2 shows close-up AFM images of the boundary between the two observed domains. Panels a (height image) and b (phase image) emphasize the difference in adsorbate coverage between the mono- (I) and bilayer (II) domains as pointed out above. Furthermore, in the phase image, a stripe pattern is visible in the bilayer region (indicated by white lines, see also panel f) as also reported by Wastl *et al.*. By further magnification a similar stripe pattern could be revealed also within the monolayer domain (I) inbetween the disordered adsorbates (Figure A.2d and e). It can be seen that the orientation of the otherwise identical stripe patterns changes at the boundary between the two domains (the boundary is indicated by the dotted line at the bottom right). The angle between the two patterns is around 115° which is close to the symmetry angle of a graphene or graphite surface (120°). This observation indicates that the stripe pattern's growth direction is governed by the underlying graphene lattice.

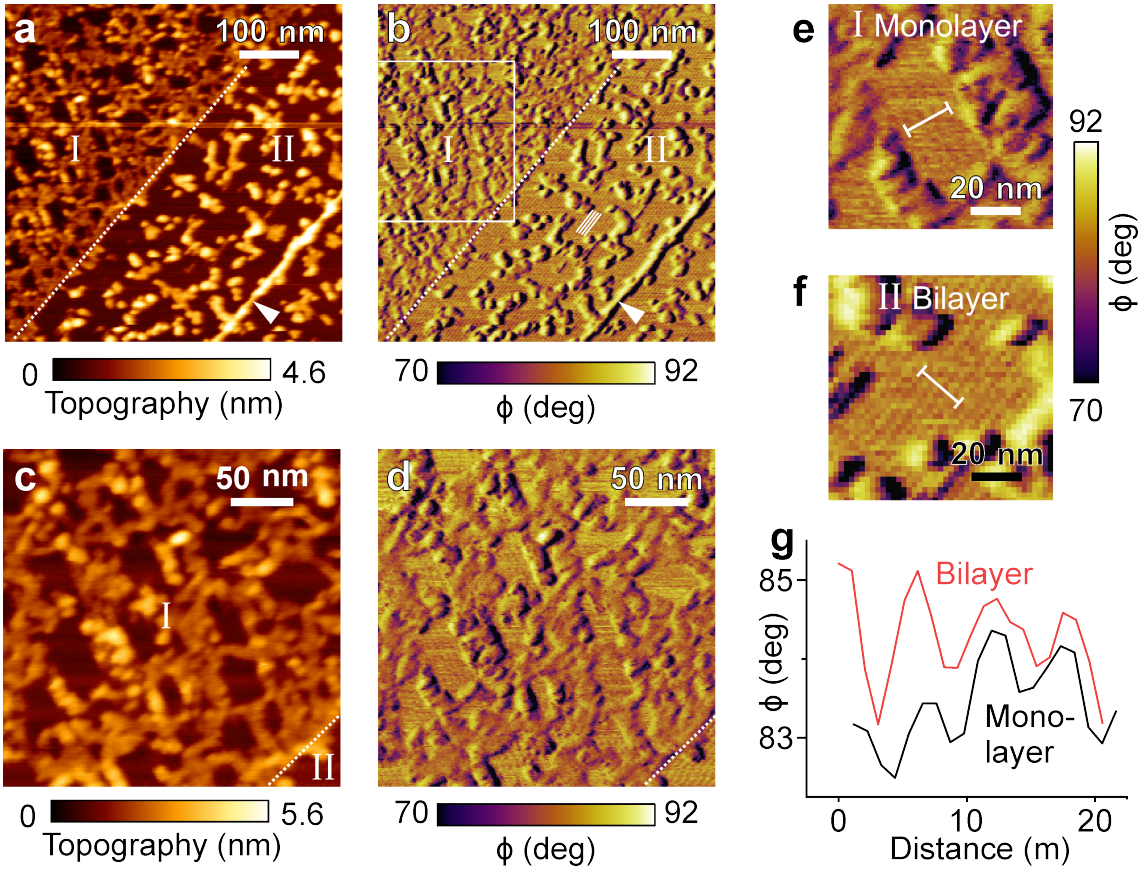

Figure A.2.: Small-amplitude AM-AFM images taken in ambient air on SiC/graphene. Panel **a** shows a magnified view around the boundary between the two domains (indicated by the white dotted line). The domains are marked by I and II and were ascribed to mono- and bilayer graphene. The different adsorbate coverage of the two domains is evident. **b.** Phase image corresponding to panel a. In the less-covered bilayer region (II), a well-organized stripe structure is visible as indicated by the fine white lines. **c.** Zoom-in into the area marked by the white dashed rectangle in panel c. **d.** Phase image corresponding to panel c. The magnified view reveals that also the monolayer graphene (I) is covered by a stripe structure inbetween the adsorbates as indicated by the fine white lines. The orientation of the stripe structures is rotated by about 115 degrees between the domains as can be seen at the boundary (the boundary is indicated by the dotted line at the bottom right). **e.-f.** Magnifications taken from panels b and d showing the mono- and bilayer domains. **g**. Cross sections along the white lines drawn in panels e–f**.** The periodicities for the mono- and bilayer domains are, respectively, 5.2 and 5.7 nm. Scan parameters: free amplitude $A_0 = 185$ pm, amplitude set-point $A_{\mathrm{sp}} = 0.90A_0$, $f_2 = 1.81$ MHz.

When returning to the initial scan area after a few minutes, the very same structures are visible which can be seen by comparing the images in **Figure A.3**a and b. As an example, one adsorbate particle is outlined in both panels in order to emphasize the

absence of changes. This means that the adsorbates are neither mobile on the surface nor removed by repeated scanning with the AFM tip, at least on the involved time scales and with the scanning parameters used here.

In the next step, UPW was injected into the open liquid cell while maintaining the very same position. Panel c shows a phase image taken at the same spot of the surface after injecting the UPW (imaging within 10 min after injection). The position of the SiC ridge (marked by the arrowheads) as well the one of the domain boundary (dotted line) confirms that it is the very same area of the graphene surface. However, in UPW, the graphene surface appears smooth and without the presence of the disordered adsorbates. In the monolayer region (I), some diffuse structures seem to have remained at the surface, whereas the bilayer region (II) is almost perfectly clean. In contrast to the disordered adsorbates, the stripe structure has remained upon injecting the UPW (see below). In particular, it has preserved its orientation. These observations lead to the conclusion that the globular, disordered adsorbates dissolved to a large extend into the water. The stripe pattern in turn is not affected by UPW, neither does it require its presence.

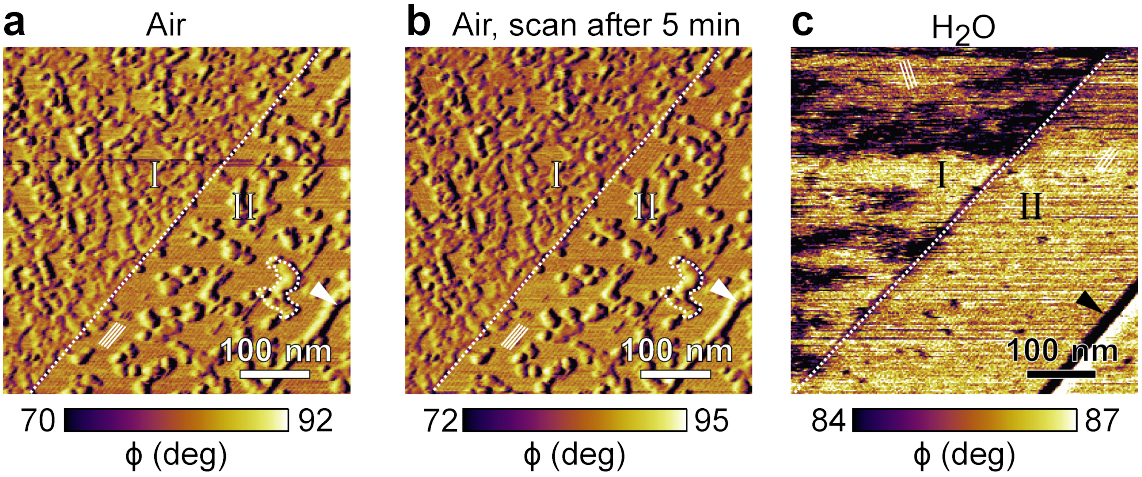

Figure A.3.: Small-amplitude AM-AFM images taken around the domain boundary on SiC/graphene before and after *in situ* injection of ultra-pure water. The domain boundary is indicated by the white dotted line, and the two domains are denoted as I and II. The domains were ascribed to mono- and bilayer graphene, respectively. An SiC ridge is marked by the arrowheads. Panel **a** shows a the same phase image as in Figure A.2a and serves as a reference. **b.** Phase image taken in the very same region after 5 min. The adsorbate structure is unchanged in spite of repeated scanning. **c.** Phase image of the very same area after injection of ultra-pure water. The disordered adsorbates have disappeared. Scan parameters in air: free amplitude $A_0 = 185$ pm, amplitude set-point $A_{sp} = 0.90A_0$, $f_2 = 1.81$ MHz. Scan parameters in ultrapure water: $A_0 = 210$ pm, $A_{sp} = 0.90A_0$, $f_2 = 925$ kHz.

As a last detail, some higher-resolution images of the now clean boundary between the two domains (I and II) are provided (**Figure A.4**c). Panel a and b show the topography and phase image, respectively. A height profile extracted from panel a along the white

line shows that the boundary represents a step whose height is very close to 0.33 nm (panel c), corresponding to a monolayer step of graphene [159]. This is fully consistent with the interpretation of Giessibl's group that the difference of the domains is caused by a monolayer step of the graphene layer, with the main part of the sample being covered by monolayer graphene (I), while a smaller fraction of bilayer regions (II) can be found around surface defects such as SiC ridges [155]. High-resolution transmission electron microscopy images of a graphene sample of the same type (purchased together with the sample investigated here, see Appendix: Figure A.7) showed indeed mono- and bilayer graphene [326]. At last, the existence of some bilayer regions is compatible with the manufacturer's specification for the graphene sample, namely (98 ± 5) % monolayer coverage. The images in panels d and e represent magnifications taken from panel a showing the ripples covering the mono- and bilayer domains. Cross sections extracted from the panels along the white lines are shown in panel f. The periodicities for the mono- and bilayer domains are, respectively, 5.8 and 5.3 nm.

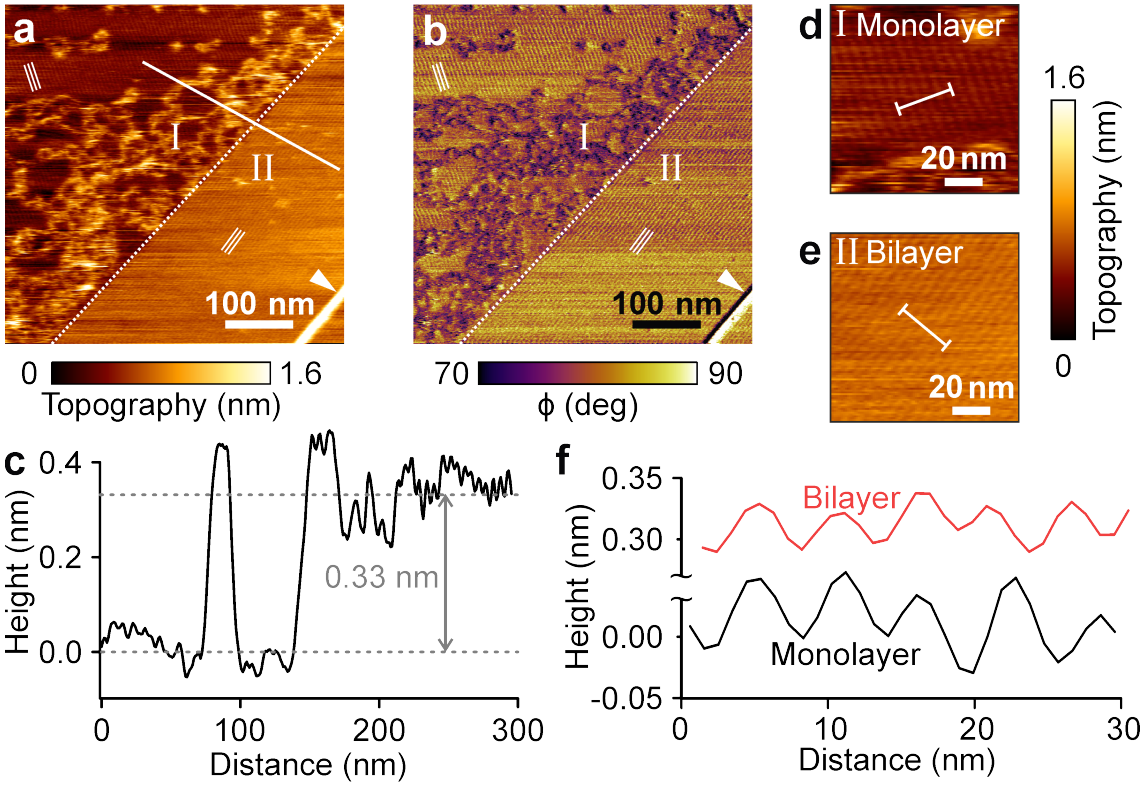

Figure A.4.: Small-amplitude AM-AFM images taken around the domain boundary on SiC/graphene after *in situ* injection of ultra-pure water. The domain boundary is indicated by the white dotted line, and the two domains are denoted as I and II. The domains were ascribed to mono- and bilayer graphene, respectively. An SiC ridge is marked by white arrowheads. **a.** Topography image spanning over the two domains taken in ultra-pure water. The earlier observed stripe structure is clearly resolved (indicated by the fine white lines). **b.** Corresponding phase image. **c.** Line profile obtained along the white line in panel a. The measured step height at the domain boundary corresponds to a monolayer step of graphene. **d.** and **e.** Magnified details cropped from the height image in panel a, highlighting the stripe structures in the mono- (I) and bilayer (II) regions, respectively. The same color scale applies. **f.** Line profiles obtained along the white lines in panels d and e. The periodicities for the mono- and bilayer domains are, respectively, 5.8 and 5.3 nm. Scan parameters: free amplitude $A_0 = 210$ pm, amplitude set-point $A_{sp} = 0.90A_0$, $f_2 = 925$ kHz.

A.2. Adsorbates on TMDCs

Stripe structures were also observed on WSe_2 surface immersed in liquid. In comparison with graphene, they are less frequently observed and less ordered. An example of such a stripe structure around a surface step is shown in **Figure A.5**. Panel a depicts the topography image, while panel b contains the phase channel. A height profile obtained along the white dashed line in panel a reveals that the step in the center of the image

corresponds to a monolayer step of WSe_2. On both sides of the step, stripes are faintly visible in the topography channel and clearly resolved in the phase channel. The periodicity of the stripe structure is $\approx$ 9.3 nm, which is larger than the one measured on graphene ($\approx$ 5 nm). The stripes' orientation changes at the monolayer step, thereby excluding an image artifact as possible reason for the periodic structure. Instead it suggests that the stripes belong to two different domains whose boundary is formed by the surface step, similar as in the case of graphene.

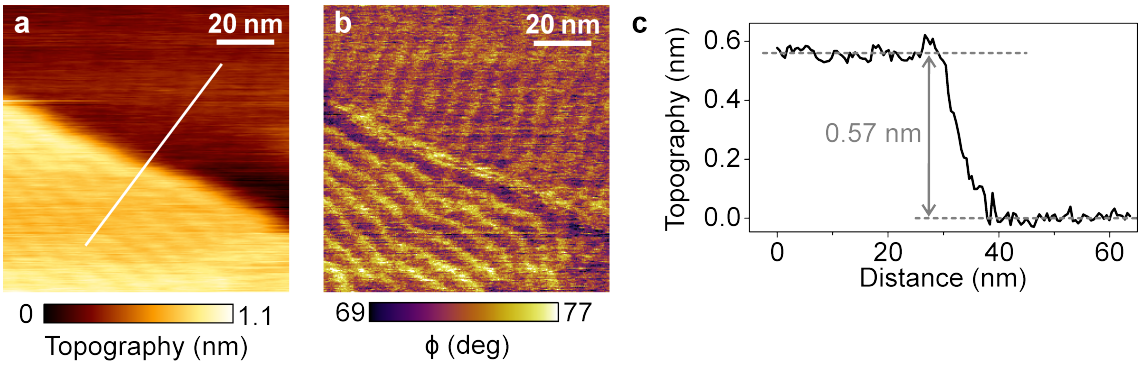

Figure A.5.: Small-amplitude AM-AFM images of a few-layer WSe_2 sample immersed in water. **a.** Topography. **b.** Phase shift. **c.** Cross-section taken along the white dashed line drawn in panel a. The periodicity is 9.3 nm. Scan parameters: free amplitude A_0 = 240 pm, amplitude set-point $A_{sp} = 0.90A_0$, f_2 = 902 kHz.. Adapted from [113].

An additional experiment was performed by imaging at a given position first in air and then liquid. Figure A.6 summarizes the results. In air, the sample surface is covered with globular features that do not change upon repeated scanning (panel a). Interestingly, the features' size is different for the two terraces, indicating that their origin is related to the layered structure of WSe_2. The fact that the structures are larger on the WSe_2-terrace which forms the step edge (the left one) allows to speculate that their origin is related to intercalation of water molecules as observed by Song *et al.* [143]. After imaging in air, UPW was injected *in situ* into the open liquid cell and the surface was scanned again without changing the position (panel b). While the globular features have entirely disappeared, a stripe structure is now visible on both sides of the step. A magnified view is shown in panel c, revealing a periodicity of the stripe structure of approximately 12 nm. Altogether, stripe structures are also commonly found on WSe_2, although not as frequent and also less ordered in comparison to SiC/graphene. The differences between the structures on both materials suggest that they have different origins, in spite of their seemingly similar character. Instead, they could be related to intercalated H_2O or other molecules, or a surface reconstruction due to the contact with the liquid.

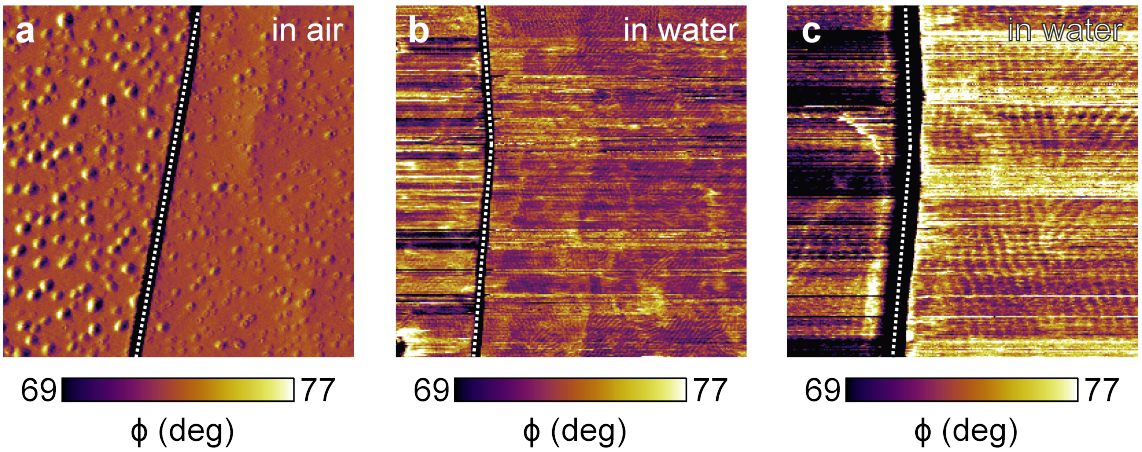

Figure A.6.: Small-amplitude AM-AFM images taken around a surface step on a WSe_2 flake before and after *in situ* injection of ultra-pure water. Panel **a** shows a phase image of sample. Globular features are visible. **b.** Phase image of the the same step after injection of ultra-pure water. The globular features have entirely disappeared. In turn, a stripe structure has become visible. Panel **c** shows a magnified view of the same region. The observed stripe structure is clearly resolved. The periodicity is 12 nm.

A.3. Additional Data

A.3.1. Cantilever parameters for 3D-AFM measurements

Table A.1.: Cantilever parameters for Chapter 3, all for liquid.

Surface	Cantilever type	n	k_n ($\frac{\mathrm{N}}{\mathrm{m}}$)	Q_n	f_n (kHz)	σ_n ($\frac{\mathrm{nm}}{\mathrm{V}}$)
SiC/graphene	PPP-NCHAuD	2	1126	20.4	961	11.53
MoS_2	PPP-NCHAuD	2	1126	20.4	961	11.53
WSe_2	PPP-NCHAuD	2	1051	26.5	957	13.25
$MoSe_2$	PPP-NCHAuD	2	1051	26.5	957	13.25
WS_2	PPP-NCHAuD	2	2338	19.4	918	7.17
HOPG	PPP-NCHAuD	2	969	22.7	904	14.05
Mica	PPP-NCHAuD	2	1128	19.5	978	10.89
Pentacene	ArrowUHFAuD	1	7.44	4.2	508	12.35
Pentacene	AC55TS	1	199	8.2	1138	13.12

A.3.2. Fit parameters for subtracted background forces

Table A.2.: Fit parameters for subtracted background forces. $F_{\mathrm{bg}}(z) = C_1 + C_2 \exp(C_3 z)$.

Material	Figure	C_1(N)	C_2(N)	C_3(m^{-1})
SiC/graphene	3.8 and 2.3.3	5.0581e-011	2.3086e-009	1.7984e+009
SiC/graphene	3.10	-6.1284e-012	3.031e-009	2.1461e+009
MoS_2	3.8	-5.922e-010	7.5173e-009	1.5169e+009
WSe_2	3.8	-1.4593e-010	2.299e-009	1.3839e+009
$MoSe_2$	3.8	-8.0886e-010	4.01e-009	7.6225e+008
WS_2	3.8	-1.481e-009	4.2096e-009	4.7469e+008
HOPG	3.9	-8.2262e-010	2.7101e-009	7.6491e+008
Pentacene	4.6	-1.5036e-010	1.0295e-009	7.2708e+008

A.3.3. Clarification regarding monolayer and bilayer graphene/SiC

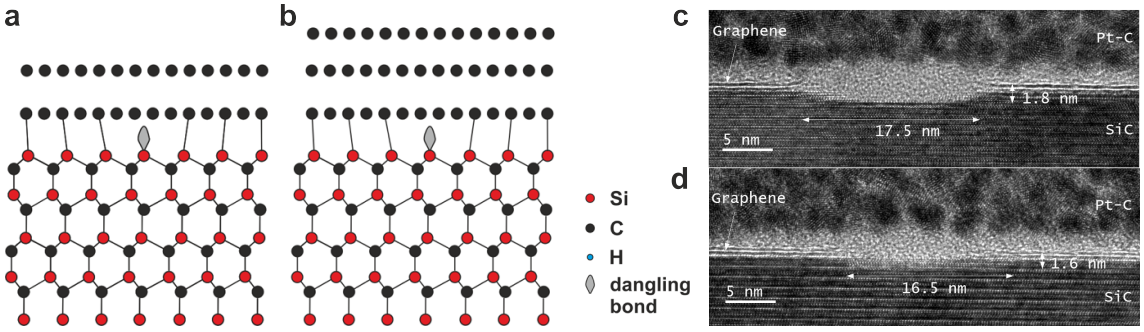

Figure A.7.: Clarification regarding monolayer and bilayer graphene/SiC **a.** Monolayer graphene grown on SiC. The monolayer sits on top of an interface layer bound to the SiC substrate. **b.** Bilayer graphene grown on SiC with the same type of interface layer. **c.** TEM image of the graphene sample showing two bright lines, corresponding to a graphene monolayer plus interface layer. **d.** TEM image of the very same graphene sample showing three bright lines, corresponding to a graphene bilayer plus interface layer. Adapted from Reference [154] and [326], respectively.

A.3.4. Influence of free amplitudes on visibility of ripples

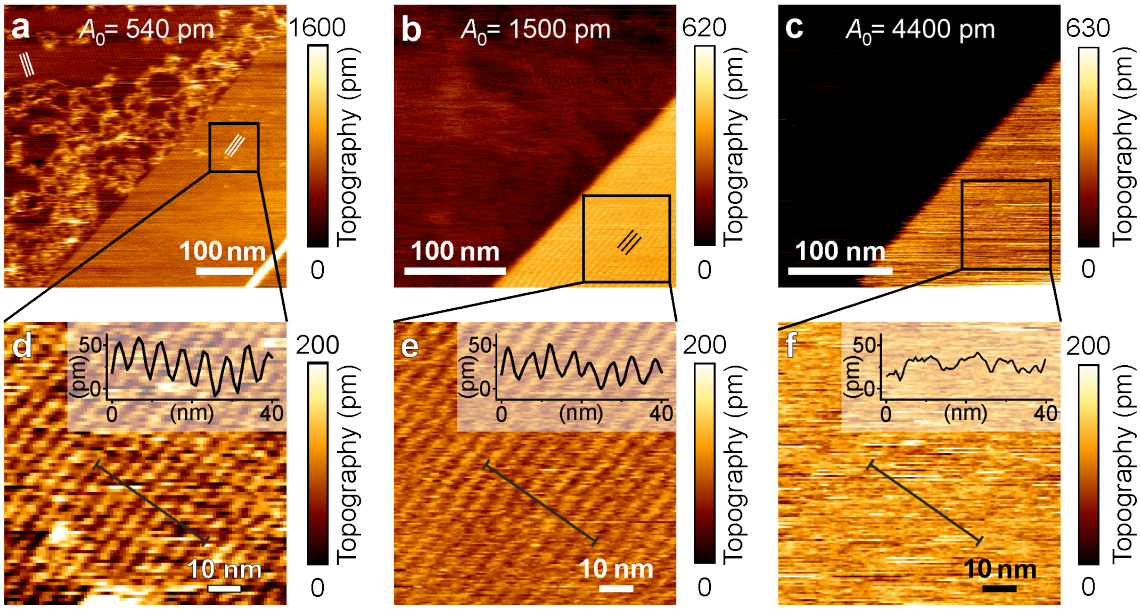

Figure A.8.: AM-AFM topography images taken with different free amplitudes A_0 around a monolayer step on SiC/Graphene in ultra-pure water. **a.** $A_0 = 540$ pm. A stripe structure is visible in the entire image. **b.** $A_0 = 1500$ pm. A stripe structure is still visible in the bottom right part of image (indicated by black fine lines). **c.** $A_0 = 4400$ pm. No stripe structure is visible anymore. **d.-f.** Magnified sections cut out from the images shown in a-c, respectively. They have the very same color range and size. Cross sections obtained along the black lines are shown in the insets.

B. Supporting Information Chapter 5

B.1. Cantilever parameters for chapter 5

Table B.1.: Cantilever parameters for Chapter 5, all for liquid.

Solution	Figure	Cantilever type	n	k_n ($\frac{\mathrm{N}}{\mathrm{m}}$)	Q_n	f_n (kHz)	σ_n ($\frac{\mathrm{nm}}{\mathrm{V}}$)
200 mM KCl	5.3	ArrowUHFAuD	1	12.02	5.6	590	16.2
	5.4						
	5.6						
	5.7						
	B.3						
	B.4						
20 mM $BaCl_2$	5.10						
	5.11						
	5.12						
	5.13						
2 mM KCl	B.1	ArrowUHFAuD	1	9.2	4.9	519	18.3
200 mM KCl	B.1						
	B.2						
200 mM KCl	5.8	ArrowUHFAuD	1	17.67	6.7	717	16.74
20 mM $BaCl_2$	B.6	AC55TS	1	191.8	9.6	1130	9.64
200 mM KCl	B.5	PPP-NCHAuD	2	1875	18.4	905	7.68
KCl, $BaCl_2$	5.9	CP-PNP-SiO	0	0.08	-	-	80.0

B.2. xy phase planes

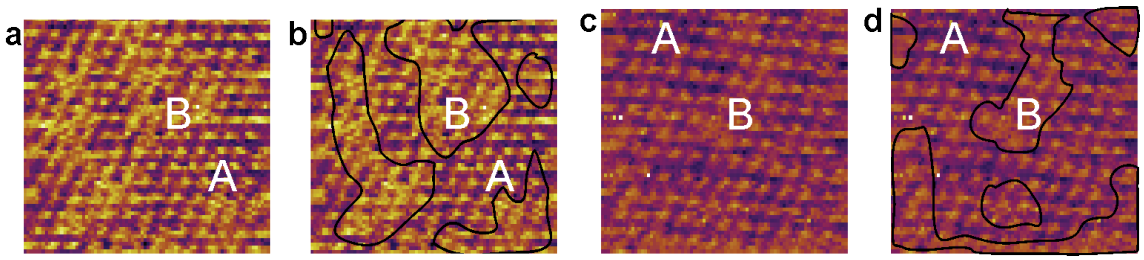

Figure B.1.: xy phase planes extracted from an xyt phase cube on mica in KCl solution (aq.) at different concentrations. By extracting the panels from the time-domain data, the plane corresponds to a distance of 0.25 nm above the respectively lowest point (which is different for each A and B, regions). Hence A and B regions appear with a different structure in the phase image and can be marked and counted. **a.** 200 mM. 50.74 % A (*i.e.,* not occupied with ions), 49.26 % B (*i.e.,* occupied with ions). **b.** 2 mM. 61 % A (not occupied), 39 % B (occupied). $k_1 = 9.2$ N/m.

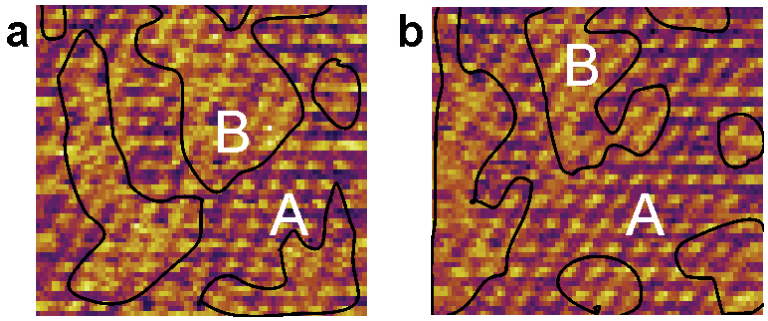

Figure B.2.: xy phase planes extracted from an xyt phase cube on mica in 200 mM KCl solution (aq.). The same area was scanned twice within 1 min. The patches of A and B are overall at the same positions. $k_1 = 9.2$ N/m.

B.3. Additional panels

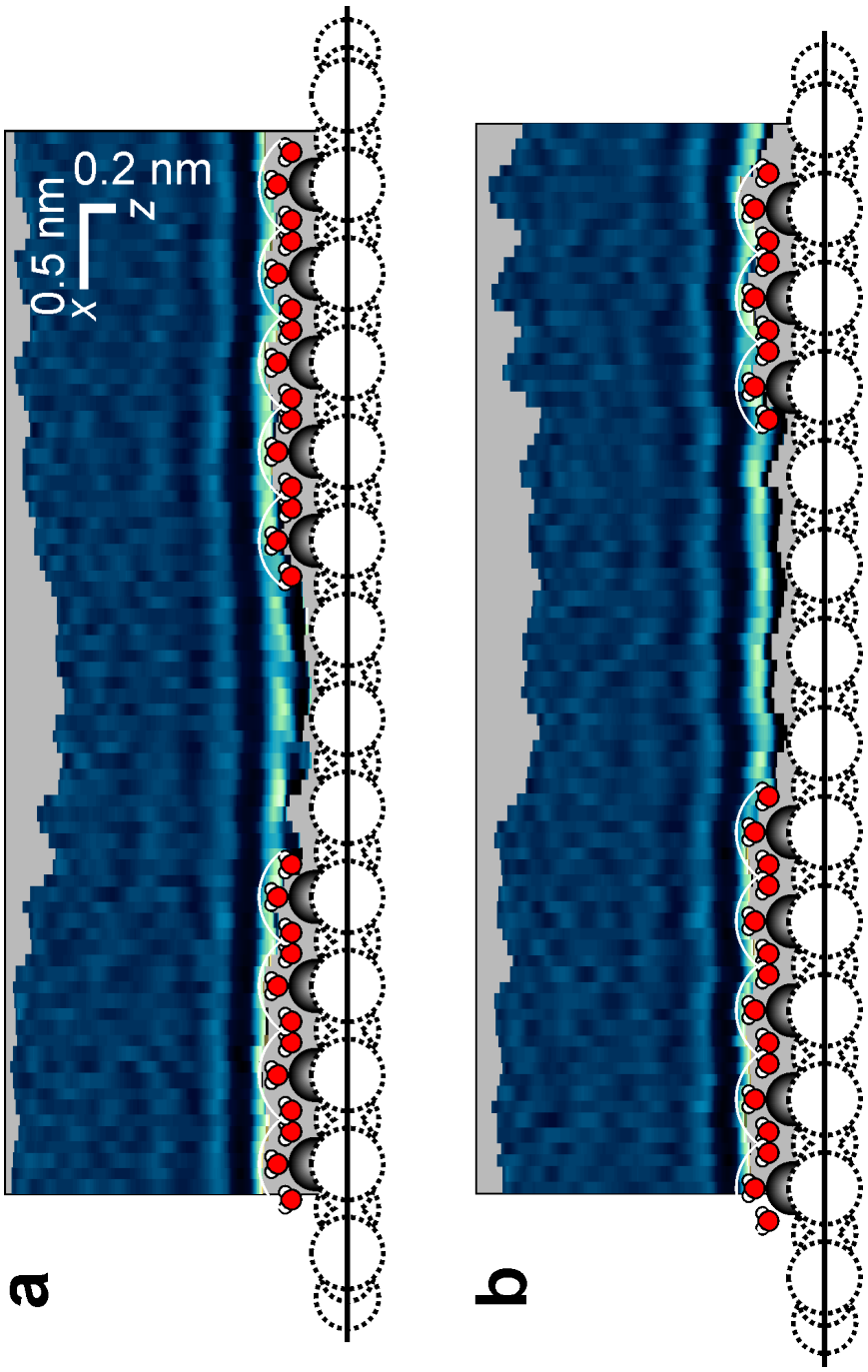

Figure B.3.: Mica immersed in 200 mM KCl (aq.). Comparison between 3D-AFM data and reported crystal structure data obtained from different X-ray methods. Further examples. $k_1 = 12$ N/m

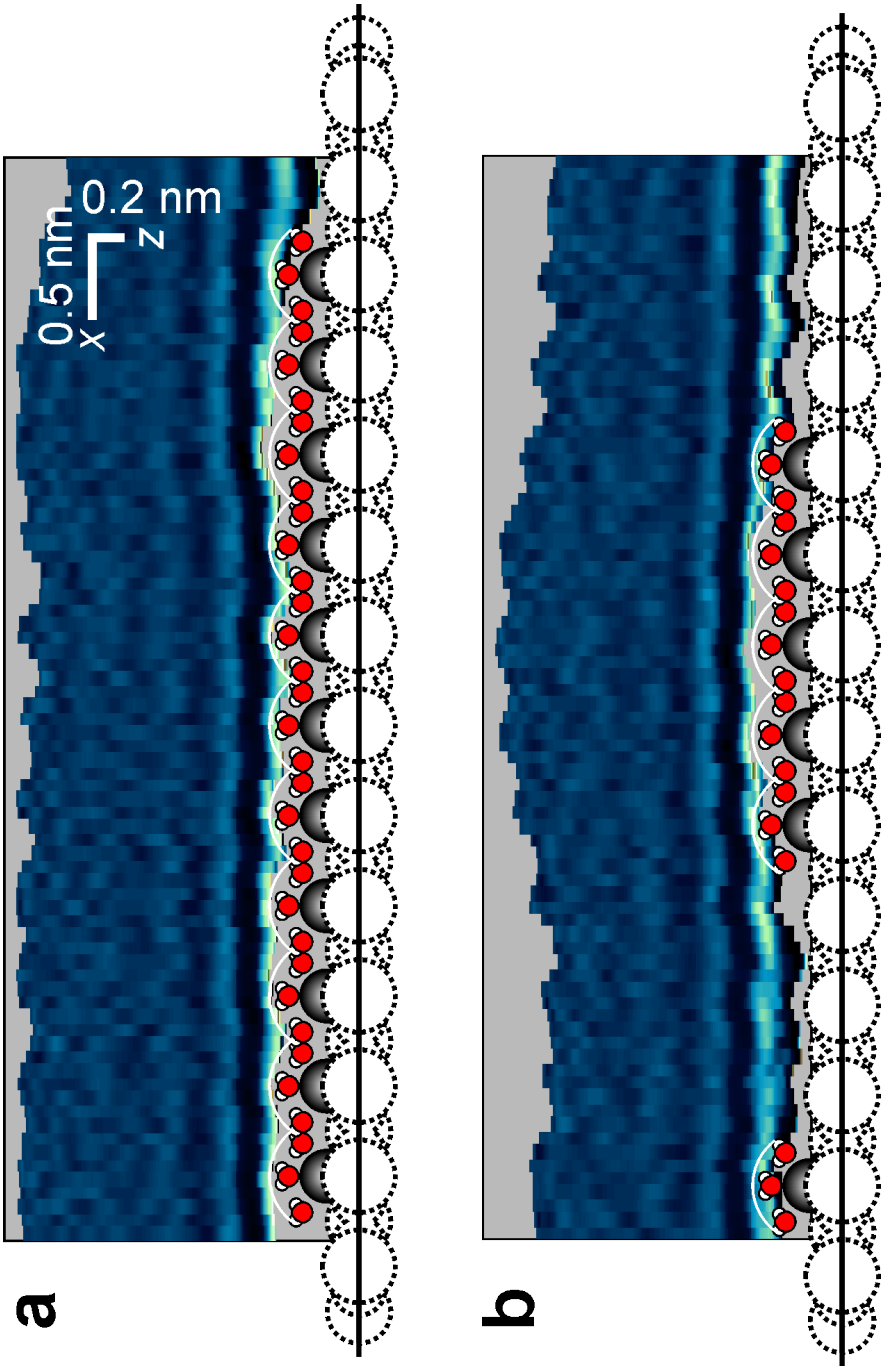

Figure B.4.: Mica immersed in 200 mM KCl (aq.). Comparison between 3D-AFM data and reported crystal structure data obtained from different X-ray methods. Further examples. $k_1 = 12$ N/m

B.4. Very stiff cantilevers

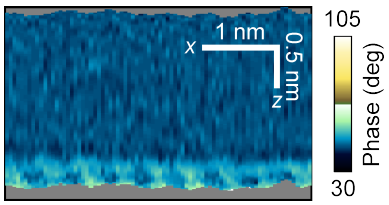

Figure B.5.: Mica in KCl. Representative xz phase panel obtained from a 3D measurement on mica immersed in 200 mM KCl (aq.). The observations coincide with the experiments acquired with softer levers at lower imaging set-point ratios. The gray areas are not accessed by the tip. $k_2 = 1875$ N/m

B.5. Comparison of different cantilevers

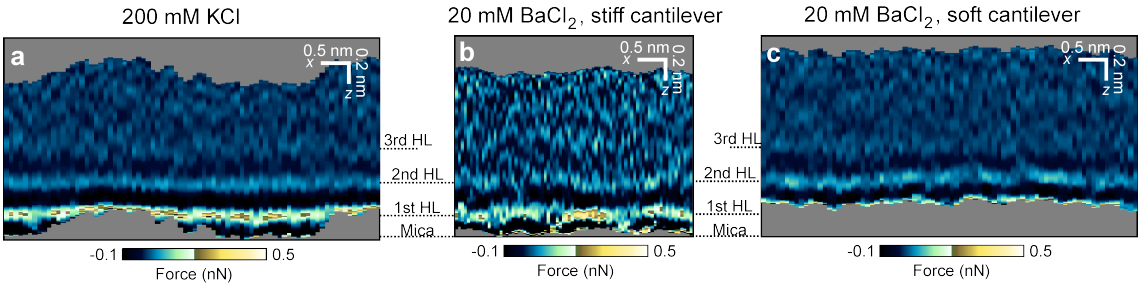

Figure B.6.: Comparison between xz force panels obtained on mica in monovalent and divalent salt solutions with different cantilevers. **a.** 200 mM KCl, $k_1 = 12$ N/m. The panel serves as a reference because it shows the 1s-3d hydration layer (HL) as well as the mica. **b.** 20 mM $BaCl_2$, $k_1 = 191$ N/m. The vertical height of the panel was shifted until the contrast matched the one in panel a. **c.** 20 mM $BaCl_2$, $k_1 = 12$ N/m. The vertical height of the panel was shifted until the contrast matched the one in panel a.

C. Supporting Information Chapter 6

C.1. Comparison of extension models

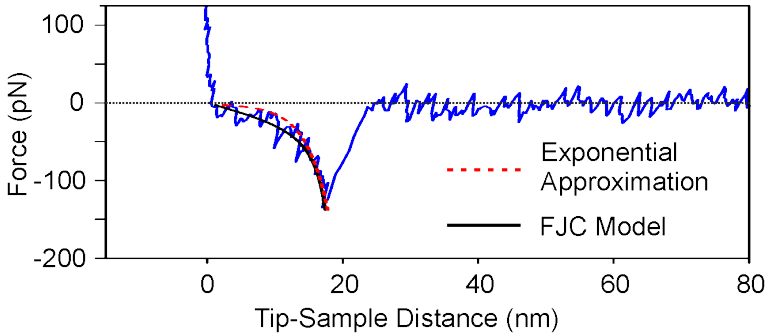

Figure C.1.: Comparison of the FJC polymer extension model and the exponential approximation. The AFM-based SMFS curve was obtained at a pulling speed of 4 µm/s. The data is the same as in Figure 6.6 of the main text.

C.2. Additional experiment

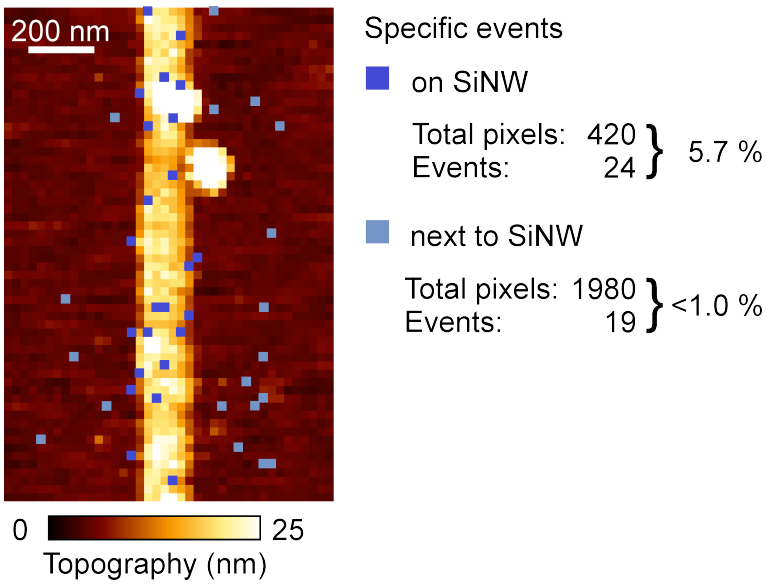

Figure C.2.: Detection of specific unbinding events on a functionalized silicon nanowire (SiNW) surrounded by an octadecyltrichlorosilane (OTS) layer. Repetition of the experiment (Experiment 2). The image shows the topography obtained over the SiNW by force-volume imaging. Each pixel corresponds to an entire force-distance curve. Pixels where specific avidin-biotin events were detected are marked in blue tones (blue: on the SiNW, light blue: next to the SiNW).

C.3. Cantilever parameters for chapter 6

Table C.1.: Cantilever parameters for Chapter 5, all for liquid.

Section	Experiment	Figure	Cantilever type	k_0 ($\frac{\text{pN}}{\text{nm}}$)	Q	f_r (kHz)	σ ($\frac{\text{nm}}{\text{V}}$)
Newton Dynamics in SMFS	Force Spectroscopy Curves	6.6	MSCT-B	29.32	1.6	3.05	20.0
		6.8					
		6.9					
SMFS on SiNW	FV Map 1	6.10	MSCT-D	32	-	-	26.3
	FV Map 2	6.10	MSCT-D	39	-	-	24.4
		6.11					
Force Spectroscopy on IgG	AM Scan	6.13	FastScan D	0.22	1.8	93	26.24
	QI Mapping	6.14	AC40TS	0.13	-	35	5.90
		6.15					

List of Publications

- Manuel R. Uhlig, Daniel Martin-Jimenez and Ricardo Garcia. Atomic-scale mapping of hydrophobic layers on graphene and few-layer MoS_2 and WSe_2 in water. *Nature Communications* **10**, 2606 (2019).
- Manuel R. Uhlig, Carlos A. Amo and Ricardo Garcia. Dynamics of breaking intermolecular bonds in high-speed force spectroscopy. *Nanoscale* **10**, 17112 (2018).